UNIVERSITY OF BIRMINGHAM

APPLICATION OF EVOLUTIONARY COMPUTATION TO OPEN CHANNEL FLOW MODELLING

by

SOROOSH SHARIFI

A thesis submitted to
The University of Birmingham
for the degree of

DOCTOR OF PHILOSOPHY

Department of Civil Engineering
School of Engineering
The University of Birmingham
August 2009

Abstract

This thesis examines the application of two evolutionary computation techniques to two different aspects of open channel flow. The first part of the work is concerned with evaluating the ability of an evolutionary algorithm to provide insight and guidance into the correct magnitude and trend of the three parameters required in order to successfully apply a quasi 2D depth averaged Reynolds Averaged Navier Stokes (RANS) model to the flow in prismatic open channels. The RANS modeled adopted is the Shiono Knight Method (SKM) which requires three input parameters in order to provide closure, i.e. the friction factor (*f*), dimensionless eddy viscosity (λ) and a sink term representing the effects of secondary flow (Γ). A non-dominated sorting genetic algorithm II (NSGA-II) is used to construct a multi-objective evolutionary based calibration framework for the SKM from which conclusions relating to the appropriate values of *f*, λ and Γ are made. The framework is applied to flows in homogenous and heterogeneous trapezoidal channels, homogenous rectangular channels and a number of natural rivers. The variation of *f*, λ and Γ with the wetted parameter ratio (P_b / P_w) and panel structure for a variety of situations is investigated in detail. The situation is complex: *f* is relatively independent of the panel structure but is shown to vary with P_b / P_w, the values of λ and Γ are highly affected by the panel structure but λ is shown to be relatively insensitive to changes in P_b / P_w. Appropriate guidance in the form of empirical equations are provided. Comparing the results to previous calibration attempts highlights the effectiveness of the proposed semi-automated framework developed in this thesis.

The latter part of the thesis examines the possibility of using genetic programming as an effective data mining tool in order to build a model induction methodology. To this end the flow over a free overfall is exampled for a variety of cross section shapes. In total, 18 datasets representing 1373 experiments were interrogated. It was found that an expression of form $h_c = \mathrm{A} h_e e^{\mathrm{B}\sqrt{S_0}}$, where h_c is the critical depth, h_e is the depth at the brink, S_o is the bed slope and A and B are two cross section dependant constants, was valid regardless of cross sectional shape and Froude number. In all of the cases examined this expression fitted the data to within a coefficient of determination (CoD) larger than 0.975. The discovery of this single expression for all datasets represents a significant step forward and highlights the power and potential of genetic programming.

TO MY FAMILY

Acknowledgments

First and foremost, I would like to express my profound appreciation and sincere thanks to my supervisors, Dr.Mark Sterling and Professor Donald W. Knight for their invaluable instruction and inspiration. I am grateful to them not only for their supervision, but for their major contribution in the formation of my character and skills as a young researcher. I eagerly hope to have another chance to work under their supervision.

I must give my special thanks to my dear friend Dr. Alireza Nazemi. He was indeed a "private tutor" providing me with invaluable advice, direction and new viewpoints while I was carrying this research. I would also like to thank my other friends and colleagues in particular Budi, Krishna and Hosein for the enjoyable discussions and their encouragement.

I would also like to offer my sincere thanks to all those who assisted me in gathering the required data for analysis. In no particular order, thank you to Prof. Donald Knight, Dr. Mark Sterling, Dr. Mazen Omran, Dr. Jennifer Chlebek, Dr. Caroline McGahey and Dr. Xiaonan Tang.

I am richly blessed to have my parents who are always there for me. I would like to thank them for their love, support, inspiration and advice. I would also like to express my deep gratitude to my parents in-law for their encouragement and support. Undoubtely, the completion of this research would not have been possible without their support.

Finally I want to thank my sweet wife Narges, who has been a constant source of emotional support, encouragement and patience. Thanks for being cheerfully understanding over the years that I worked on this thesis.

Table of Contents

Chapter 3: Evolutionary and Genetic Computation

Chapter 4: Multi-Objective Calibration Framework for the SKM

Chapter 5: Calibrating the SKM for Channels and Rivers with Inbank Flow

Chapter 6: Genetic Computation: An Efficient Tool For Knowledge Discovery

Chapter 7: Conclusions

Chapter 8: Recommendations for Future Work

List of Figures

List of Tables

List of Symbols

Latin Alphabet

A	=	constant	
A	=	area	(m^2)
a_z	=	acceleration normal to the flow direction	($m.s^{-2}$)
B	=	constant	
B	=	total channel width	(m)
b	=	half width of main channel	(m)
b'	=	half width of flat bed section of a trapezoidal channel	(m)
b''	=	width of sloping sidewall section of a trapezoidal channel	(m)
C	=	Chezy's resistance coefficient	($m^{1/2}.s^{-1}$)
C_1	=	dimensionless integration constant	
$C_{2\text{-}4}$	=	channel constants in logarithmic velocity profile	
C_5	=	constant in Percentage of wall shear force equation	
C_6	=	constants in Prandl's equation	
$C_{7\text{-}9}$	=	constant in Colebrook-White equation	
C_d	=	coefficient of discharge	
C_{sf}	=	shape factor	
c	=	regression coefficients	
D	=	diameter	(m)
d	=	outside diameter of the Pitot tube	(m)
d_n	=	particle diameter so that n % of the particles of the grain distribution is smaller	
E	=	specific energy	(m)
$\hat{E}$	=	E / h_c	
e	=	distance between the water surface and the center of area of the section	(m)
F	=	force	(N)
$F( )$	=	empirical function	
F_i	=	non-dominated sorted fronts of R_t	
F(X)	=	vector of objectives	
F_P	=	total pressure force	(N)
F_r	=	Froude number	
f	=	Darcy-Weisbach friction factor	
$f_i(X)$	=	objective function	
g	=	gravitational acceleration	($m.s^{-2}$)
gen	=	number of maximum generations	
H	=	total head	(m)
h	=	flow depth	(m)

h_f	=	head loss due to friction	(m)
h_{ep}	=	effective mean hydrostatic pressure head	(m)
$\tilde{h}$	=	h / h_c	
$\bar{h}$	=	average depth of channel	(m)
k	=	Number of clusters	
k	=	coefficient used in the analytical solution of the SKM	
k	=	turbulent kinetic energy	(J)
k_s	=	Nikuradse's equivalent roughness	(m)
L	=	length of channel / pipe	(m)
l	=	mixing length	(m)
M	=	number of objective functions	
m	=	exponent in power law velocity distribution	
N	=	number of panels / number of decision variables	
n	=	Manning's coefficient	
P	=	panel	
P	=	wetted perimeter	(m)
P	=	pressure	($N.m^{-2}$)
P_a	=	Atmospheric pressure	($N.m^{-2}$)
P_b	=	wetted perimeter of the bed	(m)
P_c	=	crossover probability	(m)
P_m	=	mutation probability	
P_t	=	parent population	
P_w	=	wetted perimeter of the wall	(m)
pop	=	population size	
Q	=	channel discharge	($m^3.s^{-1}$)
Q_t	=	offspring population	
q	=	channel discharge per unit width	($m^2.s^{-1}$)
R	=	hydraulic radius	(m)
R	=	set of real numbers	
$\overline{R}$	=	resistance hydraulic radius	(m)
Re	=	Reynolds number	
R_t	=	combination of parent and offspring population	
S_o	=	channel bed slope	
S_e	=	energy slope	
S_w	=	water surface slope	
SF	=	shear force	(N)
$\%SF_w$	=	percentage of shear force on the walls	
S_c	=	critical slope	

S_{My}	=	y momentum source term	
S_{Mz}	=	z momentum source term	
s	=	side slope (1:s = vertical: horizontal)	
T	=	top width of flow	(m)
t	=	bed thickness of circular channels	(m)
t	=	time	(s)
tps	=	tournament pool size	
U_d	=	depth averaged streamwise velocity	($m.s^{-1}$)
U_s	=	surface velocity	($m.s^{-1}$)
U_{avr}	=	Mean flow velocity	($m.s^{-1}$)
u	=	streamwise velocity	($m.s^{-1}$)
$\overline{u}$	=	time average streamwise velocity	($m.s^{-1}$)
u'	=	streamwise velocity fluctuations	($m.s^{-1}$)
u_*	=	shear or friction velocity	($m.s^{-1}$)
V	=	velocity vector	
V_i	=	components of velocity vector	
V	=	element volume	
v	=	transverse velocity	($m.s^{-1}$)
$\overline{v}$	=	time average transverse velocity	($m.s^{-1}$)
v'	=	transverse velocity fluctuations	($m.s^{-1}$)
w	=	vertical velocity	($m.s^{-1}$)
$\overline{w}$	=	time average vertical velocity	($m.s^{-1}$)
w'	=	vertical velocity fluctuations	($m.s^{-1}$)
X	=	variable vector	
X^*	=	Non-dimensional variable in Patel's (1965) calibration of the Preston tube	
x	=	streamwise coordinate	
x_i	=	decision variable	
Y	=	set of dependent variables	
Y^*	=	Non-dimensional variable in Patel's (1965) calibration of the Preston tube	
y	=	lateral coordinate	
y_i	=	dependent variable of a system	
y_n	=	normal distance	(m)
z	=	coordinate normal to bed	

Greek Alphabet

α	=	coefficient used in the analytical solution of the SKM/ energy coefficient	
β	=	coefficient used in the analytical solution of the SKM	
β	=	Boussinesq coefficient	
Γ	=	secondary flow parameter	
γ	=	Specific weight of water (=ρg)	
γ	=	coefficient used in the analytical solution of the SKM	
δ	=	boundary layer width	(m)
Δ	=	change/difference	
ε_n	=	noise term	
ε	=	viscous dissipation rate	($m^2.s^{-3}$)
ε_t	=	total eddy viscosity	($m^2.s^{-1}$)
$\bar{\varepsilon}_{yx}$	=	depth-averaged eddy viscosity	($m^2.s^{-1}$)
η	=	coefficient used in the analytical solution of the SKM	
η_c	=	real number GA crossover operator	
η_m	=	real number GA mutation operator	
θ	=	angle of inclined manometer	
κ	=	von Karman's constant	
λ	=	dimensionless eddy viscosity	
μ	=	coefficient used in the analytical solution of the SKM	
μ	=	dynamic viscosity	($N.s.m^{-2}$)
μ_l	=	dynamic laminar viscosity	($N.s.m^{-2}$)
μ_t	=	dynamic turbulent viscosity	($N.s.m^{-2}$)
ν	=	kinematic viscosity	($m^2.s^{-1}$)
ξ	=	local depth	(m)
ρ	=	fluid density	($kg.m^{-3}$)
σ	=	normal stress	($N.m^{-2}$)
$\bar{\tau}$	=	laterally averaged boundary shear stress	($N.m^{-2}$)
τ_i	=	local boundary shear stress	($N.m^{-2}$)
τ_0	=	boundary shear stress	($N.m^{-2}$)
τ_b	=	bed shear stress	($N.m^{-2}$)
τ_w	=	bed shear stress	($N.m^{-2}$)
τ_{xy}^R	=	Reynolds stress	($N.m^{-2}$)
$\bar{\tau}_{yx}$	=	depth-averaged Reynolds stress	($N.m^{-2}$)
Ω	=	design domain search space	
Ω_o	=	objective domain search space	
ψ	=	projection onto plane due to choice of Cartesian coordinate system	
ω	=	coefficient used in the analytical solution of the SKM	

Subscripts

0	=	section with hydrostatic pressure
1-5	=	panel number
avr	=	average
b	=	channel bed
c	=	critical depth section
d	=	depth
data	=	based on measurements
e	=	end section
exp	=	experimental data
fc	=	flood plain
i	=	panel number
L	=	width of channel
mc	=	main channel
n	=	normalized /normal
r	=	rough
SKM	=	predictions obtained using the SKM
s	=	surface level
T	=	total
t	=	time / total
g	=	global value of either Q or $\%SF_w$
w	=	channel wall

List of Abbreviations

ANN	=	Artificial Neural Network
AP	=	Analytical Programming
ADV	=	Acoustic Doppler Velocity
APE	=	Absolute Percentage Error
Asp	=	Aspect Ratio (*2b/h*)
ASM	=	Algebraic Stress Model
CES	=	Conveyance Estimation System
CoD	=	Coefficient of Determination
CV	=	Control Volume
EA	=	Evolutionary Algorithms
EC	=	Evolutionary Computation
EDR	=	End-Depth Ratio (h_e/h_c)
EMO	=	Evolutionary Multi-Objective
EP	=	Evolutionary Programming
ES	=	Evolution Strategy
FCF	=	Flood Channel Facility
GA	=	Genetic Algorithms
GE	=	Grammar Evolution
GP	=	Genetic Programming
HWA	=	Hot Wire Anemometer
LCS	=	Learning Classifier Systems
LDA	=	Laser Doppler Anemometer
MOEA	=	Multi-Objective Evolutionary Algorithms
MOGA	=	Multi-Objective Genetic Algorithm
MPM	=	Merged Perpendicular Method
MRSS	=	Mean Root of Sum of Squared Residuals
NAM	=	Normal Area Method
NDM	=	Normal Depth Method
NSGA-II	=	Nondominated Sorting Genetic Algorithm II
RANS	=	Reynolds Averaged Navier Stokes
RMSE	=	Root Mean Square of Errors
SBX	=	Simulated Binary Crossover
SKM	=	Shiono and Knight method
SSE	=	Sum of Squared Errors
VAM	=	Vertical Area Method
VDM	=	Vertical Depth Method
VEGA	=	Vector Evaluated Genetic Algorithm

CHAPTER 1

INTRODUCTION

1.1 OPEN CHANNEL FLOW MODELLING

Rivers, the arteries of nature, are one of the world's most valuable natural resources and are important to our lives in many ways. Rivers are critical for our health, as they are one of the main supplies of our basic need: drinking water. They nourish our crops and provide substantial transportation benefits. Furthermore, they sustain natural systems and communities, provide critical habitats for wildlife, and are significant sources of enjoyment and recreation. Their natural, cultural and historical legacies are rich, and the quality of our life is inseparably linked to them.

The essential benefits of rivers along with the relatively flat area which river valleys offer have encouraged the human populations to reside along rivers. However, living near rivers is not without any disadvantages as the flow of water in rivers is never constant. Unexpected precipitation, combined with other causes (e.g. drainage modifications of the catchment, dam failures, etc.), may increase the amount of water flowing in a river which often leads to flooding. Floods are of the most common and costly types of natural disasters (see Figure (1-1)) and due to the global climate changes in recent decades, the number of reported floods has increased significantly (7.4 % per year on average (Scheuren *et al*., 2008)). Furthermore, with limited sources of water, rivers have become one of the main sources of conflicts all over the world (Cunge and Erlich, 1999). These issues have been the main motivation to study and understand the meteorological, hydrological and hydrodynamic processes related to rivers. Managing the limited water resources of rivers and irrigation water are essential to the survival of the ever increasing population of the world.

In order to predict, control and make efficient use of rivers and open channels, measurements of different properties (e.g. depth, discharge, velocity, boundary shear stress) of the hydrodynamic flow are often required. These measurements are usually accomplished by two methods:

1- Directly, using measurement techniques, where the properties of the flow are measured with an instrument;

2- Indirectly using numerical models to predict the behaviour and properties of the flow.

Apart from their high cost, the use of measurement instruments in open channels and rivers is not always convenient and in some cases, is not even feasible (e.g. during flood events). This has, in turn, focused more attention on the development of stable, accurate and reliable models. These models are "*a set of general laws or mathematical principles and a set of statements of empirical circumstances*" (Hampel, 1963) which describe the properties of the flow, and range from simple empirical models (e.g. the Manning and Chezy model) to complicated models which are based on the numerical solution of the governing equations of the complex motion of the turbulent flow (Figure (1-2)).

Over the last few decades, considerable attention has been focused on the development of simple models based on the solution of the Saint Venant (1843) equations for one-dimensional flow (for more details see McGahey, 2006). The primary focus of these studies has been on simple channel geometries, most typically rectangular and trapezoidal cross-sections, as these geometries are easy to build and test in the laboratory, and furthermore, their results are extendable to natural rivers which are often schematized by such geometries. Outcomes from these studies have generally suggested that the performance of these simple models is approximately as accurate as complex models.

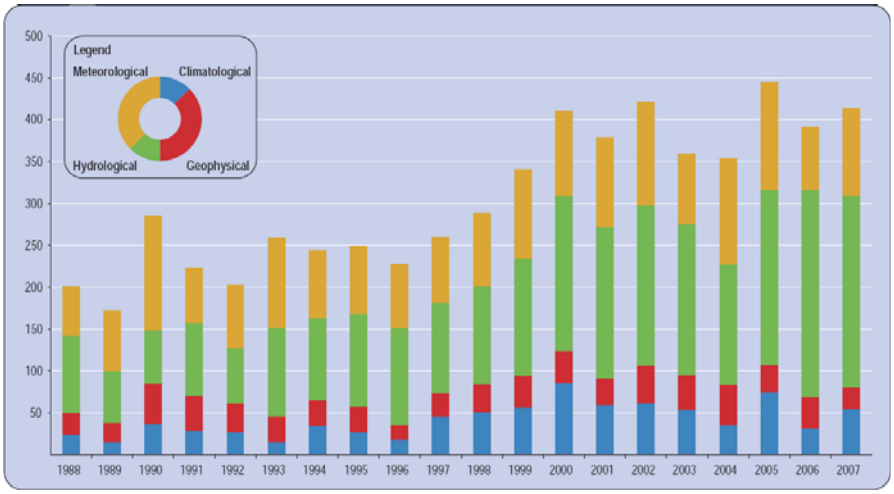

a) Occurrences

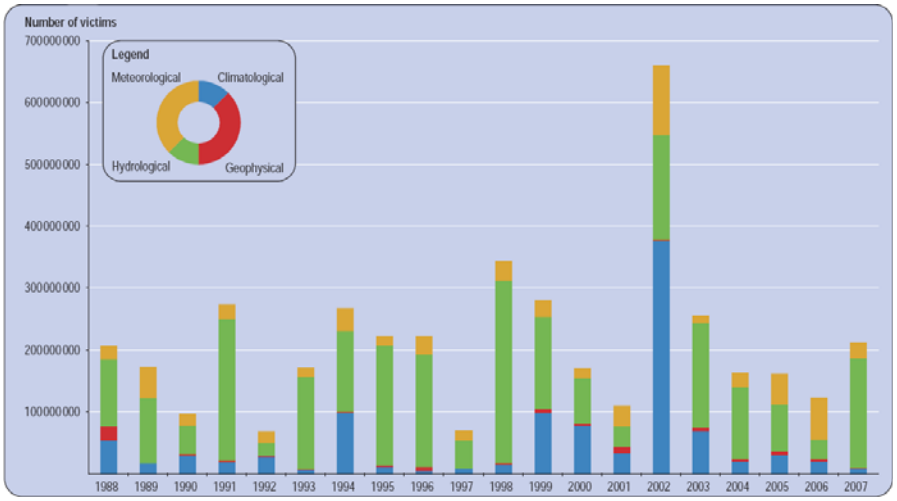

b) Number of victims

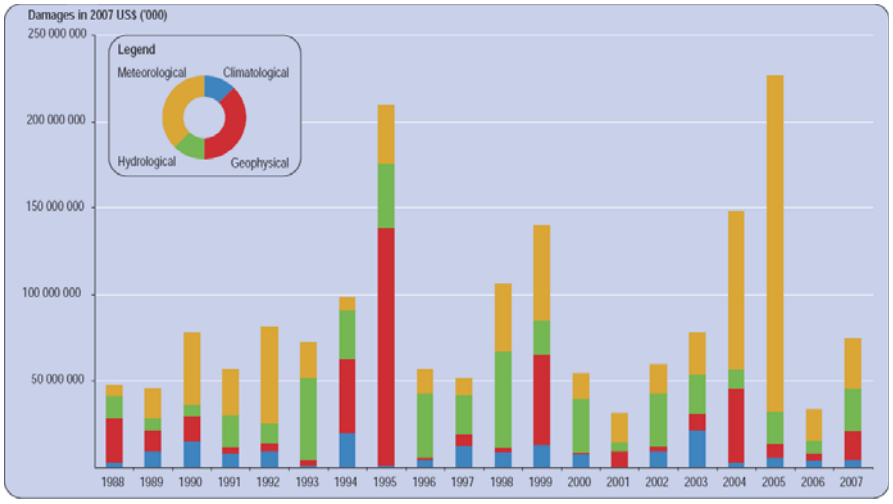

c) Damages

Figure (1-1): Trends of a) occurrences b) number of victims and c) damages of natural disasters between 1988 and 2007 (Scheuren *et al.*, 2008).

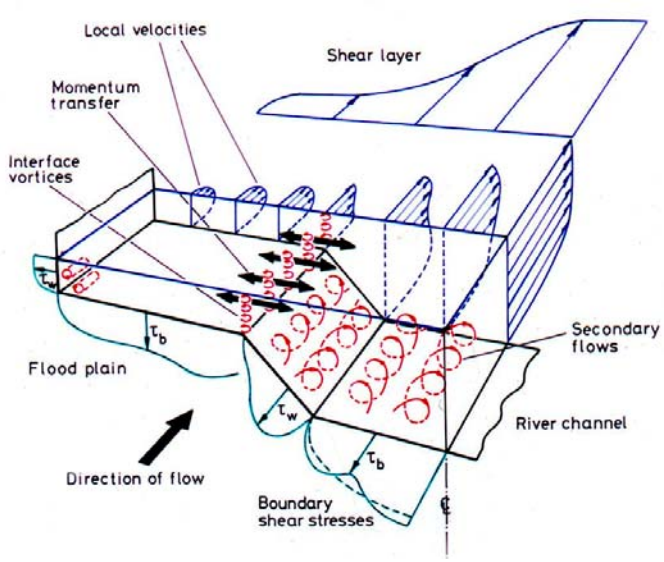

Figure (1-2): Complex 3D structure of flow in open channels (Shiono and Knight, 1991).

Among these simple models, Reynolds Averaged Navier Stokes (RANS) based models, such as the Shiono & Knight method (SKM) (Shiono and Knight, 1988; 1991), have been among the most popular methods used by researchers and have undergone significant developments in the last three decades (e.g. Wormleaton, 1988; Samuels, 1988; Lambert and Sellin, 1996; Ervine *et al*., 2000; Bousmar and Zech, 2004). The SKM provides a tool for water level prediction (by estimating or extending stage-discharge curves), for distributing flows within a cross section (for damage assessments of buildings, eco-hydraulics & habitats), and for predicting the lateral distributions of boundary shear stress (for geomorphological and sediment transport studies). Its promising results both for channels and rivers have led it to being adopted by the UK's Environment Agency for use in its 'Conveyance and Afflux Estimation System' software (www.river-conveyance.net).

1.2 GAPS IN KNOWLEDGE

All models, including hydrodynamic models, are simple approximations of the real world process and without exception all embrace some degree of deficiency. The problems with environmental modelling can be partitioned into three main components: model structure, data and parameter estimation procedures. Successful development and application of any hydrodynamic model requires careful consideration of each component and its relevance to the overall modelling problem. The problems in the model structure stem from the perception

and understanding of the flow process and also the simplifications, inadequacies and ambiguity in its description. The data related problems are caused by errors in the measurement of input and output data which are used to evaluate the model structure.

Another major problem which can have a significant influence on the model output, is the difficulty associated with estimating the model parameters. Inevitably, there are always some "*immeasurable*" parameters in the model which cannot be directly estimated through measurement or by the correlation between the model parameters and the physical characteristics of the system. This "*immeasurability*" may be down to the lack of an exact physical meaning of the parameters and/or measurement techniques. Therefore, before a model can be used to simulate the real-world processes, the values of some of its parameters should be adjusted. This process is best known as parameter estimation or model calibration, and will result in finding the "*optimal*" values of the immeasurable parameters in the model. Calibration approaches generally involve two components: (1) evaluation of the "*closeness*" between the model outputs and the corresponding measurement data, and (2) adjustment of the values of the parameters to improve the closeness. The important characteristics of any calibration approach are consistency (the results should be repeatable) and performance (the approach should find the optimal solution(s) in an efficient manner) (Gupta *et al*., 2005). Detailed analysis of model calibrations has revealed that sometimes, there is a set of model parameters that will more or less equally reproduce successful predictions of the system. It has been argued that this is mainly due to the over parameterization of the model and complex interactions of model parameters, given that there are almost never sufficient calibration data to uniquely identify the parameters. This problem is generally called "*lack of identifiability*" and in the context of hydrological modelling, it is known as the "*equifinality*" problem (Beven, 2001).

Like other environmental models, hydraulic models of rivers and open channels potentially contain several variables that may be adjusted as part of a calibration process (Vidal *et al*., 2005). Hence, the output of the hydraulic model is based on prior knowledge of these variables, but ascertaining their values often suffers from lack of definitive measurement methods, imperfections in the mathematical description of the process and/or, lack of data. Some of the problems involved in the calibration of open channel models are recognized by

theoreticians and practitioners (e.g. Romanowicz *et al*., 1996; Khatibi *et al*., 1997; Aronica *et al*., 1998). These studies have mainly applied simple optimization techniques for identifying the model parameters and the primary focus has been on obtaining the appropriate values for the roughness coefficient.

In order to apply the SKM successfully, in addition to the inputs of cross-sectional shape and longitudinal bed slope, detailed knowledge of the lateral variation of the friction factor (f), dimensionless eddy viscosity (λ) and a sink term representing the effects of secondary flow (Γ), are required. Initial guidance on choosing suitable values for f, λ and Γ for compound channels and simple rectangular channels has been provided by Knight and co-authors (Knight and Abril, 1996; Abril and Knight, 2004; Chlebek and Knight, 2006). However, at the time it was recognized that due to the large number of parameters and complex relationships, this work was limited and in some respects was provided as a stop-gap while further development was undertaken.

Another simple open channel flow problem is the free overfall: a situation where the bottom of a channel drops suddenly, causing the flow to separate and form a free nappe (Sterling and Knight, 2001). Based on various experiments in prismatic channels (e.g. Van Leer 1922; Rouse, 1936), the depth of water at the section where the overfall occurs (the end depth, h_e) bears a unique relationship with the critical depth (h_c). However, the location of the critical depth can vary with respect to discharge, whereas the location of the end depth is always fixed. Hence, since there exists a unique relationship between the h_c and the discharge, if a relationship between h_e and h_c is provided, then the free overfall can be used as a simple flow measuring device (Bauer and Graf, 1971). During the last century, many researchers (see Dey (2002b) for a detailed review) have followed different approaches and attempted to discover a relationship between the end depth and the critical depth for many types of channels. However, the proposed models lack a suitable, general notation of the free overfall process and cannot be applied to all possible geometries and flow regimes.

1.3 EVOLUTIONARY PARADIGM

150 years ago Charles Darwin (1859) published his research "on the origin of the species" and made his name synonymous with his theory of natural evolution. His thoughts evolved and his ideas were taken up by other biologists and naturalists such as Lamarck and Wallace to form "the primary unifying concept of biology" (Babovic and Zhang, 2002). The key feature of Darwin's natural evolution is natural selection or "survival of the fittest" i.e. over many generations, natural selection and random variation shape the behaviour of individuals and species to fit the demands of their surroundings. The creative aspects of Darwin's thoughts, has initiated a new renaissance in the scientific world. Various studies in the last century have suggested that "*there are no living sciences, human attitudes, or institutional powers that remain unaffected by the ideas that were catalytically released by Darwin's work*" (Collins, 1959).

Inspired by Darwin's theory of natural evolution and motivated by the development of computer technologies, Evolutionary Computation (EC) was introduced in the 1960s as a robust and adaptive search method. Imitating the two-step iterative process of natural evolution - random variation followed by selection within a computer - these techniques are capable of solving complex problems that the traditional algorithms have been unable to conquer. An EC algorithm begins by creating an initial random set of potential solutions for a particular problem. Then, the fittest "parents" are selected and "children" are generated by means of sexual reproduction (crossover) or asexual alteration (mutation). In crossover, two parents swap random pieces of information with each other while in mutation, a piece of information is replaced by another randomly generated piece. Finally, the resulting solutions (children) are evaluated for their fitness (effectiveness) and selected for reproduction. This process is repeated over successive generations until a stopping criterion is met.

More than 50 years of research in the field of evolutionary computation has proved that the imitation of the natural evolution can provide powerful tools for solving the most complex problems in various fields of science. This unique advantage has led EC to be one of the fastest growing areas of computer science and engineering. The effectiveness of these techniques in the field of hydroinformatics, has been recognized previously (e.g. Babovic and Abbott, 1997a&b; Price and Jemberie 2005; Solomatine and Ostfeld, 2008; Chen *et al.*,

2008). It is believed that EC can solve the problems indicated in the model calibration and model induction procedures. On one hand, it can provide a powerful tool for the multi-objective calibration of hydraulic models. On the other hand it can be used to evolve conceptual transparent models of the processes within the open channel flow by searching among functional structures which are beyond the scope of conventional regression techniques.

1.4 AIMS AND OBJECTIVES

This research can be viewed as a pragmatic attempt towards extracting knowledge from hydraulic data. The ultimate aim is to apply Evolutionary Computation as a powerful knowledge induction tool to bridge the gaps indicated in the field of open channel hydraulics. Two major contributions are presented in this work. First, an evolutionary algorithm called non-dominated sorting genetic algorithm II (NSGA-II) is used to:

- Build a robust multi-objective evolutionary based calibration framework for an existing depth-averaged RANS model (SKM).
- Calibrate the SKM for various simple channels and rivers with inbank flow and identify the values of its three "*immeasurable*" parameters (f, λ, Γ).
- Investigate the lateral variation of f, λ, Γ in the light of the calibration results and to provide generalized rules for their identification.

Second, Genetic Programming (GP) is implemented in a model induction framework to derive a global, conceptual, transparent model of the physical process of the free overfall. The obtained model is then evaluated on different datasets corresponding to various channel cross-sections with different flow regimes.

1.5 THESIS LAYOUT

The thesis has been divided into eight Chapters including the Introduction. Chapters 2 and 3 provide an introduction to the two different areas of the literature relevant to the current work,

namely Open Channel Flow Modelling and Evolutionary Computation. Chapters 4 and 5 address the first application of EC to open channel flow, i.e. SKM modelling, while Chapter 6 addresses the second application, i.e. the free overfall problem. Specifically, the chapters comprising this thesis are presented as follows:

Chapter 2 reviews the relevant literature on open channel flow hydraulics with the primary emphasis on modelling fully developed turbulent inbank flow in prismatic channels with simple cross-sections. The basic equations of motion are derived, the RANS modelling and more specifically, the Shiono and Knight Method are reviewed and the scientific knowledge gaps are identified. Finally, a review is presented on the classic problem of the free overfall.

Chapter 3 provides an overview of evolutionary computation of relevance to the work contained in this thesis. A multi-objective genetic algorithm called NSGA-II is outlined. Furthermore, information relating to Genetic Programming is described in detail.

Chapter 4 is dedicated to the proposed multi-objective calibration framework for the SKM. A brief overview is provided on the experimental data used in this research and a detailed step-by-step procedure of the calibration framework is presented.

Chapter 5 illustrates the calibration results of the SKM for various simple channels with trapezoidal and rectangular cross sections. Data relating to natural river cross sections with inbank flow are also examined. The Pareto calibration solutions for each dataset are investigated and the lateral variations of the SKM parameters are studied.

Chapter 6 attempts to cover another application of EC to open channel flow. A model induction methodology, which uses Genetic Programming, is presented. The method is applied to various laboratory data to find a conceptual model for the free overfall problem.

Chapter 7 summarizes the key findings and conclusions of this research and examines their implications in a broader context.

Chapter 8 highlights the limitations of this work and provides recommendations for future research, identifying fundamental data requirements, theoretical considerations and practical issues.

1.6 PUBLICATION OF RESEARCH

Some of the work presented in this thesis is published in four refereed journals and conference proceedings. The remaining unpublished sections are being prepared for submission. The following papers can be found in Appendix (I):

Sharifi, S., Knight, D.W., and Sterling, M. (2008) Modelling flow using SKM and a multi-objective evolutionary algorithm. *RiverFlow 2008*. [Eds. Altinakar, M.S.; Kokpinar, M.A.; Aydin, I.; Cokgar, S. & Kirkgoz, S.], Cesme, Turkey, 3: 2149-2158.

Sharifi, S., Knight, D.W., and Sterling, M. (2009) A novel application of a multi-objective evolutionary algorithm in open channel flow modelling. *Journal of Hydroinformatics*, 11 (1): 31-50.

Sharifi, S., Sterling, M., and Knight, D.W. (2009) End-Depth Ratio Prediction in Rectangular and Trapezoidal Channels Using Genetic Programming, *Proceedings of 17th UK Conference on Computational Mechanics ACME 2009*. [Ed. Sansour C.] Nottingham, UK, 105-108.

Sharifi, S., Sterling, M., and Knight, D.W. (2009) Prediction of End-Depth Ratio in Open Channels Using Genetic Programming. *Journal of Hydroinformatics* (in Press).

CHAPTER 2

OPEN CHANNEL FLOW MODELLING

2.1 INTRODUCTION

This chapter presents an overview of open channel flow hydraulics with the primary emphasis on modelling fully developed turbulent inbank flow in prismatic channels with simple cross-sections. Modelling inbank flow (i.e. flow within the main channel) has always been a routine priority since, except for flood events, the flow is contained within the main river channel for most of the time. Furthermore, simple prismatic cross-sections not only represent a basic shape, but are also representative of the geometries that are often used in schematizing natural rivers in numerical models. It should be noted that the explanations provided in this chapter are deliberately kept as brief as possible since all of the topics discussed can be found in a variety of textbooks and review papers (e.g. Chow, 1959; Henderson, 1966; Nezu and Nakagawa, 1993; Cunge *et al*., 1980; Morvan *et al*., 2008; Knight *et al.*, 2009).

The chapter starts with a general discussion on flow modelling and model uncertainty. A section is devoted to revisiting the main governing equations of fluid flow and the derivation of the Reynolds-averaged Navier-Stokes (RANS) equations. The energy transfer mechanisms in turbulent flow and turbulence modelling methodologies are the other topics covered in this section. The chapter continues with two sections, each dedicated to important concepts of the flow in open channels: velocity and boundary shear stress distributions. Having provided the essential background, the complete derivation of the system of equations adopted in the Shiono and Knight Method (SKM) of modelling is provided in the next section. This section continues with a review of recent developments in the SKM and a brief discussion on its internal parameters, namely, the friction factor, dimensionless eddy viscosity and the secondary flow term. The final section of this chapter includes an introduction to the

hydraulics of the free overfall problem, and a summary of the methods employed to solve this problem.

2.2 FLOW MODELLING

2.2.1 Definition

The main aim of science, including environmental sciences, is to find a single correct description of reality (Beven, 2006) and models as Kirkby (1996) states are "*thought experiments which help refine our understanding*" of this reality. In general, environmental models are lumped approximations of the heterogeneous world. These models attempt to represent the complex, spatially distributed, interactions of earth, water, vegetation and energy by means of mathematical and parametric equations (Wagner and Gupta, 2005). This is achieved by combining the physical laws of conservation and constitutive relations associated with kinetic transformations and physical properties (Rodriguez-Fernandez *et al*., 2007).

Surface water is the main source of fresh water: the necessity for much of the life on Earth. Due to this vital importance, the flow in natural rivers and man made channels has been of great interest since early civilizations. Understanding the flow has resulted in better fulfillment of many primary needs such as drinking and irrigation water, food and transportation. This has led to the development of models which can predict the behaviour of the flow. River and channel models can be simply defined as "*the simulation of flow conditions based on the formulation of and solution of mathematical relationships expressing known hydraulic principles*" (Cunge *et al*., 1980).

2.2.2 Flow model classification

Based on their structure, flow models can be classified as mathematical, physical, data-based and computational models.

Mathematical modelling is a comprehensive method of representing the flow process in terms of mathematical equations. These models are built on the discovered physical laws and known relations associated with the flow system. Hence, the model is dependent on factors

such as model dimensionality, the assumptions in the derivation, the number and nature of empirical coefficients, the imposed boundary conditions and its ability to adequately represent the true physical processes. Once the mathematical model is developed, an exact analytical solution may be found for the process. An alternative procedure for more complex models is to solve the set of equations using a step-wise approximation. In this process, which is known as *numerical modelling*, solutions are obtained by performing iterations (successively improved approximations) at each step until the numerical answer satisfies all the equations. The advantage of numerical modelling is that, once the model is set up and established, a range of scenarios may be investigated with relatively little effort. Finite difference and finite element methods are currently the most popular numerical modelling techniques.

Physical modelling is in fact recreating similar flow conditions at a smaller scale. The observations and measurements taken in the physical model provide useful information of the process. The main concern about physical modelling is whether these observations and measurements at a different scale can be generalized to the natural process. The results of this modelling process can be used to modify other mathematical models and obtain the value of some internal empirical parameters.

Data-based modelling is the process of generalizing various observations of the inputs, characteristics and outputs of the flow system. This type of modelling normally results in a simple conceptual model for predicting a particular characteristic of the flow (e.g. conveyance, mean velocity, shear stress, etc.).

Computational modelling is the final modelling level, where the basic equations of fluid motion are coupled with computational techniques to provide a more detailed prediction of the flow process and its characteristics.

2.2.3 Modelling uncertainty

In order to be able to select a suitable model for a specific application and use it for future predictions, some elements of the model (i.e. structure, parameters, initial boundary conditions) along with the inputs and outputs of the system should be defined, measured or

estimated. It is obvious that the uncertainty in each of these elements can give rise to the error between model prediction of a variable and the observational data of the same variable. Understanding this uncertainty within the predictions and decisions is essential to understanding the risk. Gupta *et al*. (2005) classify the different sources of uncertainty into the following groups:

Perceptual uncertainty is a major source of uncertainty that stems from our perception and understanding of the real-world process. It is this understanding that is translated into a mathematical (numerical) form in the model.

Model structure uncertainty is the simplifications, inadequacies and ambiguity in the description of real-world processes. This uncertainty is the most significant component of the overall predictive uncertainty. While research to date has focused mainly on the treatment of parameter and data uncertainty, it has recently become apparent that the impact of model structural error has typically been underestimated and can often be more severe than that of uncertain parameters (Carrera and Neuman, 1986).

Data uncertainty: is the uncertainty caused by errors in the measurement of input and output data or by data processing and also lack of objective approaches to evaluate the model structure (Wagner *et al*., 2003).

Parameter estimation uncertainty: describes the inability to uniquely locate a 'best' parameter set based on the available information. In fact, there are always some parameters in the model which either cannot be directly estimated through measurement or by the correlation between the model parameters and the physical characteristics of the system. Therefore various parameter sets, often widely distributed within the feasible parameter space may yield equally good results in terms of a predefined objective function (Freer *et al*., 1996).

Understanding the origins of uncertainty is a common problem in any modelling application. This problem derives from the fact there are a variety of sources for the errors but usually one measure of the deviation or residual between prediction and observation exists. Even if multiple performance measures are employed, they can produce conflicting prediction errors

(an improvement in one prediction, results in deterioration in another). In reality, it is often not possible to separate the different sources of model uncertainty as the model structure might not be correct. Therefore, identifying the error sources and their contribution to the total error is almost impossible, particularly when the model is non-linear and different sources of error may interact in a non-linear way to produce the measured deviation (Beven, 2004).

In the ideal case, the model structure and the data are assumed to be correct and hence the uncertainty over model parameters becomes "*the dominant source of uncertainty*" (Hunter et al., 2008). In this case, there is a significant possibility for calibrated parameter values to compensate for different types of errors. To deal with this problem, assumptions (which are sometimes difficult to justify) are made about the nature of the errors (Beven, 2006). A major step forward to deal with the uncertainty problem is the development of methods that quantify model uncertainty, which enable the modellers to provide an informed estimate of the uncertainty associated with a model simulation (Wheater *et al*., 2007).

2.3 DEPTH AVERAGED MOMENTUM EQUATIONS

Understanding the flow structure and its physics in open channels and rivers is a prerequisite for the development of appropriate mathematical flow models. The aim of this section is to derive and discuss those laws of fluid mechanics which are particularly important for understanding turbulence and developing RANS models like SKM.

2.3.1 Forces acting on a fluid element

The forces that act on a particle of fluid immersed in water which are important in deriving the governing equations of motion can be grouped into two categories (Cohen *et al*., 2004):

1- Surface forces: i.e. forces exerted on an element area by the surroundings through direct contact such as forces due to *pressure*, *shear*, etc. When the fluid velocity is zero, the pressure variation is due only to the weight force of the fluid. Hence, in all directions, the force due to the *pressure* at a point is evaluated from the hydrostatic pressure forces which increase with increasing depth. Relative to the hydrostatic pressure forces, the spatial

variations in atmospheric pressure at the water surface are normally negligible. *Shear* forces, also known as *viscous* forces, are present when the fluid is in motion. The resistance caused by bed friction makes the water at the channel bed regions move more slowly than the layers located vertically above them. This effect reduces as the distance from the bed increases. At the water surface level and, in the absence of other forces (e.g. wind) the shear stresses are approximately zero.

2- Body forces: i.e. forces imposed on the mass of the fluid element without physical contact as a result of the element being placed in a certain force field, which can be *gravitational*, *centrifugal*, *magnetic*, or *electromagnetic* in origin. The main body force that acts on a fluid particle is the *gravity force* which is due to the weight of the fluid particle. *Centrifugal accelerations* develop when the streamlines are curvilinear; causing a non-hydrostatic pressure distribution and the fluid particles accelerate in the direction normal to the streamlines.

Figure (2-1) shows the surface forces of pressure and shear acting on a small fluid control volume in the streamwise direction (x is the streamwise, y the lateral and z the vertical directions, respectively). In this figure, σ_{ij} and τ_{ij} are the normal and shear stresses respectively, where the subscript 'i' indicates the direction normal to the surface that the stress is acting on and 'j' indicates the direction of the force. It is to be noted that other body forces like the *Coriolis accelerations* and *Electromagnetic forces* are normally neglected due to their weak effect on the fluid particle and its motion (Goncharov, 1964).

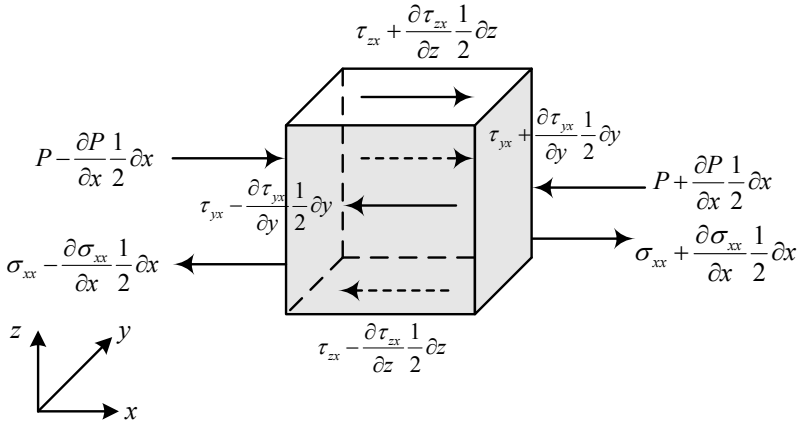

Figure (2-1): Surface forces acting on a fluid particle in the streamwise direction.

2.3.2 Main Governing Equations

Newton's second law implies that the mass of the fluid element times its acceleration, is equal to the net forces due to pressure acting on the element plus any viscous forces arising from viscous stresses (Streeter, 1985; White, 1999; Drazin and Riley, 2006):

$$\sum F = -(\nabla P)\delta V \ + viscous\ \ forces = (\rho \delta V\ )\frac{DV_i}{Dt} \tag{2-1}$$

where F is the net force, P the pressure, ρ the density of water, $\delta V\ = \delta x.\delta y.\delta z$ the element volume and V_i is the velocity components normal to the element sides. The total surface forces that act on a fluid particle in the streamwise direction can be derived from Figure (2-1):

$$\begin{aligned}\sum F_x &= \left[P - \frac{\partial P}{\partial x}\frac{1}{2}\delta x\right]\delta y\delta z - \left[P + \frac{\partial P}{\partial x}\frac{1}{2}\delta x\right]\delta y\delta z + \left[\sigma_{xx} \frac{\partial \sigma_{xx}}{\partial x}\frac{1}{2}\delta x\right]\delta y\delta z - \left[\sigma_{xx} \frac{\partial \sigma_{xx}}{\partial x}\frac{1}{2}\delta x\right]\delta y\delta z \\ &+ \left[\tau_{zx} + \frac{\partial \tau_{zx}}{\partial z}\frac{1}{2}\delta z\right]\delta y\delta x - \left[\tau_{zx} - \frac{\partial \tau_{zx}}{\partial z}\frac{1}{2}\delta z\right]\delta y\delta x + \left[\tau_{yx} + \frac{\partial \tau_{yx}}{\partial y}\frac{1}{2}\delta y\right]\delta z\delta x - \left[\tau_{yx} - \frac{\partial \tau_{yx}}{\partial y}\frac{1}{2}\delta y\right]\delta z\delta x \\ &= \left[\frac{\partial \sigma_{xx}}{\partial x} - \frac{\partial p}{\partial x}\right]\delta y\delta x\delta z + \frac{\partial \tau_{zx}}{\partial z}\delta y\delta x\delta z + \frac{\partial \tau_{yx}}{\partial y}\delta y\delta x\delta z\end{aligned} \tag{2-2}$$

For a channel in a straight reach and, in the absence of centrifugal forces, the pressure distribution is hydrostatic and given by:

$$P = P_a + \rho g(h_s - z) \tag{2-3}$$

where P_a is the atmospheric pressure which can be considered negligible and h_s is the water surface level. The gravitational acceleration, g, acts in the negative z-direction and only has a component in the x-direction if the water surface or the channel bed is not horizontal. Thus, defining the bedslope, S_o, as $-dz/dx$ (positive when the channel slopes downstream in the flow direction) and substituting the changes in water surface level with the changes of the flow depth, h, the change of pressure in the streamwise direction is:

$$\frac{\partial P}{\partial x} = \rho g\left(\frac{\partial h_s}{\partial x} - \frac{\partial z}{\partial x}\right) = \rho g\left(\frac{\partial h}{\partial x} - S_0\right) \tag{2-4}$$

Substituting Eqs. (2-3 & 2-4) in Eq. (2-1):

$$\sum F_x = \frac{\partial \sigma_{xx}}{\partial x} + \frac{\partial \tau_{yx}}{\partial y} + \frac{\partial \tau_{zx}}{\partial z} + \rho g\left(\frac{\partial h}{\partial x} - S_o\right) = \rho \frac{Du}{Dt} \tag{2-5}$$

Considering $\frac{dx}{dt} = u$ (streamwise velocity), $\frac{dy}{dt} = v$ (lateral velocity) and $\frac{dz}{dt} = w$ (vertical velocity), the total derivative of $\frac{Du}{Dt}$ can be written as:

$$\frac{Du}{Dt} = \frac{\partial u}{\partial t} + \frac{\partial u}{\partial x}\frac{\partial x}{\partial t} + \frac{\partial u}{\partial y}\frac{\partial y}{\partial t} + \frac{\partial u}{\partial z}\frac{\partial z}{\partial t} = \frac{\partial u}{\partial t} + u\frac{\partial u}{\partial x} + v\frac{\partial u}{\partial y} + w\frac{\partial u}{\partial z} \tag{2-6}$$

Expanding this through the product rule yields,

$$\begin{aligned}\frac{Du}{Dt} &= \frac{\partial u}{\partial t} + \frac{\partial uu}{\partial x} + \frac{\partial uv}{\partial y} + \frac{\partial uw}{\partial z} - u\frac{\partial u}{\partial x} - u\frac{\partial v}{\partial y} - u\frac{\partial w}{\partial z} \\ &= \frac{\partial u}{\partial t} + \frac{\partial uu}{\partial x} + \frac{\partial uv}{\partial y} + \frac{\partial uw}{\partial z} - u\left(\frac{\partial u}{\partial x} + \frac{\partial v}{\partial y} + \frac{\partial w}{\partial z}\right)\end{aligned} \tag{2-7}$$

The *conservation of mass* implies that the rate of increase of mass in a fluid element is equal to the net rate of flow of mass into the fluid element (White, 1999; Drazin and Riley, 2006):

$$\int_{CV} \frac{\partial \rho}{\partial t} dV + \sum_i (\rho_i A_i V_i)_{out} - \sum_i (\rho_i A_i V_i)_{in} = 0 \tag{2-8}$$

where A_i is the area of element sides and V_i is the velocity component normal to the element sides. Considering a small particle size:

$$\int_{CV} \frac{\partial \rho}{\partial t} dV \;;\; \frac{\partial \rho}{\partial t}\delta x \delta y \delta z \tag{2-9}$$

Substituting Eq. (2-9) in (2-8) and simplifying gives:

$$\frac{\partial \rho}{\partial t}\delta x \delta y \delta z + \frac{\partial}{\partial x}(\rho u)\delta x \delta y \delta z + \frac{\partial}{\partial y}(\rho v)\delta x \delta y \delta z + \frac{\partial}{\partial z}(\rho w)\delta x \delta y \delta z = 0 \tag{2-10}$$

Cancelling the element volume ($\delta x \delta y \delta z$) from all terms yields:

$$\frac{\partial \rho}{\partial t} + \frac{\partial}{\partial x}(\rho u) + \frac{\partial}{\partial y}(\rho v) + \frac{\partial}{\partial z}(\rho w) = 0 \quad \text{or} \quad \frac{\partial \rho}{\partial t} + \nabla.(\rho V) = 0 \tag{2-11}$$

For a steady ($\frac{\partial}{\partial t} = 0$) and incompressible fluid ($\frac{\partial \rho}{\partial t} = 0$) it can be concluded that:

$$\nabla.V = 0 \quad \rightarrow \quad \frac{\partial u}{\partial x} + \frac{\partial v}{\partial y} + \frac{\partial w}{\partial z} = 0 \tag{2-12}$$

Implementing this result into Eq. (2-7) and considering a steady state flow, Eq. (2-5) can be rewritten as:

$$\frac{\partial \sigma_{xx}}{\partial x}+\frac{\partial \tau_{yx}}{\partial y}+\frac{\partial \tau_{zx}}{\partial z}+\rho g\left(\frac{\partial h}{\partial x}-S_o\right)=\rho\left[\frac{\partial uu}{\partial x}+\frac{\partial uv}{\partial y}+\frac{\partial uw}{\partial z}\right] \tag{2-13}$$

If uniform flow is assumed, with parallel streamlines and no curvature, Eq. (2-13) can be further simplified to:

$$\frac{\partial \tau_{yx}}{\partial y}+\frac{\partial \tau_{zx}}{\partial z}+\rho g\left(\frac{\partial h}{\partial x}-S_o\right)=\rho\left[\frac{\partial uv}{\partial y}+\frac{\partial uw}{\partial z}\right] \tag{2-14}$$

In a Newtonian fluid, the viscous stresses are proportional to the element deformation rates (Stokes' Law) and the coefficient of viscosity (μ). These deformations include translation (e.g. *udt*; *vdt*), extension (e.g. *du*/*dx*.*dxdt*), rotation (e.g. *dv*/*dx*-*du*/*dy* = vorticity) and angular strains. For incompressible flow, the volumetric deformation is zero, and hence, the relevant viscous stresses are only related to the angular strains (Schlichting, 1979):

$$\tau_{yx}=\mu\left(\frac{\partial u}{\partial y}+\frac{\partial v}{\partial x}\right);\quad \tau_{zx}=\mu\left(\frac{\partial u}{\partial z}+\frac{\partial w}{\partial x}\right) \tag{2-15}$$

Substituting these stresses into Eq. (2-14) gives:

$$\frac{\partial}{\partial y}\left(\mu\left(\frac{\partial u}{\partial y}+\frac{\partial v}{\partial x}\right)\right)+\frac{\partial}{\partial z}\left(\mu\left(\frac{\partial u}{\partial z}+\frac{\partial w}{\partial x}\right)\right)+\rho g\left(\frac{\partial h}{\partial x}-S_o\right)=\rho\left[\frac{\partial uv}{\partial y}+\frac{\partial uw}{\partial z}\right] \tag{2-16}$$

Again, assuming uniform flow conditions, this can be simplified to,

$$\frac{\partial}{\partial y}\left(\mu\frac{\partial u}{\partial y}\right)+\frac{\partial}{\partial z}\left(\mu\frac{\partial u}{\partial z}\right)+\rho g\left(\frac{\partial h}{\partial x}-S_o\right)=\rho\left[\frac{\partial uv}{\partial y}+\frac{\partial uw}{\partial z}\right] \tag{2-17}$$

Eq. (2-17) represents a simplified form of the *Navier-Stokes* equation for flow in the streamwise (*x*) direction. With analogy, the Navier-Stokes equations for incompressible flow in the lateral and vertical directions are:

$$\rho\frac{Dv}{Dt}=-\frac{\partial P}{\partial y}+\frac{\partial}{\partial x}\left[\mu\left(\frac{\partial u}{\partial y}+\frac{\partial v}{\partial x}\right)\right]+\frac{\partial}{\partial y}\left[2\mu\frac{\partial v}{\partial y}\right]+\frac{\partial}{\partial z}\left[\mu\left(\frac{\partial v}{\partial z}+\frac{\partial w}{\partial y}\right)\right]+S_{My} \tag{2-18}$$

$$\rho\frac{Dw}{Dt}=-\frac{\partial P}{\partial z}+\frac{\partial}{\partial x}\left[\mu\left(\frac{\partial u}{\partial z}+\frac{\partial w}{\partial x}\right)\right]+\frac{\partial}{\partial y}\left[\mu\left(\frac{\partial v}{\partial z}+\frac{\partial w}{\partial y}\right)\right]+\frac{\partial}{\partial z}\left[2\mu\frac{\partial w}{\partial z}\right]+S_{Mz} \quad (2\text{-}19)$$

where S_{My} and S_{Mz} are the y and z momentum source terms respectively which count for the Coriolis forces, wind shear, gravity, etc. The above equations will be used in order to derive the SKM model which is employed in later parts of this thesis. However, before such a derivation is made, attention will be focused on exploring the concept of turbulence.

2.3.3 Turbulence

2.3.3.1 From laminar to turbulent flow

Fluid flow may be classified as either laminar or turbulent, or in transition between these two regimes. A flow is laminar if the viscous forces due to molecular cohesion are strong enough to overcome the fluid's inertial forces. Flows that are both steady and laminar exhibit absolutely no variation in time except for the random motion of fluid molecules. In this regime, the fluid appears to consist of thin layers that flow past one another in smooth pathways and the flow can be accurately described by the Navier-Stokes equations (Bradshaw, 1971; Nezu and Nakagawa, 1993; Drazin and Riley, 2006).

As the inertial forces are increased, a critical point is reached when the viscous forces are no longer able to maintain the laminar structure of the flow. Lumps of fluid migrate between the adjacent fluid layers in a seemingly random manner with velocity component transverse to the main direction of flow. This new regime of fluctuating motion, characterized by chaotic and stochastic property changes is referred to as turbulence (Reynolds, 1974; Nezu and Nakagawa, 1993). In this chaotic state of motion, the velocity and pressure change continuously with time, within substantial regions of flow and therefore the fluid particles continuously interchange energy and momentum (Schlichting, 1979). In open channel flow, turbulence is born near the boundaries where the primary perturbations and eddies form due to high velocity gradients. These eddies swiftly drift into the main flow field and increase in size by entraining particles of the surrounding fluid (Goncharov, 1964; Schlichting, 1979).

The first person to mathematically formulate turbulence was Osborne Reynolds (1883; 1884). Conducting experiments on pipe flow in the late 19th century, Reynolds observed the two quite different types of flow that can be formed in a given flow situation. He discovered that at lower velocities, where the flow is laminar, the velocity vector is everywhere parallel to the axis of the pipe. But in contrast, at higher velocities the magnitude and the direction of the velocity components fluctuate and a different type of flow forms. Reynolds also found that both pressure drop and heat transfer are higher in turbulent flow than in laminar flow, and showed that this difference is due to the lateral component of velocity which exists when the motion is turbulent (Leslie, 1973). To distinguish between laminar and turbulent flow, he proposed a dimensionless number (known as the Reynolds number) as a measure of the ratio of inertial forces ($V.\rho$) to the viscous forces (μ / L) (V is the velocity and L is the pipe length). Despite dedicating his life to the study of turbulence, Reynolds never realized the random characteristics of turbulence and described the motions occurring in turbulent flow as a 'sinuous' wave. For a more detailed background on the history of turbulence see Bradshaw (1971), Schlichting (1979), Nezu and Nakagawa (1993), Davidson (2004) and Drazin and Riley (2006).

2.3.3.2 Energy cascade in turbulent flows

The major difference between laminar and turbulent flow is the appearance of perturbations and formation of a broad spectrum of eddies due to the high velocity gradients. Observing this spectrum led Lewis Fry Richardson (1922 cited in Davidson, 2004) and later Kolmogorov (1941) to introduce the concept of the "energy cascade". A schematic representation of the energy cascade is shown in Figure (2-2). Based on this idea, the largest eddies, which are created by instabilities, interact with the flow domain and rapidly break and pass their energy onto smaller eddies. Smaller eddies are themselves unstable and they, in turn, pass their energy onto even smaller structures and so on. This cascade process of energy transition continues until the viscous forces become significant and dissipate the energy in the smallest eddies.

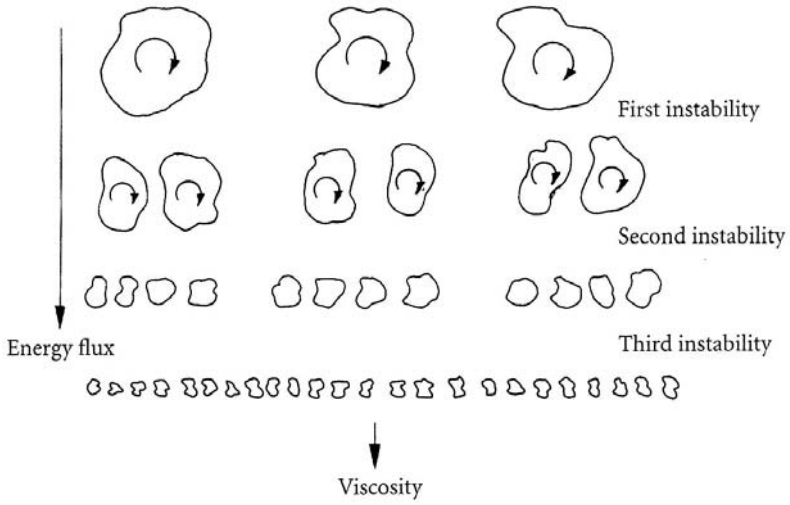

Figure (2-2): A Schematic representation of energy cascade (Davidson, 2004).

2.3.3.3 Features of turbulence

The main features and characteristics of turbulence can be summarized as follows (Goncharov, 1964; White, 1991, Davidson, 2004 and Ahmadi, 2005):

- Turbulence is a manifestation of flow and not of the fluid.
- Turbulence is a continuum phenomenon.
- Turbulence is rotational and three-dimensional motion.
- Turbulence is a chaotic and seemingly random phenomenon.
- Turbulence causes fluctuations in both velocity and pressure in all directions.
- Turbulence is associated with high levels of vorticity fluctuation.
- The transverse velocities in turbulent flows increase the internal resistance of the fluid which results in flattening the lateral profile of the streamwise velocity.
- Eddies form and mix with each other and the mean flow in all directions.
- Turbulence is highly diffusive. Rapid mixing significantly increases momentum, heat, and mass transfer.
- Turbulence is highly dissipative. It needs a source of energy to be maintained.
- The self-sustaining motion produces new eddies and disturbances that replace those lost to viscous dissipation (see Figure (2-2)).

2.3.3.4 Turbulence modelling

In certain types of laminar flow, the flow regime is simple and some non-linear terms in the Navier-Stokes equations (Eqs. 2-17 to 2-19) can be ignored, leading to exact solutions to the equations. In other more complex laminar flows, these terms cannot be ignored and no exact solutions are possible. In turbulent flow however, because of the random fluctuations of the various flow properties, the Navier-Stokes equations cannot be directly applied. To overcome this problem, many turbulence theories have been developed by a number of researchers, and attempts have been made to apply them in mathematical models (Versteeg and Malalasekera, 1995). Since the exact nature of the three-dimensional mixing action of turbulence is not yet known, all these models, as Rodi (1995) mentions, are assumptions and approximations for the dispersive, diffusive and chaotic turbulent processes. As their main objective, turbulence models attempt to model the dissipation and the energy transfer mechanisms of small size eddies where kinetic energy is transformed into to internal energy and heat. This is done by finding closure for the turbulence terms within the governing equations. In other words, the effects of turbulence on the mean flow are simulated by solving the closure problem through the application of turbulence models (Rodi, 1995). Methods for estimating this turbulence and finding closure can be classified into four major subgroups:

Algebraic Models (Zero equation models)

Algebraic models are the simplest kind of turbulence closure models which are solely based on Prandtl's mixing length hypothesis (see Section 2.3.4.4). This approach towards approximating turbulence started in 1877 with the introduction of the concept of eddy viscosity by Boussinesq (Johnson, 1998). After that, in 1895, Reynolds (Tennekes and Lumley, 1997) suggested that all the random characteristics of turbulent flow could be expressed as the summation of mean and fluctuating parts. In the beginning of twentieth century, Prandtl introduced the term "boundary layer," and after that, in 1925, he introduced the "mixing length", based on dimensional analysis and an analogy to the mean free path in gas dynamics. Following the fundamental work of Boussinesq, Reynolds and Prandtl, many researchers, including von Karman, used the mixing-length concept as a basis for turbulence models. In Algebraic closure models, which are generally used in depth-averaged models, the horizontal turbulent momentum transport is assumed to be low and a constant eddy viscosity is often introduced to relate the shear stresses to the strains.

One-Equation Models

As indicated by its name, one equation models are models where an equation for the transport of turbulent quantities is introduced. These models are an improvement on zero equation models in that they account for the convective and diffusive transport of the turbulent velocity scale. In these models, the velocity scale or length scale are found from a differential equation which is then incorporated in a length model to determine the turbulent terms (Johnson, 1998). In the mid 20th century, Prandtl introduced the first equation of this kind which he named the "*K*-equation". The main problem with the one-equation closures is that in these models, the length scale has to be taken from some empirical argument. This shortcoming has empirically been shown to seriously limit the usefulness and generality of this type of model (Nezu and Nakagawa, 1993; Johnson, 1998).

Two-Equation Models

The difficulty in determining the length scale in one-equation models has led to the devolvement of two-equation models, which determine the length scale from two transport equations. The k-ε model is the most famous model of this kind which was initially developed by Jones and Launder (1973). This closure model introduces two transport equations for the turbulent kinetic energy (k) and the rate of viscous dissipation (ε). These are then used to approximate length and velocity scales, which are used to determine the eddy viscosity. Because of its simplicity and relatively short computation time, this model has been developed and extensively used by researchers in recent years (Rodi, 1995; Johnson, 1998). Despite its popularity, this method has some shortcomings. For instance, the assumption of isotropic properties results in poor predictions of normal Reynolds stresses, turbulent shear flows and secondary flows (Speziale, 1987). Furthermore, the model does not perform well with flows that have extra large strains e.g. curved boundary layers, swirling flows, buoyancy; as well as rotational flows and some unconfined flows.

In an attempt to extend the k-ε modelling to include nonlinear effects, Speziale (1987) proposed an anisotropic eddy viscosity model which included time derivatives of the velocity gradients, along with nonlinear terms of the gradients themselves, in an analogy to the kinetic theory of gases. For channel flows, this nonlinear model satisfies the anisotropy requirement

that has been observed experimentally (Speziale, 1987) and therefore is able to predict the secondary circulations.

Reynolds Stress Models

The previously discussed models are somehow based on the Boussinesq approximation and assume that the turbulent behaviour can be characterized by relating an eddy viscosity to a velocity scale or gradient. An alternative approach is to consider the actual transport of the Reynolds stresses. Reynolds stress models attempt to correct some deficiencies of the Boussinesq approximation by including the convection, production, and diffusion of the Reynolds shear stresses and the body force terms in their formulation. These models are best-suited to flows such as curved streamlines, swirling flow and flows in non-circular pipes where turbulent anisotropy should be taken into account.

To overcome the problem of solving the traditional differential equations for the Reynolds stresses, Rodi (1976) was the first to derive a two-equation algebraic Reynolds stress model (ASM) with the help of the equilibrium hypothesis. Two assumptions were made in this closure: First, the difference between the convection and diffusion terms in the Reynolds stress equation was assumed to be proportional to the corresponding difference in the turbulent kinetic energy equation, and second, the Reynolds stress anisotropy was thought to be constant along a streamline. Following the same equilibrium hypothesis as Rodi, Pope (1975) developed a methodology to procure an explicit relation for the Reynolds stress tensor from the implicit algebraic stress model. Gatski and Speziale (1993) used this method to derive an explicit algebraic stress equation for two- and three-dimensional turbulent flows. These explicit models extend the ability of the two-equation models to account for non-equilibrium and anisotropic effects.

2.3.4 Depth averaged RANS equations

2.3.4.1 Reynolds time averaging concept

At first glance, because of the fluctuation of velocity and pressure with time and space, turbulent flow appears almost too random and complicated for mathematical modelling. However, when averaged over time, the random terms show signs of ordered behaviour.

Reynolds (1884) was the first to realize this generality and used this concept to propose a time averaging approach. Based on his observations he suggested that all flow quantities can be expressed as the summation of mean and fluctuating parts. For instance, the individual fluctuating velocity components can be defined in terms of the average velocity and a fluctuating component (see Figure (2-3)):

$$u = \bar{u} + u'; \quad v = \bar{v} + v'; \quad w = \bar{w} + w' \tag{2-20}$$

where by definition, the time-averaged components are:

$$\bar{u} = \frac{1}{\Delta t}\int_{t}^{t+\Delta t} u\,dt \neq 0; \qquad \overline{u'} = \frac{1}{\Delta t}\int_{t}^{t+\Delta t} u'\,dt = 0; \qquad \overline{uu'} = \frac{1}{\Delta t}\int_{t}^{t+\Delta t} u\,u'dt = 0 \tag{2-21}$$

In this case, the continuity relation (conservation of mass) (Eq. 2-13) would be:

$$\frac{\partial \bar{u}}{\partial x} + \frac{\partial \bar{v}}{\partial y} + \frac{\partial \bar{w}}{\partial z} = 0 \tag{2-22}$$

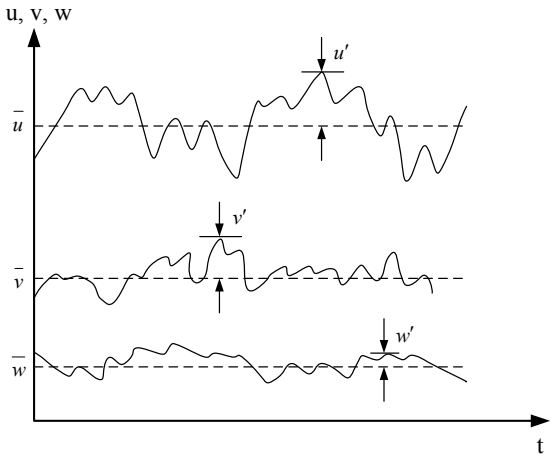

Figure (2-3): Concept of mean and fluctuating turbulent velocity components.

2.3.4.2 Reynolds stress model

Reynolds (1884) also recognized that in turbulent flow, fluid fluctuations cause shear stress by the transfer of momentum and demonstrated that turbulent stresses, τ^R, (also known as apparent or Reynolds stresses) were proportional to the time average of the product of velocity fluctuations within the flow (Nezu and Nakagawa, 1993; Nezu, 2005). In the streamwise direction, these Reynolds stresses are:

$$\tau_{xz}^{R} = \overline{-\rho u'w'}\,, \quad \tau_{xy}^{R} = \overline{-\rho u'v'}\,, \quad \tau_{xx}^{R} = \overline{-\rho u'^{2}} \tag{2-23}$$

It is to be noted that Reynolds stresses are not really a true stress but rather, represent the mean momentum fluxes induced by the turbulence. It is clear that to predict the behaviour of the mean turbulent flow, the Reynolds Stresses should be somehow approximated.

2.3.4.3 Boussinesq theory of eddy-viscosity

As mentioned in Section (2.3.3), if the flow is laminar, the internal tangential shear stresses can be related to the linear dynamic viscosity through Stoke's law (Batchelor, 1967). In the mid-nineteenth century, Saint-Venant (1843) and Boussinesq (1877) suggested a similar transformation to approximate the random characteristics of turbulent flow. In their concepts of "eddy viscosity", a general shear-stress strain-rate relationship was proposed to relate the mean rate of deformation to the turbulent stresses (Schlichting, 1979, Davidson, 2004):

$$\tau_{xz}^{R} = \overline{-\rho u'w'} = \varepsilon_t \left(\frac{\partial u}{\partial x} + \frac{\partial w}{\partial z} \right) = \left(\mu_l + \mu_t \right) \left(\frac{\partial u}{\partial x} + \frac{\partial w}{\partial z} \right) \tag{2-24}$$

where the eddy viscosity ε_t is the sum of the laminar (μ_l) and turbulent (μ_t) viscosities. The eddy viscosity can be viewed as a coefficient of momentum transfer expressing the transfer of momentum from points where the velocity is low to points where it is higher and vice versa (Finnmore and Franzizi, 2002).

2.3.4.4 Prandtl mixing length theory

Prandtl was the first to propose a distribution law for the eddy viscosity based upon a mixing length hypothesis (Schlichting, 1979; White, 1991 and Rodi, 1995). In this model, the concept of eddy-viscosity was conceived by presuming an analogy between molecular motion and the turbulent motion (Figure (2-4)). As Davidson (2004) writes, "*The turbulent eddies were thought as lumps of fluid which, like molecules, smash together and exchanged momentum*". Prandtl assumed that the molecular viscosity is proportional to the average velocity and mean free path of the molecules, and accordingly, considered the eddy viscosity to be proportional to a velocity characterizing the fluctuating motion and to a typical length of this motion, which he called the mixing length:

$$u' = l\frac{d\bar{u}}{dz} \text{ and } w' = u' \qquad \therefore \tau_{xz}^{R} = -\rho\overline{u'w'} = \rho\ell^2 \frac{d\bar{u}}{dz}\left|\frac{d\bar{u}}{dz}\right| \tag{2-25}$$

where l is the mixing length and $\bar{u}$ is the averaged streamwise velocity. Comparing Eq. (2-25) with Eq. (2-24) gives:

$$\varepsilon_t = l^2 \frac{d\bar{u}}{dz} \tag{2-26}$$

In near wall regions, the mixing length can be related to the distance from the boundary by (Schlichting, 1979; White, 1991):

$$l = \kappa h \tag{2-27}$$

where h is the depth of flow and κ is the von Karman coefficient, which has been determined experimentally as ~0.41 in clear water (Schlichting, 1979). The simple concept of the mixing length model, has made it very useful and effective, especially in two-dimensional flows, where the only significant Reynolds stress is τ_{xz}, and the only significant velocity gradient is du/dz. However, a large drawback of this model is that the definition of the mixing length is case specific, which prevents the model to perform well where processes of diffusive and convective turbulent transport are important (McGahey, 2006). Based on Prandtl's mixing length theory, other similar models have also been proposed to estimate the eddy viscosity (e.g. Lean and Weare, 1979; Cunge *et al*., 1980; Wormleaton, 1988).

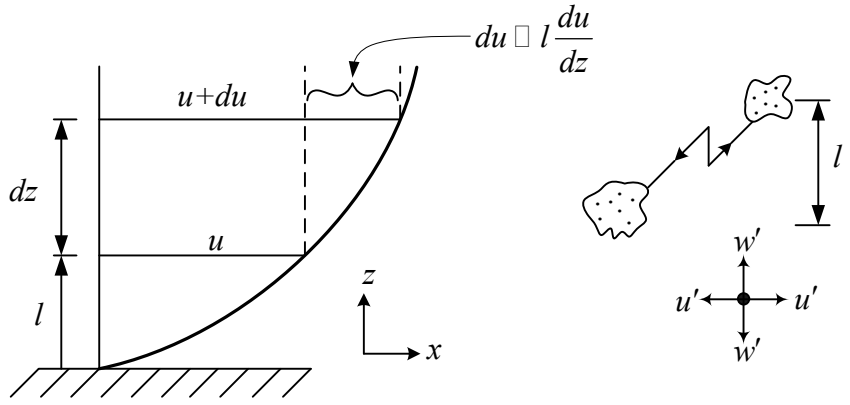

Figure (2-4): Prandl's mixing length concept (Davidson, 2004).

2.3.4.5 RANS equations

Applying the time averaging to the basic equations of motion (i.e. Navier-Stokes equations (Eqs. 2-17 to 2-19)) for incompressible and constant viscosity fluid flow yields the Reynolds equations. Originally proposed by Reynolds in 1895, these equations appear similar to the Navier-Stokes equations except that they include both mean and fluctuating quantities and an additional shear stress term. Neglecting the small fluctuations of pressure and substituting Eq. (2-20) into Eq. (2-17) yields:

$$\frac{\partial}{\partial y}\left(\mu\frac{\partial(\bar{u}+u')}{\partial y}\right)+\frac{\partial}{\partial z}\left(\mu\frac{\partial(\bar{u}+u')}{\partial z}\right)+\rho g\left(\frac{\partial h}{\partial x}-S_o\right) = \rho\left[\frac{\partial(\bar{u}+u')(\bar{v}+v')}{\partial y}+\frac{\partial(\bar{u}+u')(\bar{w}+w')}{\partial z}\right] \tag{2-28}$$

Expanding this equation gives:

$$\mu\frac{\partial^2\bar{u}}{\partial y^2}+\mu\frac{\partial^2 u'}{\partial y^2}+\mu\frac{\partial^2\bar{u}}{\partial z^2}+\mu\frac{\partial^2 u'}{\partial z^2}+\rho g\left(\frac{\partial h}{\partial x}-S_o\right) = \rho\left[\frac{\partial\bar{u}\bar{v}}{\partial y}+\frac{\partial\bar{u}v'}{\partial y}+\frac{\partial u'\bar{v}}{\partial y}+\frac{\partial u'v'}{\partial y}+\frac{\partial\bar{u}\bar{w}}{\partial z}+\frac{\partial\bar{u}w'}{\partial z}+\frac{\partial u'\bar{w}}{\partial z}+\frac{\partial u'w'}{\partial z}\right] \tag{2-28}$$

Time averaging this equation and using the expression provided in Eq. (2-21) gives:

$$\nu\frac{\partial^2\bar{u}}{\partial y^2}+\nu\frac{\partial^2\bar{u}}{\partial z^2}-\frac{\partial\overline{u'v'}}{\partial y}-\frac{\partial\overline{u'w'}}{\partial z}+g\left(\frac{\partial h}{\partial x}-S_o\right)=\frac{\partial\bar{u}\bar{v}}{\partial y}+\frac{\partial\bar{u}\bar{w}}{\partial z} \tag{2-29}$$

This is the RANS equation for flow in the x-direction (streamwise) which is also known as the St. Venant equation (Anderson, 1997).

2.3.4.6 Depth-averaged RANS

A closer look at the values of the velocity fluctuations reveals that u', v' and w' are largest near the channel bed (Schlichting, 1979). Hence, the one dimensional RANS equation can be confidently integrated over the depth, h, to obtain a simplified quasi-2D solution for estimating the depth averaged velocity and conveyance across a straight channel section:

$$\int_0^h \frac{\partial \overline{\overline{uv}}}{\partial y} dz + \int_0^h \frac{\partial \overline{\overline{uw}}}{\partial z} dz = \int_0^h \nu \frac{\partial}{\partial y}\left(\frac{\partial \overline{u}}{\partial y} - \overline{u'v'}\right) dz + \int_0^h \nu \frac{\partial}{\partial z}\left(\frac{\partial \overline{u}}{\partial z} - \overline{u'w'}\right) dz + \int_0^h g\left(\frac{\partial h}{\partial x} - S_o\right) dz \qquad (2\text{-}30)$$

(i) (ii) (iii) (iv) (v)

Using Leibnitz's rule, term (i) in Eq. (2-30) can be evaluated by:

$$\int_0^h \frac{\partial \overline{\overline{uv}}}{\partial y} dz = \frac{\partial}{\partial y}\int_0^h \overline{\overline{uv}} dz - \overline{\overline{uv}} \frac{\partial z}{\partial y}\bigg|_{surface} - \overline{\overline{uv}} \frac{\partial z}{\partial y}\bigg|_{bed} \qquad (2\text{-}31)$$

Assuming that the water level does not vary laterally across the channel section and that the streamwise velocity u at the bed is zero, the last two terms on the RHS of Eq. (2-31) tend to zero and hence:

$$\int_0^h \frac{\partial \overline{\overline{uv}}}{\partial y} dz = \frac{\partial}{\partial y}\int_0^h \overline{\overline{uv}} dz = \frac{\partial}{\partial y}\left[h\left(\overline{\overline{uv}}\right)_d\right]; \qquad (2\text{-}32)$$

where $\left(\overline{\overline{uv}}\right)_d$ is the depth averaged mean velocity products given by,

$$\left(\overline{\overline{uv}}\right)_d = \frac{1}{h}\int_0^h \overline{\overline{uv}}\, dz; \qquad (2\text{-}33)$$

Since at the bed u is zero and at the surface w is zero, the second term (ii) also tends to zero:

$$\int_0^h \frac{\partial \overline{\overline{uw}}}{\partial z} dz = \overline{\overline{uw}}\Big|_{surface} - \overline{\overline{uw}}\Big|_{bed} = 0 \qquad (2\text{-}34)$$

Using Leibnitz's rule again, term (iii) can be evaluated by:

$$\int_0^h \frac{\partial}{\partial y}\left(\nu \frac{\partial \overline{u}}{\partial y} - \overline{u'v'}\right) dz = \int_0^h \frac{\partial}{\partial y}\left(\frac{\tau_{yx}}{\rho}\right) dz = \frac{\partial}{\partial y}\int_0^h \left(\frac{\tau_{yx}}{\rho}\right) dz - \frac{\tau_{yx}}{\rho}\frac{\partial z}{\partial y}\bigg|_{surface} - \frac{\tau_{yx}}{\rho}\frac{\partial z}{\partial y}\bigg|_{bed}$$
$$= \frac{1}{\rho}\frac{\partial}{\partial y}\left(h\overline{\tau}_{yx}\right) \qquad (2\text{-}35)$$

where $\overline{\tau}_{yx}$ denotes the depth-averaged shear stress, given by

$$\overline{\tau}_{yx} = \frac{1}{h}\int_0^h \tau_{yx} dz \qquad (2\text{-}36)$$

The second term on the LHS of Eq. (2-35) is zero as τ_{yx} is zero at the water surface. The third term on the RHS, i.e. τ_{yx} at the channel bed, is also considered small and hence

negligible relative to the first term. Considering all the assumptions, Eq. (2-35) is reduced to the depth-averaged shear stress.

Term (iv) in Eq. (2-30) can also be evaluated using Leibnitz's rule,

$$\int_0^h \frac{\partial}{\partial z}\left(\nu\frac{\partial \bar{u}}{\partial z}-\overline{u'w'}\right)dz=\int_0^h \frac{\partial}{\partial z}\left(\frac{\tau_{zx}}{\rho}\right)dz=\frac{\partial}{\partial z}\int_0^h\left(\frac{\tau_{zx}}{\rho}\right)dz-\left.\frac{\tau_{zx}}{\rho}\right|_{surface}-\left.\frac{\tau_{zx}}{\rho}\right|_{bed}= \\ \frac{\partial}{\partial z}\left(h\bar{\tau}_{zx}\right)-\frac{1}{\rho}\tau_o\sqrt{1+s^2+S_o^2}=-\frac{1}{\rho}\psi\tau_o \tag{2-37}$$

The first term on the RHS reduces to zero as the depth-averaged shear stress $\bar{\tau}_{zx}$ is constant with depth. The second term on the RHS is also zero since the stress at the free surface is zero in the absence of wind or other applied stresses. Thus, the boundary shear stress term remains where, τ_o is the boundary shear stress, s is the lateral side slope and ψ is a projection onto the plane due to the choice of a Cartesian coordinate system (McGahey, 2006).

Term (v) in Eq. (2-30) is the body force,

$$\int_0^h g\left(\frac{\partial h}{\partial x}-S_o\right)dz=zg\left(\frac{\partial h}{\partial x}-S_o\right)\Bigg|_{surface}-zg\left(\frac{\partial h}{\partial x}-S_o\right)\Bigg|_{bed}=hg\left(\frac{\partial h}{\partial x}-S_o\right) \tag{2-38}$$

where S_o denotes the reach-averaged longitudinal bed slope. Substituting Eqs. (2-32), (2-34), (2-35), (2-37) and (2-38) in Eq. (2-30) yields:

$$\frac{\partial h\left(\bar{\bar{u}}\bar{\bar{v}}\right)_d}{\partial y}=\frac{1}{\rho}\frac{\partial}{\partial y}\left(h\bar{\tau}_{yx}\right)-\frac{\psi}{\rho}\tau_o+hg\left(\frac{\partial h}{\partial x}-S_o\right) \tag{2-39}$$

This is the depth-integrated Reynolds-Averaged Navier-Stokes (RANS) equation for flow in the x-direction.

The flow of water in open channels is generally governed by the RANS equations (Schlichting, 1979). Since the early 1980s, depth-averaged RANS models have become popular for estimating the lateral distribution of depth-averaged velocity U_d and the total flow rate in channels and rivers. The simplicity of the formulation and relatively good estimations have led to their popularity and development in the last three decades (e.g. Vreugdenhil and Wijbenga, 1982; Wormleaton, 1988; Samuels, 1988, 1989; Shiono and Knight

1988,1990,1991; Lambert and Sellin, 1996; Ervine *et al*., 2000; Spooner and Shiono, 2003; Bousmar and Zech, 2004). For a comprehensive review on these models see (McGahey, 2006).

2.4 VELOCITY DISTRIBUTIONS IN OPEN CHANNELS

2.4.1 Background

In an open channel cross-section, the main difference between the velocity distribution in laminar and turbulent conditions is that in laminar flow, the maximum velocity occurs at the water surface while for most turbulent flow situations, it occurs somewhat below the water surface. This is known to be mostly due to the presence of secondary flow cells. Laboratory and field data from many researchers show that the maximum streamwise velocity is found at about 5 to 25% of the water depth below the water surface (Chow, 1959). Typical streamwise velocity contour lines (isovels) for flow in various cross sections are shown in Figure (2-5). Other factors that are important in the distribution of velocity are the shape of the section, the distribution of roughness within the channel and the presence of bends, where due to the centrifugal forces, the velocity increases greatly on the convex side. It is to be noted that in most cases the surface wind has very little effect on the velocity distribution.

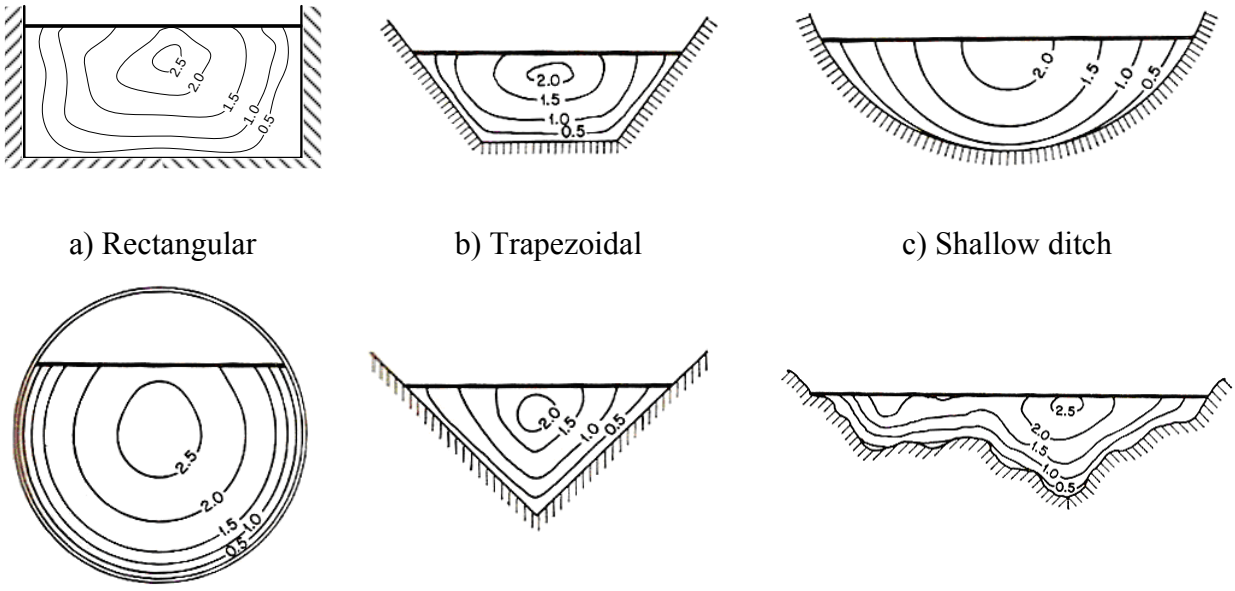

a) Rectangular b) Trapezoidal c) Shallow ditch

d) Circular e) Triangular f) Natural river

Figure (2-5): Contours of constant velocity in various open channel sections (Chow, 1959).

2.4.2 Logarithmic law

The classical "logarithmic law" formulation for the velocity profile in turbulent open channel flow is based on Prandtl's (1926) description of the "law of the wall" and the "boundary layer" concept. Figure (2-6) shows the motion of a fluid past a flat plate and the formed boundary layer. The boundary layer is a thin region of fluid near a solid surface (bed or wall) where the boundary resistance and the viscous interactions affect the fluid motion and subsequently, the velocity distribution. In the fully developed turbulent region, this layer includes two main sub-layers. Near the solid boundary, a viscous sub-layer (laminar layer) forms where the viscous force is predominant. In contrast, further away from the boundary, the turbulent shear stresses play a major role in the defect layer (turbulent layer).

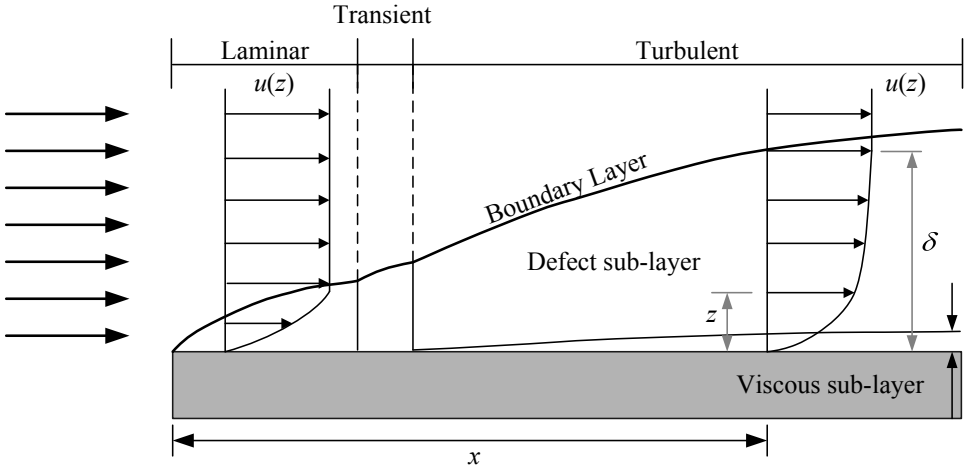

Figure (2-6): External fluid flow across a flat plate (after Massy, 1998).

The "law of the wall" states that the in the streamwise direction, the average fluid velocity in the boundary layer varies logarithmically with distance from the wall surface. This law is used to derive an empirical equation for the vertical distribution of the streamwise velocity in the sub-layers:

$$u^+ = f(z^+) \tag{2-40}$$

where the dimensionless velocity, u^+, the shear velocity, u_*, and the dimensionless normal distance from the wall, z^+, are defined as:

$$u^+ = \frac{u(z)}{u_*}; \quad u_* = \sqrt{\frac{\tau_w}{\rho}}; \quad z^+ = \frac{u_* z}{\nu} \tag{2-41}$$

where τ_w is the wall shear stress and ν is the kinematic viscosity. In the viscous sub-layer, which has the range of z^+<5, the shear stress equals the wall shear stress, which is constant for steady flow. Thus, the dimensionless velocity is directly proportional to the dimensionless distance from the wall:

$$u^+ = z^+ = \frac{u_* z}{\nu} \tag{2-42}$$

In the defect sub-layer (5> z^+), the effects of turbulent is more important than viscosity. In this region, the law of the wall (Eq. 2-40) can be written in the following form:

$$u^+ = \frac{1}{\kappa} \ln z^+ + C_1 \tag{2-43}$$

where κ is the von Karman's constant, and C_1 is a dimensionless integration constant related to the thickness of the viscous sub-layer generally, in the range of 4.9 to 7.0. For smooth surfaces, C_1 is 5.0~5.5 (Kirkgoz, 1989). Based on Nikuradse's (1933) data, the integration constant in Eq. (2-43) can be approximated as $\nu / 9u_*$ and $\kappa / 30$ for smooth and rough surfaces, respectively. This will result in the universal laws for smooth and rough turbulent flow as (Chow, 1959; Rouse, 1959; Schlichting, 1979):

$$u^+ = 5.75 \log\left(\frac{9u_* h}{\nu}\right) \qquad \text{(smooth boundary)} \tag{2-44}$$

$$u^+ = 5.75 \log\left(\frac{30h}{\kappa}\right) \qquad \text{(rough boundary)} \tag{2-45}$$

In uniform open channel flow, the boundary layer is fully developed and extends from the channel boundary throughout the flow depth and Eq. (2-43) can be used to approximate nearly the entire velocity profile. Rouse (1959) proposed a more general approximation of Eqs. (2-44 & 2-45) for open channels:

$$u^+ = C_2 \log z^+ + C_3 \tag{2-46}$$

where C_2 and C_3 are constants for a given channel. This classical formulation for the mechanics of turbulent open channel flow describes the streamwise velocity distribution as a

logarithmic function increasing from a zero velocity at the bottom of the channel and reaching a maximum at the water surface. Since its introduction, several studies have been performed either to evaluate the validity of the profile or to suggest an alternative (e.g. Coles, 1956; Nezu and Rodi, 1986; Kirkgoz, 1989; Yang, *et al*. 2004; Guo, *et al*. 2005). It has been shown that this equation sometimes does not fit with the data measured in the entire flow depth and has some shortcomings which stem from its simplifying assumptions. For example, at large depths the flow is less influenced by the boundary, resulting in less shearing and viscosity related forces, and so the logarithmic velocity distribution cannot completely describe the velocity profile.

2.4.3 Power law

An alternative function for the velocity distribution is the "power law". The general form of this law is proposed as (Barenblatt and Prostokishin, 1993; Schlichting, 1979):

$$u^+ = C_4 (z^+)^m \tag{2-47}$$

where C_4 and m are the coefficient and exponent of the power law. A significant amount of research has been undertaken to define these parameters. Assuming that the velocity gradient is dependent on molecular viscosity, Barenblatt and Prostokishin (1993) suggested that both C_4 and m are functions of the Reynolds number and proposed equations for calculating them. In contrast, Balachandar *et al*. (2002) found that for open-channel flows, the parameters C_4 and m have no significant relationship with the Reynolds number, and are constants at 7.957 and 0.1551, respectively. Chen (1991) also suggested the range of 1/12 to 3/12 for the exponent. However, extensively reviewing the power law, Schlichting (1979) showed the exponent varies slightly with the Reynolds number and suggested the range of 1/6 to 1/10 for $4 \times 10^3 <$ Reynolds $< 3.24 \times 10^6$.

2.4.4 Chiu's velocity distribution

An alternative approach from the stated empirical velocity distribution equations is the method developed by Chiu (1987, 1989). Based on the probability concept and entropy-maximization principle, Chiu derived a new two-dimensional equation for the velocity field. This equation is capable of describing the variation of velocity in both vertical and transverse

directions with the maximum velocity occurring on or below the water surface. It can also accurately describe the velocity distribution in regions near the water surface and channel bed, where most the existing measuring devices face problems. Although various measurements have confirmed the supremacy of Chiu's approach, this methods still has some weaknesses. A major drawback of this method is that knowledge of a value for the velocity (either maximum or average) and a constant are required before application. This is in contrast with the log law which does not require knowledge of the velocity but requires two empirical constants.

2.5 BOUNDARY SHEAR STRESS DISTRIBUTION

2.5.1 Background

The fluid motion in a channel is directly related to the boundary shear stress and therefore to define the fluid field and the velocity profile, knowledge of the boundary shear stress distribution is required. Computation of flow resistance, side-wall correction, sediment discharge, channel erosion or deposition, cavitation problems, and designs of channels are among the problems which can be solved by knowing the boundary shear stress distribution (Yang and Lim, 1997; Guo and Julien, 2005).

The boundary shear stress distribution is non-uniform over the wetted perimeter of a channel cross-section. This is widely proven, even for steady flows in straight prismatic channels with a simple cross-sectional geometry. The non-uniformity is mainly due to the anisotropy of the turbulence which produces transverse gradients of Reynolds stresses and secondary circulations (Gessner, 1973). Tominaga *et al*. (1989) and Knight and Demetriou (1983) showed that the boundary shear stress increases where the secondary currents flow towards the wall and decreases when they flow away from the wall. Other factors that govern the distribution of shear stress of a straight open channel are the geometry of the cross-section, lateral and longitudinal boundary roughness distributions and sediment concentration (Chlebek and Knight, 2006; Khodashenas *et al*., 2008). Figure (2-7) shows the schematic influence of secondary flow cells on the boundary shear stress of rectangular and trapezoidal channels.

2.5.2 Shear stress prediction

Several direct and indirect measurement techniques for boundary shear stress are reported in the literature (Al-Hamid, 1991). The most practised indirect measurement technique is Preston's (1954) method which has been employed for the boundary shear stress measurements of the data sets used in this research. A brief description of this technique is provided in Section (4.2.5). Due to the shortcomings and limitations of these measuring techniques, determining the actual shear stress distribution along the wetted perimeter is extremely difficult (Patel, 1965) and hence, various empirical, analytical and computational methods have been developed to predict the boundary shear stress (Khodashenas *et al*., 2008). These methods can be categorized as:

Geometrical methods

Geometrical methods rely on splitting the channel cross-section into sub-regions. The shear force along each segment of the boundary is found by balancing the forces against the weight of fluid in the corresponding sub-region. Leighly's (1932) method, Einstein's (1942) method, Vertical depth Method (VDM), Vertical Area Method (VAM), Normal Area Method (NAM), Merged Perpendicular Method (MPM) (Khodashenas and Paquier, 1999) and Normal Depth Method (NDM) (Lundgren and Johnson, 1964) are among the stated geometrical methods in literature.

Empirical methods

Empirical methods are basically simple regression models developed from fitting curves to measured experimental data. Knight's (1981) model was the perhaps the first model of this kind. His model was further developed by him and his colleagues (Knight *et al*., 1984a & b and 1994), and other researchers (Flintham and Carling, 1988). Pizzuto (1991) and Olivero *et al*. (1999) also proposed similar simple models for the boundary shear stress. Some of these empirical equations derived for the mean bed and wall boundary shear and force are discussed in Section (2.5.4).

Analytical methods

Analytical methods are based on the mechanism of energy transportation, continuity and momentum equations. Some of these methods lead to a geometric solution for computing the

shear stress in open channels. Some of the analytical methods include the work of Yang and Lim (1997, 2005), Zheng and Jin (1998), Guo and Julien (2005) and Bilgil (2005).

Computational methods

A possibly more accurate way of finding the boundary shear stress distribution is using a turbulence closure model to solve the governing equations of motion. For instance, Christensen and Fredsoe (1998) used the Reynolds stress turbulence model (RSM) and De Cacqueray *et al*. (2009) used the SSG Reynolds stress turbulence model to solve the equations of motion in a computational fluid dynamics (CFD) software to predict the boundary shear stress in open channels.

Table (2-1) shows a summary of some of the important methods stated in literature. A good review on some of these methods can be found in Ghosh and Roy, (1970) and Yang *et al*., (2006) and Khodashenas *et al*. (2008). It is to be noted that all these methods are based on assumptions and approximations and as yet, none is generally accepted for open-channel flow (Knight and Macdonald, 1979).

2.5.3 Simple approximations

The average shear stress for an open channel cross-section can be represented by:

$$\bar{\tau} = \rho g R S_e \tag{2-48}$$

where R is the hydraulic radius and S_e is the energy gradient which can be approximated from a head loss equation like Darcy-Weisbach:

$$S_e = \frac{h_f}{L} = \frac{f}{4R}\frac{U_{avr}{}^2}{2g} \tag{2-49}$$

where h_f is the head loss, L the channel length, f the Darcy-Weisbach friction factor and U_{avr} is the average velocity of the fluid. Substituting (2-49) in (2-48) the shear stress can be related to the friction:

$$\bar{\tau} = \rho \frac{f}{8} U_{avr}{}^2 \tag{2-50}$$

In depth-averaged models, Eq. (2-50) is extended to define the local boundary stress at a particular point in simple cross-section (Knight and Shiono, 1996):

$$\tau_i = \rho \frac{f}{8} U_d^{\,2} \tag{2-51}$$

where τ_i is the local boundary stress, f is the local friction factor and U_d is the streamwise depth-averaged velocity. It is shown (e.g. McGahey *et al*., 2006, Chlebek and Knight, 2006; Sharifi *et al*., 2008; 2009a) that the lateral distribution of the local boundary stress is sensitive to changes in f and h, and a sudden change in either of these variables will result in a corresponding change in the magnitude and distribution of τ_i.

2.5.4 Bed and wall shear stress

Using the concept of shear force, Knight (1981) proposed a simple method for separating the mean bed and wall shear stress for rectangular channels. He defined the shear force acting on the walls and bed as:

$$\mathrm{SF_w} = 2h\bar{\tau}_{\mathrm{w}} \tag{2-52}$$

$$\mathrm{SF_b} = 2b\bar{\tau}_{\mathrm{b}} \tag{2-53}$$

where $\bar{\tau}$ is the mean shear stress, b is the channel semi bed width, h is the flow depth, and the subscripts w and b denote walls and bed respectively. The shear force carried by the walls and the bed can be expressed as a percentage of the total shear force, $\mathrm{SF_T}$:

$$\%\mathrm{SF_w} = \frac{\mathrm{SF_w}}{\mathrm{SF_T}}.100 \tag{2-54}$$

$$\%\mathrm{SF_b} = \frac{\mathrm{SF_b}}{\mathrm{SF_T}}.100 \tag{2-55}$$

$$\text{where } \mathrm{SF_T} = \bar{\tau}.P = \rho g R S_e P \tag{2-56}$$

where P is the wetted perimeter. Examining various measurements, Knight (1981) found that the percentage shear force carried by the walls has an exponential relation with the aspect ratio, $2b/h$ in the form of:

$$\%\mathrm{SF_w} = \mathrm{e}^{\alpha} \tag{2-57}$$

where α is a function of the aspect ratio. Fitting Eq. (2-57) to the measurements in rectangular open channel and rectangular closed conduit channels, Knight *et al*. (1984a) found:

$$\alpha = -3.230\log_{10}(\frac{2b}{h}+3)+6.146 \tag{2-58}$$

Since Eq. (2-57) involves an exponential function and Eq. (2-58) involves a log function, it is concluded that the relation between $\%SF_w$ and aspect ratio is actually a power law and not exponential. Using the same functional form as Eq. (2-57), Flintham and Carling (1988) found a more general equation for calculating $\%SF_w$ in rectangular and trapezoidal channels with homogeneous boundary roughness:

$$\%SF_w = e^{\alpha};\quad \alpha = -3.230\log_{10}(\frac{P_b}{C_5 P_w}+1.0)+4.6052 \tag{2-59}$$

where C_5 is 1.5. Further study by Knight *et al*. (1994), suggested implementing a shape factor C_{sf} in Eq. (2-57) to calculate the shear stress more accurately for larger P_b / P_w values in subcritical and supercritical conditions:

$$\%SF_w = C_{sf}e^{\alpha} \tag{2-60}$$

where for subcritical flow:

$$C_{sf}=1 \quad if \quad \frac{P_b}{P_w}<6.546 \quad else \quad C_{sf}=0.5875(\frac{P_b}{P_w})^{0.28471} \quad , C_5 = 1.50 \tag{2-61}$$

and for supercritical flow:

$$C_{sf}=1 \quad if \quad \frac{P_b}{P_w}<4.374 \quad else \quad C_{sf}=0.6603(\frac{P_b}{P_w})^{0.28125} \quad , C_5 = 1.38 \tag{2-62}$$

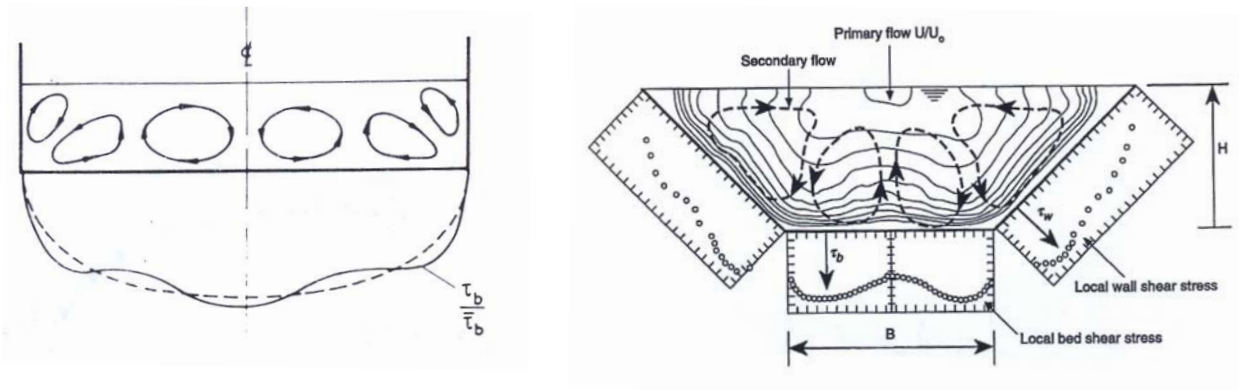

a) Rectangular cross-section (Knight et al., 1983) b) Trapezoidal cross-section (Knight et al., 1994)

Figure (2-7): Schematic influence of the secondary flow cell on the boundary shear distribution.

	Method	Cross -section	Roughness distribution	Local shear stress
Geometrical methods	Leighly (1932)	General	Homogeneous	Y
	Keulegan (1938)	Rectangular	Homogeneous	N
	Einstein (1942)	Rectangular	Homogeneous	N
	Johnson (1942)	Rectangular	Homogeneous	N
	Meyer-Peter and Muller (1948)	Rectangular	Homogeneous	N
	Preston (1954)	General	Heterogeneous	Y
	Vanoni and Brooks (1957)	Rectangular	Homogeneous	N
	VDM (Khodashenas and Paquier, 1999)	General	Homogeneous	Y
	NDM (Khodashenas and Paquier, 1999)	General	Homogeneous	Y
	VAM (Khodashenas and Paquier, 1999)	General	Homogeneous	Y
	NAM (Khodashenas and Paquier, 1999)	General	Homogeneous	Y
	Rajaratnam and Muralidhar (1969)	Rectangular	Homogeneous	N
	Ciray (1970)	Rectangular	Homogeneous	Y
	MPM (Khodashenas and Paquier, 1999)	General	Homogeneous	Y
Empirical methods	Knight *et al*. (1983)	Rectangular,	Homogeneous	N
	Knight *et al*. (1994)	Rectangular, Trapezoidal, Circular	Homogeneous	N
	Flintham and Carling (1988)	Rectangular	Homogeneous	Y
	Pizzuto (1991)	General	Heterogeneous	N
	Olivero *et al*. (1992a)	General	Heterogeneous	N
	Olivero *et al*. (1992b)	General	Heterogeneous	Y
Analytical methods	Yang and Lim (1997; 2005)	Rectangular, trapezoidal Circular and Compound	Heterogeneous	Y
	Zheng and Jin (1998)	Rectangular	Homogeneous	Y
	Guo and Julien (2005)	Rectangular	Homogeneous	N
	Bilgil (2005)	Rectangular	Homogeneous	Y
CFD	Christensen and Fredsoe (1997)	General	Homogeneous	Y
	De Cacueray *et al*. (2009)	Rectangular	Homogeneous	Y

Table (2-1): Summary of boundary shear stress prediction methods.

2.6 SHIONO AND KNIGHT METHOD (SKM)

2.6.1 Background

The Shiono and Knight Method (1988; 1990; 1991) (SKM) is a lateral distribution method based on the depth averaged RANS equations. This quasi 2-D model includes some of the key 3D flow structures that occur in rivers and compound channels and is able to predict the transverse variation of depth-averaged velocity and boundary shear stress distributions within river channels of any cross section shape. SKM provides a tool for water level prediction (by estimating or extending stage-discharge curves), for distributing flows within a cross section (for damage assessments of buildings, eco-hydraulics and habitats), and for predicting the lateral distributions of boundary shear stress (for geomorphological and sediment transport studies). Its promising results both for channels and rivers have led it to being adopted by the UK's Environment Agency for use in its 'Conveyance and Afflux Estimation System' software (www.river-conveyance.net) (see also McGahey, 2006; McGahey *et al*., 2006; 2008)

2.6.2 Governing Equations

In this method, the streamwise depth-averaged momentum equation is solved for steady uniform turbulent flow in a prismatic cross-section. The streamwise RANS equation (Eq. 2-29) for steady uniform flow is given by:

$$\rho\left[\frac{\partial \overline{u}\overline{v}}{\partial y}+\frac{\partial \overline{u}\overline{w}}{\partial z}\right]=\rho g S_0+\frac{\partial}{\partial y}\left(-\rho\overline{u'v'}\right)+\frac{\partial}{\partial z}\left(-\rho\overline{u'w'}\right) \qquad (2\text{-}63)$$

(i) (ii) (iii) (iv)

where ρ is the density of water, g the gravitational acceleration, and S_o the bed slope gradient. $\overline{u}$, $\overline{v}$ and $\overline{w}$ are the mean velocity components and u', v' and w' are the velocity fluctuations in the x (streamwise), y (lateral) and z (vertical) directions respectively. The overbar here indicates a time-averaged parameter. In this equation, term (i) which includes the lateral and vertical components of velocity is called the secondary flow term and term (ii) is the weight component term. Furthermore, the terms (iii) and (iv) account for the Reynolds stresses acting on the vertical and horizontal planes respectively.

Integrating Eq. (2-63) over the depth of water and considering the proper shear force balance as shown in Figure (2-8), the depth-averaged momentum equation becomes:

$$\frac{\partial h(\rho\overline{\overline{uv}})_d}{\partial y} = \rho g h S_0 + \frac{\partial h\bar{\tau}_{yx}}{\partial y} - \tau_o\left(1+\frac{1}{s^2}\right)^{1/2} \tag{2-64}$$

where h is the water depth, τ_o is the boundary shear stress and s the side slope (1:s = vertical: horizontal). The depth-averaged terms are defined by Eqs. (2-33 & 2-36).

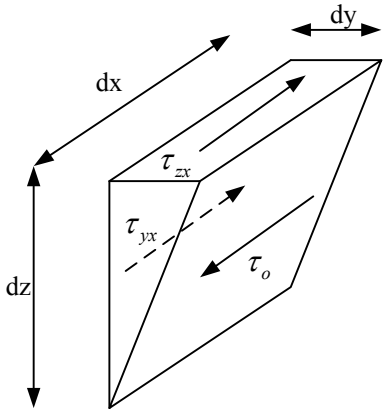

$$\tau_{yx}dxdz + \tau_{zx}dxdy = \tau_o dx\sqrt{dy^2+dz^2}$$

$$\tau_{yx}\frac{dz}{dy} + \tau_{zx} = \tau_o\sqrt{1+(\frac{dz}{dy})^2}$$

$$\tau_{yx}s + \tau_{zx} = \tau_o\sqrt{1+s^2}$$

Figure (2-8): Boundary shear stress on an inclined element (Shiono and Knight, 1988).

SKM uses the Boussinesq eddy viscosity model (described in Section 2.3.4.3) as the closure model to relate the Reynolds shear stress, $\bar{\tau}_{yx}$, to the mean flow rate:

$$\bar{\tau}_{yx} = \rho\bar{\varepsilon}_{yx}\frac{\partial U_d}{\partial y} \tag{2-65}$$

where U_d is the depth averaged streamwise velocity and $\bar{\varepsilon}_{yx}$ is the depth-averaged eddy viscosity. Based on the Cunge *et al*. (1980) assumption, this parameter is assumed to be proportional to the water depth, h, and to the shear velocity, u_*:

$$\bar{\varepsilon}_{yx} = \lambda u_* h \tag{2-66}$$

where λ is the dimensionless eddy viscosity. Incorporating the simple approximation for the boundary shear stress outlined in Eq. (2-51), the shear velocity can be reformulated as:

$$u_* = \sqrt{\frac{\tau_0}{\rho}} = \left(\frac{1}{8} f\right)^{1/2} U_d \tag{2-67}$$

Substituting Eqs. (2-65, 2-66 & 2-67) in Eq. (2-64) yields:

$$\rho g h S_o - \frac{1}{8}\rho f U_d^2 \left(1 + \frac{1}{s^2}\right)^{1/2} + \frac{\partial}{\partial y}\left\{\rho \lambda h^2 \left(\frac{f}{8}\right)^{1/2} U_d \frac{\partial U_d}{\partial y}\right\} = \frac{\partial}{\partial y}\left[h\left(\rho \overline{\overline{uv}}\right)_d\right] \tag{2-68}$$

Based on experimental evidence, Shiono and Knight (1991) suggest that the lateral gradient of the depth averaged secondary flow, $\left(\rho \overline{\overline{uv}}\right)_d$, in prismatic channels can be approximated by constant values for a given element of the cross section. Using this concept, the lateral gradient of this term per unit length of the channel may then be written as:

$$\frac{\partial}{\partial y}\left[h(\rho \overline{\overline{uv}})_{\mathrm{d}}\right] = \Gamma \tag{2-69}$$

where Γ is a dimensionless secondary flow parameter. Thus Eq. (2-68) may be expressed in a simpler form as:

$$\rho g h S_o - \frac{1}{8}\rho f U_d^2 \left(1 + \frac{1}{s^2}\right)^{1/2} + \frac{\partial}{\partial y}\left\{\rho \lambda h^2 \left(\frac{f}{8}\right)^{1/2} U_d \frac{\partial U_d}{\partial y}\right\} = \Gamma \tag{2-70}$$

This substitution enables Eq. (2-70) to become a second order linear differential equation that can be solved analytically.

2.6.3 Analytical solutions

SKM's main equation (Eq. 2-70), can be solved analytically (Shiono and Knight, 1988; 1991) or numerically (Knight and Abril, 1996; Abril and Knight, 2004). In the analytic procedure, which is used throughout this research, the cross section is divided into sub-areas (panels) with constant depth domains, or sloping side slope domains (Figure (2-9)). The analytical solution to Eq. (2-70) may then be expressed for a constant depth, *h*, domain as:

$$U_d = \left[A_1 e^{\gamma y} + A_2 e^{-\gamma y} + k\right]^{1/2} \tag{2-71}$$

where $k = \frac{8 g S_0 h}{f}(1-\beta)$; $\gamma = \sqrt{\frac{2}{\lambda}}\left[\frac{f}{8}\right]^{1/4} \frac{1}{h}$ and $\beta = \frac{\Gamma}{\rho g S_0 h}$

and for a linear-side-slope (1:s vertical : horizontal) domain as:

$$U_d = \left[A_3 \xi^{\alpha} + A_4 \xi^{-\alpha-1} + \omega\xi + \eta \right]^{1/2} \tag{2-72}$$

where $\alpha = -\frac{1}{2} + \frac{1}{2}\sqrt{1 + \frac{s\left(1+s^2\right)^{1/2}}{\lambda}\left(8f\right)^{1/2}}$; $\eta = -\frac{\Gamma}{\frac{\left(1+s^2\right)^{1/2}}{s}\rho\left(\frac{f}{8}\right)}$;

$\omega = \frac{gS_o}{\frac{\left(1+s^2\right)^{1/2}}{s}\left(\frac{f}{8}\right) - \frac{\lambda}{s^2}\left(\frac{f}{8}\right)^{1/2}}$ and $\xi = h \pm \frac{(y-b)}{s}$

here, ξ is the depth function on the side-slope domain, b is the semi width of main channel bed and A_1 to A_4 are constants which are defined through applying the boundary conditions (Section 2.6.4). Given sufficient data, the friction factor, f can be back calculated otherwise its value should be obtained along with the values of dimensionless eddy viscosity, λ, and secondary flow term, Γ, through calibration.

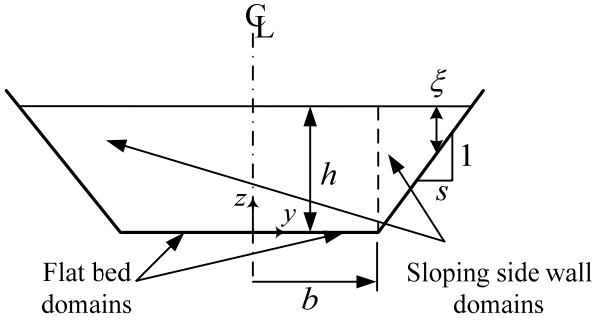

Figure (2-9): Flat bed and sloping sidewall domains.

2.6.4 Boundary conditions

As mentioned in the previous section, different boundary conditions are used to determine the unknown A constants. At the interface between two adjacent panels, three different boundary conditions can be considered (Shiono and Knight, 1988):

Continuity of depth-averaged velocity:

$$(U_d)_i = (U_d)_{i+1} \tag{2-73}$$

Continuity of the lateral gradient of the depth-averaged velocity:

$$\left(\frac{\partial U_d}{\partial y}\right)_i = \left(\frac{\partial U_d}{\partial y}\right)_{i+1} \tag{2-74}$$

Continuity of the unit force:

$$(h\bar{\tau}_{yx})_i = (h\bar{\tau}_{yx})_{i+1} \tag{2-75}$$

Omran (2005) suggested a modification to Eq. (2-74) to get realistic mean velocity distributions by smoothing the spikes caused by the abrupt changes in the local friction and dimensionless eddy viscosity:

$$\left(\mu\frac{\partial U_d}{\partial y}\right)_i = \left(\mu\frac{\partial U_d}{\partial y}\right)_{i+1} \tag{2-76}$$

where,

$$\mu = \lambda\sqrt{\frac{f}{8}} \tag{2-77}$$

At a rigid side wall, where the no-slip condition holds, the velocity should be equal to zero and hence the boundary condition may be written as:

$$(U_d)_i = 0 \tag{2-77}$$

Assuming ideal flow conditions, an additional boundary condition may also be applied at the centreline of a symmetric channel:

$$\left(\frac{\partial U_d}{\partial y}\right)_i = 0 \tag{2-78}$$

Once a cross-section is divided into different panels, as shown in Figure (2-9), and the appropriate boundary conditions are applied, a set of linear equations can be obtained in which the *A* coefficients in Eqs. (2-71 & 2-72) are the unknowns. This set of equations can be solved either by a matrix approach or by a direct approach (Rezaei, 2006), where an

elimination procedure is followed to obtain analytical expressions for the A coefficients. Once the A coefficients are defined, the lateral variation of depth-mean velocity across the channel can be obtained from Eqs. (2-71 & 2-72). Furthermore it is then possible to calculate the boundary shear stress distribution and the channel conveyance. Examples of the matrix approach, which is used throughout this research, is shown in Appendix (II).

2.6.5 Previous work relating to the SKM

Since its introduction by Shiono and Knight (1988), a number of studies have been carried out to develop the SKM and to show its accuracy in predicting the depth-averaged velocity profile, the boundary shear stress distribution and conveyance in different channels and rivers. In this section, only a small amount of the fundamental work will be examined, and only that which is relevant to the scope of this research.

Shiono and Knight (1988; 1990, 1991) and Knight and Shiono (1990) showed the efficiency of this method for compound channels and overbank flow. Knight and Shiono (1996) also compared three different calibration methods for a given dataset. In the first method, all parameters were found through calibration. Then the same data were also calibrated with constant λ values ($\lambda = 0.13$) and variable Γ values. In the final attempt, λ was again held constant at 0.13, but different f values were used, with Γ values set to zero. It was demonstrated that all three methods result in a reasonable mean velocity distribution but in order to obtain accurate boundary shear stress results, Γ should be taken into account in the model.

Revisiting the boundary conditions, Knight and Abril (1996) and Abril and Knight (2004) calibrated the SKM based on compound channel data and provided the following guidelines for determining the secondary flow term:

$$\Gamma = 0.05 h \rho g S_0 \qquad \text{for inbank flow} \tag{2-78}$$

$$\Gamma = 0.15 h_{mc} \rho g S_0 \qquad \text{for the main channel during overbank flow} \tag{2-79}$$

$\Gamma = -0.25 h_{fc} \rho g S_0$ for the floodplain during overbank flow (2-80)

where subscripts *mc* and *fc* denote the main channel and floodplain, respectively. They also found that the model is not sensitive to the value of λ and adopting a constant value of λ=0.13 for the "whole channel" (i.e. main channel and floodplains) with a uniform roughness distribution gives good results. Although giving satisfactory results for channels with overbank flow, this calibration philosophy cannot be extended to inbank flow. In the original work, the main channel and the floodplains were each considered as one panel and hence no information was derived regarding the lateral variation of the calibration parameters. Furthermore, knowing that λ is a function of channel geometry and friction (Knight and Abril, 1996), assuming a constant value for this parameter for the whole channel is not rational.

Omran (2005) applied the SKM to a number of channels and rivers, with both inbank and overbank flows. In his work, the boundary conditions of the model, particularly for simple trapezoidal channels were re-examined and a two-layer version of the model was developed for modelling flows in compound channels.

Based on the number and position of secondary flow cells in trapezoidal channels, Knight *et al*. (2007) proposed a philosophy for defining the appropriate panel structure. It was demonstrated that by using the methodology, back calculating the friction values from measured data, keeping λ constant as 0.07 and calibrating Γ, the depth-averaged velocity and boundary shear stress could be accurately computed for simple trapezoidal channels.

McGahey (2006) and McGahey *et al*. (2006) developed a 2-D model based on the main principles of SKM which they called the Conveyance Estimation System (CES). The CES was thoroughly tested against twenty-four data sets ranging from small scale laboratory experiments to measurements from large natural rivers. The results showed promising improvements when compared to existing one-dimensional hydrodynamic models (McGahey *et al*., 2008). The sensitivity of the method to its parameters was also investigated in this research. The model was later incorporated in UK's Environment Agency 'Conveyance and Afflux Estimation System' software (www.river-conveyance.net).

Chlebek and Knight (2006) showed that a simple one panel structure for half of a symmetric rectangular channel is sufficient for accurately predicting the percentage of shear force acting on the wall and the total discharge. It was concluded that for the distributions of mean velocity and boundary shear, additional panels should be considered. Continuing this work, Chlebek (2009) illustrated the capability of SKM for modelling simple homogeneous and heterogeneous channels with inbank flows. Simple calibration rules were also derived for selecting the values of f, λ, Γ. In addition, SKM was used to model the flow in compound channels with skewed floodplains. As a result, expressions for shear force and apparent shear stress acting on certain boundary elements were proposed.

2.6.7 Friction factor

As mentioned in the previous sections, the SKM uses the simple Darcy-Weisbach approximation (Eq. 2-51) for the boundary shear stress. This assumption is used in both defining the shear velocity and consequently the depth-averaged eddy viscosity (Eqs. 2-66 & 2-67) and also obtaining the boundary shear stress distribution from the velocity distribution. As a result, the friction factor, f, is one the important parameters, if not the most important internal parameter of SKM (and many other conveyance models) which should be understood and quantified. It is to be stressed that the Darcy-Weisbach friction factor is a resistance coefficient and not a roughness factor. In fact, f is a measure reflecting the dynamic behaviour of the boundary in resisting the fluid flow (Yang and Lim, 1997). This dimensionless coefficient is the representative of surface (skin) friction, drag resistance, wave resistance (from free surface distortion) and resistance associated with local acceleration or flow unsteadiness (Rouse, 1965).

Darcy (1857) and Weisbach (1845) developed an equation for calculating the head loss in pipe flow:

$$h_f = f \frac{L}{D} \frac{U_{avr}^2}{2g} \tag{2-81}$$

where f is a dimensionless friction factor, L is the pipe length and D is the pipe diameter. As recommended by the Task Force on Friction Factors in Open Channels (TFFF) (1963), this equation can be used for steady, uniform and fully developed open channel flow. Assuming a

uniform distribution for the boundary shear stress, D can be substituted by $4R$ (Chow, 1959) and hence f can be calculated by:

$$f = \frac{8gRS_e}{U_{avr}^2} \tag{2-82}$$

f can be simply related to Chezy's, C , and Manning's , n resistance coefficients:

$$C = \sqrt{\frac{8g}{f}} \tag{2-83}$$

$$n = R^{1/6}\sqrt{\frac{f}{8g}} \tag{2-84}$$

The friction factor, f, in pipes is known to be dependent on the Reynolds number, $\mathrm{Re} = UD/\upsilon$, and a relative roughness factor, i.e. the ratio of a roughness factor that represents the unevenness of the boundary (e.g. the average sediment diameter or Nikuradse's (1933) equivalent sand roughness, k_s) to a shape factor (e.g. pipe diameter, hydraulic radius). Extensive experiments in pipe flow revealed that for smooth surfaces the relative roughness effect vanishes and the friction factor depends only on the Reynolds number (Prandtl, 1932). In contrast, for rough surfaces, the Reynolds number is less effective and the friction factor becomes wholly dependent on the relative roughness at high Reynolds numbers (Nikuradse, 1933).

Based on the boundary layer theory and the semi-empirical velocity laws, Prandtl (1933) derived an equation for friction factor in smooth pipes by integrating the logarithmic velocity equations over the pipe diameter and assuming no viscous sub-layer for the flow:

$$\frac{1}{\sqrt{f}} = C_6 \log_{10}(\mathrm{Re}\sqrt{f}) + C_7 \tag{2-85}$$

He also derived a similar equation for rough pipes:

$$\frac{1}{\sqrt{f}} = C_8 \log_{10}(\frac{2R}{k_s}) + C_9 \tag{2-86}$$

where C_6, C_7, C_8, and C_9 are constants which depend on the velocity distribution constants (C_1 and κ in Eq. 2-43). Based on experiments on uniform sand grains, Nikuradse (1933) found

that values of 2.0, 8.0, 2.0 and 1.74 were appropriate for the constants C_6, C_7, C_8, and C_9, respectively. These equations do not stand for rough boundaries at relatively low Reynolds numbers, as f varies both with Reynolds number and relative roughness. Conducting similar experiments in pipes with non-uniform roughness, Colebrook and White (1937) proposed an alternative equation in the form of:

$$\frac{1}{\sqrt{f}} = -C_{12}\log_{10}\left(\frac{k_s}{C_{10}\,R} + \frac{C_{11}}{\mathrm{Re}\sqrt{f}}\right) \tag{2-87}$$

where C_{10}, C_{11} and C_{12}, are integration constants which depend on the shape of the conduit or channel. Many researchers have tested this equation on the data of various cross sections with different roughness conditions and have proposed different integration coefficients for it (Table (2-2)). Incorporating von Karman's universal constant as 0.41 in the velocity distribution, the coefficient 'C_{12}' is found to be aprroximately 2.00 for flows in open channels. A drawback in application of the Colebrook-White equation is that it is implicit in f. To overcome this problem, Moody (1947) developed a diagram by relating the friction factor f, the relative roughness $k_s/4R$ and the Reynolds Number for laminar, transitional and fully turbulent flow through a family of curves. In addition, other researchers have tried to derive alternative explicit equations for the friction factor. One such equation is Barr's (1979) equation for pipe flow, which has been provisionally adapted for wide open channels with Re > 30,000 and $R/k_s > 20$, (Yen, 1991):

$$f = \frac{1}{4}\left[-\log\left(\frac{k_s}{12R} + \frac{1.95}{\mathrm{Re}^{0.9}}\right)\right]^{-2} \tag{2-88}$$

River engineers, including Henderson (1966), realized that in open channels, in addition to the Reynolds number and the relative roughness, the free surface, secondary currents and the non uniformity of boundary shear stress distribution along the wetted perimeter may also influence the friction factor. Hence, they concluded that evaluating the friction factors by substituting the pipe diameter to $4R$ in the pipe equations is not necessarily correct, since the hydraulic radius is an arbitrary linear parameter and an unlimited number of cross sections may be characterized by the same value.

Researcher	C_{10}	C_{11}	C_{12}	Description
Colebrook (1937)	14.83	2.52	2.00	Full circular pipe
Zegzhda (1938)	11.55	0.00	2.00	Rectangular with dense sand
Keulegan (1938)	12.27	3.41	2.03	Wide & smooth flow channel
Keulegan (1938)	12.62	2.98	2.00	Wide & fully rough channel
Keulegan (1938)	12.27	3.09	2.03	Smooth trapezoidal channel
Keulegan (1938)	13.99	2.27	2.00	Rough trapezoidal channel
Rouse (1946)	10.95	1.70	2.03	Wide channels
Thijsse (1949)	12.20	3.03	2.03	Wide channels
Sayre & Albertson (1961)	8.89	7.17	2.14	Wide channels
Reinius (1961)	12.40	3.40	2.00	Wide channels
Reinius (1961)	14.40	2.90	2.00	Rectangular – width/depth = 4
Reinius (1961)	14.80	2.80	2.00	Rectangular – width/depth = 2
Henderson (1966)	12.00	2.50	2.00	Wide channels
Graf (1971)	12.90	2.77	2.00	Wide channels

Table (2-2): Constants for the Colebrook-White formula (after Yen, 1991)

Undertaking experiments in smooth rectangular channels, Tracy and Lester (1961) confirmed that the friction factor is a function of the Reynolds number. Myers (1982) also realized that f varies in a complex way with the aspect ratio ($2b/h$). He found that for the same Reynolds number, the friction factor in an open channel is around 8% higher than the equivalent pipe flow. Studying the effect of non uniform distribution of boundary shear stress on resistance, Engelund (1964) suggested replacing the hydraulic radius, R, by another shape factor which he called the resistance hydraulic radius, $\overline{R}$:

$$\overline{R} = R(1+\frac{3}{4}(\frac{e}{\overline{h}}-0.5))^2 \tag{2-89}$$

where $\overline{h}$ is the mean flow depth and e is the distance between the water surface and the centre of area of the cross-section. Using dimensional analysis in conjunction with physical experiments, Kazemipour and Apelt (1979) established a simple correlation between open channel and pipe flow and developed a shape factor for dealing with the shape effect in open channel flow. This method has been found to be appropriate for smooth, rough and

transitional turbulent flows in rectangular channels, enabling the calculation of friction factors and mean velocities by the universal resistance formulae for pipe flow. For a detailed review on open channel flow resistance and guidance on selecting the friction factor see Yen (2002), McGahey *et al*. (2009) and UK's Department for Environment, Food and Rural Affairs (DEFRA, 2003) roughness advisor.

2.6.8 Dimensionless eddy viscosity

It was shown that SKM employs the Boussinesq's hypothesis and the Cunge *et al*. (1980) approximation for the Reynolds stresses (Eq. 2-66). Therefore the value of another parameter, namely, the dimensionless eddy viscosity (λ), should be known to ensure accurate model results.

In many flows, including those in open channels, it is realistic to assume a linear shear stress distribution with a maximum at the bed and zero at the water surface together with a logarithmic velocity law and a parabolic mixing length function (Figure (2-10)):

$$\tau = \tau_b(1-\frac{z}{\delta}) \tag{2-90}$$

$$\frac{u}{u_*} = \frac{1}{\kappa}\ln(\frac{z}{z_0}) \tag{2-91}$$

$$l = \kappa z\sqrt{1-\frac{z}{\delta}} \tag{2-92}$$

where δ is the boundary layer thickness. In an infinitely wide uniform open channel, δ can be replaced with the flow depth, *h*, to give:

$$l = \kappa z\sqrt{1-\frac{z}{h}} \tag{2-93}$$

Inserting this function in Eq. (2-26), the vertical distribution of the eddy viscosity will be a parabolic function (Figure (2-10d)) in the form of:

$$\varepsilon_{xz} = \kappa u_* z\left(1-\frac{z}{h}\right) \tag{2-94}$$

This distribution has been proved by many sets of measurements (Figure (2-11)). The depth averaged vertical eddy viscosity, $\bar{\varepsilon}_{zx}$, can be obtained by integrating Eq. (2-94) over the entire depth to get (Ikeda, 1981):

$$\bar{\varepsilon}_{xz} = \frac{1}{h}\int_0^h \varepsilon_t dz = \frac{1}{h}\int_0^h \kappa u_* z\left(1-\frac{z}{h}\right)dz = \frac{\kappa u_*}{h}\left[\frac{z^2}{2}-\frac{z^3}{3h}\right]_0^h = \frac{\kappa u_* h}{6} \tag{2-95}$$

Based on the strong correlation between the vertical and transverse turbulent velocity fluctuations, some researchers (e.g. Ikeda, 1981) have considered the same formulation for the average lateral eddy viscosity, $\bar{\varepsilon}_{xy}$. Thus, comparing Eq. (2-95) with Eq. (2-66) and assuming $\kappa \approx 0.4$ for clear water, they have suggested a "standard" value in the order of 0.07 for the dimensionless eddy viscosity, λ. This value is debatable on a number of grounds, most noticeably that relating to the assumed distribution of transverse shear stress. In fact, in the lateral direction, the transverse shear stress cannot be approximated by a simple equation as in the vertical direction (Eq. 2-90) and hence no theoretical relation can be derived for $\bar{\varepsilon}_{xy}$ and λ. Further work (e.g. Elder, 1959; Glover, 1964; Shiono and Knight, 1991) has been undertaken to evaluate the dimensionless eddy viscosity. This has led to finding λ in the range of 0.25 to 0.72 for variety of flow conditions.

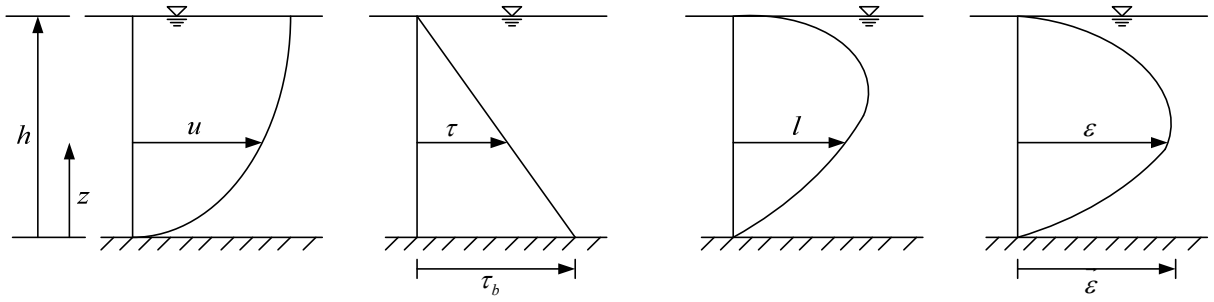

a) Velocity b) Shear stress c) Mixing length d) Eddy viscosity

Figure (2-10): Distributions of vertical velocity, shear stress, mixing length and eddy viscosity.

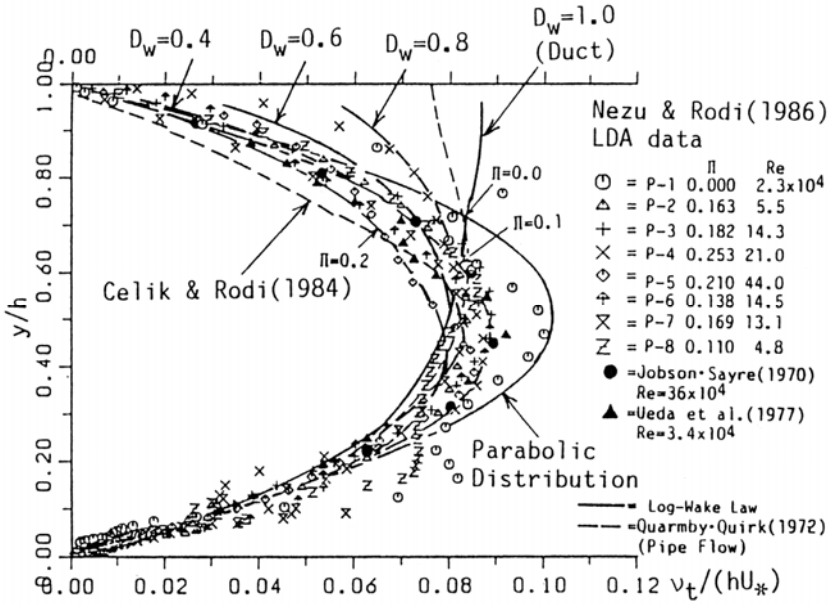

Figure (2-11): Vertical distribution of eddy viscosity for open and closed channel data ($\nu_t \equiv \varepsilon_{xz}$) (Nezu and Nakagawa, 1993).

A widely practised method of evaluating the eddy viscosity coefficient is related to the principles of dispersion in flumes and rivers. Elder (1959) used dye in a wide laboratory flume with 10 mm depth of flow and found λ as 0.23. Using polyethylene in a sand bed flume, Sayre and Chamberlain (1964) found λ=0.24. The same value was found by Fischer and Calif (1967) from their study on a channel approximately 60cm deep and 18.0m wide. Conducting laboratory experiments on rectangular channels, Holley and Abraham (1972) found λ as 0.16 for. Glover (1964) also reported a value of λ=0.36 for rectangular channels with bar roughness on the bottom. Rhodes and Knight (1995) measured λ value as 0.13 in rectangular ducts.

Shiono and Knight (1991) have shown theoretically, that λ is influenced by the physical effects of bed generated turbulence, lateral shear and secondary flows. Based on the measurements performed in the Flood Channel Facility (FCF) compound trapezoidal channel, they quantified the influence of both Reynolds stresses and secondary flows on eddy viscosity values. It was discovered that the λ value based on turbulence alone is around the standard value of 0.07, but its value based on both secondary flows and turbulence is much higher (e.g. 0.5 for the main channel and 3.0 for the floodplains).

In natural channels, the values of λ are generally larger as the rougher banks and longitudinal irregularities result in more boundary generated turbulence and strong lateral shearing. For example, Yotsukura *et al*. (1970) reported values as high as 0.7 from their experiments on the Missouri River and Glover (1964) measured λ=0.72 for the Columbia River in Washington.

Assuming that the correlation of transverse eddy viscosity with shear velocity and flow depth (Eq. 2-66) is not accurate enough, some researchers (e.g. Lau and Krishnappan, 1977; Nokes and Wood, 1988; Webel and Schatzmann, 1984) investigated the dependence of the transverse eddy viscosity coefficient on other factors like the friction factor and the aspect ratio. Lau and Krishnappan (1977) conducted experiments in rectangular flumes with smooth and rough beds. They analyzed their results together with the results from many previous studies to investigate the dependence of the transverse eddy viscosity coefficient on the friction factor and the aspect ratio. They realized that non-dimensionalizing the values of λ by the channel width gives a better picture on how this parameter changes with the change of friction and aspect ratio. Furthermore, they concluded that the transverse mixing mechanism in straight open channels is attributable to the secondary flows. Nokes and Wood (1988) showed that λ is constant and that the flow depth is the important length scale rather than the channel width. In their experiments in straight rectangular open channels with both smooth and rough beds, Weble and Schatzmann (1984) found that λ is approximately equal to 0.13 for friction factors greater than 0.09, but below this λ increases to 0.177 for smooth bed flows with friction factors about 0.03.

2.6.9 Depth averaged secondary flow term

2.6.9.1 Introduction

The three dimensional fully developed turbulent flow in open channels is characterized by the three fluctuating components of velocity and three dimensional distributions of Reynolds shear stresses. The streamwise velocity is relatively easy to measure in most cases, while the transverse components are difficult to measure accurately as they are only a few percent of the primary component values (Nezu and Nakagawa, 1993). These transverse velocity components combine together to form secondary (or transverse) currents which are superimposed on the primary flow. Examining the distributions of the primary velocity,

Nikuradse (1926) was the first to discover the presence of the secondary flows. However, it was Prandtl (1926) who suggested that turbulent velocity fluctuations cause secondary flow structures (Gessner, 1973; Tominaga *et al*., 1989).

Prandtl (1925) distinguished between the secondary flows driven by the centrifugal forces in curved or meandering channels, which he called the first kind, and the secondary flows of the second kind which are caused by the inhomogeneity of anisotropic turbulence. The secondary flows of the first type are driven by the channel geometry, which may affect non-uniform flow in the streamwise direction and hence the generation of streamwise vorticity through vortex stretching. In curved or meandering channels, the centrifugal driving force results in secondary currents in both laminar and turbulent flows with magnitudes typically 20-30% of the mainstream velocity (Nezu and Nakagawa, 1993).

Flows of the second type are generally smaller in magnitude and arise in straight channels due to the transverse gradients of the Reynolds stresses, (e.g. $\overline{v'w'}$, $\overline{v'^2}$, $\overline{w'^2}$), and anisotropy between the fluctuating velcocity components v' and w' (Gessener, 1973; Perkins, 1970). This anisotropy is caused by the boundary roughness conditions, the free surface and the channel geometry (Nezu and Nakagawa, 1993; Tominaga *et al*., 1989). The presence of secondary currents of the second kind influences the spanwise distributions of streamwise velocity and boundary shear stress, resulting in the maximum shear stress and velocity no-longer occurring at the channel centre line and free surface respectively (Knight *et al*., 1994). Tominaga *et al*. (1989) and Knight and Demetriou (1983) also stated that boundary shear stress increases where the secondary currents flow towards the wall and decrease when they flow away from the wall.

The SKM incorporates the average effects of Prandtl's second kind of secondary flows through an advection term called Γ (Eq. 2-69). Figure (2-12) illustrates typical streamwise and transverse velocity profiles, with a secondary flow cell rotating in a counter clockwise direction. Assuming a logarithmic profile for the streamwise velocity, u is always positive, with larger values near the free surface. The lateral velocity, v, is only a small fraction of u and its vertical distribution satisfies three constraints (Wormleaton, 1996): i) zero velocity at the bed, ii) zero shear at the water surface ($\partial v / \partial z = 0$) and iii) continuity for steady flow

($\int_0^h v dz = 0$). Since the lateral velocity at the side edge of the secondary current cell is zero, $(\overline{\overline{uv}})_d$ would be zero at this position. Thus, it is not unreasonable to assume that $(\overline{\overline{uv}})_d$ varies from zero at the edge of the secondary cell to a maximum at the centreline of the cell and then back to zero at the other edge of the cell. Based on the assumed coordinates, $\bar{v}$ and consequently $(\overline{\overline{uv}})_d$ will be positive when the rotation is counter clockwise and negative when the rotation is clockwise.

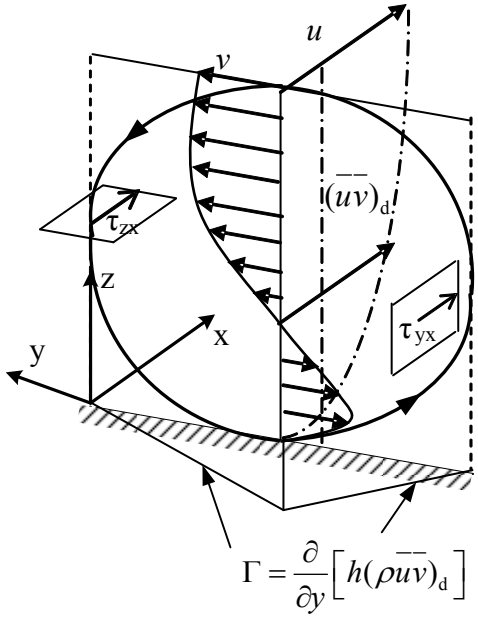

Figure (2-12): Visualization of the averaged secondary flow term (Chlebek and Knight, 2006).

According to Eq. (2-69), the secondary current term, Γ, is equal to the lateral derivative of $h\rho(\overline{\overline{uv}})_d$, which, based on experimental evidence of Shiono and Knight, (1991) may be regarded as constant in certain regions. Hence, depending on the number, position, and strength of secondary flow cells, Γ can have either negative or positive values throughout the channel. It should be further noted that Γ was initially included in the SKM system of equations as a sink term to count for the planform vorticity in compound channels. Furthermore, it was also concluded that including this term for reflecting the effect of streamwise vorticities in inbank flow, would result in more satisfactory model outcomes. This assumption is debatable since the lateral variation of the apparent shear stress due to the secondary flow term ($\rho(\overline{\overline{uv}})_d$) seems to be linear only in certain regions (mostly flood plains)

of the overbank flow and there is not enough evidence to confidently extend this to inbank flow.

2.6.9.2 Rectangular channels

The secondary currents in closed rectangular conduits have been measured by Brundrett and Bains (1963), Gessner (1973) and Perkins (1970) using a Hot Wire Anemometer (HWA) and also by Melling and Whitelaw (1965) using a Laser Doppler Anemometer (LDA). They all observed that the two symmetric contra-rotating secondary cells flow along the bisector toward the corner and then from the corner toward the centre of the channel near the bed, finally rising toward the core of channel to complete the cycle.

Using a low power LDA, Muller and Studerus (1979) were the first to measure the secondary currents of the second kind in a rectangular flume. Based on their measurements, Odgaard (1984) observed that the secondary currents in rectangular open channels are similar to those in air conduits, with the difference that in ducts, due to the absence of the free surface, the intensity of the secondary flow is somewhat depressed near the symmetry plane.

The most remarkable secondary flow measurement in rectangular channels has been carried out by Nezu and Rodi (1985). In their work, they accurately measured the streamwise (u) and vertical velocities (w) using a two colour LDA system. They then calculated the transverse velocity (v) from the equation of continuity on the condition of fully developed flow. Plotting the velocity vectors of the secondary currents (Figure (2-13)), they observed two main cells of secondary currents separated by the horizontal plane near the sidewalls. Near the surface, a strong vortex called the "free-surface vortex" is generated which transports momentum and energy from the side wall toward the channel centre near the surface. At the channel bed, a smaller "bottom vortex" is formed which rotates in the opposite direction to the upper vortex.

Nezu and Rodi (1985) also related the cause of the velocity dip at the channel centre to the transportation of momentum from the free surface to the mid-depth by the free-surface vortex. Furthermore, they realized that the pattern of the secondary currents depends on the ratio between water depth and channel width ($h/2b$) and hence classified rectangular channels to narrow ($h/2b$ <6) and wide ($h/2b$ >6) channels. In narrow channels, the velocity dip at the

channel centre is caused by the free surface effect, which dampens the vertical velocity fluctuations (w'). In wide channels, the side-wall effects are not "felt" in the channel centre, and a series of secondary circulations occurs across the channel width.

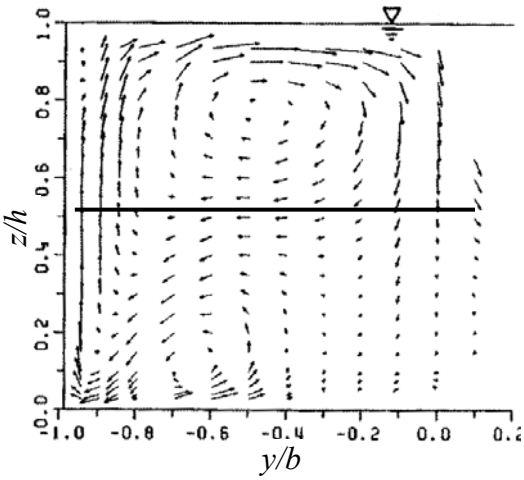

Figure (2-13): Secondary currents in half of a symmetric rectangular channel (Nezu and Rodi, 1985).

Evaluating the boundary shear stress distributions in smooth rectangular open channels and closed rectangular ducts, Knight and Patel (1985) and Knight *et al*. (1983) observed a strong link between the perturbations in the boundary shear stress distribution and the location of secondary flow cells. They concluded that the number and position of the contra rotating secondary flow cells depends on the channel aspect ratio.

Further investigations on the secondary currents in rectangular channels where made by Tominaga *et al*. (1989). Using a Hot Film Anemometer, they studied the effects of geometry and wall roughness on the pattern of secondary currents (Figures (2-14) & (2-15)) and compared the results with measurements in closed conduits. They found that pattern of vortices in channels are different from closed conduits and the free surface affects the pattern of the secondary currents as it causes the secondary currents to flow toward the side wall along a horizontal plane at around 0.6 of the flow depth. It was also observed that while the spanwise scale of bottom vortex is confined to less than about the flow depth, at larger aspect ratios, the free surface vortex stretches and reaches about two times the depth. They also realized that lateral variation of boundary roughness does not change the basic structure of the

secondary currents. However, the scale of the transverse vortex was found to increase as the wall becomes rougher than the bed.

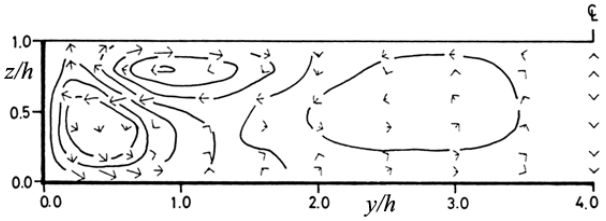

a) case S1 (b=0.20m, $2b/h$=8.00)

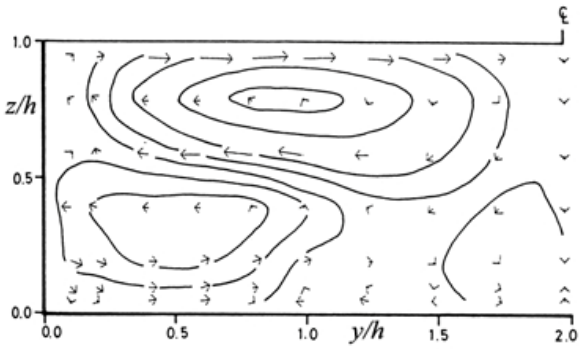

b) case S2 (b=0.20m, $2b/h$=3.94)

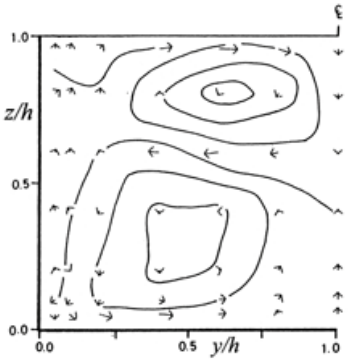

c) case S3 (b=0.20m, $2b/h$=2.01)

Figure (2-14): Secondary current vectors in smooth rectangular channels (Tominaga *et al*., 1989).

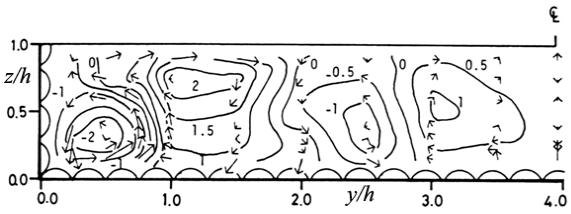

a) case R11 (b=0.158m, $2b/h$=7.9)
Rough bed and wall (k_s=1.2 cm)

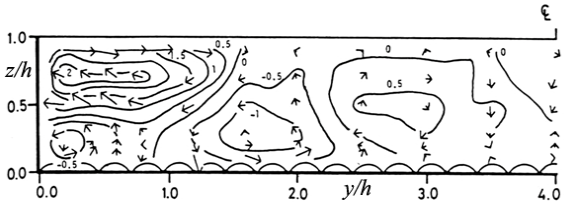

b) Case R21 (b=0.200m, $2b/h$=8.0)
Rough bed (k_s=1.2 cm) and smooth wall

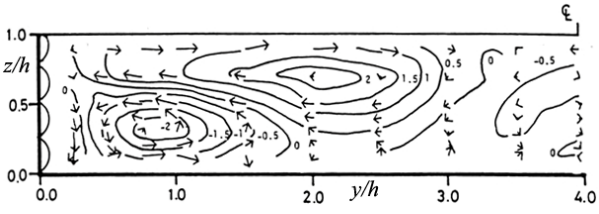

c) case R31 (b=0.158m, $2b/h$=7.9, k_s=1.2 cm); Smooth bed and rough wall (k_s=1.2 cm)

Figure (2-15): Secondary current vectors in rough rectangular channels (Tominaga *et al*., 1989).

2.6.9.3 Trapezoidal channels

In addition to rectangular channels, Tominaga *et al*. (1989) also studied the 3D turbulent structure of flow in smooth trapezoidal channels with different wall inclinations (Figure (2-16)). They observed that, the pattern of secondary flow cells in trapezoidal channels is quite different from that of rectangular channel flows as an additional "longitudinal" vortex is generated between the side wall and the "free surface" vortex. It was concluded that as the side slope angle reduces, the free surface vortex gets weaker and the bottom surface expands. It was also realized that maximum value of the secondary current is of the same magnitude as that in rectangular channels.

Examining the peaks and troughs in the lateral shear stress and mean velocity profiles of several trapezoidal data sets, Knight *et al*. (2007) observed that when the aspect ratio is larger than 2.2, ($2b/h > 2.2$), an additional cell appears in the flat bed domain. They also found that the sign of the secondary current term, Γ, could be determined from the location and rotation of the secondary current cells. Based on the sign of Γ and the number of secondary current cells, they defined a panel structure (i.e. number and location of the panels) for modelling the flow with the SKM (Figure (2-17)).

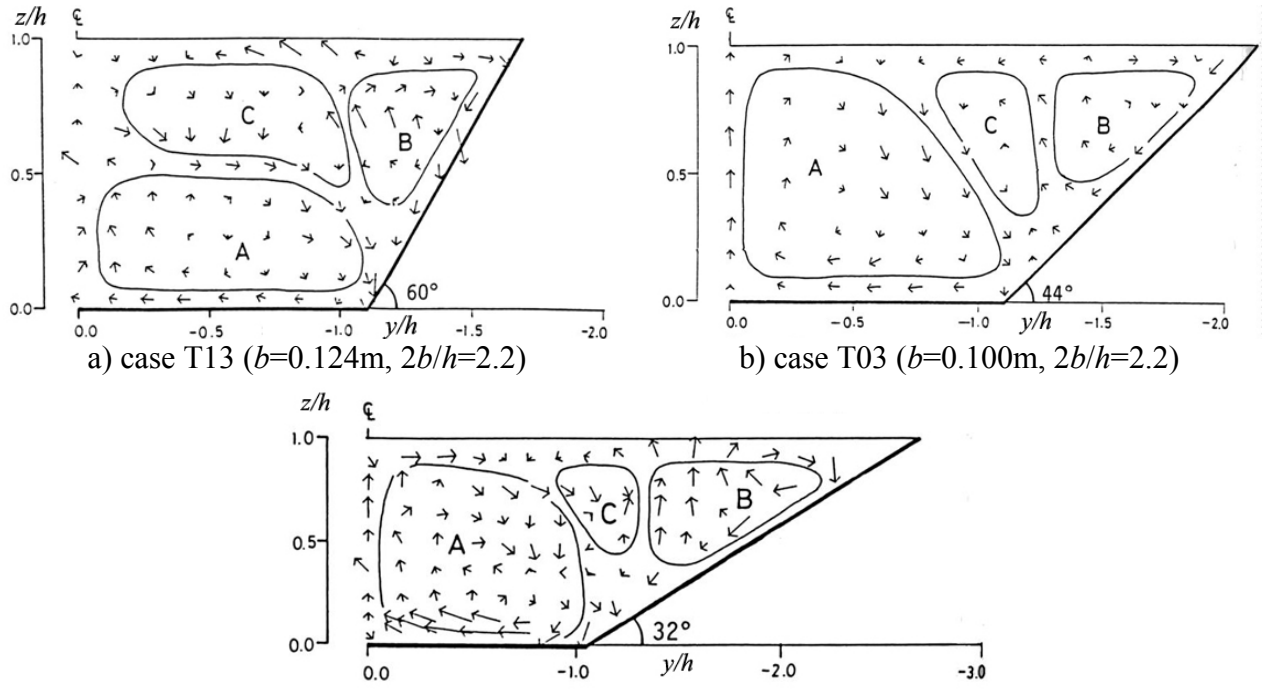

a) case T13 (b=0.124m, $2b/h$=2.2)

b) case T03 (b=0.100m, $2b/h$=2.2)

c) case T23 (b=0.076m, $2b/h$=2.1)

Figure (2-16): Secondary current vectors in smooth trapezoidal channels (Tominaga *et al*., 1989).

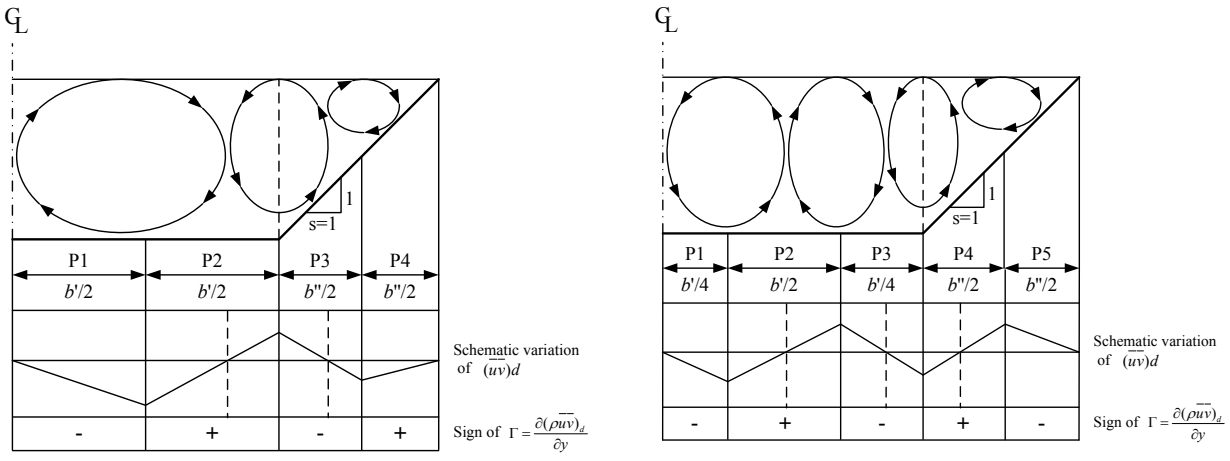

a) $2b/h < 2.2$ b) $2b/h > 2.2$

Figure (2-17): Number of panels and sign of secondary current term for simple trapezoidal channels (Knight *et al*., 2007).

In this section, a brief review of literature relating to the SKM was presented. Its governing equations were derived, its analytical solutions were introduced and appropriate comments relating to the underlying assumptions were presented. Furthermore, discussion sections were provided on the three immeasurable parameters of f, λ and Γ. In the following section, a review will be presented on the free overfall: a classic problem in the field of open channel flow which is intended to be solved using Evolutionary Computation.

2.7 FREE OVERFALL

2.7.1 Background

A free overfall is a situation where the bottom of a channel drops suddenly, causing the flow to separate and form a free nappe (Sterling and Knight, 2001). The depth of water at the section where the overfall occurs is known as the end depth (h_e) or brink depth (Figure (2-18)). Aside from its close relation to the broad crested weir, the free overfall forms the starting point in computations of the surface profile in gradually varied flows and hence has a distinct importance in hydraulic engineering (Chaudhry, 1993). In addition, based on various experiments on prismatic channels, the end depth (h_e) bears a unique relationship with the critical depth (h_c). As there exists a unique stage-discharge relationship at the critical depth,

this relationship enables the free overfall to be used as a simple flow measuring device (Sterling and Knight, 2001; Gupta *et al*., 1993).

Van Leer (1922, 1924 cited in USBR, 2001) was probably the first who used the free overfall principle to measure flow in pipes flowing partially full. Ledoux (1924) and Rouse (1936) also realized that the end depth of flow in a rectangular channel could be used as a simple flow measuring device that requires no calibration. Since then, because of its importance and also relatively simple laboratory setup, a large number of theoretical and experimental studies have been carried out to understand the hydraulics of the end-depth problem and to determine the end-depth ratio ($EDR=h_e/h_c$) in a wide range of channels.

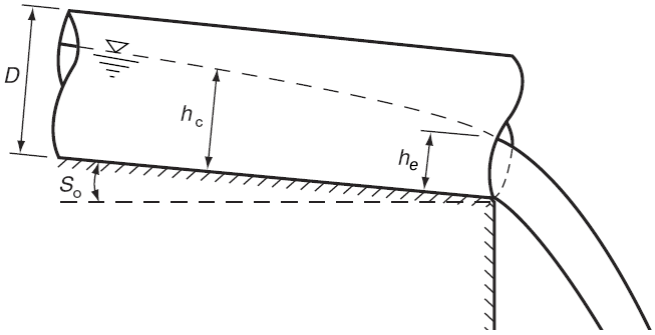

Figure (2-18): A free overfall in a circular channel (Sterling and Knight, 2001).

In the following sub-sections, the hydraulics of the free overfall will be initially described. The theoretical approaches for solving this problem will then be briefly explained.

2.7.2 The hydraulics of the free overfall

Figure (2-19a) shows a schematic view of the pressure and velocity distributions along a channel with a free overfall. At the brink section, the pressure above and below the falling nappe is atmospheric and therefore the pressure distribution at this section differs from the hydrostatic pressure distribution. This pressure distribution has a mean pressure considerably less than the corresponding hydrostatic value.

Figure (2-19b) shows the variation of streamline curvature, being finite at the free surface and zero at the channel bed. The strong vertical component of acceleration due to the gravity affects the curvature of the free nappe in the vicinity of the brink section. Since the free

surface profile is continuous, this effect is extended to a short distance upstream the brink section, causing an acceleration of the flow. This guarantees that the depth of flow at the brink section is less than critical depth. As a result, at sections upstream from the brink, the water surface curvature gradually decreases until a control section where the vertical component of acceleration is weak and the pressure is hydrostatic (Sterling and Knight, 2001; Dey, 2002b).

In channels with a mild slope, the flow upstream of the brink is subcritical, becoming supercritical just before the brink section. Therefore at a short distance upstream of the brink, there is section where the pressure distribution is hydrostatic, the specific energy attains a minimum value and the depth of flow is critical. When the slope is steep and the approaching flow is supercritical, a critical section does not exist upstream of the brink (Sterling and Knight, 2001; Dey, 2002b). Furthermore, in supercritical conditions, every single disturbance creates cross-waves leading to difficulties in determining the depth of flow which makes the measurements difficult.

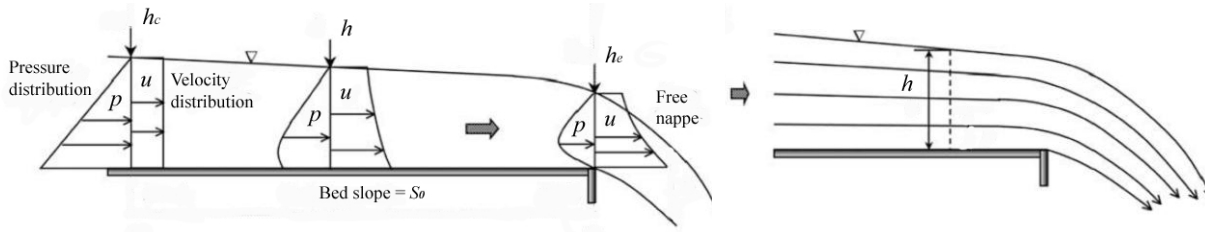

(a) (b)

Figure (2-19): (a) Schematic view of a typical free overfall and the hydraulic aspects; (b) Streamline pattern of a free overfall (Dey, 2002b).

2.7.3 Problem formulation

Despite the relatively simple experimental setup, the theoretical investigation of the free overfall phenomena is a complicated task. Parallel to the experimental investigations, many researchers have tried to explain the physics of the free overfall and establish an expression for the *EDR* for different channels by applying the governing equations and making some assumptions relating to the velocity and pressure distributions. Although providing some promising solutions, inadequacies in these studies have lead researchers to continue working

on this topic (Ozturk, 2005). The most common theoretical approaches are briefly explained in the following sections. Table (2-3) also shows some of the equations derived for *EDR* in rectangular, trapezoidal and circular channels. For a complete state of the art review on the free overfall, see Dey, (2002b).

2.7.3.1 Boussinesq approach

In curvilinear flow, assuming a constant acceleration normal to the direction of flow (a_z), the intensity of pressure, P, at any depth z is determined from the integration of the Euler's equation, that is:

$$-\frac{\partial}{\partial z}(P+\rho g z)=\rho a_z \tag{2-96}$$

As illustrated in Figure (2-19b), the streamline curvature of a free overfall varies from a finite value at the free surface to zero at the channel bed. According to the Boussinesq approximation (Jaeger, 1957) the variation of the streamline curvature with height above the channel bed (z) is assumed to be linear. Integrating Eq. (2-96) with this assumption, an equation for the effective mean hydrostatic pressure head (h_{ep}) is found (Dey, 2002a & b):

$$h_{ep}=h+\frac{kh^2}{3g};\quad k=\frac{{U_{avr}}^2}{h}\frac{d^2h}{dx^2} \tag{2-97}$$

where h is the flow depth, U_{avr} the mean flow velocity and g is the gravity. This equation is a suitable starting point for solving problems with small curvature at the free surface such as the free overfall (Dey, 2002b).

2.7.3.2 Energy approach

This method was first introduced by Anderson (1967) and later extended by others (e.g. Hager 1983). Normalizing the specific energy at the end section of the free overfall (E_e) and the change of free surface curvature by the critical depth (h_c), using $Q^2/g=A_c^3/T_c$ and equating the obtained equations, it can be shown that the generalized equation of end-depth ratio (*EDR*) is:

$$6\hat{E}_e-4\tilde{h}_e-3f(\tilde{h}_e)=0 \tag{2-98}$$

where $\hat{E}_e = E_e / h_c$, $\tilde{h}_e = EDR = h_e / h_c$, $f(\tilde{h}_e) = A_c^3 / (A_e^2 T_c h_c)$, T is the top width of flow and the subscript 'e' refers to the end section. It is to be further noted that in Eq. (2-98) the energy coefficient, α, is assumed to be unity.

2.7.3.3 Momentum approach

This approach is the perhaps the most popular theoretical approach towards the free overfall problem as it has been extensively applied to different channels by many researchers (e.g. Delleur *et al.*,1956; Diskin, 1961; Rajaratnam and Muralidhar, 1964a & b; 1970, Keller and Fong, 1989; Bhallamudi, 1994; Dey, 1998; 2001b, 2002b; 2003; Dey and Kumar, 2002).

Because of the accelerated flow and the inclined streamline pattern, the pressure at the end section is non-hydrostatic (Figure (2-19a)). In this approach, a control volume is considered between a section upstream which has hydrostatic pressure, and another at the brink. Furthermore for analytical simplicity, pseudo-uniform flow (Hager and Hutter, 1984; Dey, 1998) is assumed within the control volume, where the boundary frictional resistance is compensated for by the streamwise component of the gravity force of fluid. Hence, considering one-dimensional momentum equations between the mentioned sections, the difference of force due to pressure will be equal to the rate of change of momentum:

$$F_0 - F_P = \rho Q(\beta V - \beta_0 V_0) \tag{2-99}$$

where F_P is the total force due to pressure, ρ the mass density of the fluid, β the Boussinesq coefficient. Subscript '0' refers to the section with hydrostatic pressure. Assuming a pressure distribution at the end section, Eq. (2-99) is solved for the *EDR*.

2.7.3.4 Weir approach

Assuming a zero pressure distribution and parallel streamlines at the end section and neglecting the narrowing of the nappe, the flow of a free overfall in a channel can be assumed to be similar to the flow over a sharp-crested weir having the same section with crest height equaling zero. The discharge Q of a weir is computed from:

$$Q = C_d \sqrt{2g} \int_0^{h_0} 2b\sqrt{(H - z_n)}dy \qquad (2\text{-}100)$$

where C_d is the coefficient of discharge, b is the channel semi width at an elevation z_n and H is the total head. Considering the flow at the upstream section to be critical, and substituting the total head ($H = h_0 + \frac{V_0^2}{2g}$), Eq. (2-63) is solved for the *EDR* (Rouse, 1936; Ferro, 1999; Dey, 2001a & c, 2002b).

2.7.3.5 Free vortex approach

In the free vortex approach, firstly introduced by Ali and Sykes (1972), the flow at the end of a horizontal channel is simulated by the velocity distribution and curvature of a free-vortex. Expressing the discharge as the integration of the product of velocity and curvature of the free vortex, and assuming there is no loss of energy in the surface and bed streamlines, the *EDR* for channels with different cross sections can be derived (Dey, 2002b).

2.7.3.6 Potential flow approach

Using an iterative process, the finite difference approximations in the Laplace and Bernoulli equations for the potential flow in a free overfall are solved together with boundary conditions and the consistency of the total head and zero pressure at the free streamlines. The relaxation method (Marchi, 1993; Markland, 1965; cited in Dey, 2002b) is normally applied to solve the finite difference approximations (Southwell and Vaisey, 1943; Dey, 2002b).

2.7.3.7 Empirical approaches

In addition to the mentioned approaches, numerous researchers (e.g. Gupta *et al*., 1993; Pagliara, 1995; Davis *et al*.; 1998, Sterling and Knight, 1991; Dey, 2002b) have obtained relationships for the *EDR* and/or the *Q* by applying regression analysis on the experimental data.

2.7.3.8 Machine learning approaches

Recently, the existence of a relatively large database on the free overfall in various channels has led some researchers to apply machine learning and data modelling techniques for investigating the end-depth relationship. For example Raikar *et al*. (2004) used a four-layer Artificial Neural Network (ANN) model to analyze the experimental data to determine the *EDR* for a smooth inverted semicircular channel in all flow regimes. Ozturk (2005) used the same technique and investigated the *EDR* in rectangular channels with different roughnesses. Most recently, Pal and Guel (2006, 2007) applied a support vector machine (Bishop, 2006) based modelling technique to determine the *EDR* and discharge of a free overfall occurring over inverted smooth semi-circular channels, circular channels with flat base and also trapezoidal channels with different bed slopes.

2.7.3.9 Turbulence modelling approaches

A complete solution of the free overfall requires an integration of the turbulent Navier-Stokes equations, using an adequate turbulence model to represent the turbulent shear stresses. Many researchers have followed this approach and tried to find exact solutions for this problem. Finnie and Jeppson (1991) were perhaps among the first who stepped in this path and attempted this type of calculation for the related problem of flow under a sluice gate using the k-ε method. Mohapatra *et al*. (2001) also provided a numerical solution method based on the generalized simplified marker and cell (GENSMAC) flow solver and Young's volume of fluid (Y-VOF) surface-tracking technique to the Euler equations of motion, for ideal flow past a free overfall of rectangular channels.

Guo (2005) treated the free overfall in a rectangular channel by using two-dimensional steady potential flow theory. Based on the theory of the boundary value problem of analytical function and the substitution of variables, he derived the boundary integral equations in the physical plane for the free overfall in a rectangular channel. In continuation of the previous work, Guo *et al*. (2006) applied the volume of fluid (VOF) technique to solve the 2D incompressible RANS and continuity equations for rough rectangular channels. Ramamurthy *et al*. (2006) also applied the three-dimensional two-equation k-ε turbulence model together with the volume of fluid (VOF) turbulence model to obtain the pressure head distributions,

velocity distributions, and water surface profiles for the free overfall in a trapezoidal open channel.

Even though the mentioned approaches yield a number of promising solutions, various inadequacies, mainly relating to the assumed distributions of velocity and/or pressure, have foreclosed the arising of a firm, suitable and general notation of the free overfall process. As it will be shown latter, an attempt will be made to use Evolutionary Computation to derive knowledge from various sources of data and to induce a global conceptual model for the free overfall which can be applied to all possible geometries and flow regimes.

2.8 CONCLUDING REMARKS

It was shown that the SKM is a simple depth-averaged flow model, based on the RANS equations which can be used to estimate the lateral distributions of depth-averaged velocity and boundary shear stress for flows in straight prismatic channels with the minimum of computational effort. However, in order to apply the SKM successfully, the channel cross section should first be divided into a number domains (panels) based on an adopted panelling philosophy. Then, in addition to the inputs of cross-sectional shape and longitudinal bed slope, the correct lumped values of the friction factor (f), dimensionless eddy viscosity (λ) and a secondary flow term (Γ), for each panel should be fed to the model as inputs. Although there are some initial guidelines for the selection of the named parameters (Knight and Abril, 1996; Abril and Knight, 2004; Chlebek and Knight, 2006), their lateral variation is still unknown largely.

The final section of the chapter introduced the free overfall as an effective and simple discharge measuring device. The amount of published work in the literature indicates the high attention of hydraulic engineers to this problem. However, all the applied approaches for determining the *EDR* or the discharge are accompanied with faults, uncertainties and lack of generality.

Having introduced the above, the tools used in this research for bridging the identified knowledge gaps will be presented in the following Chapter. In Chapter 3 an attempt is made to provide a conceptual view on Evolutionary Computation and describe its application in multi-objective model calibration and symbolic regression.

Channel	$EDR = h_e/h_c$	Channel status	Approach	Researcher
Rectangular	0.715	Horizontal, Smooth	Weir	Rouse (1936)
	0.731	Horizontal, Smooth	Momentum	Diskin (1961)
	0.649	Sloping, Smooth	Energy	Anderson (1967)
	0.781	Mild slope, Roughness	Empirical	Bauer and Graf (1971)
	0.678	Horizontal, Smooth	Free-vortex	Ali and Skyes (1972)
	0.667	Horizontal, Smooth	Momentum	Ali and Skyes (1972)
	$9F_0^2/(9F_0^2+4)$	Sloping, Smooth	Energy	Hager (1983)
	0.696	Sloping, Smooth	Momentum	Hager (1983)
	0.760	Horizontal, Smooth	Momentum	Ferro (1992)
	0.706	Sloping, Smooth	Free-vortex	Marchi (1993)
	$134.84S_0^2 - 12.66S_0 + 0.778$	Sloping, Rough	Empirical	Davis *et al*. (1998)
	$0.848e^{(-0.225F)}$	Sloping, Rough	Empirical	Davis *et al*. (1998)
	$0.846 - 0.219(S_0/n)^{0.5}$	Sloping, Rough	Empirical	Davis *et al*. (1998)
	$0.77 - 2.05S_0^{0.5}$	Sloping, Smooth	Empirical	Firat (2004)
	$0.76 - 1.29S_0^{0.5}$	Sloping, Rough	Empirical	Firat (2004)
	$0.76 - 0.02S_0^{0.5}/n$	Sloping, Smooth-rough	Empirical	Firat (2004)
	$0.6701 - h_n/h_c$	Sloping, Smooth-rough	Empirical	Firat (2004)
	0.7016	Sloping , Smooth	Free-vortex	Beirami *et al*. (2006)
Trapezoidal	0.745	Horizontal	Empirical	Gupta *et al*. (1993)
	$0.7267e^{-5.5S_0}$	Sloping , Smooth	Empirical	Gupta *et al*. (1993)
	$0.705 + 0.029(mh_c/B)$	Horizontal	Empirical	Pagliara (1995)
Circular	0.715	Horizontal, Smooth	Momentum	Smith (1962)
	0.75, $(h_c/d) < 0.82$	Sloping , Smooth	Momentum	Dey (1998)
	$2F_0^2/(1+2F_0^2))^{2/3}$	Sloping , Smooth	Momentum	Clausnitzer & Hager (1997)
	0.743	Sloping , Smooth	Empirical	Sterling & Knight (2001)

Table (2-3): *EDR* for rectangular, trapezoidal and circular channels.

CHAPTER 3

EVOLUTIONARY AND GENETIC COMPUTATION

3.1 INTRODUCTION

The aim of this chapter is to review the essential knowledge required for the implementation of the genetic algorithm and genetic programming used in subsequent chapters. The chapter starts with presenting a short history and conceptual view of Evolutionary Computation (EC) and describes the main operations used in this paradigm. Then, a simple genetic algorithm (GA) and its operators are described as a subset of EC techniques. This opening section is followed by two separate sections each dedicated to the EC approaches employed in this research. The first approach is evolutionary multi-objective (EMO) optimization for model calibration. In this section, the concepts of model parameter estimation, multi-objective optimization and Pareto optimality are explained. Then, an EMO method named non-dominated sort genetic algorithm II (NSGA-II) which is the primary element of the proposed calibration framework for the SKM will be examined in detail. The second approach is related to evolutionary knowledge discovery. After providing a brief background on knowledge discovery and explaining its processes, symbolic regression is introduced as an effective data mining tool for knowledge discovery and model induction. This section ends with a brief explanation of another EC method: Genetic Programming (GP). This technique will be used to derive a novel formulation of the physical laws of the free overfall.

3.2 EVOLUTIONARY COMPUTATION

Inspired by Darwin's theory of natural evolution and motivated by the development of computer technologies, EC was introduced in the 1960s as a robust and an adaptive search method. Simulating the natural evolutionary process, these techniques are able to look for the

best (fittest) solution(s) among an enormous number of possible candidates. In the following sections, a short history of EC, the related biological terminology and the EC process are discussed.

3.2.1 Short history of evolutionary computation

Although some ideas underlying research in EC can be traced to the first half of the 20th century, the effective beginning of the field should be placed in the 1960s, concordant with the computer technology revolution (De Jong, 2006; Back *et al*., 1997b). Rechenberg (1965; after Bach and Shcwefel, 1993) is acknowledged as one of the pioneers in this field. In his early work, he developed an evolutionary based method for solving real-valued parameter optimization problems. The main genetic operator in the original version of this method was high level mutation (asexual alteration) and no crossover (sexual recombination) was used (see Section 3.2.2 for terminology). His work was the building block of a method which is today called Evolution Strategy (ES). Two other main streams which emerged from the basic idea of EC can be identified as Evolutionary Programming (EP), originally developed by Fogel, Owens and Walsh (1966) and Genetic Algorithms (GAs) by Holland (1962, 1975). Compared to ES, EP used a more flexible representation and was applied to evolve finite state machines to solve various problems. In the milestone book of "Adaptation in natural and artificial systems" Holland (1975) introduced ECs (particularly genetic algorithms) as a robust method of nonlinear optimization. This approach introduced the crossover operator and used binary strings as representation.

Overcoming the methodological shortcomings and the advent of powerful computational platforms during the 1980s enabled EC to solve difficult real-world problems (Back *et al*., 1997b). This attracted the research community and resulted in the combination, refinement and modification of the main stream. As a result, by the early 1990s, the word "Evolutionary Computation" started to appear in the scientific terminology. More than thirty years of practical application of EC in different fields has demonstrated that this paradigm is capable of dealing with a large variety of problems (Back and Shcwefel, 1993). Nevertheless, the current state of knowledge is still far behind the real concept of evolution in the natural life

which makes the field of EC an exciting one for further scientific applications (Nazemi, 2008).

3.2.2 Biological Terminology

Since natural biological evolution is the basis of EC, it is essential to understand its basic terminologies and discovered rules. The main principle of Darwinian evolution is "survival of the fittest", i.e. only highly fit organisms will be able to survive and reproduce in their environments (Mitchell, 1999). To be more concise, evolution can be defined as a long time scale process that changes a population of organism by generating better offsprings through reproduction. The basic terminologies of biological evolution, which are commonly used in the context of EC, can be summarized as follows:

Chromosomes:	are strings of coiled DNA that contain the coded characterization information of an organism. A chromosome can be conceptually divided into *genes*.
Genes:	are elementary blocks of information in the DNA structure which encode a particular protein (e.g. eye colour).
Traits:	are the physical characteristic encoded by a gene (e.g. eye colour, hair colour…).
Alleles:	are the different possible settings for a trait (e.g. brown, blue . . .).
Locus:	is the location of a gene on the chromosome.
Genome:	is the complete collection of all chromosomes in an organism's cell.
Genotype:	is a particular set of genes contained in a genome.
Phenotype:	Is the physical and mental realization of a genotype (e.g. height, brain size, and intelligence).
Fitness:	is the probability that the organism will live to reproduce (viability) or the number of offspring the organism has (fertility).
Crossover:	is a genetic operator where chromosomes from the parents exchange genetic materials to generate a new offspring.
Mutation:	is the error occurring during DNA replication from parents.

3.2.3 Evolutionary computation process

Conceptually, all EC methods are based on initializing a population of potential candidates (Chromosomes) using a coding scheme, evaluating each individual within the population and giving fitter solutions more chance to evolve and pass through next generations. In the search for the best solution, evolution tries to gradually improve the quality of individuals by selecting, recombining (crossover) and altering (mutation) the fittest individuals. This general procedure can be algorithmically shown in the form of a "pseudo-code" (Michalewicz, 1996):

$t := 0$;
`code` [problem representation]
`initialize` [P_t]
`evaluate` [P_t]
while not `terminate` **do**
    $Q_t :=$ `variation` [P_t]
    `evaluate` [Q_t]
    $P_{t+1} :=$ `select` [$P_t \cup Q_t$]
    $t := t + 1$
End while

In this algorithm, P_t denotes a population of individuals at generation t and Q_t is the offspring population created from the evolution of selected population individuals by means of variation operators such as recombination and mutation. Any algorithm that adopts this general structure is called an Evolutionary Algorithm (EA).

3.2.4 Evolutionary Algorithms (EAs)

Recalling the general EC procedure, an EA must have the following four basic components (Michalewicz, 1992):

1- an evolutionary representation of the solutions to the problem,
2- a way to create an initial random pool of candidate solutions,
3- an evaluation function for rating solutions in terms of their "fitness" and
4- genetic operators that evolve the population towards fitter solutions during reproduction.

Obviously, the distinction between different types of EAs lies in variations in the named key elements. Figure (3-1) shows the common classification of EAs based on their semantic. This family encompasses five members:

Evolution Strategies (ES):
Developed by Rechenberg (1965), this method adopts vectors of real numbers as representations, and typically uses self-adaptive mutation rates to solve optimization problems.

Evolutionary Programming (EP):
This technique was pioneered by Fogel, Owens and Walsh (1966) to develop artificial intelligence. In contrast to other more adopted EAs, in EP no exchange of material between individuals in the population is made. The developed versions of this method are used for solving general tasks including prediction problems, optimization, and machine learning.

Genetic Algorithm (GA):
Introduced by Holland (1975), GA is perhaps the most popular type of EA. GA seeks the solution of a problem in the form of strings of numbers (traditionally binary) by applying recombination operators in addition to selection and mutation. This type of EA is often used in optimization problems (see Section 3.2.5 for more details).

Learning Classifier Systems (LCS):
LCS are rule-based systems that are able to automatically build the ruleset they manipulate. They were invented by Holland (1975) in order to "model the emergence of cognition based on adaptive mechanisms" (Sigaud and Wilson, 2007).

Genetic Programming (GP):
GP was introduced by Koza (1990; 1992) with the aim of allowing computers to solve problems automatically by evolving computer programs. The representations which evolve through the generation are structures of programs or expressions. GP is used in solving many types of problems in the field of artificial intelligence (see Section 3.4.4 for more details).

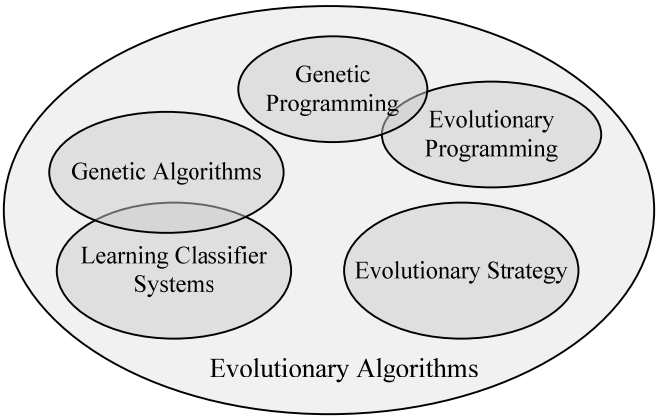

Figure (3-1): The family of evolutionary algorithms (Weise, 2009).

The recombination and mutation operators used in most EAs have made them successful in solving a wide variety of problems. Furthermore, due to the stochastic nature of these methods, no gradient or special knowledge is usually required about the problem. This flexibility has allowed EAs to be successfully applied to multimodal, complex problems where most traditional methods are largely unsuccessful (Deb, 1997). However, like other traditional search and optimization methods, there are some drawbacks in using EAs. One major limitation emerges from the improper choice of EA parameters such as population size, crossover and mutation probability. In order to successfully apply an EA to a problem, the user must be aware of the proper choices for the parameters as these methods may not work efficiently with an arbitrary parameter setting. Another problem in using EAs is that since most of the operators are based on random generated numbers, the overall performance largely depends on the chosen random number generator. Hence, an unbiased random number generator must be used to preserve the stochasticity in the operators and ensure the correctness of the results. The total computational effort is another drawback of EAs. Since generally no gradient information, or problem knowledge is used, compared to classical search methods, EAs may require more function evaluations for simple, differentiable, unimodal functions (Deb, 1997).

In addition to main categories of EAs, there are also many hybrid approaches which incorporate various features of the evolutionary paradigm, and consequently are hard to classify (Michalewicz, 1996). The detailed description of different EAs is far beyond the

scope of this thesis. However, GA and GP which are incorporated in this research will be described in more detail in what follows.

3.2.5 Simple Genetic Algorithms (GA)

A simple Genetic Algorithm (GA) has been adopted as the representative of EA for two reasons. Firstly, it is relatively easy to understand and can be briefly explained and secondly, it contains all the genetic-based processes which are incorporated in the more sophisticated EA approaches. In the following sections, a brief background of simple GA and its elements are provided. For detailed explanation and history the reader is referred to Holland (1975), Goldberg (1989), Koza (1992), Coley (1999) and Osyczka (2002).

3.2.5.1 Background

Inspired by evolutionary biology, John Holland invented GAs in the 1960s with the goal of developing search methods for importing the mechanisms of natural adaptation into computer systems. His ingenious idea was further developed by him and his co-workers at the University of Michigan in the 1960s and the 1970s. Their findings were published in 1975 under the title of "*Adaptation in Natural and Artificial Systems*". The book presented the genetic algorithm as an abstraction of biological evolution and provided a theoretical framework for EC.

Genetic algorithms have undergone several modifications since their introduction, which have made them capable of solving many large complex problems. The main characteristics of these techniques that have made them popular for scientists and engineers are (Coley, 1999):

1- their ability to tackle search spaces with many local optima.
2- their ability to estimate many parameters that interact in highly non-linear ways.
3- their ability to deal with non-continues search spaces.
4- they are generally insensitive to initial conditions.
5- they are more efficient at locating a global peak than traditional techniques.

These abilities have resulted in an excellent reputation that has led GA to be successfully applied to problems where other methods have experienced difficulties. Acoustics and signal processing (Sato *et al*., 2002), Aerospace engineering (Obayashi *et al*., 2000), Astronomy (Charbonneau, 1995), Chemistry (Gillet *et al*., 2002), Financial marketing (Andreou *et al*., 2002) Game playing (Chellapilla and Fogel, 2001), Geophysics (Sambridge and Gallagher, 1993), Material engineering (Giro *et al*., 2002), Medicine (Yardimci, 2007) and Water engineering (Bekele, 2007) are among the many fields which GAs have been successfully applied to.

3.2.5.2 Representation

In GA, the search starts with an initial set of random candidate solutions represented as chromosomes. Each chromosome consists of genes which stand for a particular element (e.g. a parameter in a multi-variable optimization problem) of the candidate solution. Simple GA uses binary coding where the genes are formed of bit strings of 0's and 1's. Figure (3-2) shows a chromosome with 5 genes, each representing a parameter of a potential solution. This chromosome is equivalent to the parameter set of {5,7,5,3,11}. The main drawback with this coding is that it requires long chromosomes to represent all the potential solutions in large search domains. This will result in the requirement of more memory and processing power.

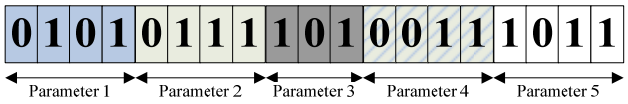

Figure (3-2): A chromosome with 5 genes.

The main alternatives to binary-coding are Gray coding (Caruana and Schaffer, 1988), fuzzy coding (Sharma and Irwin, 2003) and real number coding (Deb and Kumar, 1995). In real number coding, which is incorporated in this thesis, real numbers are used to form a chromosome-like structure for the decision variable. This enables the assignment of large domains (even unknown domains) for variables (Deb and Kumar, 1998). For an in-depth review on different EA representations see Rothlauf (2006).

3.2.5.3 Genetic Algorithm process

The general GA process can be summarized as continuously moving from one population of candidate solutions (chromosomes) to a new population of fitter solutions by using a kind of *natural selection* together with the genetic operators of *crossover* and *mutation*. This cycle of evaluation – selection – reproduction is continued until an optimal or a near-optimal solution is found (Goldberg, 1989; Michaelwicz, 1992). Figure (3-3) illustrates the flow chart of a simple GA process.

Once the initial population is generated, each chromosome is evaluated and its "goodness" (fitness) is measured using some measure of fitness function. Then, based on the value of this fitness function, a set of chromosomes is selected for breeding. In order to simulate a new generation, genetic operators such as *crossover* and *mutation* are applied to the selected parents. The offsprings are evaluated and the members of the next generation population are selected from the set of parents and offsprings. This cycle continues until the termination criterion is met.

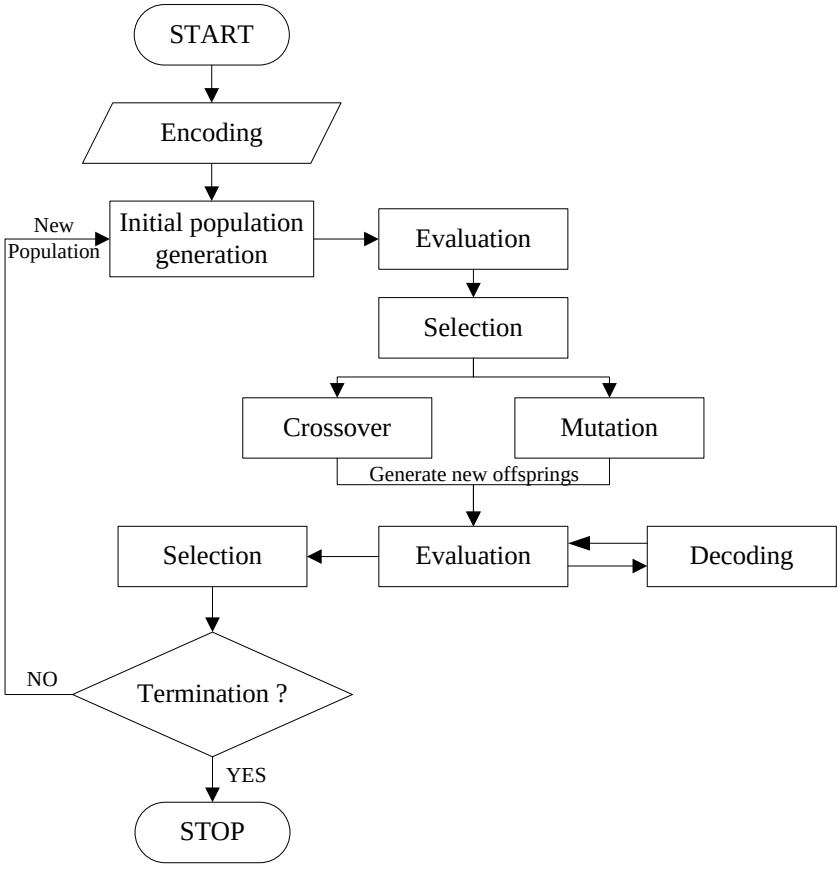

Figure (3-3): Process of simple Genetic Algorithm.

3.2.5.4 Initialization

In simple GA, the process of initialization involves the random production of a set of binary strings. The only internal parameter in this process is the population size (number of chromosomes). It has been shown (Lobo, 2000) that the population size can have an important role in the evolutionary search and therefore has to be considered carefully. If the population size is too small, the diversity in the population is too low and the population will soon suffer from premature convergence. On the other hand, if the size is too large the convergence towards the global optimum is slow and requires large computation resources.

3.2.5.5 Evaluation (measuring performance)

Fitness is the driving force of Darwinian natural selection (Koza, 1990) and the performance measure is the main feedback to an evolutionary algorithm. Selection of a performance measure clearly depends on the kind of task and desired characteristics of the discovered solution. A good performance measure should be able to give a fine-grained differentiation between competing solutions, focus on the eventual use of the program and avoid giving false information (Keijzer, 2002). One common fitness function is the sum of the squared distances between the value returned by the individual chromosome and the corresponding observed value. Using this fitness function for measuring the fitness increases the influence of more distant points. Obviously, the closer this sum of distances is to zero, the better the individual.

3.2.5.6 Selection

The selection operator chooses those chromosomes in the population that will be allowed to reproduce and also the individuals that will be passed to the next generation. As a result of this natural selection, better performing (fitter) individuals would have a greater than average chance of reproducing and promoting the information they contain to the next generation. The three most commonly used selection schemes are proportionate selection, rank selection, and tournament selection (Goldberg and Deb, 1991). In proportionate selection, also known as “roulette wheel” selection, the likelihood of selecting a chromosome is equal to the ratio of the fitness of the chromosome to the sum of the fitness of all chromosomes. One serious limitation of this method is that one comparatively very fit chromosome can very quickly overcome a population. Rank and tournament selection are designed to overcome this

problem. In rank selection, the population is sorted from best to worst fitness, and the probability of selection is some (linear or nonlinear) function of rank. In tournament selection, some small number of chromosomes (frequently two) are chosen at random, compared, and the fittest chromosome is selected; this process is repeated until sufficient chromosomes have been selected. For an authorative study on selection methods, see Goldberg and Deb (1991).

3.2.5.7 Crossover

Crossover has been cited as the main genetic operator of GA and other EC techniques (e.g. Colley 1999; Osyczka, 2002). This operator allows solutions to exchange information in a way similar to that used by a natural organism undergoing reproduction. There are many ways to perform crossover (Michalewicz, 1992). The simplest method is single point crossover, where the chromosomes are split at a randomly selected point, and genes to the left of the split from one chromosome are exchanged with genes to the right of the split from the other chromosome, and vice versa (Figure (3-4)). The effect of crossover is controlled by crossover rate (probability) which defines the ratio of the number of offspring produced in each generation based on crossover. It has been shown (Lobo, 2000) that the crossover rate can have a major effect on the quality of evolutionary search. A higher crossover rate allows exploration of more of the solution space and reduces the chances of getting trapped in local optima. On the other hand, a very high crossover rate can result in unnecessary searches in unpromising regions.

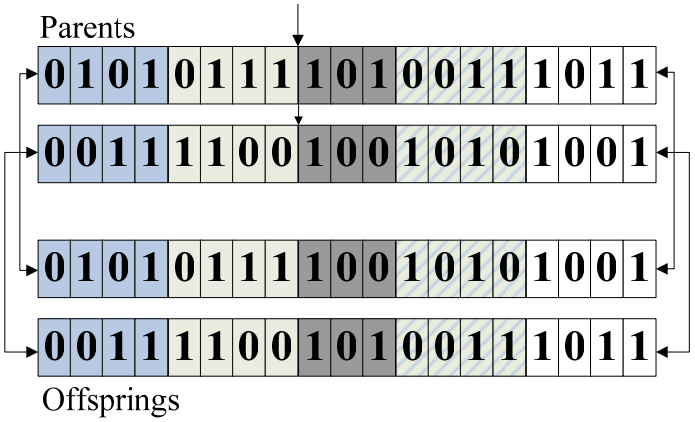

Figure (3-4): Single point binary crossover operator.

3.2.5.8 Mutation

Mutation is another genetic operator which introduces extra diversity in the population by making "accidental" changes in randomly chosen chromosomes. This will ensure the search of the entire solution space over the course of the entire evolution (Michalewicz, 1992). In its simplest version, this operator randomly changes the value of single bits within individual strings to keep the diversity of a population and to help a genetic algorithm get out of a local optimum (Figure (3-5)). Like crossover, the contribution of mutation in evolutionary search is controlled by the so-called mutation rate (probability) which has certain influence on the evolutionary search. If the mutation rate is too high, then the offspring will lose their relationship with their parents (Back *et al*., 1997a). That means the resulting generation forgets the history of evolution.

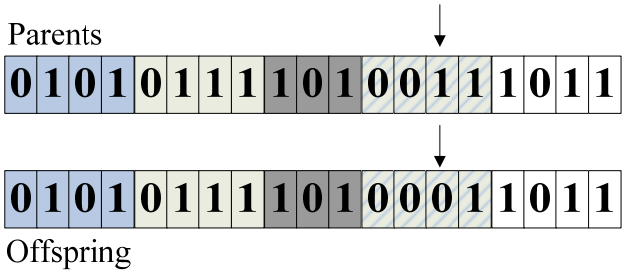

Figure (3-5): Binary mutation operator.

3.2.5.9 Termination

The evolutionary cycle of evaluation-selection-reproduction continues until a stopping criterion is met. The easiest and most common termination criterion is the maximum number of generations, which is the one that has been incorporated in this thesis. Other stopping criteria which have been used in literature include:

- Stopping after a maximum number of function evaluations.
- Stopping after a predefined fitness has been achieved.
- Stopping when the rate of fitness improvement slows to a predefined level.
- Stopping when the population has converged to a single solution.

3.3 EVOLUTIONARY MULTI-OBJECTIVE MODEL CALIBRATION

3.3.1 Model parameter estimation (model calibration)

Environmental models are "*lumped approximations of the heterogeneous world*" (Wagner and Gupta, 2005). These models attempt to represent the complex, spatially distributed, interactions of earth, water, vegetation and energy by means of combining the physical laws of conservation and the physical properties of the system (Wagner and Gupta, 2005). Inevitably, there are always a number of parameters in the system whose values, mainly due to "*immeasurability*", are not known precisely. This immeasurability is down to the lack of an exact physical interpretation of the parameters (e.g. friction factor (see Section 2.6.7)) and/or measurement techniques (e.g. eddy viscosity (Section 2.6.8) and secondary flow term (Section 2.6.9)). Therefore, before a model can be used to simulate the real-world processes, the values of some of its parameters should be adjusted. This process is best known as parameter estimation or model calibration, and will result in finding the "optimal" values of the immeasurable parameters in the model.

The objective of parameter estimation is to calibrate the model so that the observed and calculated system responses show a significantly high degree of similarity (Wagner *et al*., 2003). Gupta *et al*. (2005) define three necessary conditions for an environmental model to be "well-calibrated":

1- The input–state–output behaviour of the model is consistent with the measurements of the system behaviour.
2- The model predictions are accurate (i.e. they have negligible bias) and precise (i.e. the prediction uncertainty is relatively small).
3- The model structure and behaviour are consistent with a current environmental understanding of reality.

The process of model calibration is normally performed either manually or by using computer-based automatic procedures. Manual calibration is a trial-and-error procedure, which the modeller uses a number of different measures of performance and visual inspection of the model output to define the optimum parameter values (Gupta *et al*., 1998). This

procedure might yield good results in simpler models but is generally very labour-intensive, time consuming, and requires considerable experience with a specific model structure. Furthermore, it is less successful in complex models where a high number of non-linearly interacting parameters are present in the model and also an objective analysis of parameter uncertainty is not possible in this procedure (Wagener *et al*., 2003; Cheng *et al*., 2006).

As a result, a significant amount of research has been directed towards the development of automatic calibration procedures. An automatic approach uses a computer algorithm to search the parameter space, performing multiple trials of the model. The performance of the model in each trial is specified by one or many objective functions. The failure of traditional automatic procedures like gradient-based methods and linear and dynamic programming techniques in solving problems with large number of variables and non-linear objective functions has contributed to the development of alternative solutions. Evolutionary based optimization algorithms such as genetic algorithms (e.g. Wang, 1991; Yapo *et al*., 1998), shuffled complex evolution (SCE) algorithm (Duan *et al*., 1992; Madsen, 2000) and simulated annealing (Sumner *et al*., 1997) have been extensively used as powerful global optimization tools.

3.3.2 Multi-objective optimization problem

Many practical problems involve multiple measures of performance, or objectives, which are competing or conflicting and need to be optimized simultaneously. Simple examples are maximizing profit and minimizing the cost of a product and maximizing performance and minimizing fuel consumption of a vehicle. The concept of optimizing multiple, but equally important, objectives was originally introduced by two economists, Edgeworth (1881) and Pareto (1897).

The general form of a multi-objective optimization problem can be defined as the minimization or maximization of a vector of objectives, $\mathrm{F}(X)$, according to certain criteria:

$$\begin{aligned} &\min \textit{ or } \max \mathrm{F}(X) = \{f_1(X), f_2(X), ..., f_M(X)\} \\ &\textit{subject to}: g(X) \le 0 \quad \textit{and} \quad h(X) = 0 \end{aligned} \tag{3-1}$$

where $X = (x_1, x_2, ..., x_N)$ is the decision variables vector in the domain search space, Ω, and $f_1(X), f_2(X), ..., f_M(X)$ are M objective functions that are to be minimized or maximized. Furthermore, $g(X) \le 0$ and $h(X) = 0$ are inequality and equality constraints representing the majority of practical and physical constraints arising in engineering problems (Farina, 2001). Accordingly, two subspaces known as the feasible design domain search space, Ω, and the objective domain search space, Ω_0, are defined as:

$$\Omega : \left\{ X \in R^N \; s.t. \; g(X) \le 0 \; and \; h(X) = 0 \right\} \tag{3-2}$$

$$\Omega_0 : \left\{ \mathrm{F}(X) \in R^M \; s.t. \; X \in \Omega \right\} \tag{3-3}$$

Where R is the set of real numbers and Ω_0 is the image of Ω through function F. It should be noted that based on the nature of the problem, the design variables may not always belong to R^N.

In contrast to single objective optimization problems, multi-objective optimization problems may not have a single solution which simultaneously satisfies all objectives to the same extent. In fact there exists a set of equally good optimum solutions (trade-offs) none of which without any further preference information, can be said to be better than the others. A variety of methods exist to solve multi-objective problems. The traditional methods convert multi-objective optimization problems into a series of equivalent single-objective problems and try to find the optimum solutions with conventional techniques (e.g. linear programming, gradient methods). The most frequently adopted methods and their limitations are listed below:

1- In certain cases, objective functions may be optimized separately from each other and an insight gained concerning the "best" that can be achieved in each performance dimension. Applying this method, suitable solutions to the overall problem can seldom be found. The optimal performance according to one objective, if such an optimum exists, often implies unacceptably low performance in one or more of the other objective dimensions (Fonseca and Fleming, 1995).

2- Aggregating approaches are methods which assign weights to each objective and then re-formulate a single-objective by adding the weighted objectives and find the optimum of the new objective. These methods tend not to lead to a suitable solution as the decision regarding the "best" solution relies on the so called human decision-maker (Ghosh and Dehuri, 2004).

3- In the ε-constrained method (Hirschen and Schafer, 2006) one of the objectives is selected as the main objective and the other objectives are imposed as constraints to the problem.

3.3.3 The concept of Pareto optimality

Generally, when multiple solutions of a given multi-objective problem are available, in order to distinguish between different solutions, it is necessary to rank them according to an order criterion. Based on the Pareto optima theory (Goldberg, 1989), the solutions are ranked according to the Pareto dominance concept which is defined as:

For any two solutions X_1 *and* $X_2 \in \Omega$, and assuming a minimization problem, X_1 dominates solution X_2 if:

$$f_i(X_1) \le f_i(X_2) \text{ for all } i \in [1,2,...M] \tag{3-4}$$

$$f_j(X_1) < f_j(X_2) \text{ for at least one } j \in [1,2,...M] \tag{3-5}$$

In other words, if solution X_1 is not worse than X_2 in all objectives, but is strictly better in at least one objective, then it is said that X_1 dominates X_2. Figure (3-6) illustrates a set of solutions for a typical two-objective problem where the goal is to minimize both objectives. The horizontal and vertical axes represent the value of the first and second objective respectively and each circle represents a decision vector (X_i) in the objective space (Ω_0). Based on the Pareto dominance concept, all empty circles are dominated by the filled ones. The union of all non-dominated solutions (filled circles) is called the Pareto set and its image in the Ω_o, is known as the Pareto-optimal front. In fact the Pareto front represents best compromise solutions for which none has any precedence over any other. Once the Pareto

front of a problem is found, the engineer is able to choose the best compromise solution according to the user's preferences.

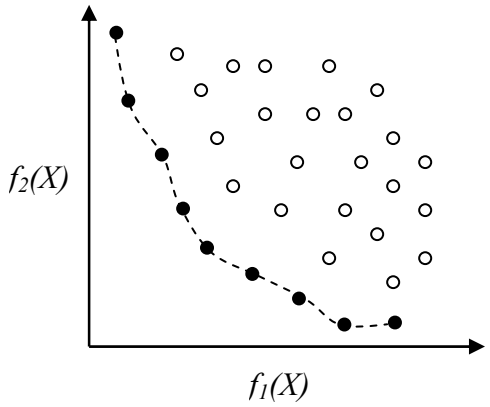

Figure (3-6): The Pareto front of a two objective optimization problem.

Although being relatively simple, at their best, traditional optimization techniques are only able to find one solution on the Pareto front at each run, i.e. for each equivalent single objective problem being solved. Hence, they are not convenient for solving a multi-objective problem.

3.3.4 Evolutionary multi-objective optimization (EMO)

Since EC methods deal with a population of solutions, it can be expected that these search algorithms can have a great potential in the discovery of Pareto optimal solutions. In addition, because of their nature, evolutionary algorithms are less susceptible to the shape and continuity of the Pareto front; the weakness of most search methods. Therefore, EMOs have the ability to handle complex problems, involving features such as discontinuities, multimodality and disjoint feasible spaces (Fonseca and Fleming, 1995). These are the features that make them suitable for solving complex multi-objective problems.

The first design of a multi-objective evolutionary algorithm (MOEA) was undertaken in the mid-1980s by Schaffer (1984). Schaffer's approach, called Vector Evaluated Genetic Algorithm (VEGA) consisted of a simple genetic algorithm with a modified selection mechanism. After VEGA, several researchers have proposed other MOEAs which over the years have been used in many applications and their performances have been tested in several comparative studies. There are two common goals in all MOEA implementations. First, to

move the population toward the Pareto optimal front and second, to maintain diversity in the population so that multiple solutions can be developed (Deb, 1999). A detailed description of these algorithms is beyond the scope of this thesis. For an excellent comprehensive survey on EMO the reader is directed towards Coello (2006). Among these algorithms only the Non-dominated Sorting Genetic Algorithm-II (NSGA-II), the primary element of the proposed calibration framework of the SKM, will be considered in more detail.

3.3.5 Non-dominated Sorting Genetic Algorithm-II (NSGA-II)

The Non-dominated Sorting Genetic Algorithm II (NSGA-II) is a fast and elitist, second generation MOEA proposed by Deb *et al*. (2000; 2002). The main features of this method are:

1- at each generation, the best solutions found are preserved and included in the following generation using an elite-preserving operator;

2- a fast algorithm is used to sort the non-dominated fronts;

3- a two level ranking method is used to assign the effective fitness of solutions during the selection process.

Figure (3-7) illustrates the general procedure of this method. In this figure, P_t is the parent population, Q_t is the offspring population, R_t is the combined population ($R_t = P_t \bigcup Q_t$) and F_i are the non-dominated sorted fronts of R_t. The algorithm starts with a random population and generates the children using the genetic operators. Then, a fast non-domination sorting algorithm is used to rank the solutions according to their dominance rank and organize fronts of equal rank. In this ranking method, an individual, k, is randomly chosen from the population R_t and inserted in an intermediate set named F_1. Then, another solution k' is drawn from R_t and compared to all individuals from F_1. If k' dominates k, k' enters F_1 and k is deleted, but if k dominates k', then k' is deleted and k stays in F_1. Continuing this comparison for all individuals, F_1 will consist of all non-dominated individuals of R_t, the Pareto front by definition. Now the first Pareto front is removed from the original population

and the same procedure is iteratively continued to identify other layers of Pareto fronts $\{F_i, i = 1,...\}$.

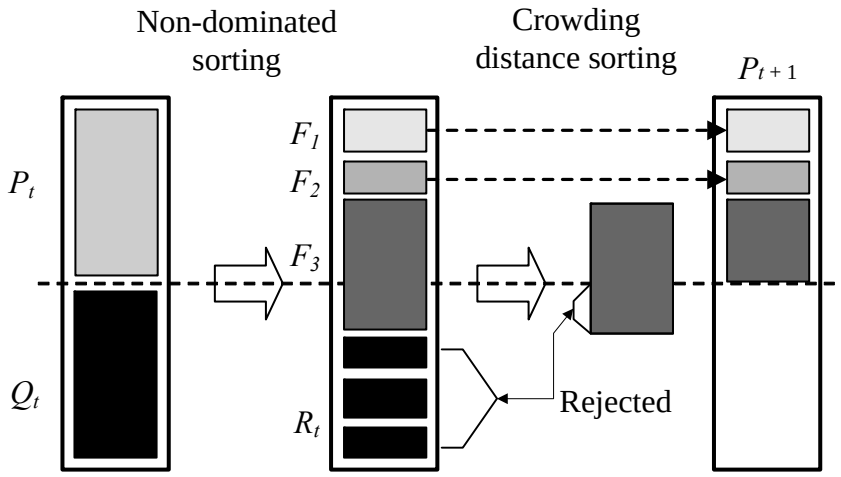

Figure (3-7): Procedure of NSGA-II (Deb *et al*., 2002)

Subsequently, individual solutions within each front are ranked according to a density measure using the *crowding operator*. This operator, as pictured in Figure (3-8), measures the diversity of each individual by measuring half of the perimeter of the rectangle that encloses a solution in the objective function space and assigning infinite distance to the extreme points of the Pareto-front. This operator is designed in a way to ensure the selection of those individuals which reside in less crowded regions of the objective space. This will guarantee a spread along the Pareto and prevent the algorithm focusing solely on a certain part of the front.

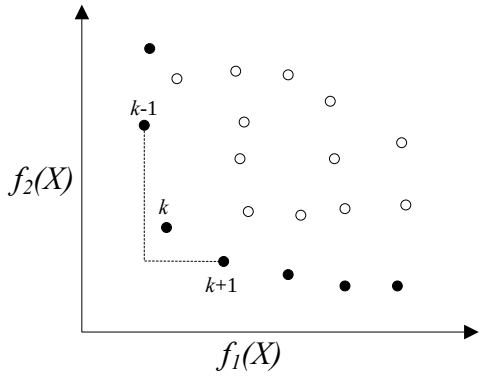

Figure (3-8): Distance assignment in NSGA-II (Hirschen & Schafer, 2006).

The next generation, P_{t+1}, which has the same size as the first generation is filled with consecutive Pareto fronts $\{F_i, i = 1,...\}$, until no full Pareto front can be fully accommodated anymore. Then, the solutions in the next Pareto layer are sorted in descending order according to their distance assignment and the empty spaces in the proceeding generation are filled with higher ranked solutions.

The next offspring population, Q_{t+1}, is created by using the *crowded tournament selection operator*. Two attributes can be considered for each individual solution: First, a non-domination rank (equal to the Pareto layer rank) and second, a crowding distance (as explained beforehand). In the tournament selection, competitions are set up between individuals. The tournament is "won" by that individual which has the better non-dominated rank (lies on an outer Pareto front). If both individuals are on the same Pareto front, ties are broken by the crowded distance and the tournament is "won" by the one which is least crowded (Hirschen & Schafer, 2006). The procedure outlined in Figure (3-7) is repeated until the termination criterion is met and the best-known Pareto front is saved in an archive. The solutions in this archive are the Pareto optimal solutions of the problem under consideration. For an in-depth explanation of this method the reader is referred to Deb *et al*. (2000; 2002).

Studying a variety of test cases (e.g. Deb *et al*. 2002; Khare *et al*., 2003), it has been shown that compared to other elitist multi-objective evolutionary algorithms, NSGA-II has a better diversity preservation and therefore is able to compete with them regarding to its convergence to the true Pareto-optimal front in both constraint and non-constraint problems (Nazemi *et al*., 2006). This superiority has lead to the successful application of NSGA-II in several real world problems such as long-term groundwater monitoring design (Reed *et al*, 2007), water distribution network design (Babayan *et al*., 2005), calibrating hydrological models (Bekele, and Nicklow, 2007; Liu *et al*., 2005), traffic signal timing optimization (Sun *et al*., 2003) and medicine (Lahanas *et al*., 2003).

3.4 EVOLUTIONARY KNOWLEDGE DISCOVERY

3.4.1 Background

Early observations of the world through quantitative and numerical data by mankind can be dated as far back as 3500 B.C. (Powell, 1995). Although these observations and measurements were apparently taken for purposes other than for scientific laws, they formed the initial foundation for the development of classical science. Generally, when a set of observations of the physical system is collected, classical science attempts to describe the behaviour of the system by generating a hypothesis that represents a generalization of the data (Keijzer, 2002), whereas modern science gives a more refined and coherent representation of the physical and conceptual processes in the form of equations in a physical symbol structure (Babovic and Abbott, 1997a). Once the formulation of a scientific law or theory is obtained, additional justification is provided by finding a proper conceptualization of the problem.

Modern experimental and observational methods generate enormous datasets and the amount of data stored in databases continues to grow rapidly. These large databases can contain valuable hidden knowledge, which, if extracted, can be used to improve the understanding of real-world processes. The amount of stored data grows at a much larger rate than the number of human data analysts. Hence, there is a need for (semi-)automatic methods to assist the human analyst in extracting knowledge from data. This need has led to the emergence of a field known as Knowledge Discovery (Freitas, 2002). This is an interdisciplinary field where methods of several research areas such as Machine Learning and Statistics are used to extract high level knowledge from real-world datasets. Knowledge Discovery has Data Mining as its heart and also consists of several pre-processing methods aimed at facilitating the application of the data mining algorithm, and post-processing methods to refine and improve the discovered knowledge (Freitas, 2002). The discovered knowledge, as stated by Freitas (2002), should satisfy three general properties: it should be accurate, comprehensible and interesting.

3.4.2 Knowledge discovery process

As stated above, the Knowledge Discovery process consists of three main distinctive stages: data preprocessing, data mining and discovered-knowledge post-processing (Freitas, 2002). All the tools used in this process, facilitate the conversion of data into a number of forms that convey a better understanding of the process that generated or produced these data (Keijzer, 2002). Figure (3-9) illustrates an overview of the entire Knowledge Discovery process. The directions of the arrows in the Figure indicate that this process is inherently iterative, i.e. the output of a step can either be sent to the next step in the process, or be sent back to a previous step as a feedback (Freitas, 2002).

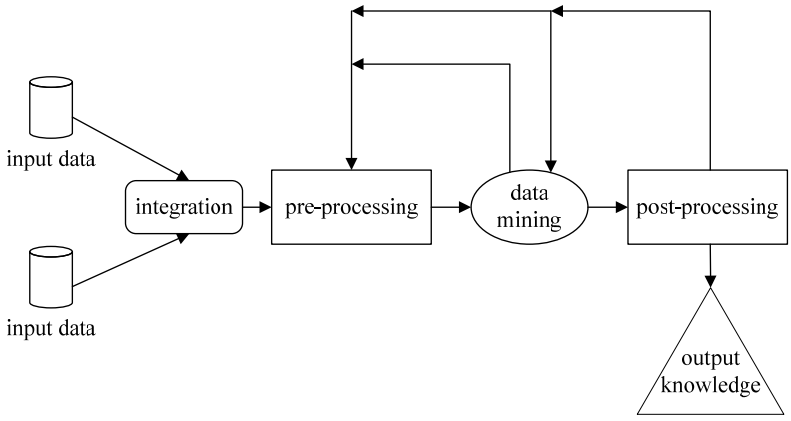

Figure (3-9): An overview of the Knowledge Discovery process (Freitas, 2002).

3.4.2.1 Data preprocessing

Data preprocessing (or data preparation) is the first stage of Knowledge Discovery where the data are cleaned and transformed to ensure accurate and efficient results. The following procedures may be performed in this procedure (Pyle, 1999):

a) Data Integration: If the data come from different sources, such as several departments of an organization or various research papers, it becomes necessary to integrate all the data in one suitable format. This involves tasks such as removing inconsistencies in attribute names or values between data sets of different sources.

b) Data Cleaning: It is important to make sure that the data are as accurate as possible. This step may involve detecting and correcting errors in the data, filling in missing values, etc. Some data cleaning methods for data mining are discussed in Guyon *et al*. (1996) and Simoudis *et al*. (1996).

c) Discretization: This step is particularly required when the data mining algorithm cannot handle continuous attributes. For this purpose, continuous attributes are transformed into a categorical (or nominal) attribute which only take a few discrete values. For instance the real-valued attribute "uncertainty" can be discretized to undertake only three values: low, medium and high.

d) Attribute Selection: As indicated by its name, this step comprises selecting a subset of attributes among all original attributes, which are relevant for the Knowledge Discovery process.

3.4.2.2 Data mining

Data Mining is defined as the (semi-)automatic extraction of interesting knowledge from data and is considered as the core step of the Knowledge Discovery process. Some problems which can be solved by data mining algorithms are: classification, dependence modelling, clustering, discovery of association rules and model induction problems. In the context of this research, the favourable application of data mining is model induction where the main objective is to deduce a closed-form explanation of the system based solely on observations. In this approach, the modeller uses the data mining techniques in an attempt to drive a complete model from the limited information of the physical system that can account for both the entire range of observed and unobserved phenomena within the physical system. The important point about this type of modelling is, as Keijzer (2002) states, "*the confidence in model performance cannot be based on data alone, but might be achieved by grounding models in the domain so that appropriate semantic content is obtainable*". As a result, the obtained models can be used to reinforce, inspire or abandon the scientists' view of the problem (Keijzer, 2002).

3.4.2.3 Post-processing stage

After applying the data mining algorithm to the processed data, the discovered knowledge normally needs to undergo some post-processing treatment to improve its comprehensibility and/or interestingness. Using his interpretation, analysis and available understanding of the physical processes, the modeller plays a pivotal role at this stage by extracting a subset of "interesting" patterns of knowledge (models) (Keijzer, 2002). It is argued (Silberschatz and Tuzhilin, 1996) that in many applications, a different notation of "interestingness" is required, however, novelty, simplicity, implicity, validity on test data and potential usefulness are the general attributes of an interesting pattern (Ghosh and Jain, 2005).

Methods for the selection of interesting models can be divided into subjective and objective methods (Freitas, 1998; 1999; Ghosh and Jain, 2005). Subjective methods are user-driven and domain-dependent whereas objective methods are data-driven and domain-independent. The most common subjective approach is specifying model templates, i.e. the modeller can set rules to indicate which combination of attributes must occur in the model for it to be considered interesting (Klemettinen *et al*., 1994). By contrast, in objective approaches the discovered models are compared with each other with respect to their performance and not the modeller's beliefs. Some objective measures of model interestingness are discussed in Freitas (1998; 1999). It is generally believed that in order to find interesting knowledge, an ideal combination of subjective and objective approaches should be used in the post-processing stage.

3.4.3 Evolutionary symbolic regression

The most practised method of empirical model induction is deriving the relation between the variables of a system in a symbolic form (equation) by regression analysis. In the process of traditional regression (e.g. simple linear, polynomial, Fourier, etc.), the functional structure between dependent variables is predefined, and the goal is to discover a set of numerical coefficients which minimize a measure of performance between the observed and computed values of the dependent variable(s). If $X = (x_1, x_2, ..., x_n)$ is the set of independent input variables and Y is the desired dependent output variables of a system, the regression task is to search the potential search space and approximate Y using X and coefficients c such that:

$$Y = f(X, c) + \varepsilon_n \tag{3-6}$$

where ε_n represents a noise term. With standard regression techniques the functional form f is pre-specified. Using linear regression for example, f would be:

$$f(X, c) = c_0 + c_1 x_1 + \ldots + c_n x_n \tag{3-7}$$

where the coefficients c are found using an optimization method e.g. least square regression. For complex and unknown systems, a predefined structure may not give a fit that appeals to the eye and even if it does, the model might not necessarily make much sense from the physical point of view. In contrast to the traditional methods, symbolic regression methods (Keijzer, 2002) discover both the correct functional form that fits the data and the appropriate related numeric coefficients (Koza, 1990). This has made them a popular tool for data mining and solving model induction and empirical discovery problems (Langley and Zytkow, 1989). Symbolic regression methods include any method of inducing a symbolic description from the observed data of a system, by searching a space of potential solutions. Genetic Programming (GP) (Koza, 1990; Koza, 1992), Grammar Evolution (GE) (Ryan *et al*., 1998) and Analytic Programming (AP) (Zelinka *et al*., 2005) are the most famous symbolic regression techniques. In the following section, Genetic Programming will be introduced as an effective evolutionary data mining tool for symbolic regression and model induction.

3.4.4 Genetic Programming (GP)

Genetic programming (Koza, 1990; Koza, 1992) is a collection of EC techniques based on the principles of Darwin's theory of evolution, that allow computers to solve problems automatically by evolving computer programs (Poli *et al*., 2008). GP was first introduced by Koza (1990) as a powerful tool for solving problems in various fields of artificial intelligence. Starting with a number of random solutions, this technique is able to tackle any problem which can be viewed as a problem of discovering a computer program by improving the quality of the solutions by means of some natural variation operators. These problems can be categorized as symbolic function identification, symbolic regression, empirical discovery, symbolic "data to function" integration and symbolic "data to function" differentiation, solving functional equations, machine learning of a function, planning in artificial intelligence and robotics, automatic programming, pattern recognition and game playing (Koza, 1990).

In the context of Knowledge Discovery and model induction, a distinct advantage of GP over other modelling techniques such as artificial neural networks is that the provided answer in the form of a symbolic expression is in a language the user understands and can be interpreted by scientists (Keijzer and Babovic, 1999). This mathematical representation provides a great benefit in empirical modelling of unknown phenomena where an underlying theoretical model does not exist (Keijzer, 2002). This has resulted in the successful application of GP to a wide range of practical problems over the last two decades. Image and signal processing (Marko and Hampo, 1992), industrial process control (Castillo *et al*., 2006), medicine and bioinformatics (Koza and Andre, 1996) and economic modelling (Chen and Liao, 2005) are just a small number of problems which have been tackled by GP.

3.4.4.1 Overview

Being from the family of genetic-evolutionary techniques, GP follows a similar procedure as genetic algorithms (GAs). The standard GP starts with an initial population of randomly generated symbolic expressions (also known as parse trees) composed of functions and terminals appropriate to the problem domain. These functions may be standard arithmetic operations (such as addition, subtraction, multiplication, and division), standard mathematical functions (such as SIN, EXP, etc.), standard programming operations (such as If-Then-Else, Do-Until, etc.), Boolean functions (such as, AND, OR, XOR, NOT, etc.) and various domain-specific functions (Koza, 1990). The terminals may be variable arguments, such as the attributes of the system, constant arguments, such as 0 and 1 or a random generated number.

A fitness function is then used to measure the performance of each individual symbolic expression in the particular problem environment. Predictably, the majority of the initial random symbolic expressions have exceedingly poor fitnesses but nonetheless, some individuals are more fit than others. Then, a sexual genetic reproduction process is performed on pairs of expressions, which are selected in proportion to their fitness, and offsprings are created. The resulting offsprings are composed of sub-expressions (also known as building blocks) from their parents and form the new generation which replaces the old population of parents. The fitness function is again used to measure the fitness of each individual in the new population. Repeating this algorithm will gradually produce populations which, over a period of generations, reach a high average fitness in dealing with their environment. Figure

(3-10) shows the flowchart of the computational procedure of GP. As in this research, the GP algorithm is going to be used for symbolic regression and model induction purposes, its components related to this type of environment will be briefly described in the following sections.

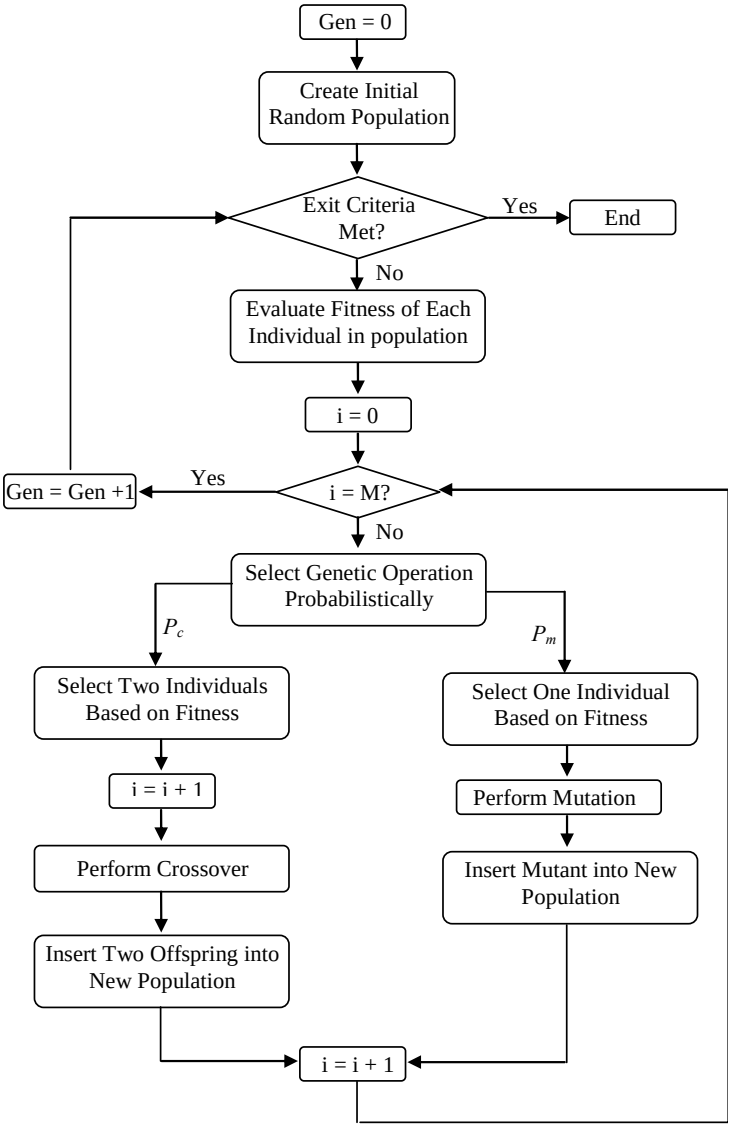

Figure (3-10): Computational procedure of Genetic Programming
(adapted from Koza, 1992)

3.4.4.2 Principal structures

The search space for the genetic programming paradigm is the hyperspace of all valid symbolic expressions that can be recursively created by compositions of the available functions and terminals for the problem (Koza, 1990). When the problem is in a form of symbolic regression, the functions can be standard arithmetic operations (such as addition, subtraction, multiplication, and division) or standard mathematical functions (such as SIN, EXP, etc.) and the terminals usually consist of independent variables of a problem, constants, and random generated numbers. Each candidate symbolic expression (chromosome) is usually represented by a parse tree (see Figure (3-11)). In tree representations, the internal nodes of a tree (shown with circles) are composed of elements from the set of defined functions and the leaf nodes (squares) consist of elements from the set of terminals (Koza, 1990; Keijzer, 2002). Figure (3-11) illustrates a parse tree with three internal nodes and four leafs. This tree represents an expression in the form of {exp (B/H) + 2B}.

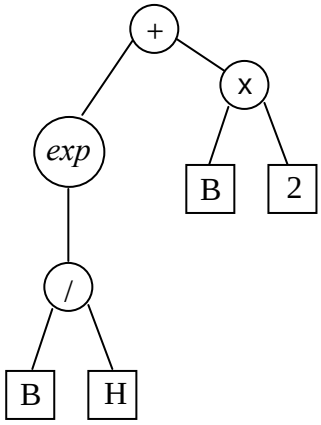

Figure (3-11): Parse tree representation of {exp(B/H)+2B}in GP.

Choosing appropriate functions and terminals by the modeller is one of the key factors influencing the GP performance (Sastry, 2007). There are only vague guidelines for choosing a particular function and terminal set. But generally, the user must try to select a suitable set of functions accompanied by a set of terminals that are most descriptive for the problem and, when combined, form relatively small parse trees which can implement diverse and powerful solutions (Keijzer, 2002).

3.4.4.3 Initialization

To generate a random individual expression for the initial population, first, one of the functions from the function set is randomly selected as the root of the parse tree. Then depending on the number of arguments it takes, branches are radiated out from the root. Next, for each created branch, an element is selected at random from the entire combined set of functions and terminals to be the node for the endpoint of that branch. If the selected element is a terminal, that node becomes a leaf (node) and the process is complete for that portion of the tree. If a function is chosen, that node becomes an internal node and the process of selecting random elements from the combined set of functions and terminals continues for that function. Figure (3-12) shows the process of creating a tree.

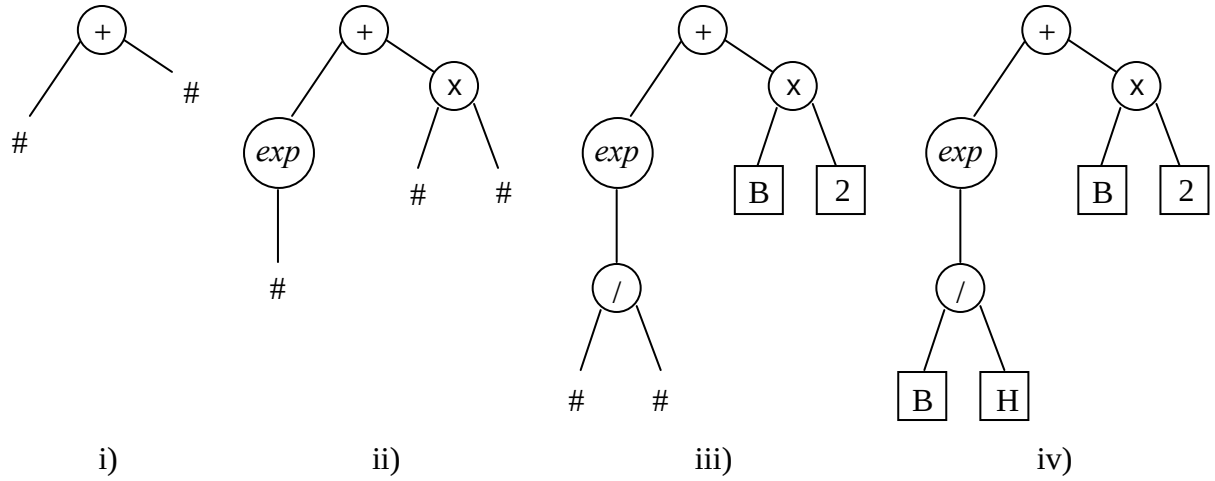

Figure (3-12): Creating a parse tree. (Empty spots are denoted by #)

The average size for the trees generated by this initial random generation process is determined by the number of arguments taken by each function and the probability distribution over the terminals and functions in the combined set of functions and terminals (Koza, 1990). Except for the root of the tree which must be a function, a uniform random probability distribution is usually considered for the function and terminal selection. In solving some problems, specific individuals might be seeded into the initial population or a non-uniform distribution might be assumed to in order to bias the initial random generation towards particular structures (Koza, 1990). Three most common methods of generating parse trees are:

Grow method:

A node is selected uniformly at random from the combined set of functions and terminals, and as long as there are unresolved subtrees, the process is repeated. After a pre-specified depth or size limit is reached, only terminals are chosen (Keijzer, 2002).

Full method:

A function from the entire function set is selected randomly for each node until the pre-specified depth or size limit is reached. Beyond this point only terminal nodes are chosen (Koza, 1990).

Ramped-half-and-half method:

Using the grow and full method each for 50% of the population is known as the ramped-half-and-half initialization method (Koza, 1992).

For an overview of alternative tree initialization routines and the comparison between all methods, the reader is referred to Luke and Panait, (2001). It is to be noted that like GAs, the population size is one of the most important parameters that should be set in the GP process. In general, the larger the population size, the better (Goldberg, 1989), however not much is known on the optimal or even minimal population size in genetic programming (Keijzer, 2002). The complexity of the problem and the available computational resources are the variables which must be considered when selecting the population size (Koza, 1990).

3.4.4.4 Measuring performance

Once the initial population of potential solutions is formed, each individual tree in a population is assigned a fitness value as a result of its interaction with the environment. Selection of a suitable performance measure obviously depends on the type of the problem and desired characteristics of the discovered solution. This performance measure is essential in evolving "fitter" generations since it is the fitness value that denotes the probability of a tree to be selected for reproduction. In symbolic regression problems, the sum of the squared distances between the dependent variable values calculated by the symbolic expression and the original observed values is typically adopted as the fitness function. It is believed

(Keijzer, 2004) that this performance measure can give a fine differentiation between competing solutions.

3.4.4.5 GP operators

In this section, the common genetic operators which try to mimic biological evolution in the GP process are briefly described.

Fitness proportionate selection operator

Reproduction and survival of the fittest is the basic engine of Darwinian evolution and expectedly, the fitness proportionate reproduction operator is the heart of GP. Each time this operator is performed, a parental symbolic expression is selected with a probability proportionate to its fitness, to be directly copied to the next generation or to undergo other different operators (i.e. mutation and crossover) and produce offspring expressions. It is to be noted that the selected parent may still remain in the population and therefore can potentially be selected again during the current generation (Koza, 1990).

Subtree crossover

As mentioned previously, in GP, symbolic expressions are presented by parse trees where the internal nodes represent the functions and leafs the terminals. In subtree crossover, a crossover point for each solution is randomly chosen and subtrees below the crossover points are swapped to create two new solutions (Koza, 1992). Figure (3-13) gives an example of subtree crossover. Depending on the environment of the problem and the shape and size of the parse trees, selecting crossover points between internal nodes (functions) and leaves (terminals) should be made based on a proper distribution (e.g. selecting a function 90% of the time and a terminal 10% of the time) so that enough amount of information is exchanged between trees by performing this operator (Koza, 1992).

Subtree and point mutation

Two mutation techniques are widely used in GP. Subtree mutation replaces a randomly chosen subtree in a tree with another randomly generated subtree, whereas in point mutation, a node is randomly modified. Figure (3-14) shows both types of mutation.

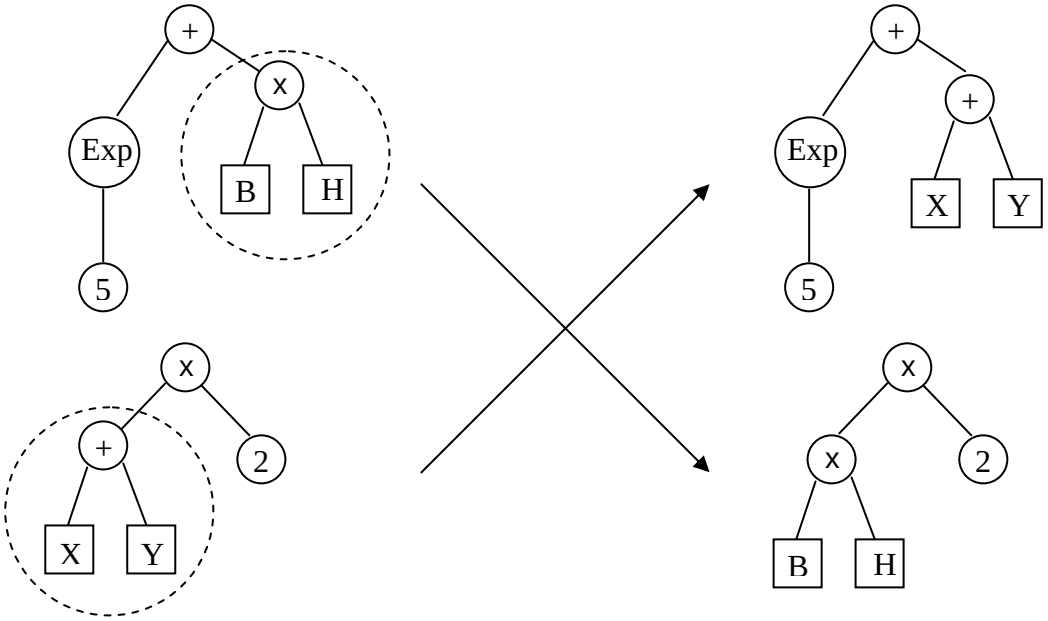

Figure (3-13): Example of a subtree crossover.

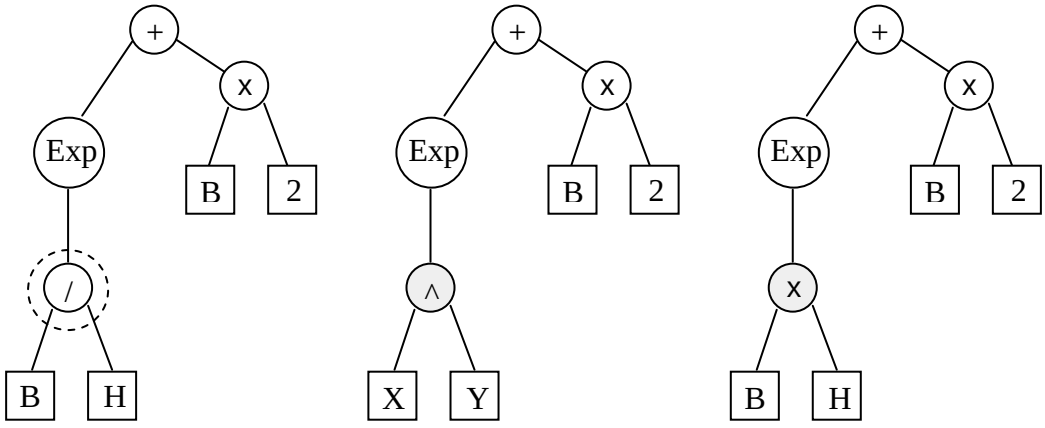

Figure (3-14): Examples of subtree and point mutation.

3.5 THE INCORPORATION OF EVOLUTIONARY COMPUTATION IN OPEN CHANNEL FLOW MODELLING

Recalling the conclusions made in the previous Chapters, this thesis intends to find a closure for two gaps in the field of open channel flow modelling:

- In order to use the SKM to predict the flow, knowledge of the lateral variation of the lumped values of the friction factor (f), dimensionless eddy viscosity (λ) and a secondary flow term (Γ), is required. Due to the "immeasurability" of the named variables, there are currently no complete guidelines for selecting their values.

- In a free overfall, the end depth bears a relationship with the critical depth. Over the years, many approaches have been developed to approximate the end depth ratio. However, all the approaches are accompanied with faults and uncertainties and there is no global method which can be applied to any channel section and flow regime.

The review presented in this chapter outlines the potentials of Evolutionary Computation in bridging these gaps. The EMO can be used in building a multi-objective calibration framework for the SKM. In the light of the model calibration results, general rules can be derived for the variation of the immeasurable parameters within the model. Furthermore GP can be used as a platform for discovering the hidden relationship between the critical depth, end depth and other attributes of the channel and flow. The following Chapters will focus on the implementation of EC techniques in open channel modelling with respect to the afore-mentioned purposes.

CHAPTER 4

MULTI-OBJECTIVE CALIBRATION FRAMEWORK FOR THE SKM

4.1 INTRODUCTION

The process of modifying the input parameters to a numerical model until the output from the model matches an observed set of data, to within an acceptable level of accuracy, is best known as parameter estimation or model calibration. This procedure will result in finding the optimal values of the "*immeasurable*" parameters in the model. This Chapter deals mainly with one of the key research objectives and illustrates the application of an evolutionary computation technique in developing a multi-objective calibration framework for the SKM.

The Chapter begins with a brief overview of the general experimental data used in this research, with a focus on the measurement techniques. Then, the key issue of defining the appropriate number, size and distribution of panels to be used in the SKM is discussed. The Chapter then continues with a descriptive section on the multi-objective calibration of the SKM model. With respect to calibration the following issues are addressed:

- Defining the appropriate objective functions.
- Selecting a suitable search method.
- Describing the search method elements and its colligation with the SKM.
- Finding the robust internal parameterization set for the search method.

This is then followed by a detailed explanation of the quintessence of this research: the calibration framework. The framework is introduced as a two phase process, namely, the

calibration phase (where the search method is applied) and the post-validation phase (where the suitable parameter set is selected). The section ends with a detailed step-by-step explanation of the calibration and post-validation phases.

4.2 EXPERIMENTAL DATA

The majority of the experimental data used in this research comes from various laboratory channels at the University of Birmingham and from the Flood Channel Facility (FCF) at HR Wallingford. The main motivation behind these experiments was to study the distribution of mean streamwise velocity and boundary shear stress for a wide range of channels under sub and super-critical flow conditions. The following sections provide a brief overview of the experimental arrangements and measurement techniques used in the process of data collection in University of Birmingham's hydraulics laboratory. Full details can be found in Knight (1992), Yuen (1989), Al-Hamid (1991), Sterling (1998), Rezaie (2006) and Chlebek, (2009).

4.2.1 Experimental arrangements

All the experiments were conducted in channels built either in a long tilting flume or a fixed bed flume. The bed and walls were normally constructed from PVC panels glued together. The water was conveyed to the flume by different supply pipelines, each connected to a suitable discharge measurement apparatus. The total channel discharge was calculated by summing the individual discharges measured by a Dall tube, Venturi meter, Electro Magnetic Flow meter (EMF) or an Orifice plate.

To reduce large disturbances in the outgoing flow from the pumps, water was first conducted into a stilling tank. A honeycomb screen was used to separate the region around the inlet pipes from the rest of the inlet tank and a smooth bell mouth transition section was made to improve the inflow conditions from the inlet tank to a specific channel. To reduce the remaining water surface fluctuations, a polystyrene panel was placed on the water surface at the entrance. At the downstream end of the fixed bed flume a series of adjustable tailgates were used to achieve uniform flow for a specific flow depth. Figure (4-1) shows the two flumes and their control elements.

(a) A 18 m fixed bed flume

(b) PVC channel in 22 m tilting flume

(c) Stilling tank and transition section

(d) Adjustable tailgates

Figure (4-1): Elements of typical flumes (www.flowdata.bham.ac.uk).

A pointer gauge, located on a mobile instrument carriage (Figure (4-2a)), was used to measure the water level at different locations along the flume to an accuracy of 0.1 mm. The depth averaged velocity and the velocity distribution were measured using a miniature propeller current meter (Figure (4-2b)). Boundary shear stresses were measured using a Preston tube, with the related pressure heads being measured using inclined manometers. Some further details can be found in Chapter 5.

(a) Pointer gauge on a mobile carriage

(b) Miniature propeller current meter

Figure (4-2): Depth and velocity measurement devices.

4.2.2 Tailgate setting

In uniform flow, the energy slope (S_e), the water surface slope (S_w) and the bed slope (S_o) are all equal to each other, i.e. $S_e=S_w=S_o$. Since it is only under this condition that the depth and velocity can be assumed to be constant at all cross sections, before any measurement could be taken in the channel, uniform flow conditions had to be achieved. The adjustable tailgates at the downstream end of the flume were used for this purpose. For sub-critical flow and a particular discharge Q, the tailgates were adjusted in such a way to give several (normally 3 to 5) M1 and M2 water surface profiles (Knight and Demitriou, 1983). The mean water surface slopes and related depths were then plotted against tailgate level, and the tailgate setting which gave a mean water surface slope equal to the flume bed slope was interpolated from the graphs. Typically, errors of ± 2% were tolerated, and the depth related to this tailgate setting was then accepted as the normal depth. This procedure was repeated for every single experiment in order to obtain accurate stage-discharge relationships for channels with different widths. Figure (4-3) illustrates a schematic tailgate setting procedure.

4.2.3 Normal depth measurement

A pointer gauge located on the instrument carriage was used to measure the water surface profile. The readings of water surface, which were taken at 1.0 m intervals down the length of the flume, were used to calculate the water surface slope and the related flow depth in the channel for a given discharge.

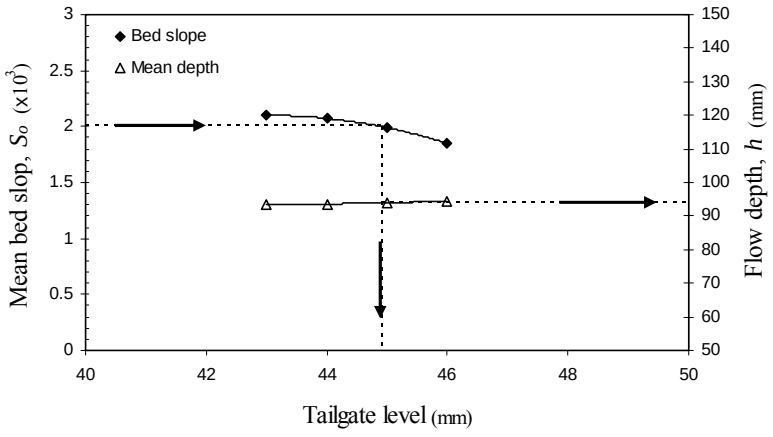

Figure (4-3): A schematic tailgate setting procedure.

4.2.4 Depth-averaged velocity measurements

Once normal depth conditions were established for a given discharge, point velocity measurements were made across one section of the channel at $z = 0.4h$ from the bed using a propeller current meter. At each lateral position, a number of readings were taken at constant intervals and then averaged to reduce error. Using a linear calibration equation provided by the manufacturer, the initial readings in terms of number of times the propeller turns/sec were converted from frequency (in Hertz) to local velocity (in $m.s^{-1}$). The average value of these readings was taken to obtain the depth-averaged velocity at each lateral position. In a number of experiments where the aim was to measure the entire velocity field, at each lateral position, the streamwise velocity was measured at 10mm vertical intervals. Then, the measured velocities where averaged over the depth to give the depth averaged streamwise velocity.

At low depths (typically less than 16.25mm) where the use of propeller current meter was impossible, the water surface velocity was measured. In this case, a piece of paper was dropped in the shallow zone and its travel time between two defined sections was measured. The local depth-mean velocity, U_d, was then calculated using the seventh power law equation:

$$(\frac{u}{U_s}) = \left(\frac{z}{h}\right)^{\frac{1}{7}}, \quad z = 0.4h \rightarrow U_d = (0.4)^{1/7} U_s \tag{4-1}$$

where U_s is the surface velocity, h is the local water depth and u is the point streamwise velocity at a distance z above the bed.

Subsequently, the individual depth averaged velocities were numerically integrated and compared with the value from discharge measurement apparatus. The error was calculated and errors of ± 3% were tolerated. The individual depth-averaged velocities were then adjusted over the cross section to give the same overall discharge rate.

4.2.5 Local boundary shear stress measurements

4.2.5.1 Smooth surfaces

Local boundary shear stress measurements were made around the wetted perimeter of smooth surfaces using Preston's (1954) technique together with the calibration equations of Patel (1965). Preston developed a simple shear stress measurement technique for smooth

boundaries in a turbulent boundary layer using a Pitot tube. Based on the *law of the wall* assumption (Bradshaw and Huang, 1995), i.e. the velocity distribution near the wall can be empirically inferred from the differential pressure between the dynamic and static pressures, Preston presented a non-dimensional relationship between the differential pressures, ΔP, and the boundary shear stress, τ_o:

$$(\frac{\tau_o d^2}{4\rho\nu^2}) = F\left(\frac{\Delta P}{4\rho\nu^2}\right) \tag{4-2}$$

where d is the outside diameter of the tube, ρ is the density of the flow, ν is the kinematic viscosity of the fluid and F is an empirical function. Following this work, Patel (1965) produced *definitive calibration* curves for the Preston tube presented in terms of two non-dimensional parameters:

$$X^* = Log_{10}\left(\frac{\Delta P d^2}{4\rho\nu^2}\right) \tag{4-3}$$

$$Y^* = Log_{10}\left(\frac{\tau_0 d^2}{4\rho\nu^2}\right) \tag{4-4}$$

The calibration of X^* and Y^* for different regions of the velocity distribution (i.e. viscous sublayer, buffer layer and logarithmic layer) is expressed by three different formulae:

$$Y^* < 1.5 \qquad Y^* = 0.037 + 0.5X^* \tag{4-5}$$

$$1.5 < Y^* < 3.5 \qquad Y^* = 0.8287 - 0.1381X^* + 0.1437X^{*2} - 0.006X^{*3} \tag{4-6}$$

$$3.5 < Y^* < 5.3 \qquad X^* = Y^* + 2\log_{10}(1.95Y^* + 4.10) \tag{4-7}$$

In practice, boundary shear stresses were measured at the same sections where the depth-averaged velocity measurements were taken. The static pressure tube was fixed in the middle of the flow depth to measure the pressure due to the static head of the flow. To measure the dynamic pressure head, the dynamic pressure tube was placed within the boundary shear layer, facing the flow. The differential pressure was then calculated from the readings on the inclined manometer:

$$\Delta P = \rho g \Delta h \sin\theta \tag{4-8}$$

where Δh is the difference between the two readings from the dynamic and static and θ is the angle of inclined manometer. Patel's equations (Eqs. 4-3 to 4-7) were then used to calculate the shear stress. Figure (4-4) illustrates a Pitot tube and an inclined manometer.

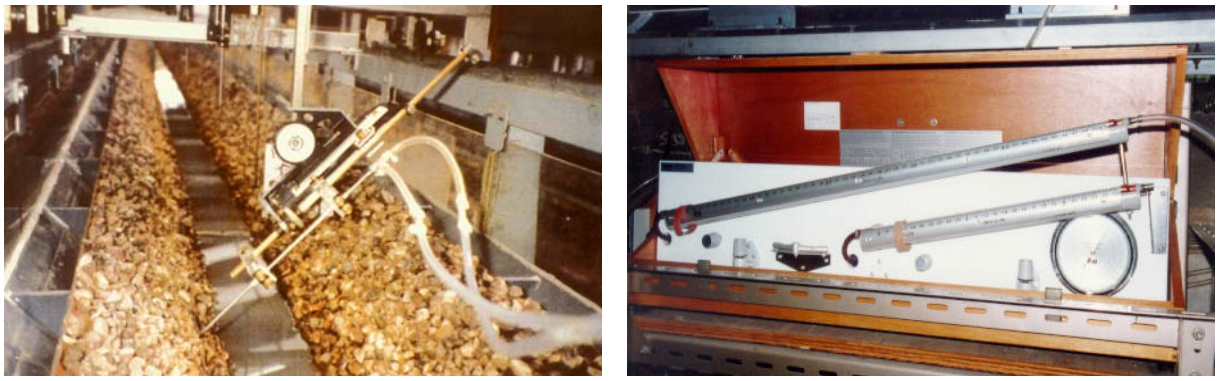

(a) Pitot tube (b) Inclined manometer

Figure (4-4): A view of a Pitot tube and inclined manometer (www.flowdata.bham.ac.uk).

Similar to the velocity measurements, the individual readings were subsequently numerically integrated and compared with the energy slope. Typically, errors of ± 6% were tolerated and individual shear stresses were adjusted to give the same energy slope.

4.2.5.2 Rough surfaces

Over rough surfaces, local shear stresses were evaluated from point velocities measured close to the surface with a Pitot-static tube, as shown in Figure (4-4a). At the points where the local shear stresses were to be evaluated, 3 to 5 point velocities where measured at 5mm spacings normal to the boundary surface. The local boundary shear stresses were then evaluated at 5mm to 20mm spacing intervals on the walls, using the corresponding logarithmic velocity law for turbulent rough flow, as indicated by Al-Hamid (1991).

4.2.6 Laboratory datasets and test cases

In the context of this thesis, a *dataset* is referred to a number of *test cases* conducted by a researcher. The datasets are named after the researcher (e.g. Yuen, Al-Hamid) while the original numbering used by the researcher is preserved for the test cases. Table (4-1) shows a

typical test case of the experimental data. In this table $\%SF_w$ is the percentage of shear force on the walls of the trapezoidal channel and y is the lateral distance from the centreline of the channel.

4.2.6.1 Trapezoidal datasets

Three sets of experimental data relating to uniform flow in trapezoidal channels were used in this research: the Flood Channel Facility (FCF) Series 04 (Knight, 1992), Yuen's (1989) data and Al-Hamid's (1991) data. Table (4-2) shows a summary of these datasets and their test cases. Most of these data, along with other data, are available on the website www.flowdata.bham.ac.uk. More detailed information about each dataset will be provided in the next Chapter.

4.2.6.2 Rectangular datasets

Two datasets were used for inbank flow in simple rectangular channels: Knight *et al*. (1984) and Tominaga *et al*. (1989). The detailed information regarding these datasets were obtained through private communication. Table (4-3) shows a summary of the rectangular datasets and their test cases.

Test case	Al-Hamid Exp 05	y (m)	U_d (m.s^{-1})	y (m)	τ (N.m^{-2})
$2b$ (m)	0.107	0.000	0.367	0.000	0.385
h (m)	0.0430	0.020	0.372	0.010	0.393
$2b/h$	2.49	0.040	0.346	0.020	0.407
P_b/P_w	1.76	0.070	0.212	0.030	0.384
S_0 (x10^{-3})	3.920	0.080	0.159	0.040	0.308
Re (x10^4)	3.489	0.097	0.000	0.050	0.253
Fr	0.544			0.054	3.238
Q (l.s^{-1})	2.01			0.056	3.392
SF_w (%)	84.69			0.059	3.557
				0.064	3.085
				0.069	3.699
				0.073	2.021
				0.078	1.808
				0.083	0.898
				0.097	0.000

Table (4-1): A typical test case (Al-Hamid Exp 05).

Channel type	Dataset / Test case	S_0 (x10^{-3})	$2b$ (m)	h (m) min	h (m) max	$2b/h$ min	$2b/h$ max	P_b/P_w min	P_b/P_w max	Re (x10^4) min	Re (x10^4) max	Fr min	Fr max	Q (l.s^{-1}) min	Q (l.s^{-1}) max
Smooth Bed and Smooth Walls	**FCF**	1.027	1.500	0.049	0.301	4.980	30.850	0.352	2.181	6.317	99.151	0.584	0.762	29.900	656.30
	Yuen 000	1.027	0.150	0.050	0.150	1.000	3.000	0.354	1.061	4.101	15.638	0.559	0.590	3.500	26.300
	Yuen 200	8.706	0.150	0.029	0.099	1.515	5.263	0.536	1.861	7.145	35.804	1.882	2.000	4.700	41.100
	Yuen 400	23.37	0.150	0.029	0.099	1.515	5.263	0.536	1.861	12.443	61.831	3.243	3.227	8.100	66.300
Smooth Bed and Rough Walls (R1)	**Al-Hamid 01-05**	3.920	0.107	0.043	0.126	0.850	2.491	0.601	1.761	3.489	11.870	0.520	0.544	2.009	13.688
	Al-Hamid 23-25	3.920	0.256	0.051	0.085	3.011	5.004	2.129	3.538	6.745	12.600	0.654	0.659	6.713	15.532
	Al-Hamid 26-30	3.920	0.399	0.040	0.067	5.989	9.987	4.235	7.062	7.130	13.302	0.853	0.884	9.300	20.053
Smooth Bed and Rough Walls (R2)	**Al-Hamid 09-13**	3.920	0.121	0.048	0.142	0.849	2.513	0.601	1.777	4.257	14.730	0.607	0.638	3.113	21.947
	Al-Hamid 17-19	3.920	0.272	0.055	0.091	2.994	4.990	2.117	3.528	11.210	86.550	0.798	0.830	9.996	22.246
	Al-Hamid 31-35	1.935	0.416	0.042	0.070	5.986	10.005	4.233	7.074	5.623	11.610	0.690	0.708	8.030	18.470
Rough Bed and Rough Walls (R1)	**Al-Hamid 06-08**	3.920	0.140	0.056	0.095	1.492	2.495	1.055	1.764	3.649	7.852	0.390	0.511	2.816	9.497
Rough Bed and Rough Walls (R2)	**Al-Hamid 14-16**	3.920	0.143	0.057	0.095	1.505	2.516	1.064	1.779	3.714	7.852	0.440	0.511	3.313	9.497
	Al-Hamid 20-22	3.920	0.297	0.050	0.074	3.997	6.056	2.827	4.282	4.835	8.802	0.499	0.550	5.581	11.783
	Al-Hamid 36-38	4.030	0.441	0.044	0.059	7.491	9.982	5.297	7.058	4.453	7.029	0.493	0.540	6.660	11.430

Table (4-2): Summary of trapezoidal datasets.

Channel type	Datasets	S_0 (x10^{-3})	$2b$ (m)	h (m) min	h (m) max	$2b/h$ min	$2b/h$ max	P_b/P_w min	P_b/P_w max	Re (x10^4) min	Re (x10^4) max	Fr min	Fr max	Q (l.s^{-1}) min	Q (l.s^{-1}) max
Smooth Bed and Smooth Walls	**Knight**	0.966	0.152	0.086	0.153	0.993	1.772	0.497	0.886	6.484	9.402	0.346	0.401	4.800	9.850
	Tominaga	0.641 ~ 1.160	0.400	0.050	0.066	6.033	8.065	3.017	4.032	5.079	8.118	0.416	0.471	5.806	9.853

Table (4-3): Summary of rectangular datasets.

4.3 DEFINING PANEL STRUCTURES

As mentioned in Chapter 2, one of the main issues in applying methods such as the SKM is defining the number, position and width of the panels within the cross-section of the channel or river which is to be modelled. This matter is especially important as one of the main goals of this research is to find the lateral variation of lumped model parameters, i.e. parameters averaged in time and space (channel depth and panel width). Therefore any decisions on the number, position and width of the panels would directly affect the results and might lead to misinterpretation of the final obtained values.

In this research, the philosophy of Knight and co-workers (2007) for panel selection was adopted for homogeneous trapezoidal channels. As stated in Section 2.6.9.3, continuing the work of Tominaga *et al*. (1989), Knight *et al*. (2007) proposed a panel structure for smooth trapezoidal channels based on the number and size of the observed contra-rotating secondary flow cells and interpreting the secondary flow term (Γ) (Figure 4-5).

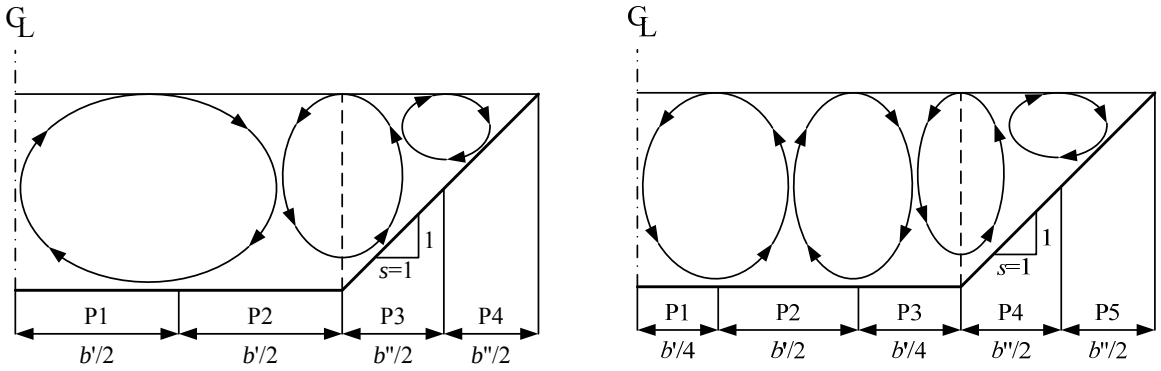

a) $2b/h < 2.2$ b) $2b/h > 2.2$

Figure (4-5): Secondary flow cells and the number of panels for simple homogeneous smooth trapezoidal channels (Knight *et al*., 2007). (b' is half width of the flat bed region and b'' is the width of the sloping sidewall section)

In keeping with the above work on homogeneous channels, a similar panel structure was found for heterogeneous trapezoidal channels. For smooth rectangular channels, four different panel structures were investigated and the results were compared to select a suitable structure. On the other hand, the rivers cases were modelled with 8 equally spaced panels. More detailed information on the panel structure is provided in the following Chapter.

4.4 MULTI-OBJECTIVE CALIBRATION OF THE SKM MODEL

In this section, the methodology of investigating the lateral variation of three lumped parameters inside a channel through the process of calibrating a hydraulic model (i.e the SKM) via a multi-objective evolutionary algorithm (i.e. NSGA-II) is described. First, the essential stages for the preparation of the calibration platform are explained. Then a detailed step-by-step elucidation of the main calibration framework is proposed.

4.4.1 Deriving the objective functions

To fulfill the aim of finding the lateral variation of different parameters through the process of model calibration, the available observed experimental data were reviewed to identify the proper objective functions. Figure (4-6) illustrates the experimental and model predicted lateral distributions of depth-averaged velocity and bed shear stress distribution for a typical test case (Al-Hamid Exp 05). The two primary objective functions (Eqs. 4-9 & 4-10) were defined as a measure of difference between observed and model generated data (dotted lines in the Figure). As the mean streamwise velocity and local boundary shear stress distributions for each case consisted of many experimental points, the sum of squared errors (SSE) was selected as the most appropriate goodness-of-fit measure, since it inherits the feature of increasing the influence of more distant points.

By integrating the model results, the total discharge (Q) and the percentage of shear force on the walls of the channel ($\%SF_w$) could also be obtained. Based on these predictions, two additional objective functions (Eqs. 4-11 & 4-12) were defined as measures of difference between the single calculated and measured values of Q and $\%SF_w$. In contrast to the first two objective functions, the absolute percentage error (APE) was selected as the appropriate performance measure. The selected objective functions are as follows:

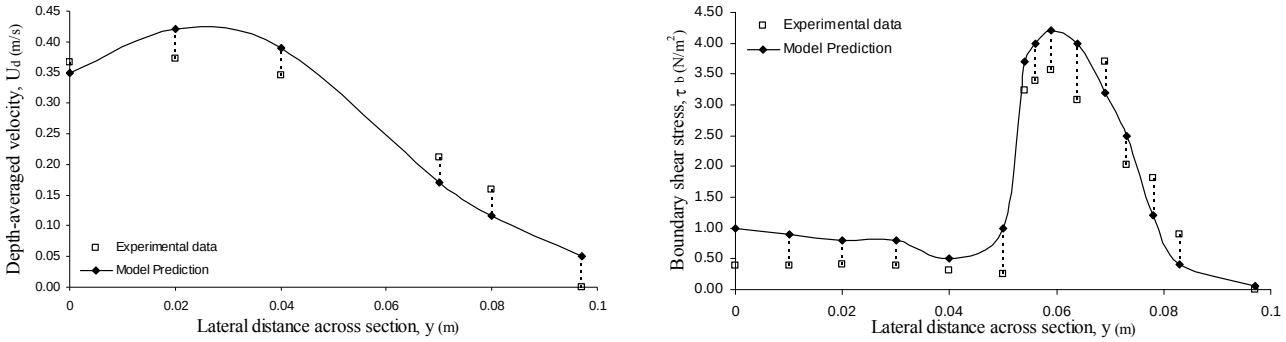

a) Depth-averaged velocity distribution b) Shear stress distribution

Figure (4-6): Experimental and Model Predicted distributions (Al-Hamid Exp 05).

$$f_1(X) = \sum_i \left((U_d)_{\text{SKM}} - (U_d)_{\text{exp}} \right)^2 \tag{4-9}$$

$$f_2(X) = \sum_i \left((\tau_b)_{\text{SKM}} - (\tau_b)_{\text{exp}} \right)^2 \tag{4-10}$$

$$f_3(X) = \left| \frac{Q_g - Q_{\text{SKM}}}{Q_g} \right| \times 100 \tag{4-11}$$

$$f_4(X) = \left| \frac{\%(SF_w)_g - \%(SF_w)_{\text{SKM}}}{\%(SF_w)_g} \right| \times 100 \tag{4-12}$$

where $X = (f_1, \lambda_1, \Gamma_1, ..., f_N, \lambda_N, \Gamma_N)$ is the variable vector in the parameter search space, Ω, and N is the number of panels. The subscripts SKM and exp refer to the predictions obtained using the SKM model and experimental data respectively. In $f_3(X)$ and $f_4(X)$ the subscript "g" is used to denote the global value of either Q or $\%SF_w$ and indicates that for these two functions the channel is considered as a whole, i.e. with the panels 'removed'. Depending on the available data, any combination of the above objectives can be minimized simultaneously.

It is known that the choice of the objective functions can influence the optimum model parameters and consequently change the quality of modelling (Legates and McCabe, 1999; Wagener *et al*., 2004). It has also been stated that the choice of objective function can change the amount of correlation between the parameters (Wagener *et al*., 2004). It is acknowledged that additional objective functions could have been used. However, it is felt that those listed above made use of the best available data and enabled a good comparison with previously published experimental results (Sharifi *et al*., 2009).

It is to be further noted that the parameter search space, Ω, was defined by adding sufficient margins to the stated range of the calibration parameters in literature (see Sections 2.6.7 to 2.6.9):

$0.005 \le f_i \le 0.100$ smooth boundary; $0.005 \le f_i \le 1.000$ rough boundary (4-13)

$$0.005 \le \lambda_i \le 2.50 \tag{4-14}$$

$$-3.50 \le \Gamma_i \le 3.50 \tag{4-15}$$

4.4.2 Selecting a suitable search algorithm

The next step in building an *evolutionary-based model calibration framework* is to select a suitable search algorithm. Some important considerations in selecting a suitable search algorithm for the proposed problem are:

1- There are more than one objective functions to be optimized simultaneously.
2- There are a large number of decision variables in each of the objective functions (3 parameters for each panel) which result in a high dimension search space.
3- The experimental data has some irregular noise (especially in boundary shear stress measurements over rough surfaces).
4- Due to the relatively long computation time in evaluating a decision variable set with the available processor capacity, an efficient stochastic search algorithm is essential.

As stated in Chapter 3, multi-objective evolutionary algorithms (MOEA's) have been extensively reviewed by various researchers (e.g. Fonseca and Fleming, 1998; Coello, 1999; Zitzler *et al*., 1999; Tan *et al*., 2002; Ghosh and Dehuri, 2004; Raghuwanshi and Kakde, 2006). Although these proposed algorithms have been successfully applied in practice, there is no single algorithm which can consistently outperform the others in every problem class. In fact, the performance of a search algorithm depends on whether its search strategy fits the features and requirements of the underlying problem.

Studying a variety of test cases (e.g. Deb *et al*., 2002; Khare *et al*., 2003), it has been shown that compared to other multi-objective evolutionary algorithms, NSGA-II has a better diversity preservation and therefore is able to compete with them regarding its convergence to the true Pareto-optimal front in both constraint and non-constraint problems (Nazemi *et al*., 2006). This superiority has lead to the successful application of NSGA-II in several real world problems (see Section 3.3.5). Based on problem requirements and successful application in similar problems the NSGA-II algorithm was adopted and will be shown to be an efficient tool for the proposed calibration framework.

4.4.3 Non-dominated sort genetic algorithms II (NSGA-II)

The MATLAB implementation of NSGA-II, based on the description provided by Deb *et al.* (2002), has been adopted for the current work. Tournament selection, Simulated Binary Crossover (SBX) (Deb and Agarwal, 1995) and Polynomial Mutation Operators (Deb and Agarwal, 1995) were selected as the genetic operators of the real-coded NSGA-II algorithm. Figure (4-7) shows the main algorithm structure. These functions are presented in Appendix (III).

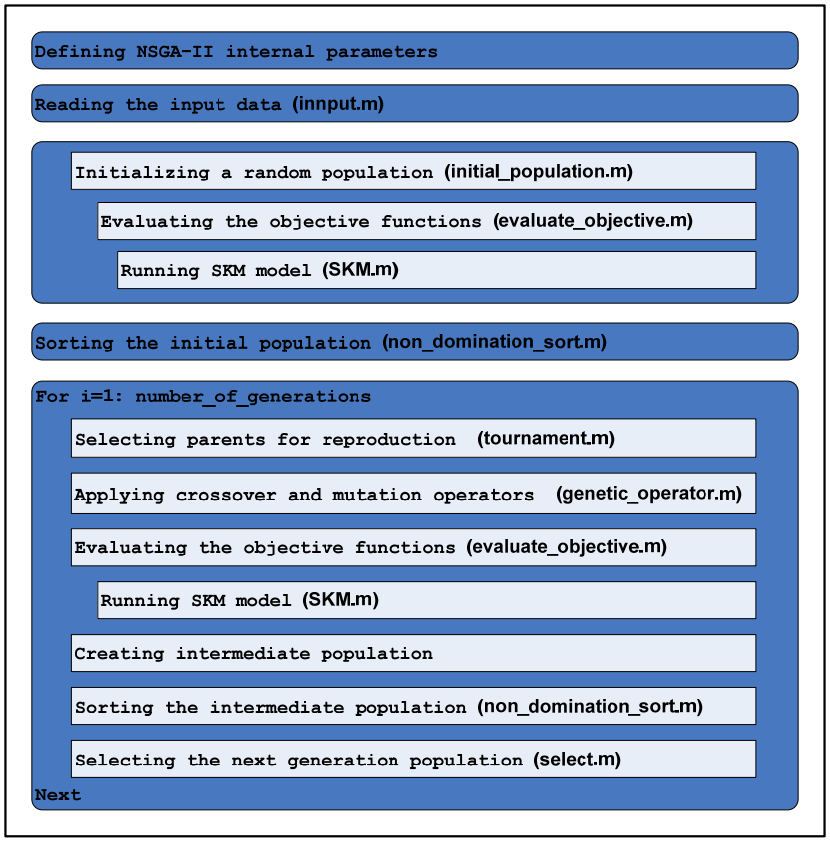

Figure (4-7): NSGA-II algorithm structure.

4.4.4 Finding a robust parameterization set for NSGA-II

Many researchers (e.g. De Jong, 1975; Harik *et al.*, 1997; Deb and Agrawal, 1998) have investigated the interdependencies of GA parameters in order to determine their optimal settings. However, due to the complex interactions among these parameters, the task of tuning the GA internal parameters has been proven to be difficult and as Michalewicz, (1992) reports, it is more of "*an art than a science*". De Jong, (1975) was one of the pioneers who

attempted to study the complex interactions of GA parameters and introduced a good set of parameter settings based on his findings, which have been widely adopted and are sometimes referred to as "standard" settings (Tran, 2005). However, later theoretical studies (e.g. Goldberg *et al*., 1992; Harik *et al*., 1997) have illustrated the shortcomings of these "standard" settings and have shown that the optimal parameter set varies from problem to problem (Davis, 1991).

A number of studies have been conducted to find the optimal GA operators for water related models. Comparing several GAs for the calibration of conceptual rainfall run-off models, Franchini and Galeati (1997) found that the optimum parameter set was not influenced by the GA operators, and concluded that a robust GA operator range was adequate to provide efficient solutions. Wardlaw and Sharif (1999) and Ng and Perera (2003) also studied the GA operators in calibrating a reservoir system operation and a river water quality model, respectively and found different optimum GA operators. Most recently Perera and Siriwardene (2006) analyzed the sensitivities of GA operators through repetitive simulations for an urban drainage model and realized that, generally, the operator sensitivity increases with the increase in the number of decision variables. All these studies indicate that there are no clear conclusions regarding optimum GA operators and no general guidelines are available to be used in specific model parameter optimization. Therefore, a detailed study was conducted to investigate the significance of GA operators on the SKM parameter optimization, and to find the optimum GA parameter set.

As mentioned in the previous section, the selected genetic operators, (i.e. maximum number of generations (*gen*), population size (*pop*), crossover probability (P_c), crossover distribution index (η_c), mutation probability (P_m), mutation distribution index (η_m) and tournament pool size (*tps*)) should be assigned prior to the algorithm implementation. To find the suitable parameter set, first, a preliminary sensitivity analysis was performed on a test case. The initial results revealed the low sensitivity of the algorithm to the tournament pool size (*tps*), mutation probability (P_m) and mutation distribution index (η_m). Accordingly, and in keeping with previous studies (e.g. Nazemi *et al*., 2006; Sarkar and Modak, 2006) their values were set as 2, 0.05 and 20, respectively. In the next step, a comprehensive sensitivity analysis was performed to address the effect of the other internal settings of the algorithm on the quality of

convergence and to obtain a robust algorithm parameter set. Table (4-4) shows different possibilities for these internal parameters. In total 81 settings were considered and used for a two-objective (Eqs. 4-9 & 4-10) calibration of a test case based on the outlined procedure.

Operator	Candidates	Considered options
population size (*pop*)	3	*pop* ={100, 200, 300}
number of generations (*gen*)	3	*gen* ={250, 500, 750}
crossover probability (P_c)	3	P_c ={0.5, 0.7, 0.9}
crossover distribution index (η_c)	3	η_c ={10, 20, 30}

Table (4-4): Different options for NSGA-II parameters considered in this study.

Two measures of convergence: the number of solutions on the Pareto front and minimum values of objective functions, along with the measured computation time were defined as the main criteria for selecting the suitable internal parameter. Figures (4-8 & 4-9) show the effect of different GA internal parameters on the number of Pareto solutions and minimum values of the objective functions respectively.

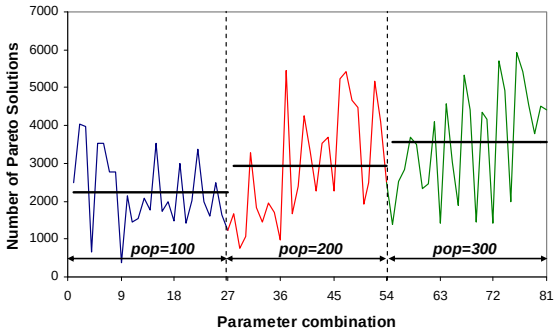

(a) Population size

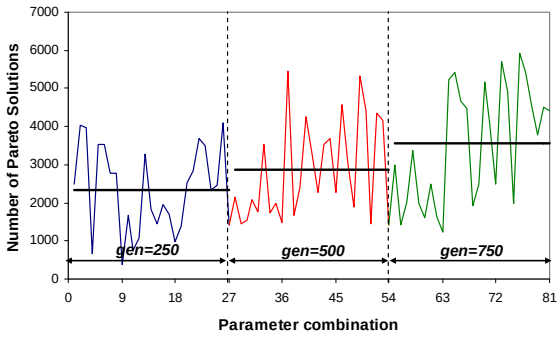

(b) Number of generations

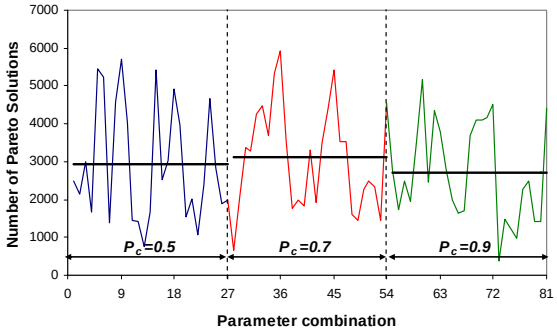

(c) Crossover probability

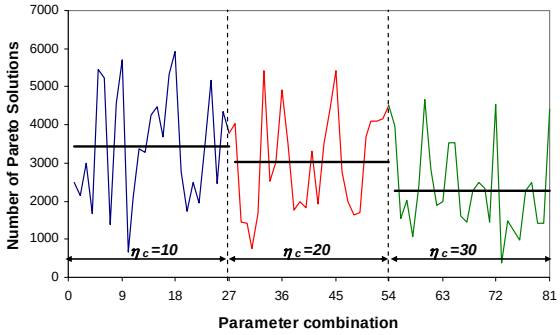

(d) Crossover distribution index

Figure (4-8): Effect of different GA internal parameters on the number of Pareto solutions. (Solid horizontal lines represent the average values).

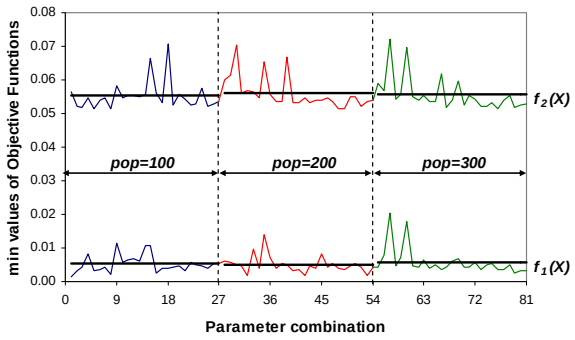

(a) Population size (*pop*)

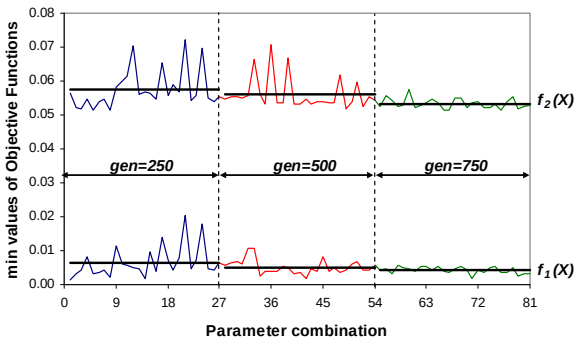

(b) number of generations (*gen*)

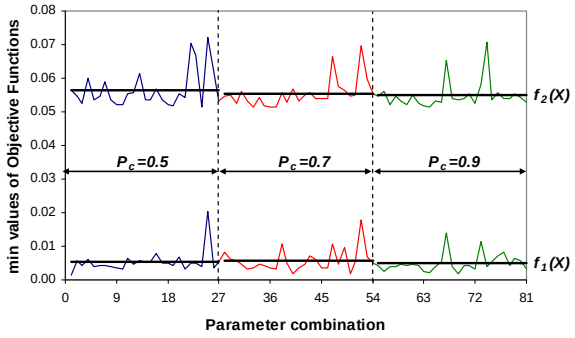

(c) Crossover Probability (P_c)

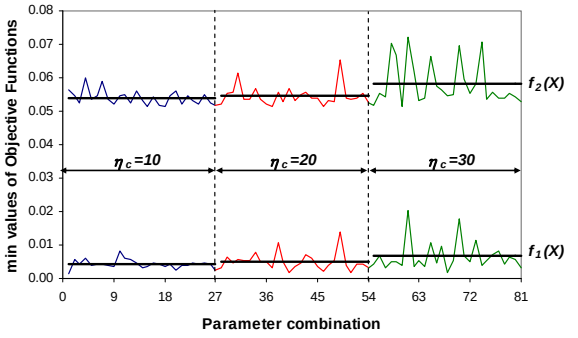

(d) Crossover distribution index (η_c)

Figure (4-9): Effect of different GA internal parameters on the minimum values of the objective functions (solid horizontal lines represent the average values).

4.4.4.1 Population size

One of the most important settings in a GA-based algorithm is the population size which has to be considered carefully. If the population size is too small, the diversity in the population will be too low and the population will soon suffer from premature convergence. However, if the size is too large the convergence towards the global optimum is slow, demanding high processor power and memory requirements.

Figure (4-8a) shows that the number of population for each generation has a direct effect on the number of Pareto solutions. In contrast, Figure (4-9a) implies that the lower bounds of the objectives are not affected much by the number of population. A similar trend can be observed for individual model parameters. Hence, since there is insignificant change in the level of optimality when the number of population is increased from 200 to 300, a population size of 200 is selected as the suitable value for the problem.

4.4.4.2 Number of generations (function evaluations)

Another important setting is the number of generations or number of function evaluations. Usually, this setting is set based on a *tradeoff* between the quality of convergence and computation time. Figures (4-8b & 4-9b) show that by increasing the number of total function evaluations, the quality of convergence, in terms of both the number of Pareto solutions and robustness in the lower-bounds of the objective convergences, will improve. Therefore, it can be judged that a total number of 500 generations achieves a more favourable tradeoff between computation and level of optimality.

4.4.4.3 Crossover probability and crossover distribution index

Like other GA internal parameters, the setting of the crossover probability is the subject of debate (Mitchell, 1999). However, Lobo (2000) states that the performance of a GA is not so much influenced by this parameter, as it is by population size and number of generation.

Figure (4-8c) implies that unlike other internal parameters investigated, the increment of crossover probability does not always result in finding more Pareto solutions. Figure (4-9c) shows that the averages of lower-bound values regarding the objectives functions remain constant when the crossover probability is changed. Based on the observations the optimal value for the crossover probability is found as 0.7. Figure (4-8d) also shows that the average number of Pareto solutions is at the highest level when crossover distribution is set as 10. Table (4-5) shows the obtained robust algorithm parameter set.

Operator	**value**
Maximum number of generations (gen)	500
population size (pop)	200
crossover probability (P_c)	0.7
crossover distribution index (η_c)	10
mutation probability (P_m)	0.05
mutation distribution index (η_m)	20

Table (4-5): Real coded NSGA-II internal parameters used in this study.

4.4.5 Calibration phase

Having derived the objective functions, selected the suitable search method and set its internal parameters, the platform was now ready for applying the algorithm to each individual dataset. Since, like all other GA algorithms, NSGA-II starts with a random generated population, to limit the effect of randomness on the results, the algorithm needed to be run a number of times with different seedings. Analyzing the results of various simulations on a number of test cases revealed that after running the algorithm for about 15 times, no significant improvement could be obtained for the Pareto solutions. Thus, the algorithm was run 15 times for each individual test case, changing the seeding in each run. This resulted in a set of fronts of non-dominated solutions (Figure 4-10). Subsequently, the non-domination sort algorithm was applied on this set (i.e. accumulated Pareto solutions) and an ultimate "*representative*" Pareto front was found for each test case (i.e. circles in Figure (4-10)).

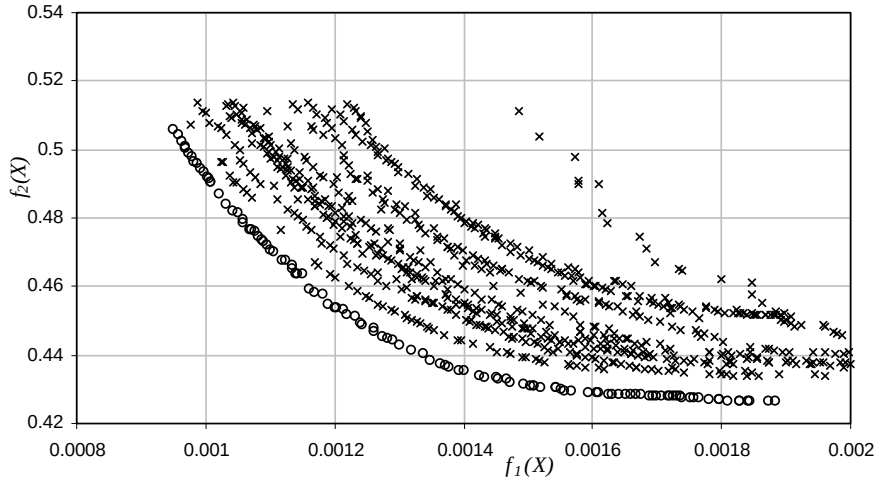

Figure (4-10): Accumulation of all Pareto solutions and the ultimate representative Pareto.

4.4.6 Post-validation phase

After finding a representative Pareto for each test case, a series of operations were performed on the remaining multi-objective calibration solutions to select an optimum variable set for each data case. The aim was to find the "best" set of variables which resulted in the following conditions (Sharifi *et al*., 2009a):

1- Gives results with smooth predictions for the mean streamwise velocity and local boundary shear stress distribution.

2- Has the ability to predict the total discharge (Q) and percentage of shear force on the walls ($\%SF_w$) with high accuracy (errors less than 5%).

3- Inherits an appropriate Γ sign pattern in adjacent panels, in accordance with the nature of the secondary flow cells which come in pairs (Perkins, 1970; Knight *et al*., 2007).

4.4.6.1 Locating the effective portion of the Pareto front

As mentioned in sections 4.2.4 and 4.2.5, errors in the experimental data in the range of ± 3% and ± 6% were tolerated for discharge and bed shear stress measurements respectively. To keep within this range of accuracy, the third and fourth objective functions (Eqs. (4-11) and (4-12)) were evaluated for all the non-dominated solutions on the representative Pareto front. The solutions which estimated Q and $\%SF_w$ to within less than 5% error were preserved and the remaining were discarded. After this filtering, the "effective" portion of the Pareto front was found (Figure (4-11)).

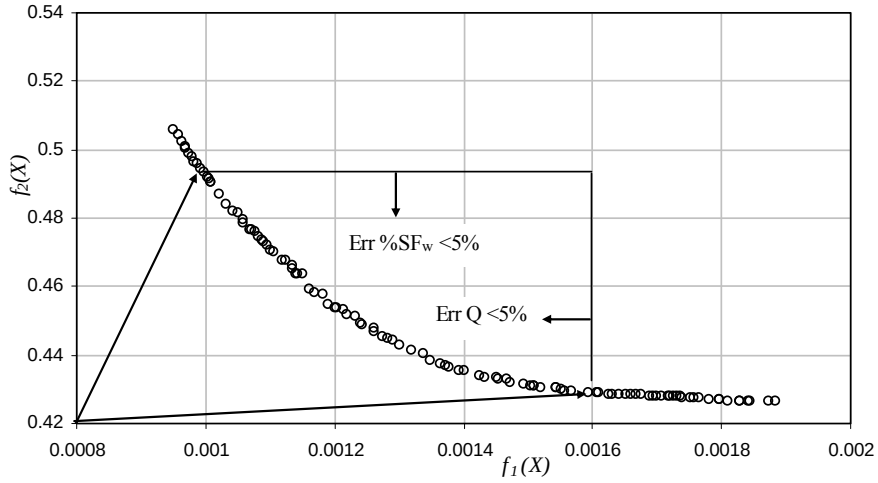

Figure (4-11): Selecting the acceptable solutions on the Pareto front based on the value of the third and fourth objective function (case Al-Hamid Exp05).

4.4.6.2 Cluster analysis on the effective portion of the Pareto

Due to the significant effect that the friction factor has on the bed shear stress distribution calculations and consequently on the second objective function, among all model variables, the friction factor value of each panel quickly converges to a specific range. Mapping the effective Pareto solutions to a sub-space of the decision search space, Ω, defined only by the three parameters of f_2, f_3 and f_4, a number of regions (typically ranging between 3 to 7) were identifiable (Figure (4-12)).

In the second stage of the post-validation phase, the solutions lying on the effective portion of the representative Pareto front were mapped to the mentioned parametric sub-space and the number of *regions of attraction* were defined. Then a non-hierarchical clustering analysis adopting the k-means method (Gnanadesikan, 1977) (see Appendix (V) for detailed explanation) was undertaken on the solutions and the clusters representing each region were found for each test case. Figure (4-13) shows the position of the clusters on the Pareto front of case Al-Hamid Exp 05 and Table (4-6) shows the specifications of the found clusters for another typical test case.

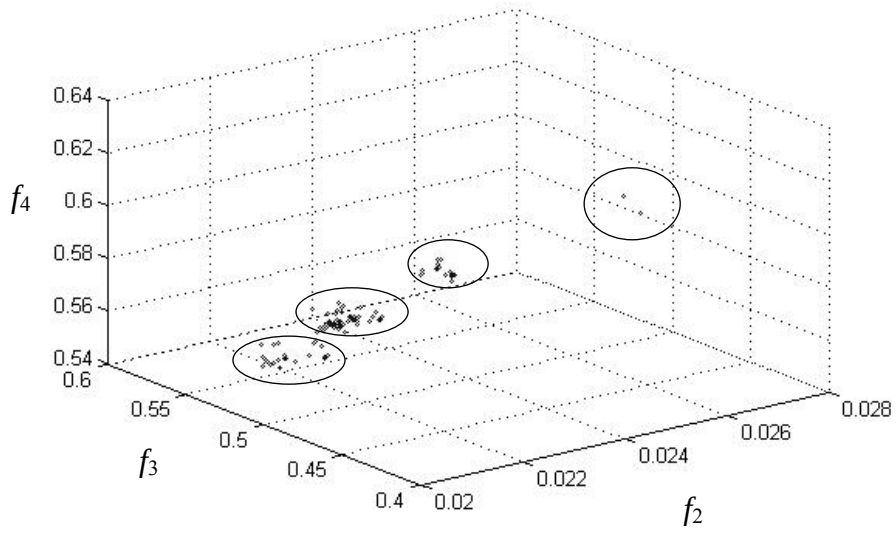

Figure (4-12): The position of regions of attraction on the decision search space (Ω).
(f is the friction factor and the index represents the panel).

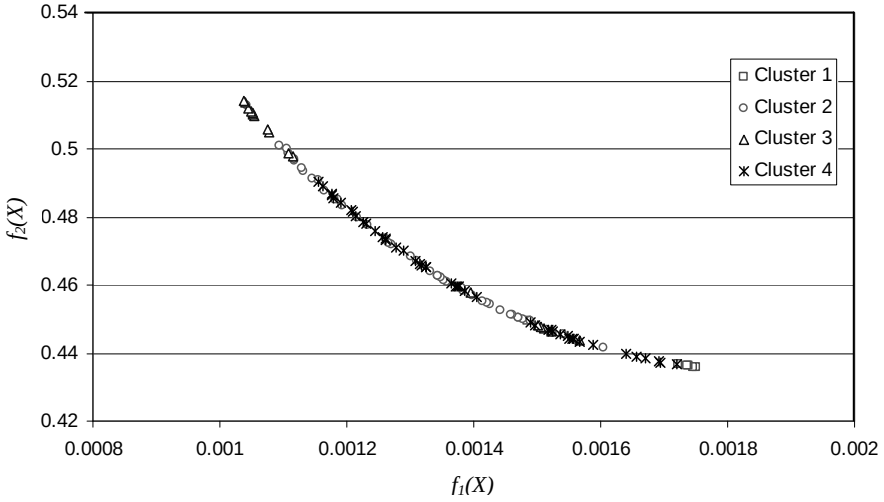

Figure (4-13): The position of the found clusters on the front of the Pareto front.
(case Al-Hamid Exp05).

		Panel 1			Panel 2			Panel 3			Panel 4		
		f	λ	Γ	f	λ	Γ	f	λ	Γ	f	λ	Γ
Cluster 1	min	0.01500	1.93	-1.34	0.01604	0.83	1.57	0.328	1.63	1.81	0.562	0.04	-2.82
	max	0.01531	1.97	-1.30	0.01627	0.84	1.63	0.339	1.72	2.04	0.589	0.04	-2.79
	mode	**0.01515**	**1.95**	**-1.32**	**0.01613**	**0.84**	**1.60**	**0.334**	**1.68**	**1.91**	**0.576**	**0.04**	**-2.80**
	average	0.01518	1.94	-1.34	0.01618	0.83	1.61	0.328	1.63	1.81	0.562	0.04	-2.79
	Standard deviation	1.5E-08	2.3E-04	2.6E-04	8.8E-09	1.8E-05	3.6E-04	2.2E-05	1.7E-03	9.1E-03	1.3E-04	6.5E-07	1.8E-04
Cluster 2	min	0.01493	2.43	0.78	0.01327	0.36	-0.32	0.434	1.69	0.63	0.745	0.04	-2.89
	max	0.01580	2.50	0.86	0.01559	0.37	-0.24	0.476	1.82	0.98	0.801	0.05	-2.73
	mode	**0.01540**	**2.46**	**0.82**	**0.01459**	**0.37**	**-0.29**	**0.453**	**1.76**	**0.80**	**0.778**	**0.04**	**-2.83**
	average	0.01498	2.46	0.79	0.01541	0.37	-0.29	0.434	1.78	0.95	0.745	0.04	-2.82
	Standard deviation	1.3E-07	3.0E-04	6.5E-04	6.5E-07	3.8E-06	2.0E-04	2.0E-04	2.3E-03	1.9E-02	6.0E-04	3.2E-06	1.9E-03
Cluster 3	min	0.01621	0.30	0.68	0.01445	0.40	-0.58	0.353	0.53	0.32	0.771	0.04	-1.41
	max	0.01664	0.35	0.77	0.01590	0.46	-0.15	0.542	0.83	0.66	1.014	0.05	-1.81
	mode	**0.01652**	**0.31**	**0.69**	**0.01570**	**0.41**	**-0.21**	**0.433**	**0.57**	**0.54**	**0.832**	**0.04**	**-1.60**
	average	0.01635	0.32	0.71	0.01569	0.41	-0.25	0.455	0.59	0.50	0.893	0.05	-1.66
	Standard deviation	2.3E-08	4.5E-12	6.0E-04	7.3E-08	1.7E-04	6.0E-04	2.5E-05	7.5E-03	1.4E-04	1.5E-04	2.4E-06	1.2E-03
Cluster 4	min	0.01671	2.26	-0.50	0.01578	0.88	0.29	0.379	0.16	-1.92	0.908	3.19	0.11
	max	0.01728	2.27	-0.46	0.01672	0.90	0.29	0.382	0.16	-1.91	0.911	3.48	0.19
	mode	**0.01706**	**2.27**	**-0.48**	**0.01625**	**0.89**	**0.29**	**0.381**	**0.16**	**-1.92**	**0.909**	**3.35**	**0.15**
	average	0.01680	2.27	-0.50	0.01648	0.88	0.29	0.382	0.16	-1.92	0.908	3.45	0.14
	Standard deviation	5.1E-08	1.6E-05	2.5E-04	1.1E-07	6.2E-05	2.7E-06	1.5E-06	1.5E-06	4.2E-06	1.1E-06	1.3E-02	5.3E-04

Table (4-6): The cluster of solutions found for a typical test case.
(case Al-Hamid Exp27).

4.4.6.3 Selecting the robust parameter set

In the final stage of post-validation, the solutions resulting in the highest solubility (see Section 3.3.1) were finally tested for their generic attributes. This stage consisted of the following steps:

- First, the major patterns for the sign of the secondary flow term (Γ) were recognized for each channel type (e.g. see Table (4-7)) and the clusters which had the major patterns were preserved for each test case.
- Next, the mode value of each variable in each of the remaining clusters was selected as the representative of that cluster, and used in conjunction with the SKM to predict the depth average streamwise velocity and boundary shear stress distributions. The obtained distributions were then plotted along with the experimental data for all cases. A typical set of results is illustrated in Figure (4-14).
- A cross-case analysis was then undertaken along with visual inspection of the obtained distributions of all cases in each dataset. Based on the frequency of appearance of patterns in Pareto sets across cases and also the general look of the distributions, the dominant sign pattern of the secondary flow term (Γ) was selected for each dataset.
- For each test case, the predictions of the representatives (mode values) of clusters with the selected Γ sign pattern were compared, and representatives resulting in similar distribution shapes (with the other test cases in the dataset) were chosen as the "*best*" answer of each case.

Sign of Γ		Panel 1	Panel 2	Panel 3	Panel 4	Panel 5
FCF data ($2b/h$ >2.2)	Pattern 1	-	+	+	-	+
	Pattern 2	-	+	-	-	+
Yuen's data ($2b/h$ <3.0)	Pattern 1	-	+	-	+	
	Pattern 2	+	+	-	+	
Al-Hamid's Smooth Bed and Rough Walls	Pattern 1	+	-	+	-	
	Pattern 2	-	+	+	-	
	Pattern 3	-	+	-	+	
Al-Hamid's Rough Bed and Rough Walls	Pattern 1	-	+	-	+	
	Pattern 2	-	+	+	-	
	Pattern 3	+	-	+	-	

Table (4-7): The most frequent observed patterns for the sign of the secondary flow term in different trapezoidal datasets.

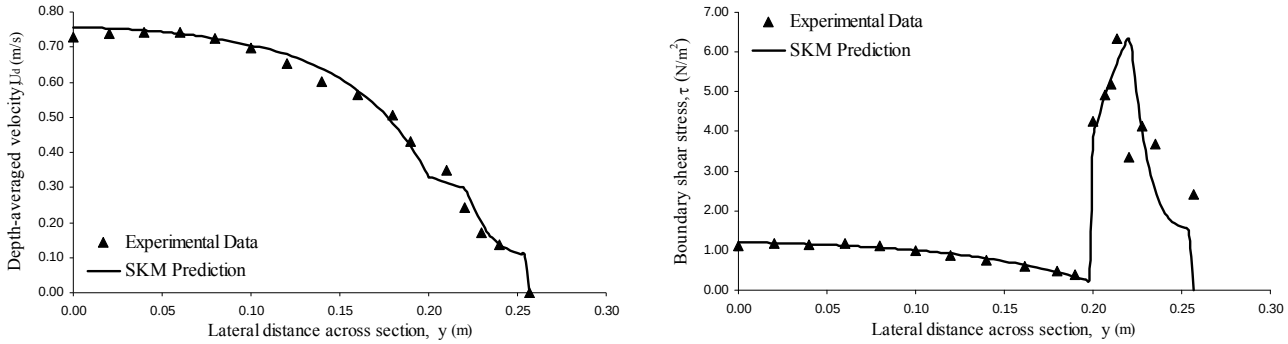

a) + - + -

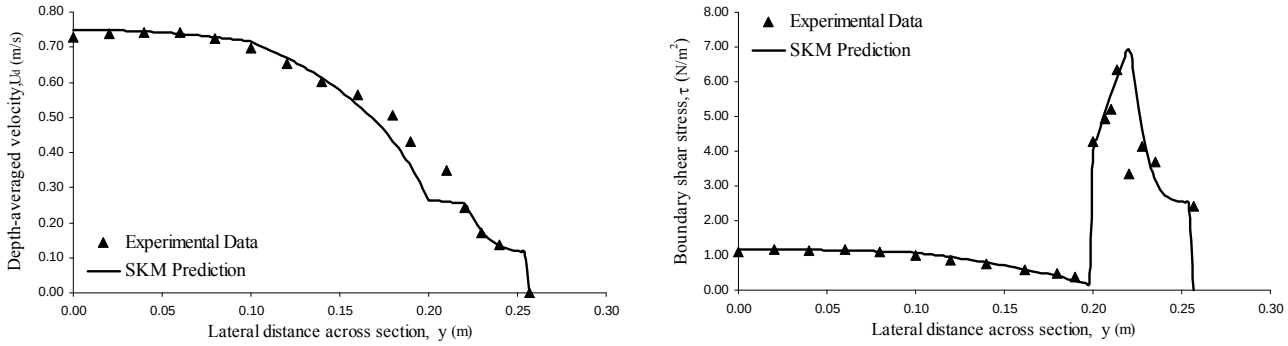

b) - + + -

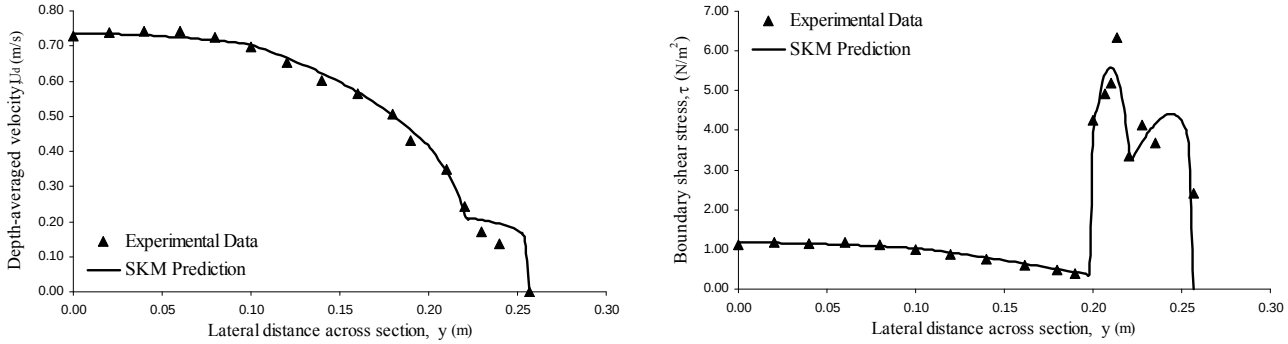

c) - + - +

Figure (4-14): Best mean velocity and boundary shear stress distribution of different patterns for Al-Hamid Exp 27 (Aspect ratio = 7.032 Smooth bed and R1 on the wall).

4.4.6.4 Anomalous cases

In a small number (less than 15%) of the total test cases, due to the non-uniqueness of the optimum parameter set, or as a result of over-fitting the experimental data (Bishop, 2006), the obtained optimum variable values from the first Pareto front were not concordant with the optimum variables found for other cases of the dataset. More specifically, the representative of all the clusters found on the effective portion of the Pareto would either have a secondary

flow term (Γ) sign pattern other than the dominant one, a set of optimum variables which were not close to the obtained range from other test case results or both dissimilarities. At this point, in order to be able to generalize the calibration results, an algorithm was developed to carefully search the succeeding ranked non-dominated Pareto fronts and find optimum solutions that not only had the selected Γ sign pattern (for the dataset), but also had variable values concordant with the other test cases.

4.5 DISCUSSION ON PARAMETER IDENTIAFABILITY

Finding various clusters of solutions on the Pareto front which, if mapped on the parametric space, would each represent a specific region, indicates that the SKM model suffers from *lack of identifiability* or *equifinality* (Beven and Binley, 1992; Beven and Freer, 2001; Beven, 2006) in its parameterization. This is the problem of which different optimum parameter sets are better than each other in terms of one or more performance measures but can all acceptably represent the observed behaviour of the system and thus none can be easily rejected. This *non uniqueness* of solutions, gives no guarantee of convergence to the true value of parameters and therefore usually gives rise to confusing results. The insensitivity of the model to the value of λ in different panels and finding various optimum patterns for the sign of Γ, are all results of this problem. The probable sources of this problem can be defined as:

1- *Experimental data uncertainty*: the limitations and errors in the measurements of input experimental data might have caused the available data not to be informative enough to identify the model parameters and find a unique and accurate value for them. Even if they can be fitted, there is the possibility that data limitations will ensure *lack of identifiability* in the model parameters and that a change in one parameter can be compensated almost completely by a proportional shift in another, while still producing a satisfying fit between the model predictions and the data.

2- *Model structure uncertainty and complexity*: the assumptions made in building the model, especially regarding the dimensionless eddy viscosity (Section 2.6.1), secondary flow term (Section 2.6.1) and boundary shear stress calculations (Section 2.5.4) along with the mathematical properties of the model might have caused complex interactions between model

parameters which results in *lack of identifiability* in the model parameters. Furthermore, the selected number of panels directly affects the model complexity as each panel imposes 3 parameters to the problem. The greater the number of panels, and hence greater complexity of the model, the better it can reflect the changing response of the system to different conditions, but more parameters are to be defined by calibration. In fact, increasing the number of parameters in a model is equivalent to increasing the degrees of freedom in specifying input data and adding additional dimensions in the search space (Beven, 2006). Since usually the quality and quantity of the data collected are not sufficient for determining the parameters, a robust calibration is unlikely to be achieved.

3- *Parameter estimation uncertainty*: the inability to uniquely locate a '*best*' parameter set based on the available information is the result of the first two uncertainty sources. In fact, there are always some parameters in the model which either cannot be directly estimated through measurement or by the correlation between the model parameters and the physical characteristics of the system. Therefore, various parameter sets, often widely distributed within the feasible parameter space may yield equally good results in terms of predefined objective functions. This perplexity is reflected in the shape of the response surface. Studying the specific characteristics of the response surface, the following major problems might be diagnosed (Duan *et al*., 1992; Wheater *et al*., 2007):

- The response surface contains more than one main region of attraction.
- Each region of attraction contains many local optima.
- It is flat in many regions, particularly in the vicinity of the optimum, with significantly different parameter sensitivities.
- Its shape includes long and curved ridges caused by the interdependence of parameters.
- It contains a number of saddle points, where first derivatives vanish but minima (or maxima) are not reached.
- Insensitive directions exist in the parameter space.

The procedures set out in the calibration framework in this Chapter are intended to overcome the identifiability problem and make robust estimation of model parameters possible. The use of multiple objective functions (Section 4.4.1), selecting a powerful search algorithm (Section

4.4.2), refining the search by locating the effective portion of the Pareto front (Section 4.4.6.1), distinguishing clusters of solutions (Section 4.4.6.2) and finally a post-calibration process through *visual inspection* of the model output (4.4.6.3) are all in line with this goal.

4.6 SUMMARY

This Chapter started with a brief overview of the experimental data. The experimental setup, uniform flow settings, measurement apparatus and techniques were concisely presented. This was followed by an introduction to all "*datasets*" and their "*test cases*" used in this research. Then a section was devoted to the discussion of defining panel structures in SKM. The core section of this Chapter was dedicated to the detailed description of the three stages of the proposed evolutionary multi-objective calibration framework:

- the calibration platform preparation,
- the calibration phase,
- the post-validation phase.

Figure (4-15) is a chart indicating the different steps of the calibration framework. With minor alterations, this framework can be used for calibrating other hydrodynamic models. In the next Chapter, the calibration framework is applied to the datasets introduced in Section (4.2.6). The results will give us an insight on the lateral variation of the immeasurable parameters of SKM for channels and rivers with inbank flow.

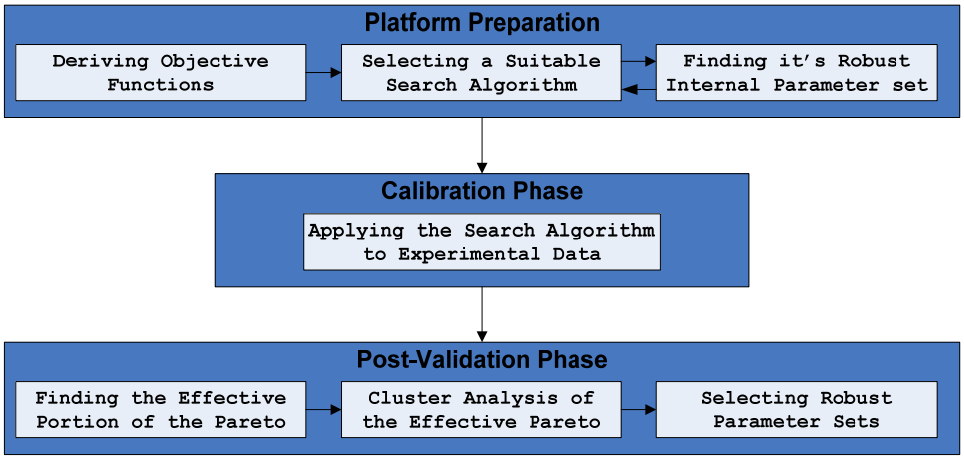

Figure (4-15): Calibration framework.

CHAPTER 5

CALIBRATING THE SKM FOR CHANNELS AND RIVERS WITH INBANK FLOW

5.1 INTRODUCTION

Having developed an effective calibration framework (Chapter 4), the platform was applied to channels and rivers with inbank flow. In this Chapter, the variation of the SKM parameters in trapezoidal channels, rectangular channels and natural river sections are investigated through the proposed calibration procedure. Although the majority of the work presented in this Chapter deals with idealized small-scale laboratory trapezoidal and rectangular channels, natural rivers are often schematized by such geometries in numerical models, and therefore it is envisaged that the results are generally applicable to natural rivers.

As discussed in the previous Chapters, the panelling philosophy of Knight *et al*. (2007) is adopted for modelling trapezoidal channels (Section 2.6.9.3). But, for rectangular channels, since there is little knowledge on the exact size and position of the secondary flow cells (Section 2.6.9.2), this methodology cannot be directly applied. Furthermore, the quantity and quality of the available rectangular datasets are not sufficient enough for generalization purposes, and therefore in this Chapter, the rectangular cases are investigated with a focus on selecting a suitable panel structure for depth-averaged modelling.

Being aware of the fact that the SKM, in its standard format used in this research, was developed initially from laboratory data, the calibration framework is also applied to a number of river cross-sections in order to show the capability of the SKM for modelling flows in rivers and also to show the effectiveness of the calibration framework for more complicated

channel sections. The river datasets used in this research are based on seven sites in two continents and three countries: the River Severn at Montford Bridge (Knight, 1989b), the River Main at Bridge End Bridge (Myers and Lyness, 1989) and the River Trent, North Muskham (Knight, 1989b)) in UK, the River Colorado and the River La Suela (McGahey, 2006) in Argentina and the River Cuenca and the River Tomebamba (McGahey, 2006) in Ecuador. All the natural river datasets are available in McGahey (2006).

In this Chapter, the calibration of smooth trapezoidal channels (FCF and Yuen's (1989) data), uniformly and partially roughened trapezoidal channels (Al-Hamid's (1991) data), rectangular channels (Knight *et al*. (1984) and Tominaga *et al*. (1989)) and some natural rivers are covered in individual sections. In each section, a brief description of the dataset is given first together with a summary of all the test cases. 'The experimental data', 'panel structure selection', 'objective functions' and 'shear stress calculations' are covered in the 'Considerations and assumptions' sub-section. Finally, a sub-section is devoted to the calibration results and their interpretation. The final part of this Chapter shows the advantage of this calibration approach over other previous attempts. Furthermore, a cross-referencing analysis is proposed in order to verify the optimum values of individual SKM parameters. It is to be mentioned that the main figures of this Chapter are provided in Appendix (IV), while key Figures are shown in the text to help the reader.

5.2 TRAPEZOIDAL CHANNELS

Three sets of experimental data relating to uniform flow in trapezoidal channels were used in this research: the Flood Channel Facility (FCF) Series 04 (Knight, 1992), Yuen's (1989) data and Al-Hamid's (1991) data. This represented a combined total of 51 experimental test cases. The first two datasets included measurements in uniformly roughened channels, i.e. the bed and wall of the channels where made of the same material. Al-Hamid's data consisted of both uniformly and partially roughened test cases. The main motivation behind each dataset was to study the distributions of mean streamwise depth-averaged velocity and boundary shear stress for a wide range of inbank flows under sub and super-critical flow conditions.

5.2.1 FCF Series 04

5.2.1.1 Introduction to the dataset

The EPSRC Flood Channel Facility (FCF) was constructed in 1986 at HR Wallingford to enable engineers to understand the hydraulic processes involved in the flood flows of rivers and flood alleviation channels. The FCF flume was 60m long, 10m wide and 0.4m deep with an average bed slope of 1.027×10^{-3}. The Facility could be configured to conduct studies in a wide range of channels with floodplains (e.g. straight, meandering and free formed) with either rigid or mobile boundaries. Water was fed into the flume by six pumps. At the inlet, the water flowed over a sharp-crested weir into a stilling pool, before spilling onto the floodplains and into the main channel. Five separate tailgates at the downstream end were used to control the water surface slope and the depth of water in the model. The main research program, carried out in 3 phases, covered a wide range of flow conditions and provided valuable datasets for many researchers. Figure (5-1) shows a view of the FCF flume along with the sketch of its layout. For more information about the facility and an in-depth analysis of all FCF datasets, the reader is referred to Knight and Sellin (1987), Knight (1992) and the website www.flowdata.bham.ac.uk.

Measurements of inbank flow in simple trapezoidal channels were conducted in the fourth series of phase A (straight prismatic channels). This dataset consisted of detailed mean velocity and boundary shear stress distributions for 12 simple trapezoidal channels having a fixed bed width of 1.50m, bed slope of 1.027×10^{-3}, side slope of 1:1 and varying depths, changing between 0.296m to 0.049m, giving aspect ratios (i.e. channel width/depth ratio = $2b/h$) between 5 and 30 (Table ((5-1)). The stage-discharge curve for this dataset is shown in Figure (5-2). Comparing the distribution of mean velocity and boundary shear stress for all cases, it was observed that the distributions of three test cases with the lowest aspect ratios included abnormal data points which made the general trend of the distributions different from other cases. For this reason, these test cases were removed from the entire dataset.

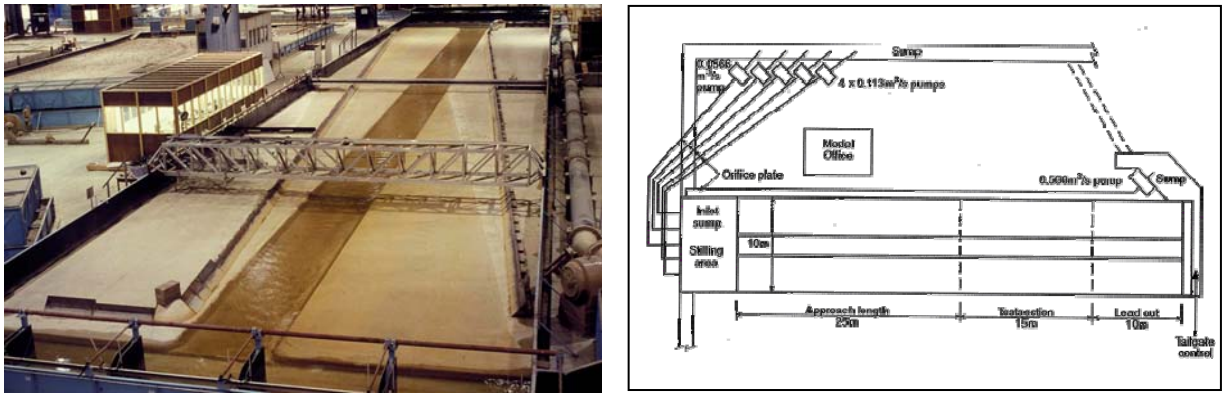

(a) General view (b) Layout of Facility

Figure (5-1): EPSRC Flood Channel Facility (www.flowdata.bham.ac.uk.).

Test case	*2b* (m)	*h* (m)	*2b/h*	P_b/P_w	S_0 ($x10^{-3}$)	*Q* ($l.s^{-1}$)	*R* (m)	U_{avr} ($m.s^{-1}$)	τ_{avr} ($N.m^{-2}$)	R_e ($x10^4$)	F_r
FCF 0501	1.500	0.0486	30.85	10.91	1.027	29.90	0.0460	0.3970	0.4628	6.317	0.584
FCF 7501	1.500	0.0755	19.86	7.02	1.027	64.00	0.0694	0.5378	0.6988	12.921	0.640
FCF 1002	1.500	0.1009	14.87	5.26	1.027	103.50	0.0905	0.6408	0.9104	20.056	0.664
FCF 1502	1.500	0.1488	10.08	3.57	1.027	202.30	0.1277	0.8249	1.2849	36.924	0.713
FCF 0401	1.500	0.1580	9.49	3.36	1.027	223.70	0.1346	0.8538	1.3542	40.279	0.718
FCF 0402	1.500	0.1662	9.03	3.19	1.027	241.40	0.1406	0.8718	1.4144	42.957	0.716
FCF 0403	1.500	0.1753	8.56	3.02	1.027	262.30	0.1472	0.8930	1.4808	46.680	0.716
FCF 0404	1.500	0.1869	8.03	2.84	1.027	290.90	0.1554	0.9228	1.5635	51.204	0.718
FCF 0405	1.500	0.1992	7.53	2.66	1.027	324.00	0.1641	0.9570	1.6507	56.209	0.724
FCF 0406	1.500	0.2130	7.04	2.49	1.027	363.10	0.1735	0.9952	1.7494	61.306	0.728
FCF 040703	1.500	0.2474	6.06	2.14	1.027	479.10	0.1965	1.1083	1.9774	76.859	0.760
FCF 040802	1.500	0.3009	4.98	1.76	1.027	656.30	0.2305	1.2110	2.3193	99.151	0.762

Table (5-1): FCF Series 04 test cases.

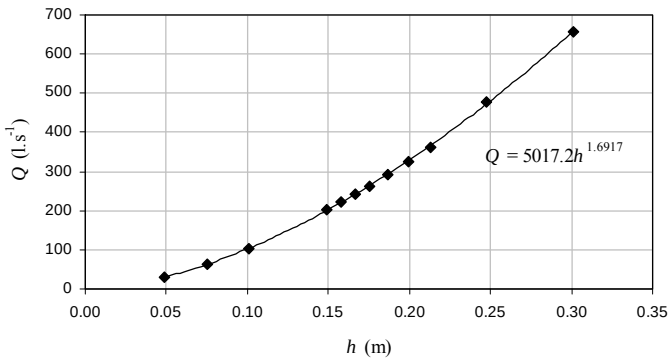

Figure (5-2): Stage-discharge curve for FCF series 04 data.

5.2.1.2 Considerations and assumptions

Panel Structure Selection

Since all the channels had an aspect ratio larger than 2.2, based on Knight and co-workers' (2007) hypothesis (Sections 2.6.9.3 and 4.3), a five panel structure for half of the symmetric channel was selected for modelling this dataset. Figure (5-3) shows this panel structure.

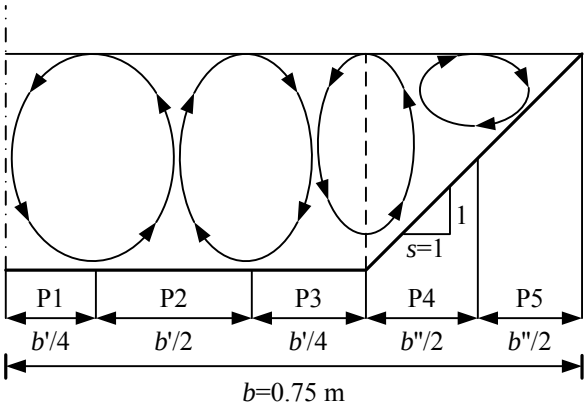

Figure (5-3): The panel structure and assumed secondary flow cells for FCF channels.

Objective functions

Since distributions of depth-averaged velocity and boundary shear stress were available for all test cases, Eqs. (4-9 & 4-10) were set as the optimization objective functions, i.e. the sum of squared difference between observed and model generated mean streamwise velocity and local boundary shear stress.

5.2.1.3 Calibration results

After applying the calibration framework to all test cases, the best set of solutions (as defined in Chapter 4) for each case was obtained (i.e. a combination of individual panel values of f_i, λ_i and Γ_i) and sorted based on the aspect ratio of the channel (Table (5-2)). Based on these results, the variation of each parameter was plotted against the panel number and wetted perimeter ratio (P_b / P_w) (Figures (5-4)). Here, the subscript i represents the panel number, starting from 1 for the panel adjacent to the centre line, and then increases progressively towards the edge of the channel. The experimental and simulated distributions of depth-

averaged velocity and boundary shear stress for a typical test case (FCF 0402) are shown in Figure (5-5). The distributions for the remaining cases are provided in Appendix (IV.1).

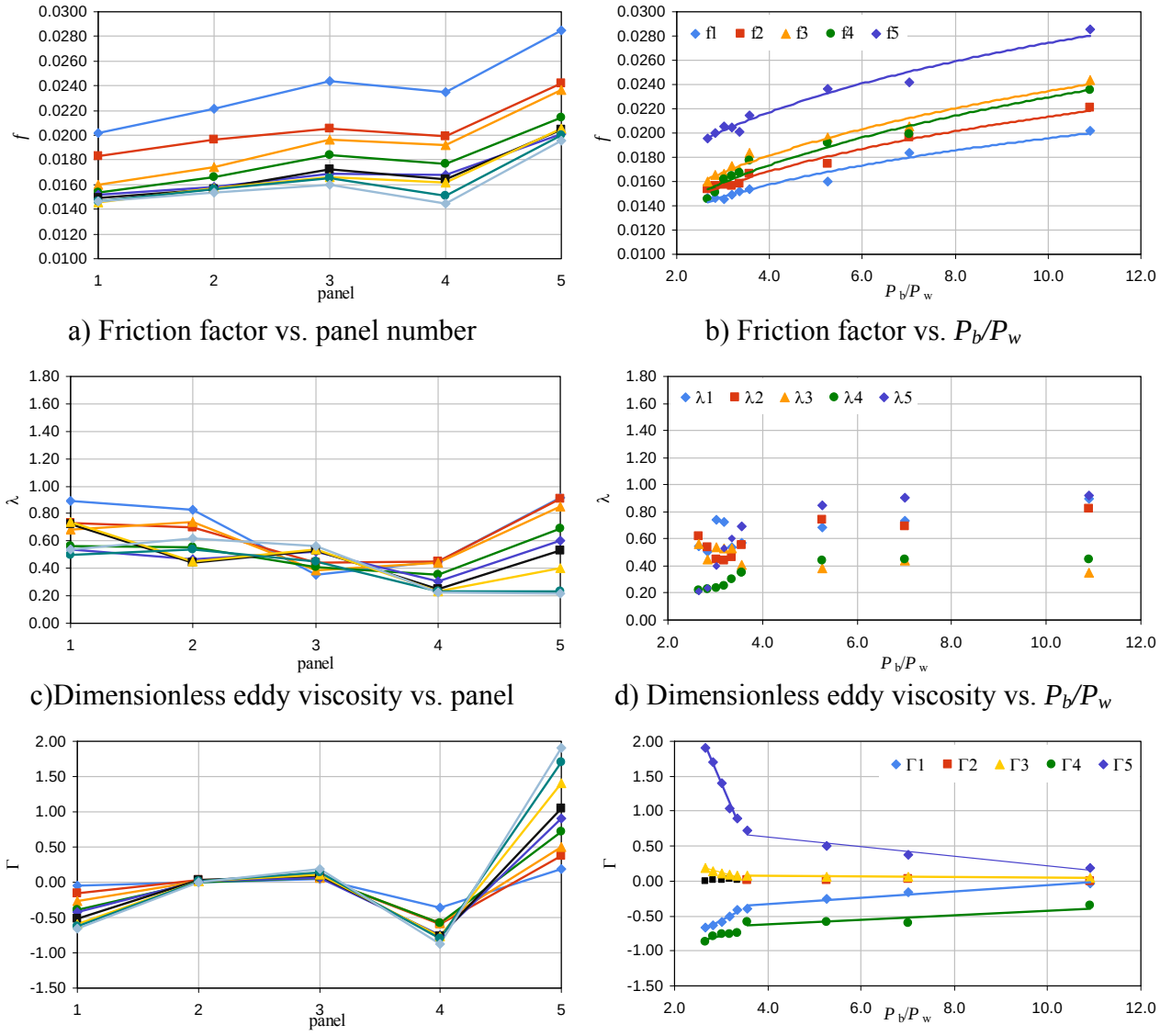

a) Friction factor vs. panel number

b) Friction factor vs. P_b/P_w

c)Dimensionless eddy viscosity vs. panel

d) Dimensionless eddy viscosity vs. P_b/P_w

e) Secondary flow term vs. panel number

f) Secondary flow term vs. P_b/P_w

Figure (5-4): Variation of the friction factor, dimensionless eddy viscosity and secondary flow term against the panel number and wetted perimeter ratio (P_b/P_w) for FCF data ($7.5<2b/h<30$ and $S_0=1.027\text{x}10^{-3}$).

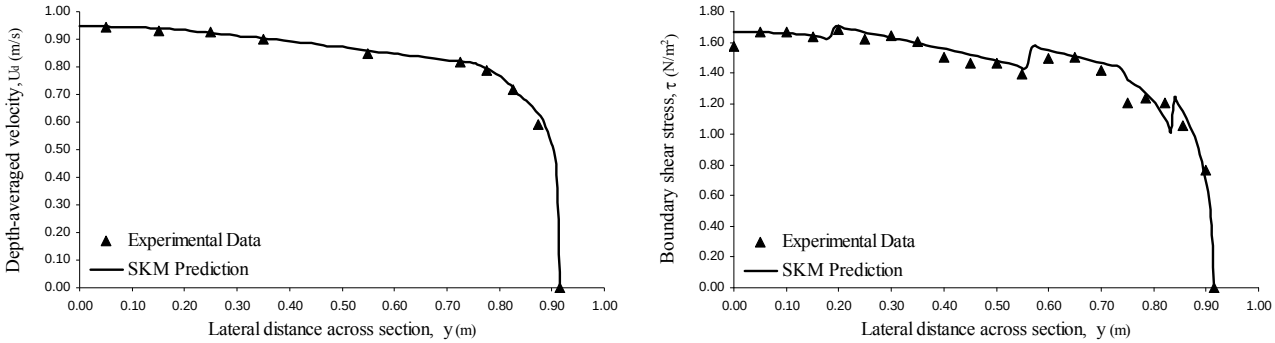

a) Depth-averaged streamwise velocity b) Boundary shear stress

Figure (5-5): Distributions of depth-averaged velocity and boundary shear stress for case FCF 0402 (h=0.1662m; 2b/h=9.03)

FCF Test case		**0501**	**7501**	**1002**	**1502**	**0401**	**0402**	**0403**	**0404**	**0405**
$2b/h$		30.85	19.86	14.87	10.08	9.49	9.03	8.56	8.03	7.53
P_b/P_w		10.91	7.02	5.26	3.57	3.36	3.19	3.02	2.84	2.66
Panel 1	f	0.0202	0.0183	0.0160	0.0153	0.0152	0.0149	0.0146	0.0146	0.0146
	λ	0.89	0.73	0.68	0.57	0.54	0.72	0.74	0.50	0.54
	Γ	-0.04	-0.15	-0.26	-0.39	-0.41	-0.51	-0.59	-0.63	-0.66
Panel 2	f	0.0221	0.0196	0.0175	0.0166	0.0158	0.0156	0.0157	0.0156	0.0153
	λ	0.83	0.70	0.74	0.56	0.47	0.44	0.45	0.54	0.62
	Γ	0.00	0.03	0.02	0.01	0.01	0.03	0.02	0.01	0.00
Panel 3	f	0.0244	0.0205	0.0197	0.0184	0.0169	0.0173	0.0166	0.0165	0.0160
	λ	0.35	0.44	0.39	0.41	0.53	0.53	0.54	0.45	0.56
	Γ	0.05	0.06	0.07	0.07	0.07	0.09	0.11	0.14	0.19
Panel 4	f	0.0235	0.0199	0.0192	0.0177	0.0168	0.0164	0.0162	0.0151	0.0145
	λ	0.45	0.45	0.44	0.35	0.30	0.25	0.24	0.23	0.22
	Γ	-0.35	-0.59	-0.58	-0.58	-0.75	-0.76	-0.77	-0.79	-0.87
Panel 5	f	0.0285	0.0242	0.0237	0.0214	0.0201	0.0205	0.0206	0.0200	0.0195
	λ	0.92	0.91	0.85	0.69	0.60	0.53	0.40	0.23	0.22
	Γ	0.19	0.38	0.51	0.72	0.90	1.04	1.40	1.71	1.90

Table (5-2): The optimal values of each Parameter in different panels of FCF experiments.

Based on the results shown in Table (5-2), Figure (5-4) and Appendix (IV.1) the following conclusions can be drawn (Sharifi *et al*., 2008; 2009a):

1- For all cases, visual observations indicate that the velocity and boundary shear stress magnitudes are reasonably well simulated.

2- For the lowest depth (FCF 0501; h=0.0486m) the boundary shear stress is under predicted by approximately 8 %.

3- The "dip" in the velocity profile near the channel centerline is not captured by the model.

4- Significant increases are observed in the simulated shear stress profile at the location of panel boundaries. This is due to the assumption of constant friction throughout each panel.

5- For trapezoidal channels with aspect ratios between 7.5 and 30, the friction factor linearly increases from the first to the third panel, then appears to remain constant or reduce before increasing to its highest value in the fifth panel.

6- The value of the zonal friction factor in each panel is shown to increase with increase in the wetted perimeter ratio, P_b/P_w.

7- The value of the dimensionless eddy viscosity does not appear to follow any specific pattern in the panels positioned in the constant depth region.

8- In the panels on the sidewall region, the value of λ increases significantly as the wall is approached.

9- For trapezoidal channels with aspect ratios higher than 7.5, the secondary flow term, Γ, is initially negative in the first panel and then rises towards zero in all cases. The value of this parameter then increases slightly in the third panel to a value near 0.10 before decreasing to a negative value in the fourth panel. Finally, a maximum positive value is obtained in the fifth panel.

10- The absolute value of Γ in all the panels decreases by the increase in the wetted perimeter ratio.

11- For this range of aspect ratios, the values of λ and Γ are linearly related to changes in wetted perimeter ratio.

5.2.2 Yuen's (1989) data

5.2.2.1 Introduction to the dataset

Experiments were conducted in a 22m long tilting flume at the University of Birmingham (Figure (5-6)). The channel was constructed from PVC providing a smooth surface for both

the bed and the wall. The main trapezoidal channel had a base width of 0.150m and the side slopes were fixed at 1:1. Five series of tests were undertaken at 5 different bed slopes: 1.000, 3.969, 8.706, 14.52 & 23.37 ($x10^{-3}$), with the aim of obtaining detailed velocity and boundary shear stress data in both sub-critical and super-critical flows ($0.39 < Fr < 3.59$). Detailed measurements of boundary shear stress distributions were available for the first (S_0=1.000 $x10^{-3}$), third (S_0=8.706 $x10^{-3}$) and last (S_0=23.37 $x10^{-3}$) series, but the corresponding mean velocity distributions were only measured for 7 test cases within these series. The stage-discharge curve for this dataset is illustrated in Figure (5-7). Table (5-3) shows a summary of the test cases in this study. The measurements regarding all test series can be found in www.flowdata.bham.ac.uk. For more information relating to Yuen's data, the reader is referred to Yuen (1989) and Yuen and Knight (1990).

Figure (5-6): University of Birmingham 22m long trapezoidal tilting flume (Yuen, 1989).

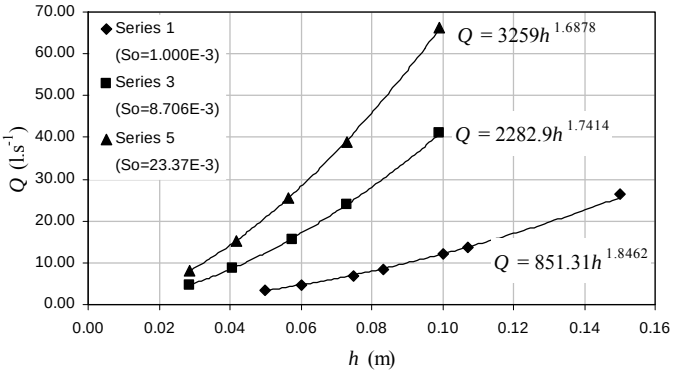

Figure (5-7): Stage-discharge curve for Yuen's data.

Test case	$2b$ (m)	h (m)	$2b/h$	P_b/P_w	S_0 ($x10^{-3}$)	Q (ls^{-1})	R (m)	U_{avr} ($m.s^{-1}$)	τ_{avr} ($N.m^2$)	R_e ($x10^4$)	F_r
Yuen 004	0.150	0.0500	3.00	1.06	1.000	3.50	0.0343	0.3500	0.3365	4.101	0.559
Yuen 006	0.150	0.0600	2.50	0.88	1.000	4.65	0.0394	0.3690	0.3865	5.019	0.546
Yuen 008	0.150	0.0750	2.00	0.71	1.000	7.00	0.0466	0.4148	0.4570	6.565	0.559
Yuen 010	0.150	0.0833	1.80	0.64	1.000	8.55	0.0504	0.4400	0.4944	7.569	0.567
Yuen 013	0.150	0.1000	1.50	0.53	1.000	12.00	0.0578	0.4800	0.5664	9.466	0.574
Yuen 014	0.150	0.1071	1.40	0.50	1.000	13.70	0.0608	0.4975	0.5964	10.216	0.577
Yuen 016	0.150	0.1500	1.00	0.35	1.000	26.30	0.0784	0.5844	0.7685	15.638	0.590
Yuen 201	0.150	0.0285	5.26	1.86	8.706	4.70	0.0221	0.9239	1.8834	7.145	1.882
Yuen 203	0.150	0.0409	3.67	1.30	8.706	8.68	0.0294	1.1117	2.5071	11.488	1.937
Yuen 205	0.150	0.0575	2.61	0.92	8.706	15.60	0.0382	1.3075	3.2582	17.539	1.968
Yuen 206	0.150	0.0730	2.05	0.73	8.706	23.90	0.0457	1.4681	3.8988	24.305	1.999
Yuen 207	0.150	0.0990	1.52	0.54	8.706	41.10	0.0573	1.6673	4.8942	35.804	2.000
Yuen 401	0.150	0.0285	5.26	1.86	23.370	8.10	0.0221	1.5922	5.0558	12.443	3.243
Yuen 403	0.150	0.0420	3.57	1.26	23.370	15.33	0.0300	1.9010	6.8757	20.255	3.270
Yuen 405	0.150	0.0565	2.65	0.94	23.370	25.55	0.0377	2.1899	8.6310	28.988	3.320
Yuen 406	0.150	0.0730	2.05	0.73	23.370	39.00	0.0457	2.3957	10.4660	44.714	3.262
Yuen 407	0.150	0.0990	1.52	0.54	23.370	66.30	0.0573	2.6895	13.1382	61.831	3.227

Table (5-3): Yuen's test cases.

5.2.2.2 Considerations and assumptions

As mentioned in the previous section, among all test cases, the depth averaged velocity distributions were measured for only 7 test cases: Yuen 008, 013, 016, 206, 207, 406, and 407. For the remaining test cases only measurements of bed shear stress were available.

Panel Structure Selection

Following the work of Knight *et al*., (2007), a four panel structure for half of the symmetric channel was selected for modelling these experiments, since all the 7 mentioned cases had an aspect ratio smaller than 2.2. Figure (5-8) illustrates this panel structure. The remaining cases were modelled with both four panel (Figure (5-8)) and five panel (Figure (5-3)) structures, regardless of their aspect ratio. Initial analysis revealed that introducing an additional panel for aspect ratios higher than 2.2 did not increase the level of optimality, significantly. Hence, the calculations were continued with a four panel structure for all test cases.

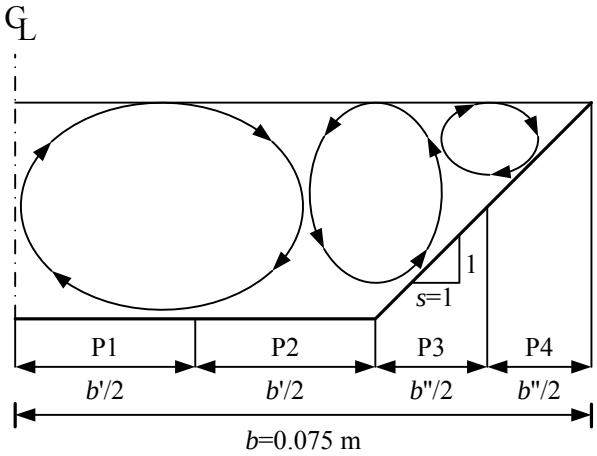

Figure (5-8): The panel structure and assumed secondary flow cells for Yuen's channels.

Objective Functions

Similar to the analysis of the FCF dataset, Eqs. (4-9 & 4-10) were set as two of the multi-objective optimization functions for the cases where distributions of mean velocity and boundary shear stress were available. For the remaining cases, only Eqs. (4-10 & 4-11) were selected as the objective functions (i.e. the difference between observed and model generated mean local boundary shear stress and single calculated and measured values of Q).

Shear Stress Calculations

Reviewing model predictions of FCF data (Appendix (IV.1)), significant increases were observed in the simulated shear stress profile at the location of panel boundaries. This was thought to be a result of imposing constant friction values throughout the entire panel. In this dataset the measured mean velocity profile was available for all cases which lead to a fast convergence of most model parameters. In contrast, for most of Yuen's test cases the mean velocity profile is absent and the optimal parameter values are more dependent on the calculated values of boundary shear stress. To overcome this problem and increase the accuracy of the SKM, the friction factor was varied linearly through the panels and the interpolated values of friction factor were used for calculating the local shear stresses. Figure (5-9) illustrates the concept of using spatially varying friction factor values.

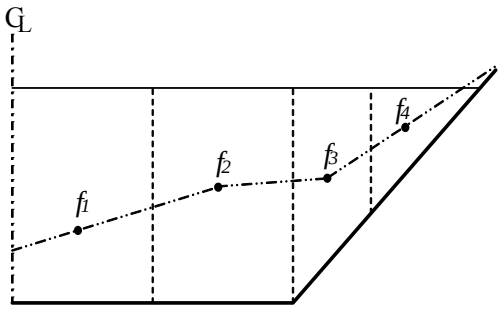

Figure (5-9): Spatially varying friction values in the SKM model.

5.2.2.3 Calibration results

Table (5-4) shows the obtained optimal values of the SKM parameters after applying the calibration methodology for the 7 cases where both mean velocity and boundary shear stress data were available. The variation of these parameters is illustrated in Figure (5-10). Figure (5-11) also shows the distributions of depth-averaged velocity and boundary shear stress for a typical test case (FCF 0402). The complete set of results regarding test series 1, 3 and 5 along with the experimental and simulated distributions of depth-averaged velocity and boundary shear stress for all cases are provided in Appendix (IV.2).

Yuen test case		**008**	**013**	**016**	**206**	**207**	**406**	**407**
$2b/h$		2.00	1.50	1.00	2.05	1.52	2.05	1.52
P_b/P_w		0.71	0.53	0.35	0.73	0.54	0.73	0.54
Panel 1	f	0.0187	0.0170	0.0159	0.0150	0.0144	0.0144	0.0136
	λ	1.29	0.79	1.07	0.55	0.78	0.64	0.64
	Γ	-0.54	-0.57	-0.72	-0.79	-0.96	-0.97	-1.10
Panel 2	f	0.0207	0.0182	0.0171	0.0162	0.0157	0.0157	0.0149
	λ	0.38	0.28	0.16	0.11	0.11	0.12	0.12
	Γ	0.13	0.15	0.12	0.22	0.20	0.18	0.18
Panel 3	f	0.0221	0.0200	0.0185	0.0179	0.0167	0.0167	0.0159
	λ	0.84	0.82	0.71	0.29	0.24	0.22	0.20
	Γ	-0.36	-0.55	-0.64	-0.89	-1.14	-1.30	-1.41
Panel 4	f	0.0250	0.0228	0.0210	0.0194	0.0185	0.0185	0.0176
	λ	1.50	1.47	1.36	0.49	0.40	0.31	0.30
	Γ	0.79	0.89	0.96	1.70	1.80	1.91	1.98

Table (5-4): The optimal values of each Parameter in different panels of Yuen's experiments.

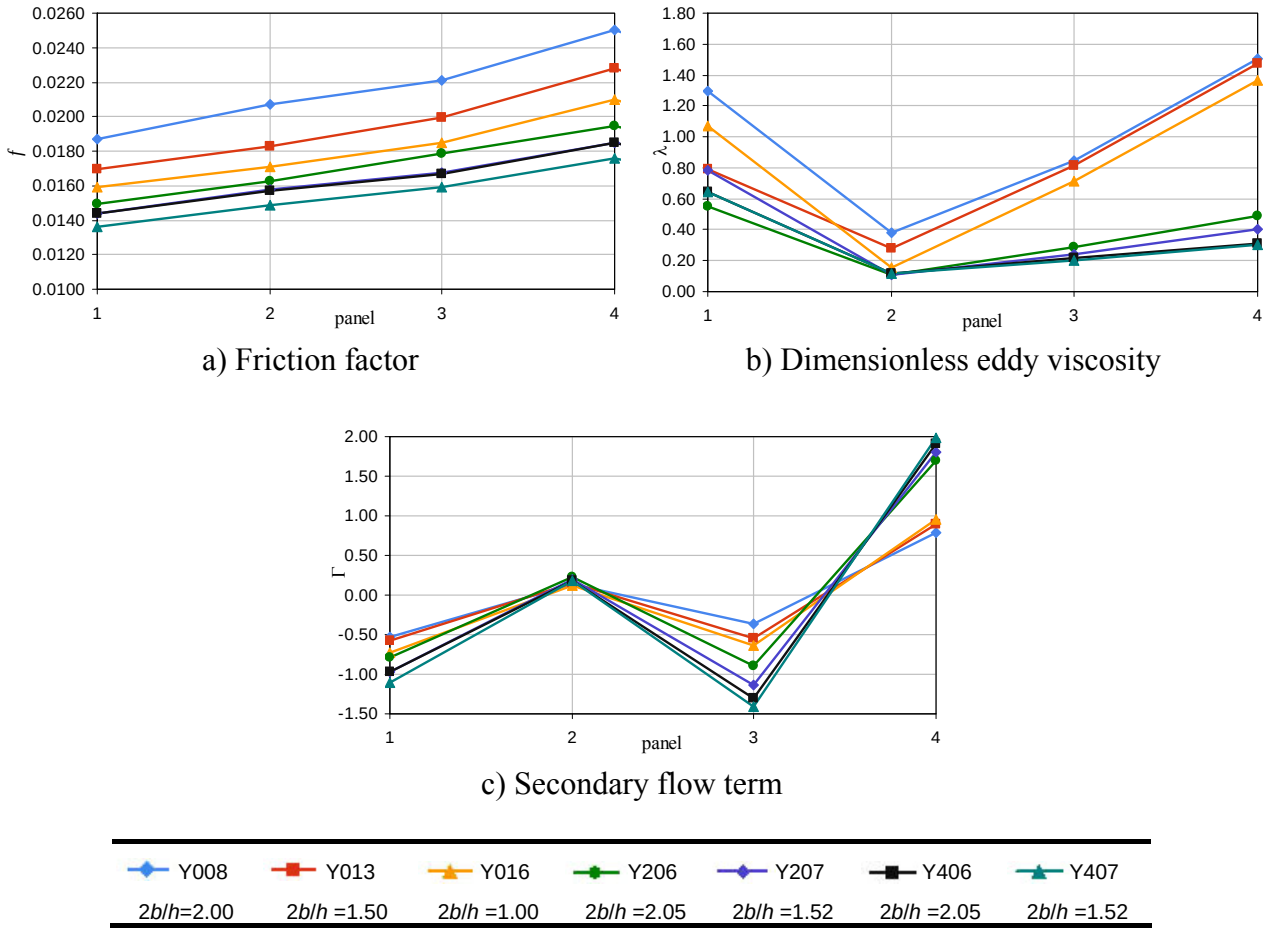

Figure (5-10): Variation of the friction factor, dimensionless eddy viscosity and secondary flow term against the panel for Yuen's data ($1.52<2b/h<2$).

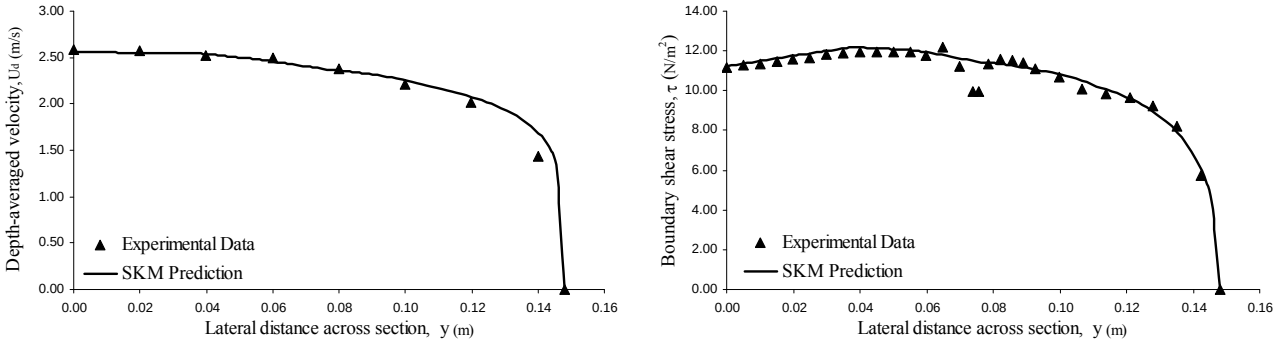

Figure (5-11): Distributions of depth-averaged velocity and boundary shear stress for case Yuen 406 (h=0.0730 m; $2b/h$=2.05)

Based on the results shown in Table (5-4), Figure (5-10) and Appendix (IV.2) the following conclusions can be derived (Sharifi *et al*., 2008; 2009a):

1- For all test cases, visual observations indicate that the velocity and boundary shear stress magnitudes are reasonably well simulated. For cases where the experimental velocity distribution is available, the predicted distributions are smoother and more accurate than the other cases.

2- Using spatially varied friction factor values, the predicted shear stress distributions are smooth and without any sudden increases at the location of panel boundaries.

3- The lateral variation of the three model parameters follows a similar trend to FCF cases (modelled with five panels).

4- For trapezoidal channels with aspect ratios between 1.0 and 5.26, the friction factor increases almost linearly from the centerline of the channel towards the wall.

5- The value of the zonal friction factor in each panel is shown to increase with increase in the wetted perimeter ratio, P_b/P_w.

6- The value of the dimensionless eddy viscosity does not appear to follow any specific pattern in the panel adjacent to the channel centerline. As the bed slope increases, the model becomes more sensitive to the value of this parameter in this region. In the panels on the sidewall region, the value of λ increases as the wall is approached.

7- For trapezoidal channels with aspect ratios between 1.0 and 5.26, the secondary flow term, Γ, is initially negative in the first panel and then rises towards 0.15 in all cases. The value of this parameter then decreases to a negative value in the third panel. Finally, a maximum positive value is obtained in the fourth panel. This pattern of negative and positive values found for Γ in adjacent panels agrees with the findings of Knight *et al*., (2007).

8- For this range of aspect ratios, the values of λ and Γ are linearly related to changes in wetted perimeter ratio.

9- With the increase in the wetted perimeter, the value of λ in all the panels increases and the absolute value of Γ in all the panels decreases.

5.2.3 Al-Hamid's (1991) data

5.2.3.1 Introduction to the dataset

Al-Hamid's (1991) datasets included experiments undertaken in simple trapezoidal channels with both differentially and uniformly roughened boundaries for uniform, steady and fully developed turbulent flow (Figure (5-12)). Two types of gravel distributions (d_{84} values of 18.0 and 9.3 mm referred to as R1 and R2 respectively) were used for roughening the channel boundaries (i.e. walls only or walls and bed together). Figure (5-13) shows close up pictures of the roughening gravels and their arrangements. The channels where built from thick PVC in a 22 m long, 0.615 m wide and 0.365 m deep rectangular tilting flume at the University of Birmingham. The experiments were conducted within the ranges of aspect ratio, $0.85<2b/h<10.0$, Reynolds number, $3.4x10^4< Re<8.6x10^5$, and Froude number, $0.39<Fr<0.89$, for channel bed slopes $3.92x10^{-3}$, $4.03x10^{-3}$ and $1.935x10^{-3}$ with 1:1 wall side slopes. The aim was to study velocity distributions, boundary shear stress distributions, shear forces, mean and maximum shear stresses, resistance coefficients and eddy viscosity for differentially and uniformly roughened trapezoidal channels. Table (5-5) shows a summary of Al-Hamid's test cases. The stage-discharge curve for this dataset is illustrated in Figure (5-14). For more information about Al-Hamid's datasets, the reader is referred to Al-Hamid (1991) and Knight *et al*., (1994).

(a) Differentially roughened (b) Uniformly roughened

Figure (5-12): Trapezoidal channels with differential and uniform boundary roughness. (Al-Hamid, 1991)

(a) R1; d_{84} =18.0 mm

(b) R2; d_{84} =9.3 mm

Figure (5-13): The roughening gravels used in Al-Hamid's experiments (Al-Hamid, 1991).

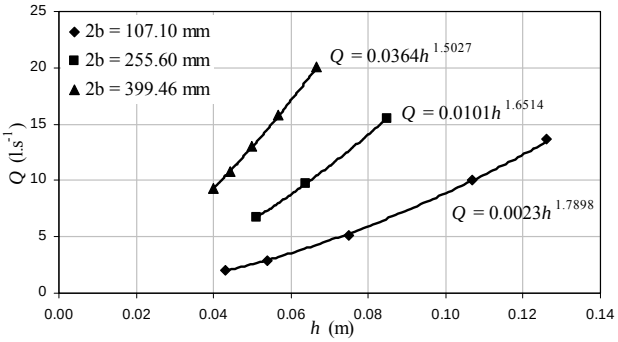

a) Smooth bed and R1 on the wall
($0.6 \le P_b / P_w \le 7.06$ and S_o =3.920x10^{-3}).

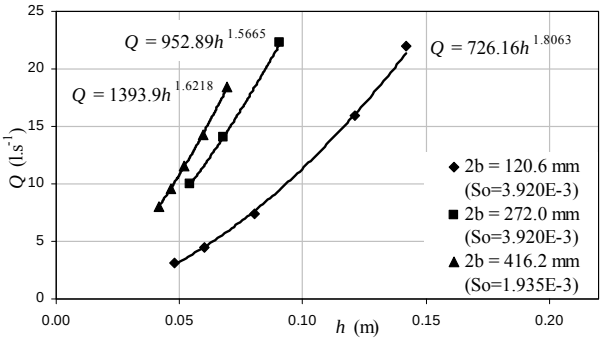

b) Smooth Bed and R2 on the wall
($0.6 \le P_b / P_w \le 7.07$).

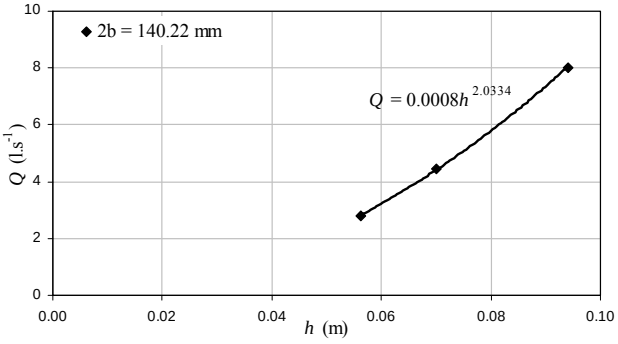

c) R1 on bed and walls
($1.05 \le P_b / P_w \le 1.76$ and S_o=3.920x10^{-3}).

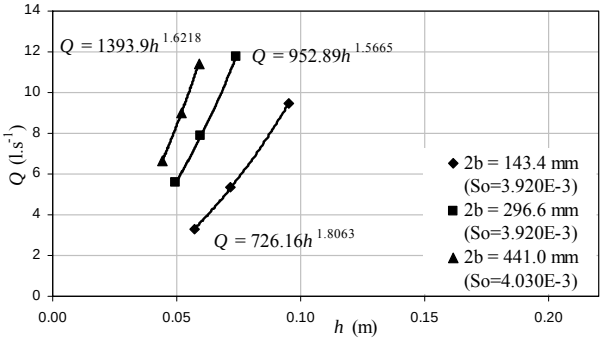

d) R2 on bed and walls
($1.06 \le P_b / P_w \le 7.06$).

Figure (5-14): Stage-discharge curve for Al-Hamid's experiments.

Bed	Wall	Test case	2b (m)	h (m)	2b/h	P_b/P_w	S_0 (x10^{-3})	Q (ls^{-1})	R (m)	U_{avr} ($m.s^{-1}$)	τ_{avr} ($N.m^{-2}$)	R_e (x10^4)	F_r
Smooth	Rough (R1)	**AH 01**	0.107	0.1260	0.85	0.30	3.920	13.69	0.0634	0.4660	0.8965	11.870	0.520
		AH 02	0.107	0.1070	1.00	0.35	3.920	9.99	0.0559	0.4362	0.8805	9.920	0.522
		AH 03	0.107	0.0750	1.43	0.50	3.920	5.15	0.0428	0.3772	0.8121	6.182	0.523
		AH 04	0.107	0.0540	1.98	0.70	3.920	2.91	0.0335	0.3339	0.7465	4.389	0.530
		AH 05	0.107	0.0430	2.49	0.88	3.920	2.01	0.0282	0.3113	0.6975	3.489	0.544
		AH 23	0.256	0.0849	3.01	1.06	3.920	15.53	0.0583	0.5374	0.9005	12.600	0.658
		AH 24	0.256	0.0638	4.01	1.42	3.920	9.68	0.0467	0.4755	0.8288	8.928	0.659
		AH 25	0.256	0.0511	5.00	1.77	3.920	6.71	0.0392	0.4285	0.7572	6.745	0.654
		AH 26	0.399	0.0667	5.99	2.12	3.920	20.05	0.0529	0.6449	0.9667	13.302	0.853
		AH 27	0.399	0.0568	7.03	2.49	3.920	15.76	0.0463	0.6080	0.9294	11.040	0.864
		AH 28	0.399	0.0500	8.00	2.83	3.920	12.99	0.0415	0.5787	0.8574	9.485	0.872
		AH 29	0.399	0.0443	9.03	3.19	3.920	10.83	0.0374	0.5515	0.8454	8.102	0.878
		AH 30	0.399	0.0400	9.99	3.53	3.920	9.30	0.0343	0.5291	0.7880	7.130	0.884
Smooth	Rough (R2)	**AH 09**	0.121	0.1420	0.85	0.30	3.920	21.95	0.0714	0.5886	0.9633	14.730	0.619
		AH 10	0.121	0.1210	1.00	0.35	3.920	15.91	0.0632	0.5442	0.9497	12.210	0.612
		AH 11	0.121	0.0805	1.50	0.53	3.920	7.38	0.0465	0.4559	0.8802	7.429	0.607
		AH 12	0.121	0.0603	2.00	0.71	3.920	4.48	0.0375	0.4109	0.8264	5.396	0.617
		AH 13	0.121	0.0480	2.51	0.89	3.920	3.11	0.0316	0.3847	0.7784	4.257	0.638
		AH 17	0.272	0.0908	2.99	1.06	3.920	22.25	0.0623	0.6749	1.0406	15.880	0.798
		AH 18	0.272	0.0679	4.01	1.42	3.920	14.09	0.0497	0.6105	1.0240	11.210	0.820
		AH 19	0.272	0.0545	4.99	1.76	3.920	10.00	0.0418	0.5616	0.9292	8.655	0.830
		AH 31	0.416	0.0695	5.99	2.12	1.935	18.47	0.0551	0.5469	0.7338	11.610	0.708
		AH 32	0.416	0.0594	7.01	2.48	1.935	14.30	0.0483	0.5065	0.6979	9.605	0.704
		AH 33	0.416	0.0520	8.00	2.83	1.935	11.53	0.0432	0.4736	0.6461	7.691	0.699
		AH 34	0.416	0.0465	8.96	3.17	1.935	9.61	0.0393	0.4470	0.6147	6.598	0.695
		AH 35	0.416	0.0416	10.00	3.54	1.935	8.03	0.0357	0.4216	0.5720	5.623	0.690
Rough (R1)	Rough (R1)	**AH 06**	0.140	0.0940	1.49	0.53	3.920	8.02	0.0542	0.3643	1.4230	7.658	0.449
		AH 07	0.140	0.0700	2.00	0.71	3.920	4.43	0.0435	0.3013	1.4109	5.084	0.420
		AH 08	0.140	0.0562	2.50	0.88	3.920	2.82	0.0369	0.2551	1.2976	3.649	0.390
Rough (R2)	Rough (R2)	**AH 14**	0.143	0.0953	1.50	0.53	3.920	9.50	0.0551	0.4175	1.4410	7.852	0.511
		AH 15	0.143	0.0717	2.00	0.71	3.920	5.33	0.0445	0.3453	1.3852	5.252	0.475
		AH 16	0.143	0.0570	2.52	0.89	3.920	3.31	0.0375	0.2900	1.2740	3.714	0.440
		AH 20	0.297	0.0742	4.00	1.41	3.920	11.78	0.0543	0.4283	1.6741	8.802	0.550
		AH 21	0.297	0.0596	4.98	1.76	3.920	7.86	0.0456	0.3700	1.5158	6.357	0.523
		AH 22	0.300	0.0495	6.06	2.14	3.920	5.58	0.0393	0.3223	1.3831	4.835	0.499
		AH 36	0.441	0.0589	7.49	2.65	4.030	11.43	0.0484	0.3884	1.6824	7.029	0.540
		AH 37	0.441	0.0519	8.50	3.01	4.030	9.01	0.0435	0.3524	1.5612	5.765	0.520
		AH 38	0.441	0.0442	9.98	3.53	4.030	6.66	0.0379	0.3107	1.4161	4.453	0.493

Table (5-5): Al-Hamid's test cases.

5.2.3.2 Considerations and assumptions

Extracting Experimental Data

As the digitized data of the mean velocity and bed shear stress distributions were not available for this data series, a code was generated in Visual Basic to digitize the plots of Al-Hamid's (1991) thesis and extract the measured values. For this purpose the related plots were scanned and loaded in AutoCad's interface. Then the code was run and the experimental data points were saved in an Excel ® spreadsheet. It is appreciated that the procedure of scanning graphs and extracting the data, results in more uncertainty in measurements which might affect the final results. Although unavoidable, it is felt that these additional uncertainties are within the level of experimental error and hence their inclusion in the thesis is warranted.

Panel Structure Selection

Based on the considered hypothesis, the number and position of the panels for modelling a channel should be directly related to the number and size of secondary flow cells. Since no accurate measurements of the transverse velocity component in differentially and uniformly roughened channels were available, a preliminary analysis was performed on all 38 cases and the sensitivity of the model to the number and position of panels was assessed. The analysis revealed that regardless of the channel aspect ratio, a total number of four panels (two in the constant depth domain and two in the sloping sidewall domain) would result in the same level of optimality as a five panel structure for most cases. Further thorough inspection of the model velocity and boundary shear stress distributions coupled by a trial and error procedure in the optimization algorithm unveiled that a slight shift in the position of panel boundaries would result in smoother and more accurate distributions especially in the rough wall region. The final selected panel structures are illustrated in Figure (5-15).

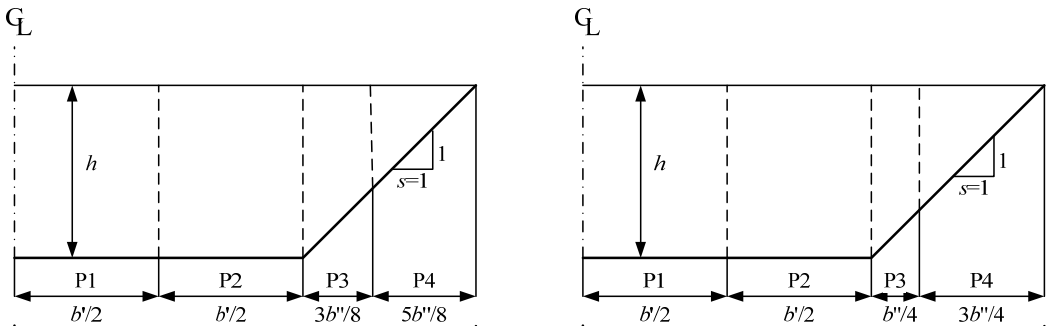

a) Smooth bed and rough walls. b) Rough bed and rough walls.

Figure (5-15): Selected panel structure for Al-Hamid's data series.

Objective Functions

Based on the availability of the mean velocity distributions, boundary shear stress distributions, total discharge and percentage of the shear force that act on the walls, the first two objective functions (Eqs. 4-9 & 4-10) were selected as the main optimization objective functions. The latter two (Eqs. 4-11 & 4-12) were used for filtering the non-dominated Pareto solutions (Section 4.4.1).

Shear Stress Calculation

Abrupt changes in the values of local shear stress in physically roughened regions made the use of varied friction factor for calculating shear stress inevitable. Furthermore, in the mentioned preliminary analysis for selecting the panel structure, when the channels were modelled with three panels in the bed area, the obtained optimum value for the third panel friction factor, f_2, was found to be almost the average of f_1 and f_3. This also confirmed the linear variation of friction in adjacent panels. As a result, the friction was assumed to vary linearly in bed and wall regions (Figure (5-16)).

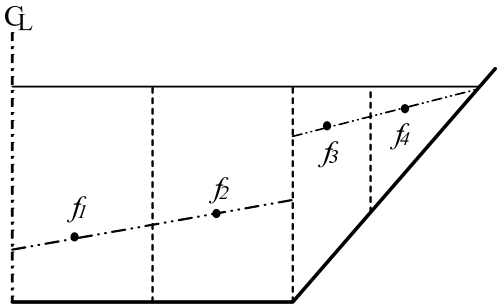

Figure (5-16): Friction factor variations in differentially and uniformly roughened channels.

5.2.3.3 Calibration results

Tables (5-6 to 5-8) show the obtained optimal values of SKM parameters for Al-Hamid's test cases after applying the calibration methodology. The variation of these parameters against wetted perimeter ratio is illustrated in Figures (5-17 to 5-19). Figure (5-20) also shows the simulated distributions of depth-averaged velocity and boundary shear stress for a differentially (Al-Hamid 27) and a uniformly (Al-Hamid 16) roughened test case. The lateral variation of these parameters in adjacent panels along with the experimental and simulated

distributions of depth-averaged velocity and boundary shear stress for all cases are provided in Appendix (IV.3).

Al-Hamid		01	02	03	04	05	23	24	25	26	27	28	29	30
$2b/h$		0.85	1.00	1.43	1.98	2.49	3.01	4.01	5.00	5.99	7.03	8.00	9.03	9.99
P_b/P_w		0.60	0.71	1.01	1.40	1.76	2.13	2.83	3.54	4.23	4.97	5.65	6.38	7.06
Panel 1	f	0.0164	0.0192	0.0206	0.0220	0.0231	0.0197	0.0233	0.0229	0.0158	0.0165	0.0174	0.0183	0.0202
	λ	0.23	0.28	0.39	0.51	0.53	0.65	0.88	0.65	0.69	0.31	0.55	0.32	0.37
	Γ	1.11	1.01	0.98	0.94	0.18	0.83	0.77	0.74	0.74	0.69	0.51	0.42	0.30
Panel 2	f	0.0151	0.0179	0.0199	0.0219	0.0221	0.0170	0.0199	0.0214	0.0142	0.0157	0.0141	0.0190	0.0174
	λ	0.19	0.24	0.25	0.26	0.29	0.30	0.33	0.43	0.38	0.41	0.66	0.71	0.85
	Γ	-0.21	-0.28	-0.41	-0.55	-0.43	-0.24	-0.28	-0.28	-0.23	-0.21	-0.16	-0.19	-0.10
Panel 3	f	0.1216	0.1081	0.1885	0.2689	0.4324	0.2432	0.3645	0.5270	0.2989	0.4334	0.3108	0.4459	0.4320
	λ	0.24	0.38	0.56	0.73	0.85	0.57	0.80	0.99	0.76	0.57	0.80	0.73	1.7000
	Γ	0.20	0.23	0.24	0.25	0.27	0.30	0.33	0.38	0.47	0.54	0.61	0.66	0.85
Panel 4	f	0.2432	0.2323	0.2777	0.3231	0.5231	0.4585	0.4864	0.7500	0.6104	0.8323	0.5674	0.7743	0.6081
	λ	0.093	0.063	0.045	0.026	0.009	0.024	0.006	0.006	0.054	0.044	0.010	0.005	0.006
	Γ	-0.54	-0.60	-0.63	-0.65	-0.73	-0.85	-1.28	-1.33	-1.48	-1.60	-1.84	-2.10	-2.52

Table (5-6): The optimal parameter values in channels with smooth bed and R1 on the wall.

Al-Hamid		09	10	11	12	13	17	18	19	31	32	33	34	35
$2b/h$		0.85	1.00	1.50	2.00	2.51	2.99	4.01	4.99	5.99	7.01	8.00	8.96	10.00
P_b/P_w		0.60	0.70	1.06	1.41	1.78	2.12	2.83	3.53	4.23	4.96	5.66	6.33	7.07
Panel 1	f	0.0149	0.0183	0.0218	0.0220	0.0249	0.0180	0.0201	0.0199	0.0153	0.0170	0.0164	0.0175	0.0188
	λ	0.47	0.51	0.50	0.51	0.57	0.65	0.55	0.70	0.13	0.14	0.22	0.32	0.37
	Γ	1.25	1.18	1.07	0.84	0.78	0.74	0.68	0.56	0.52	0.36	0.26	0.18	0.15
Panel 2	f	0.0152	0.0174	0.0200	0.0216	0.0223	0.0166	0.0182	0.0191	0.0140	0.0151	0.0167	0.0174	0.0184
	λ	0.11	0.19	0.20	0.24	0.24	0.25	0.30	0.37	0.36	0.62	0.66	0.74	0.78
	Γ	-0.25	-0.22	-0.20	-0.24	-0.23	-0.26	-0.24	-0.24	-0.24	-0.22	-0.21	-0.25	-0.16
Panel 3	f	0.0709	0.0664	0.0733	0.1092	0.1081	0.1211	0.1621	0.1976	0.1150	0.1312	0.1778	0.2297	0.1867
	λ	0.21	0.24	0.26	0.29	0.29	0.30	0.33	0.50	0.57	0.76	0.68	0.80	0.8990
	Γ	0.14	0.16	0.18	0.22	0.24	0.24	0.30	0.40	0.61	0.70	0.93	1.14	1.31
Panel 4	f	0.1788	0.1891	0.2432	0.3054	0.2972	0.2702	0.2972	0.3513	0.2092	0.1942	0.2590	0.4039	0.4378
	λ	0.102	0.068	0.036	0.034	0.036	0.032	0.010	0.020	0.018	0.018	0.006	0.017	0.016
	Γ	-0.40	-0.48	-0.52	-0.59	-0.63	-1.22	-1.34	-1.40	-1.44	-1.41	-1.04	-0.85	-0.73

Table (5-7): The optimal parameter values in channels with smooth bed and R2 on the wall.

Al-Hamid		06	07	08	14	15	16	20	21	22	36	37	38
Roughness		R1	R1	R1	R2	R2	R2	R2	R2	R2	R2	R2	R2
$2b/h$		1.49	2.00	2.50	1.50	2.00	2.52	4.00	4.98	6.06	7.49	8.50	9.98
P_b/P_w		1.05	1.42	1.76	1.06	1.41	1.78	2.83	3.52	4.28	5.30	6.01	7.06
Panel 1	f	0.0904	0.1328	0.1453	0.0941	0.1152	0.1306	0.0803	0.0976	0.0989	0.0873	0.0963	0.1002
	λ	0.32	0.38	0.45	0.46	0.51	0.59	0.60	0.63	0.69	1.37	1.45	1.63
	Γ	-1.61	-1.54	-1.45	-1.41	-1.38	-1.27	-1.20	-0.83	-0.71	-0.67	-0.62	-0.42
Panel 2	f	0.1407	0.1845	0.2014	0.0852	0.1113	0.1464	0.1142	0.1012	0.1194	0.1214	0.1349	0.1452
	λ	0.28	0.34	0.40	0.12	0.19	0.27	0.33	0.37	0.50	0.98	1.17	1.47
	Γ	0.22	0.18	0.24	0.18	0.19	0.24	0.19	0.22	0.20	0.24	0.20	0.22
Panel 3	f	0.1919	0.2443	0.2765	0.1133	0.1901	0.2543	0.2023	0.2636	0.2837	0.1539	0.1927	0.2147
	λ	0.12	0.31	0.75	0.80	0.90	0.97	1.05	1.14	1.23	1.03	1.26	1.56
	Γ	-0.27	-0.35	-0.42	-0.47	-0.76	-0.95	-1.13	-1.26	-1.65	-1.62	-1.90	-2.17
Panel 4	f	0.2192	0.1933	0.2264	0.1441	0.1988	0.2640	0.1345	0.1621	0.2229	0.2088	0.2031	0.2357
	λ	0.543	0.650	0.730	0.852	0.331	0.730	0.899	0.930	0.966	0.919	1.265	1.354
	Γ	0.65	0.74	0.80	0.85	0.95	1.04	1.19	1.40	1.51	1.69	2.01	2.38

Table (5-8): The optimal parameter values in channels with rough bed and wall.

The following conclusions can be drawn based on Figures (5-17 to 5-20), Appendix (IV.3) and the individual panel values (Sharifi *et al*., 2009a):

1- For all differentially roughened cases, visual observations indicate that the velocity and boundary shear stress magnitudes are reasonably well simulated. In cases where the aspect ratio is less than 5, the calculated boundary shear in the rough wall region deviates from the measured data by up to 50% in certain regions. This difference is mainly due to the shear stress measurement technique (Section 4.2.5) and other sources of uncertainty (e.g. averaging errors and digitizing errors).

2- For uniformly roughened cases, the mean velocity is predicted well but the calculated shear stress distribution seems to be a reasonable fit to the measured values.

3- For differentially roughened trapezoidal channels, Figures (5-17a and 5-17b) show that the value of the friction factor in the second bed panel, f_2, is slightly lower than in the first panel, f_1. In the rough wall region the value of f increases significantly from the bed-wall intersection, f_3, to its maximum at the channel edge, f_4.

4- Figures (5-17a and 5-17b) also show that the values of the friction factors in the sloping sidewall region panels, f_3 and f_4, of differentially roughened channels increase with an increase in the wetted perimeter ratio.

5- Generally, in the flat bed region, for the same aspect ratios, larger values of f_1 and f_2 are found for channels with rougher walls (R1). As the aspect ratio increases, the difference between the values of f_1 and f_2 in both channels decreases.

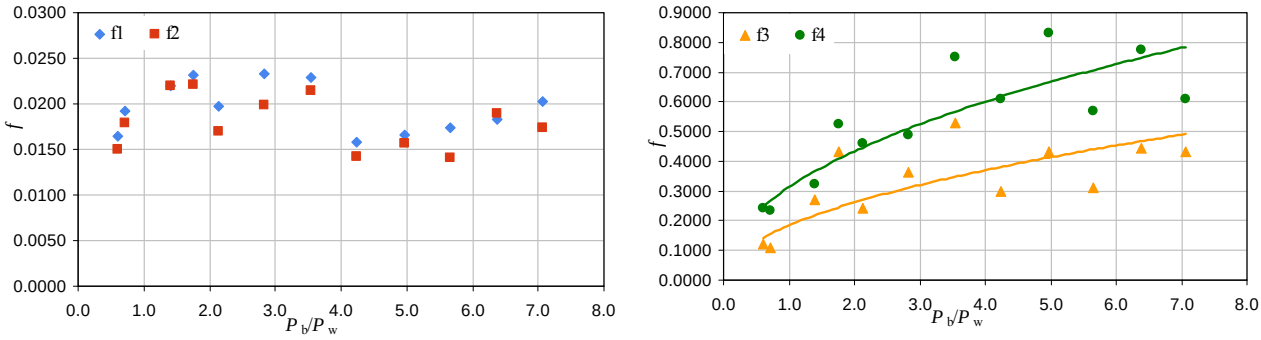

a) Smooth Bed and R1 on the wall ($0.6 \le P_b / P_w \le 7.06$ and S_o =3.920x10^{-3}).

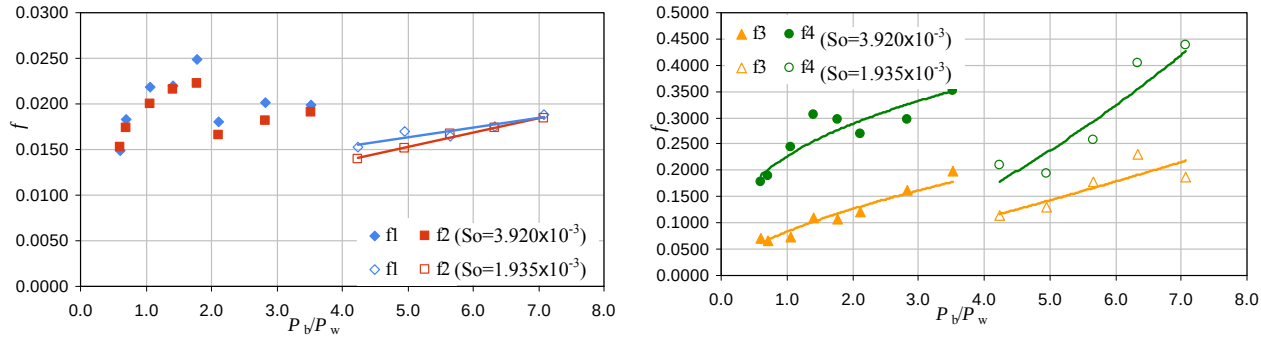

b) Smooth Bed and R2 on the wall ($0.6 \le P_b / P_w \le 7.07$).

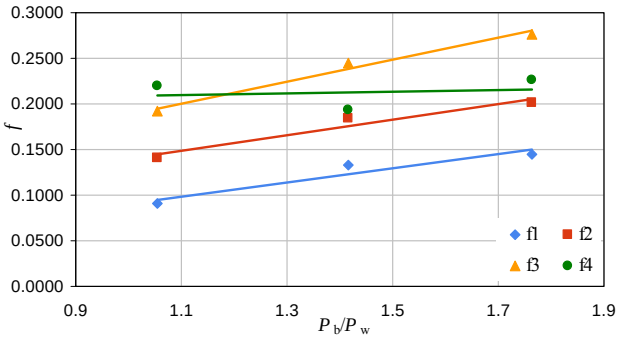

c) R1 on bed and walls
($1.05 \le P_b / P_w \le 1.76$ and S_o =3.920x10^{-3}).

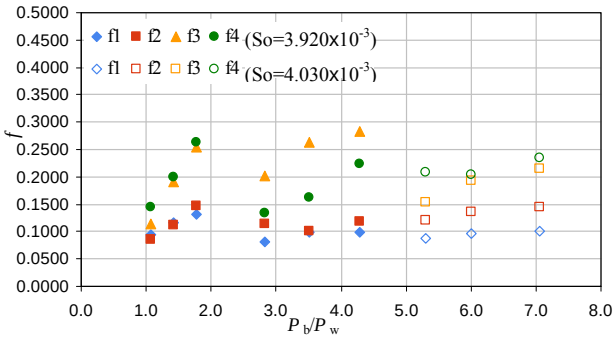

d) R2 on bed and walls
($1.06 \le P_b / P_w \le 7.06$).

Figure (5-17): Friction factor vs. wetted perimeter ratio in differentially and uniformly roughened trapezoidal channels.

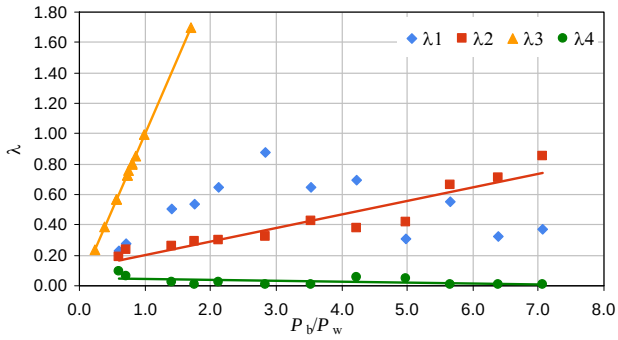

a) Smooth Bed and R1 on the wall ($0.6 \le P_b / P_w \le 7.06$ and S_o=3.920x10^{-3}).

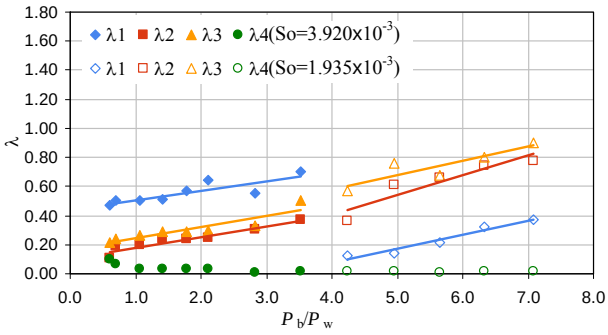

b) Smooth Bed and R2 on the wall ($0.6 \le P_b / P_w \le 7.07$).

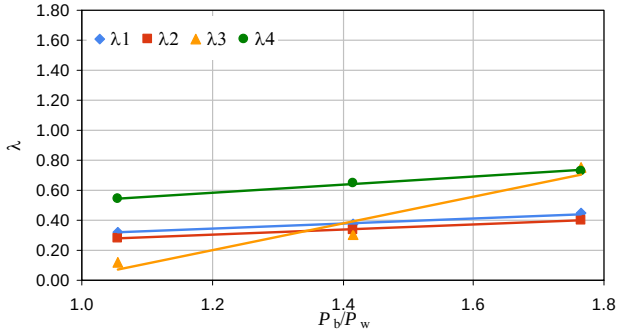

c) R1 on bed and walls ($1.05 \le P_b / P_w \le 1.76$ and S_o=3.920x10^{-3}).

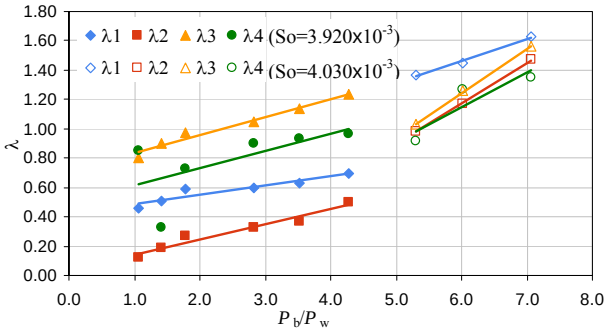

d) R2 on bed and walls ($1.06 \le P_b / P_w \le 7.06$).

Figure (5-18): Dimensionless eddy viscosity vs. wetted perimeter ratio in differentially and uniformly roughened trapezoidal channels.

6- Figure (5-17c) indicates that for uniformly roughened channels with R1 on the bed and walls and bed slope of 3.92x10^{-3}, the friction factor in all panels increases almost linearly with the increase in the wetted perimeter ratio, with an exception in the last panel where the friction factor remains more or less constant. Figure (5-17d) also shows a somewhat similar pattern for channels with R2 on the bed and walls and bed slope of 4.03x10^{-3}. In contrast, when the bed slope is reduced to 3.92x10^{-3} a general trend for the lateral variation of the friction factor cannot be recognized.

7- The optimum values found for λ in the smooth bed region of partially roughened channels are again scattered. This again implies that the model is not sensitive to λ in these smooth regions. On the other hand, the model is very sensitive to the value of λ in the third and fourth panels.

8- Figures (5-18c and 5-18d) indicate that in homogeneously roughened channels, the zonal dimensionless eddy viscosity, λ, increases with the increase in the wetted perimeter ratio, P_b/P_w.

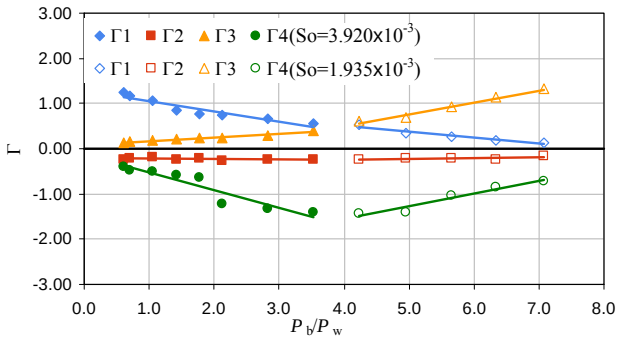

b) Smooth Bed and R2 on the wall ($0.6 \le P_b / P_w \le 7.07$).

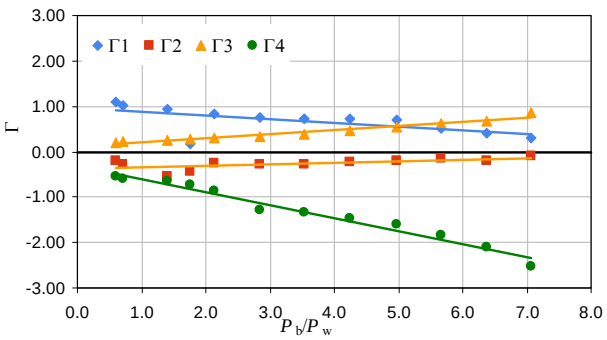

a) Smooth Bed and R1 on the wall ($0.6 \le P_b / P_w \le 7.06$ and S_o=3.920x10^{-3}).

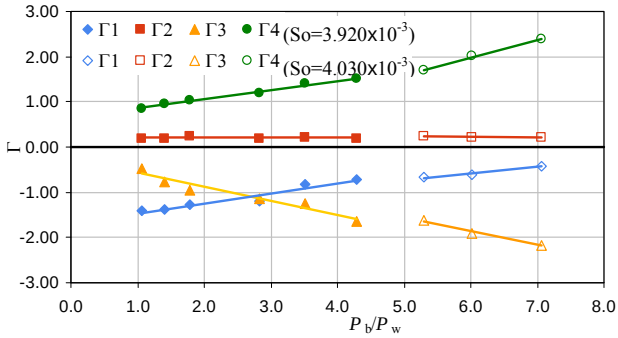

d) R2 on bed and walls ($1.06 \le P_b / P_w \le 7.06$).

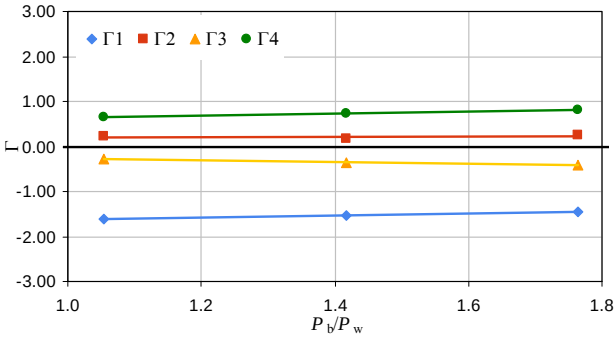

c) R1 on bed and walls ($1.05 \le P_b / P_w \le 1.76$ and S_o=3.920x10^{-3}).

Figure (5-19): Secondary flow term vs. wetted perimeter ratio in differentially and uniformly roughened trapezoidal channels.

9- The best pattern for the sign of Γ in differentially roughened channels is found to be + - + - which is exactly the opposite pattern found for uniformly smooth and uniformly roughened channels. This change in the sign of Γ can be interpreted as a change in the rotating direction of all the secondary flow cells.

10- The lateral variation of the absolute optimum values of Γ is similar to that of uniformly roughened channels. The absolute value of Γ in the second panel of all cases again converges to a value near 0.25 which is slightly different from the smooth cases. The important difference is that the maximum value of Γ for differentially roughened channels does not appear in the final panel.

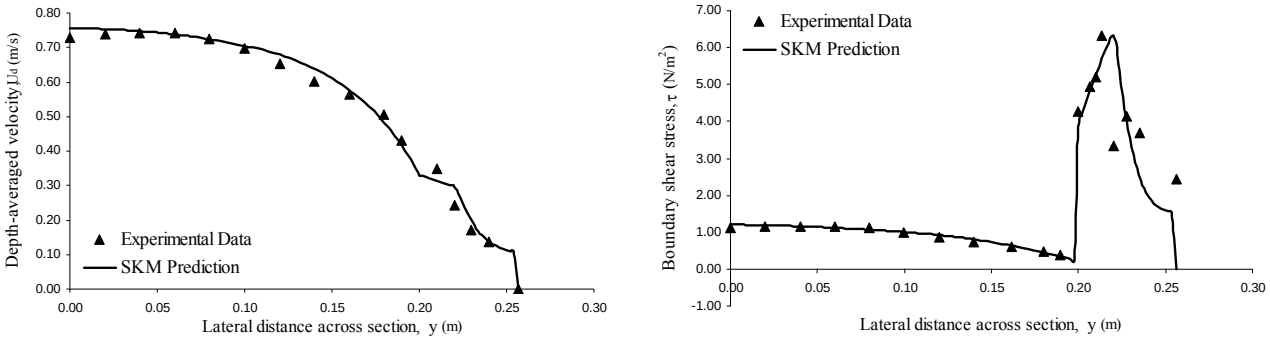

a) Al-Hamid 27 (smooth bed and R1 on the walls; h=0.057 m; 2b/h=7.03).

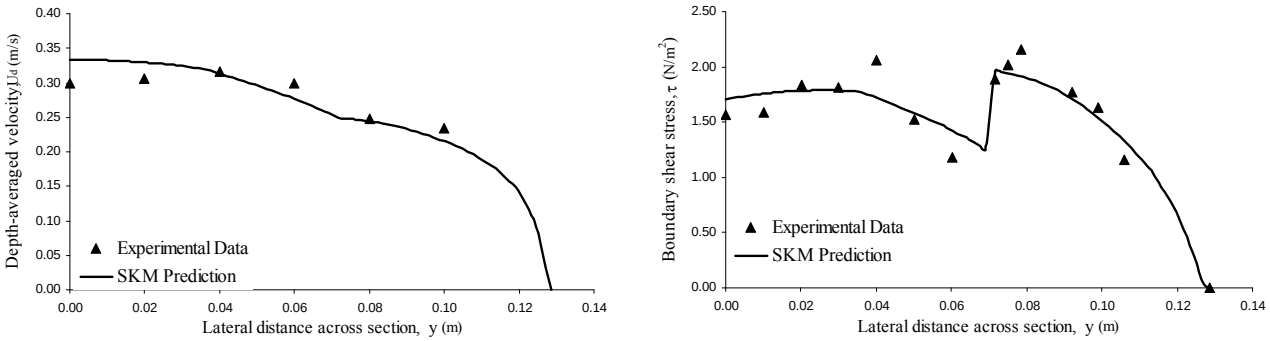

b) Al-Hamid 16 (R2 on the bed and walls; h=0.057 m; 2b/h=2.52).

Figure (5-20): Distributions of depth-averaged velocity and boundary shear stress for a a) differentially roughened and b) uniformly roughened trapezoidal channel.

5.2.4 Parameter guidelines

The results of calibrating the model according to various trapezoidal datasets revealed how each of these parameters change with respect to aspect ratio and panel number. Furthermore in order to add to the degree of applicability of the results, an attempt was made to provide general rules and guidance on choosing the appropriate values of f, λ and Γ in smooth homogeneous trapezoidal channels. Based on this exploratory work, a set of equations is proposed which relate the values of f, λ and Γ in each panel to the channel's wetted perimeter ratio (Tables (5-9 to11)). It should be noted that for panels in which the model is not sensitive to the value of the zonal dimensionless eddy viscosity, a constant value of 0.6 is selected for this parameter. These preliminary guidelines provide some practical rules in choosing the appropriate parameters for use in the SKM model.

Aspect ratio ($2b/h$)	Panel	A	B
$0< Asp <3$	1	0.0196	0.2122
	2	0.0226	0.2976
	3	0.0240	0.2719
	4	0.0277	0.2846
$7.5< Asp <30$	1	0.0113	0.2369
	2	0.0117	0.2594
	3	0.0123	0.2799
	4	0.0114	0.3049
	5	0.0153	0.2545

Table (5-9): Equations for finding the friction factor in the form of $f = A(P_b/P_w)^B$.

Aspect ratio ($2b/h$)	Panel	A	B
$0< Asp <3$	1	0	0.60
	2	0.4832	0.0054
	3	0.1773	0.6933
	4	0.2773	1.2965
$7.5< Asp <10$	1	0	0.60
	2	0	0.60
	3	0	0.60
	4	0.1442	-0.1822
	5	0.5754	-1.3427
$10< Asp <30$	1	0	0.60
	2	0	0.60
	3	0	0.60
	4	0.0107	0.3513
	5	0.0274	0.6583

Table (5-10): Equations for finding the dimensionless eddy viscosity in the form of

$$\lambda = A\ (P_b/P_w) + B.$$

Aspect ratio ($2b/h$)	Panel	A	B
$0< Asp <3$	1	0.2739	-0.7593
	2	0	0.15
	3	0.7548	-0.9331
	4	-0.3911	1.0928
$7.5< Asp <10$	1	0.3459	-1.6026
	2	0	0.01
	3	-0.1712	0.6371
	4	0.1581	-1.2626
	5	-1.5306	6.0043
$10< Asp <30$	1	0.0465	-0.5221
	2	0	0.01
	3	-0.0024	0.0785
	4	0.0320	-0.7419
	5	-0.0689	0.9101

Table (5-11): Equations for finding the secondary flow term in the form of

$$\Gamma = A\ (P_b/P_w) + B.$$

5.3 RECTANGULAR CHANNELS

As discussed in Section 2.6.9.2, due to the formation of a different structure of secondary flow cells in rectangular channels (i.e. free-surface and bottom vortex), accurate modelling of the flow with a depth-averaged model is a difficult task. In fact, the existence of two contra rotating cells at two depth levels results in a completely different transverse velocity distribution. This phenomenon, along with the effects of a near vertical side-wall, directly affects the interpretation of all depth-averaged parameters in the model, especially the dimensionless eddy viscosity and secondary flow term.

After building a calibration framework on the basis of flow in trapezoidal channels and calibrating homogeneous and heterogeneous trapezoidal channels, an attempt was made to assess the applicability of the developed methodology to rectangular channels. Due to the low number of available test cases and different uncertainties, the focus was directed more to finding a suitable panel structure rather than studying the variation of SKM parameters.

5.3.1 Introduction to the datasets

Two simple rectangular datasets based on the experimental work of Knight *et al*. (1984a) and Tominaga *et al*. (1989) were analyzed in this research. The first dataset included six test cases performed in a smooth rectangular channel in one of the University of Birmingham's main flumes. The channel width and bed slope were fixed at $2b$=0.152m and S_0=0.966x10^{-3} respectively, and the depth was varied from 0.0858m to 0.1530m to get aspect ratios in the range of $0.99< 2b/h <1.77$. Tominaga's dataset was limited to detailed measurements of depth-averaged velocity and boundary shear stress in a 0.4m wide simple channel for four different depths and bed slopes. Since the measured discharge was not available for this set, the mean velocity profile was integrated to find the approximate values. Table (5-12) shows a summary of the test cases in both datasets. Figure (5-21) also shows the stage-discharge curve for the first dataset.

Test case	$2b$ (m)	h (m)	$2b/h$	P_b/P_w	S_0 ($x10^{-3}$)	Q (ls^{-1})	R (m)	U_{avr} ($m.s^{-1}$)	τ_{avr} ($N.m^{-2}$)	R_e ($x10^4$)	F_r
DWK 01	0.152	0.0858	1.77	0.89	0.966	4.80	0.0403	0.3681	0.3908	6.484	0.401
DWK 02	0.152	0.0970	1.57	0.78	0.966	5.60	0.0426	0.3798	0.4124	7.075	0.389
DWK 03	0.152	0.1026	1.48	0.74	0.966	6.07	0.0437	0.3892	0.4370	7.429	0.388
DWK 04	0.152	0.1136	1.34	0.67	0.966	7.00	0.0455	0.4054	0.4644	8.070	0.384
DWK 05	0.152	0.1259	1.21	0.60	0.966	8.00	0.0474	0.4180	0.4745	8.661	0.376
DWK 06	0.152	0.1530	0.99	0.50	0.966	9.85	0.0508	0.4235	0.4744	9.402	0.346
AP1001	0.400	0.0653	6.13	3.06	0.802	9.85	0.0492	0.3772	0.3969	8.118	0.471
AP1002	0.400	0.0499	8.02	4.01	0.641	5.81	0.0399	0.2909	0.2638	5.079	0.416
AP1601	0.400	0.0663	6.03	3.02	1.160	9.25	0.0498	0.3490	0.5824	7.596	0.433
AP1602	0.400	0.0496	8.06	4.03	1.130	5.87	0.0397	0.2958	0.4570	5.139	0.424

Table (5-12): Knight *et al*. (1984a) test cases.

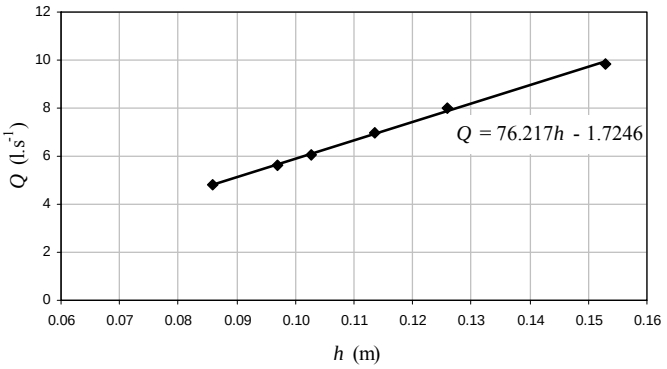

Figure (5-21): Stage-discharge curve for Knight *et al*. (1984a) dataset.

5.3.2 Modelling the flow with one panel

The first attempt was made to investigate the possibility of modelling flow accurately by considering half of the symmetrical channel as one panel. The first two objective functions were minimized simultaneously in order to find the best fits for the lateral mean velocity and boundary shear stress. Figure (5-22) illustrates the Pareto front found for a typical case. The shape of the Pareto indicates that there are two main clusters of solutions: a) solutions which result in almost the same value for the first objective function and consequently the best mean velocity distribution (shown with circles) and b) solutions which result in almost the same value for the second objective function (shown with crosses). Accordingly all the solutions in this cluster result in good boundary shear stress distributions. Under these conditions, the solution that had the least Euclidian distance from the origin and resulted in the overall best distributions of mean velocity and boundary shear stress was selected as the "*best solution*".

Table (5-13) shows the obtained optimum values of f, λ and Γ for each case and the relative objective function values. The variation of optimum friction and secondary flow term with wetted perimeter ratio is illustrated in Figure (5-23). Figures (5-24 & 5-25) show the SKM predicted and measured mean velocity distribution for DWK01 and AP1001 respectively.

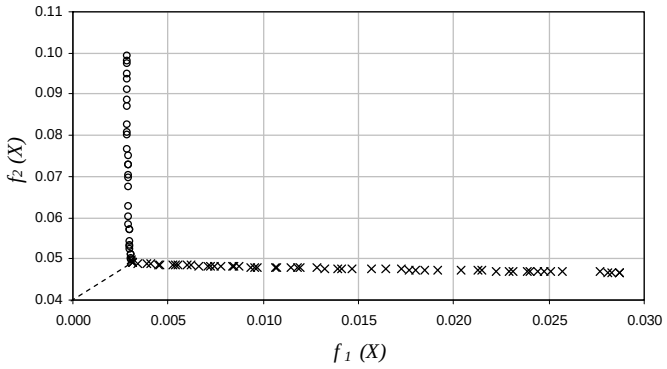

Figure (5-22): Pareto front of a typical rectangular case.

Test case	*h* (m)	*2b/h*	P_b/P_w	*Q* ($l.s^{-1}$)	*f*	λ	Γ	$f_1(X)$	$f_2(X)$	*Err Q* %	*Err* %SF_w %
DWK01	0.0858	1.77	0.89	4.80	0.0238	0.001	0.38	0.0066	0.0483	4.27	2.13
DWK02	0.0970	1.57	0.78	5.60	0.0235	0.001	0.46	0.0086	0.0567	4.84	2.48
DWK03	0.1026	1.48	0.74	6.07	0.0239	0.001	0.49	0.0121	0.0805	5.37	3.38
DWK04	0.1136	1.34	0.67	7.00	0.0233	0.001	0.55	0.0118	0.0727	5.07	2.37
DWK05	0.1259	1.21	0.60	8.00	0.0213	0.001	0.65	0.0222	0.0999	3.78	3.16
DWK06	0.1530	0.99	0.50	9.85	0.0205	0.001	0.89	0.0213	0.0794	3.75	2.47
AP1001	0.0653	6.13	3.06	9.25	0.0192	0.003	0.10	0.0075	0.0158	5.36	5.46
AP1002	0.0499	8.02	4.01	5.87	0.0208	0.018	0.02	0.0045	0.0109	7.46	19.68
AP1601	0.0663	6.03	3.02	9.85	0.0321	0.008	0.13	0.0061	0.0451	6.39	6.24
AP1602	0.0496	8.06	4.03	5.81	0.0350	0.024	0.05	0.0022	0.0170	6.50	12.47

Table (5-13): Optimum parameters values and the relative objective function values for rectangular cases modelled with on panel.

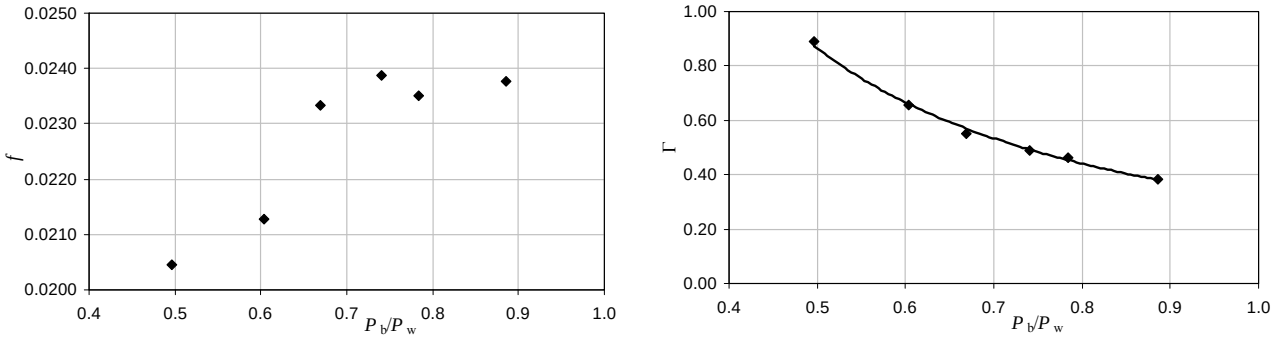

Figure (5-23): Variation of *f* and Γ vs. wetted parameter ratio in rectangular cases modelled with one panel.

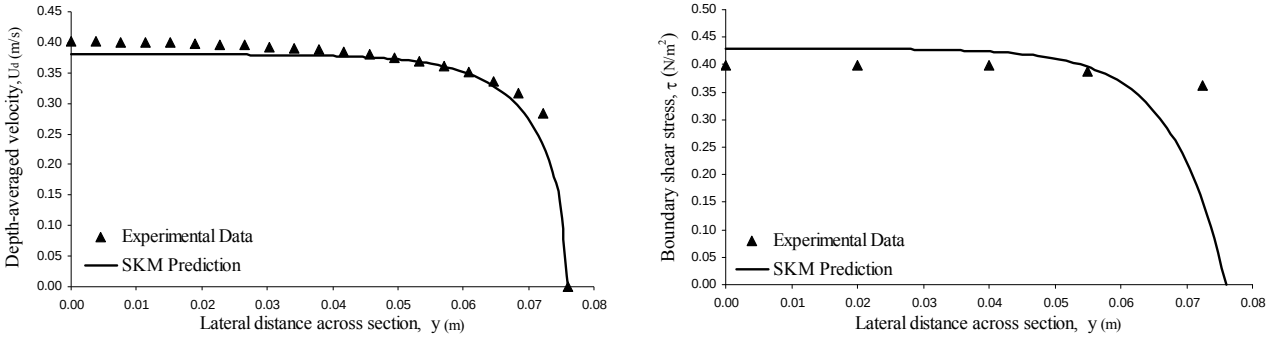

Figure (5-24): Mean velocity and Boundary shear distributions for case DWK01.

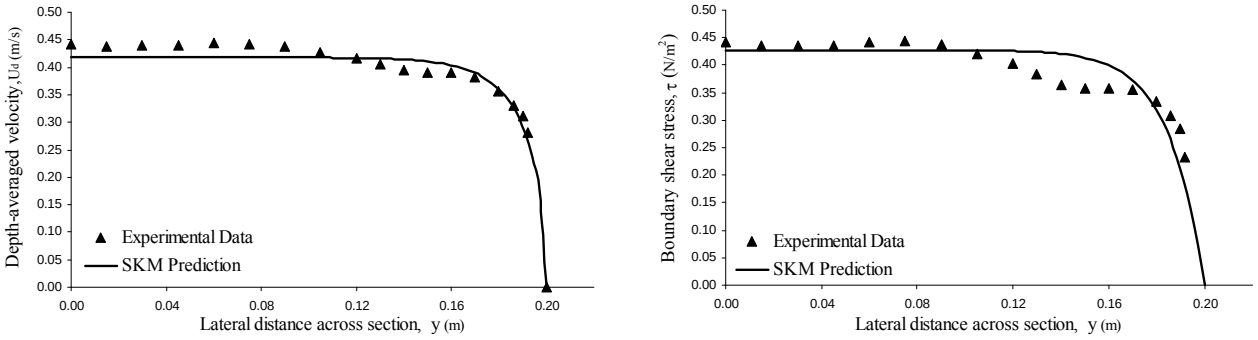

Figure (5-25): Mean velocity and Boundary shear distributions for case AP1001.

The following main observations can be made from the presented results:

1- The optimum dimensionless eddy viscosity for all Knight's cases is found as 0.001. This is the defined lower bound for this parameter.

2- The optimum secondary flow term is positive in all cases.

3- With increase in the wetted perimeter ratio (P_b/P_w), the friction factor increases and the secondary flow term decreases.

4- The simulated depth-averaged velocity magnitudes are reasonable but the boundary shear stress simulations have poor quality, particularly at greater depths.

5- The predicted discharge and $\%SF_w$ for Knight's cases are within almost 5 percent of the measured values. For Tominga's cases the predicted discharge is acceptable but $\%SF_w$ predictions are not acceptable. This is due to not capturing the sudden dip in the boundary shear stress distribution near the side-walls.

In conclusion, one panel seems to be insufficient for accurate modelling and more panels should be considered.

5.3.3 Modelling the flow with two panels

5.3.3.1 Two identically spaced panels

The calibration procedure was continued by considering two identical panels for half of the symmetrical channel. The same shape was found for the Pareto front of all cases and again the solution with the minimum Euclidian distance was selected as the best solution. Table (5-14) shows the calibration results and the variation of SKM parameters are illustrated in Figure (5-26).

Test case	2b/h	P_b/P_w	Panel 1			Panel 2			$f_1(X)$	$f_2(X)$	Err Q	Err %SFw
			f	λ	Γ	f	λ	Γ			%	%
DWK01	1.77	0.89	0.0215	1.37	0.52	0.0215	0.005	0.01	0.0113	0.0605	1.12	4.93
DWK02	1.57	0.78	0.0212	1.29	0.67	0.0220	0.005	-0.12	0.0128	0.0636	0.90	2.87
DWK03	1.48	0.74	0.0215	2.19	0.72	0.0223	0.005	-0.19	0.0151	0.0842	1.30	3.76
DWK04	1.34	0.67	0.0226	1.58	0.91	0.0214	0.005	-0.45	0.0220	0.0634	1.73	1.73
DWK05	1.21	0.60	0.0209	1.09	1.12	0.0200	0.005	-0.64	0.0282	0.0843	0.85	2.27
DWK06	0.99	0.50	0.0204	0.25	1.45	0.0202	0.005	-0.83	0.0247	0.0568	1.67	1.26
AP1001	6.13	3.06	0.0199	2.25	0.07	0.0198	0.005	0.11	0.0044	0.0195	3.97	8.43
AP1002	8.02	4.01	0.0199	1.73	0.00	0.0214	0.006	0.07	0.0016	0.0028	8.27	20.09
AP1601	6.03	3.02	0.0318	2.18	0.08	0.0353	0.005	0.20	0.0024	0.0131	4.78	8.67
AP1602	8.06	4.03	0.0336	0.33	0.02	0.0366	0.012	0.11	0.0012	0.0079	6.98	13.77

Table (5-14): Optimum parameters values and the relative objective function values for rectangular cases modelled with two identical panels.

Comparing Tables (5-13) and (5-14), it is observed that for Knight's cases, considering two identical panels results in higher values of the first objective function (worse predictions of mean velocity distribution), but lower errors in estimating the discharge. For Tominaga's cases, the objective functions have lower values but the errors in estimating $\%SF_w$ increase. It is also observed that the values of λ in the second panel tend to the lower bound of the defined range (0.005) and its values in the first panel seem to be scattered. This indicates that the model is not sensitive to the value of this parameter in the first panel and any $\lambda_1 \geq 0.1$ would result in same distributions. The secondary flow term is found to be positive and negative for

the first and second panels respectively. The variation of *f* does not seem to follow a certain pattern but the absolute value of Γ decreases linearly with the increase in the aspect ratio.

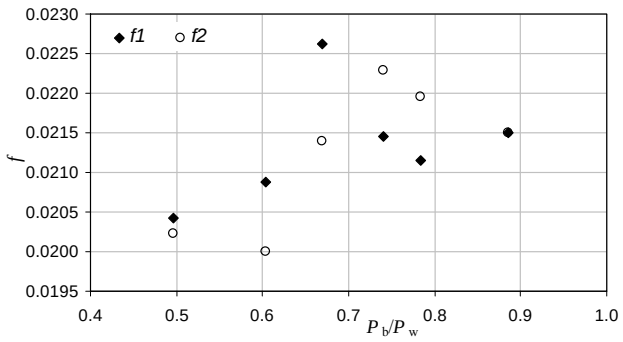

(a) Friction factor.

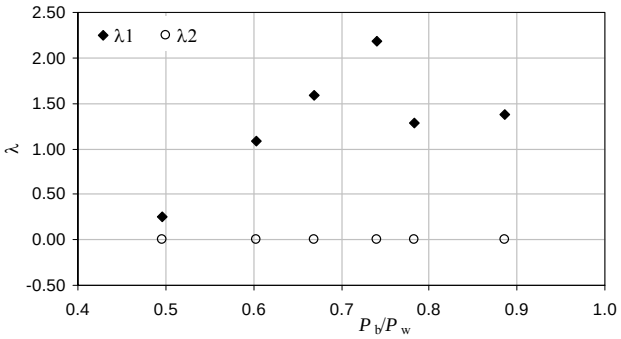

(b) Dimensionless eddy viscosity.

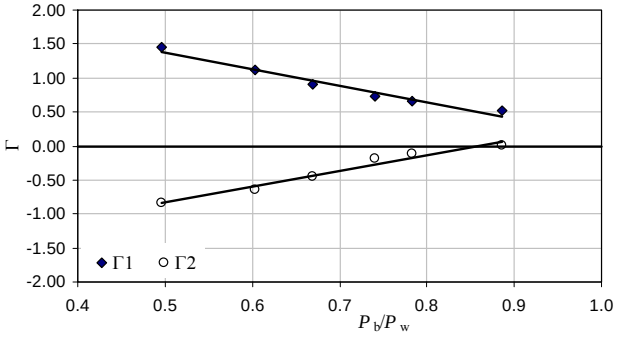

(c) Secondary flow term.

Figure (5-26): Variation of f, λ and Γ vs. wetted parameter ratio in rectangular cases modelled with two identical panels.

5.3.3.2 Two differentially spaced panels (80:20 split)

If the local value of the friction factor, *f*, is back calculated from the boundary shear stress profile using the Darcy-Weisbach equation ($\tau = \rho(f/8)U_d^2$) and its lateral variation is plotted (Figure (5-27)), it can be observed that *f* slightly increases from its lowest value at the channel centerline until nearly 80% of the channel width. Afterwards, *f* increases dramatically with a steep gradient, to its maximum value at the channel side-wall. Further investigation of the secondary flow cell structures in rectangular channels (Figures 2-12 & 2-13), also indicates that the velocity mixture of free-surface and bottom vortices in the last 20% of the channel width is different from the rest of the channel. Based on these

observations, the panel division line was moved to 80% of the channels width and the model calibration was performed. Table (5-15) shows the calibration results.

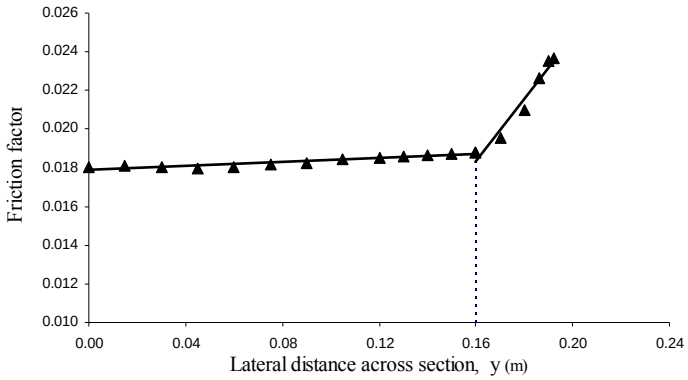

Figure (5-27): Lateral variation of the back-calculated friction factor for case AP1001.

Test case	2b/h	P_b/P_w	Panel 1			Panel 2			$f_1(X)$	$f_2(X)$	Err Q	Err %SF_w
			f	λ	Γ	f	λ	Γ			%	%
DWK01	1.77	0.89	0.0210	0.01	0.40	0.0500	0.005	-1.44	0.0026	0.0008	0.50	8.51
DWK02	1.57	0.78	0.0208	0.01	0.48	0.0500	0.005	-1.97	0.0024	0.0011	0.55	7.93
DWK03	1.48	0.74	0.0215	0.89	0.47	0.0500	0.005	-2.43	0.0066	0.0005	0.65	9.41
DWK04	1.34	0.67	0.0209	0.05	0.42	0.0500	0.005	-2.13	0.0053	0.0032	0.90	7.45
DWK05	1.21	0.60	0.0196	1.51	0.42	0.0477	0.005	-2.46	0.0124	0.0023	0.66	6.01
DWK06	0.99	0.50	0.0197	0.06	0.45	0.0482	0.005	-2.50	0.0111	0.0028	1.25	4.99
AP1001	6.13	3.06	0.0185	3.27	-1.08	0.0234	0.182	2.13	0.0022	0.0021	6.85	5.73
AP1002	8.02	4.01	0.0203	1.47	-0.31	0.0246	0.240	-1.84	0.0009	0.0008	7.98	16.60
AP1601	6.03	3.02	0.0315	2.65	0.08	0.0359	0.005	0.21	0.0024	0.0129	4.85	9.41
AP1602	8.06	4.03	0.0343	0.13	0.00	0.0059	0.124	-2.90	0.0023	0.0044	8.46	13.47

Table (5-15): Optimum parameters values and the relative objective function values for rectangular cases modelled with two panels (80:20).

The results show remarkable improvements in the values of $f_1(X)$, $f_2(X)$ for both datasets. However, the discharge estimation error has been reduced only for Knight's experiments and higher levels of accuracy have been reached for %SF_w predictions in Tominaga's dataset.

Reaching higher levels of optimality by changing the panel boundary position to 80% of the width was encouraging. By modifying the calibration code, the location of panel division line was added to the variable set. The calibration code was then run for all cases to find optimum SKM parameters and panel size. The calibration results revealed that for most cases, the panel position line lies between 83% and 96% of the channel width. This causes the values of

all objectives to decrease greatly. Figure (5-28) shows the mean velocity and boundary shear stress distribution for a selected case. This figure shows that both the simulated depth-averaged velocity and boundary shear stress magnitudes are reasonable, however, the measured lateral inflections related to the secondary currents are still not perfectly captured.

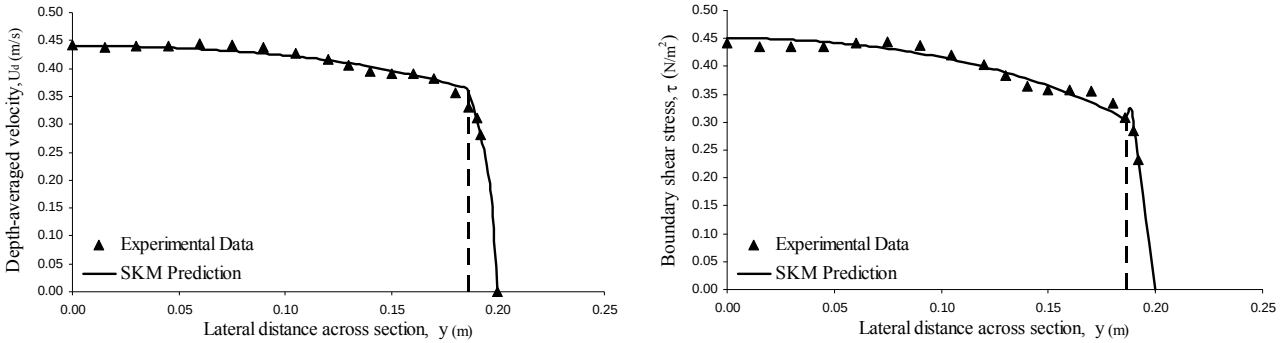

Figure (5-28): Mean velocity and Boundary shear distributions for case AP1001.

5.3.4 Modelling the flow with four panels

A final attempt was made to investigate the effects of using four equally spaced panels on the optimality level. The results (Table (5-16)) revealed that this assumption not only does not improve the minimization of $f_1(X)$, $f_2(X)$ and discharge estimation error, but also increases the errors of $\%SF_w$ estimations for all cases. Furthermore as the degrees of freedom increase by adding additional panels, the model becomes insensitive to many of its parameters.

Test case	$2b/h$	P_b/P_w	$f_1(X)$	$f_2(X)$	*Err Q* %	*Err* $\%SF_w$ %
DWK01	1.77	0.89	0.0054	0.0005	0.66	15.74
DWK02	1.57	0.78	0.0029	0.0009	0.53	12.42
DWK03	1.48	0.74	0.0042	0.0013	0.84	14.75
DWK04	1.34	0.67	0.0047	0.0025	0.84	12.21
DWK05	1.21	0.60	0.0130	0.0031	0.61	10.47
DWK06	0.99	0.50	0.0147	0.0017	1.24	7.55
AP1001	6.13	3.06	0.0029	0.0018	6.59	9.30
AP1002	8.02	4.01	0.0005	0.0006	8.42	16.72
AP1601	6.03	3.02	0.0024	0.0043	6.91	12.76
AP1602	8.06	4.03	0.0010	0.0011	7.63	15.11

Table (5-16): Optimum parameters values and the relative objective function values for rectangular cases modelled with two panels.

Comparing the results of modelling rectangular channels with different panel settings, a two panel structure which divides half of the symmetric channel to 80% and 20% of its width was

found to reach the highest level of optimality and be the most suitable structure for modelling all rectangular cases. The predicted mean velocity and boundary shear stress distributions of all cases modelled with this panel structure are provided in Appendix (IV.4)

5.4 RIVERS

Continuing the calibration of the SKM for channels with simple cross sections, the calibration framework was applied to a number of natural rivers with inbank flow. This was an attempt to show the capability of SKM for modelling flows in rivers and also the effectiveness of the calibration framework for more complicated channel sections. In addition, the variations of the SKM parameters were investigated in a section where the mean velocity distribution was available for different depths.

5.4.1 Introduction to the datasets

Measurements relating to three rivers in the UK, (i.e. River Severn at Montford Bridge (Knight, 1989b); River Main at Bridge End Bridge (Myers and Lyness, 1989); River Trent, North Muskham (Knight, 1989b)), two rivers in Argentina (i.e. River Colorado and River La Suela (McGahey, 2006)) and two rivers in Ecuador (i.e. River Cuenca and River Tomebamba (McGahey, 2006)) were used in this research. All river cross sections were located at straight reaches and the mean velocity distribution and discharge measurements were available for inbank flow conditions. The detailed velocity measurements were normally made using an Acoustic Doppler Velocity (ADV) meter or a cable supported directional current meter. Among all the named rivers, measurements for different depths were only available for two rivers: River Colorado and River La Suela. For more information relating to the river locations, specifications, previous studies and measurement techniques the reader is referred to McGahey, (2006).

5.4.2 Considerations and assumptions

Panel structure selection

Since there were no data regarding the size and position of the secondary flow cells and also the shear stress measurements, it was felt that an 8 panel structure was sufficient for

simulating flow in all river sections. For each section, the position and size of the panels were selected in a way that mostly all panels could have a constant side slope and cover nearly the same proportion of the channel. In the case of channels with different depths, the two panels located at the channel sides were modified to satisfy the conditions and the remaining panels were kept the same. Figure (5-29) shows a typical river section and the defined boundary division lines. It is acknowledged that extra panels could have been used to reach higher levels of optimality. However, since each panel imposes three unknown parameters (i.e. three extra degrees of freedom or three extra dimensions in the search space), based on the quantity and quality of the available measurements, it is unlikely that the additional panels would give any extra information regarding the flow or the SKM parameters.

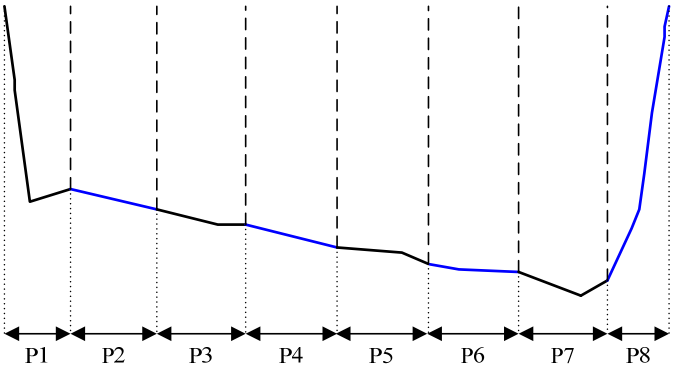

Figure (5-29): Surveyed cross section of river Colorado and the defined panels.

Objective functions

Since only the measurements of mean velocity distribution and discharge were available, the first and third objectives (Eqs. 4-9 & 4-11) were selected as the objective functions.

5.4.3 River Colorado

For the current purposes, the most reliable and useful dataset were the measurements made in River Colorado in Argentina (Figure (5-30)). The main channel of this section of the river is around 60m wide, 3.6m deep with an average longitudinal bed slope of 0.0013. The surveyed cross section is shown in Figure (5-29). The mean velocity profile and discharge measurements were available for 10 different depths between 1.9m and 3.7m.

(a) Downstream view (b) Cross river view

Figure (5-30): River Colorado (McGahey, 2006).

The calibration results for different depths of this cross section is shown in Table (5-17). In this table, the channel top width, T, and the ratio of T/h are used rather than cross-section width and aspect ratio ($2b/h$), respectively. The simulated and measured depth-averaged velocity profiles for the lowest and highest depths are shown in Figure (5-31). The remaining profiles regarding other depths are provided in Appendix (IV.5.1).

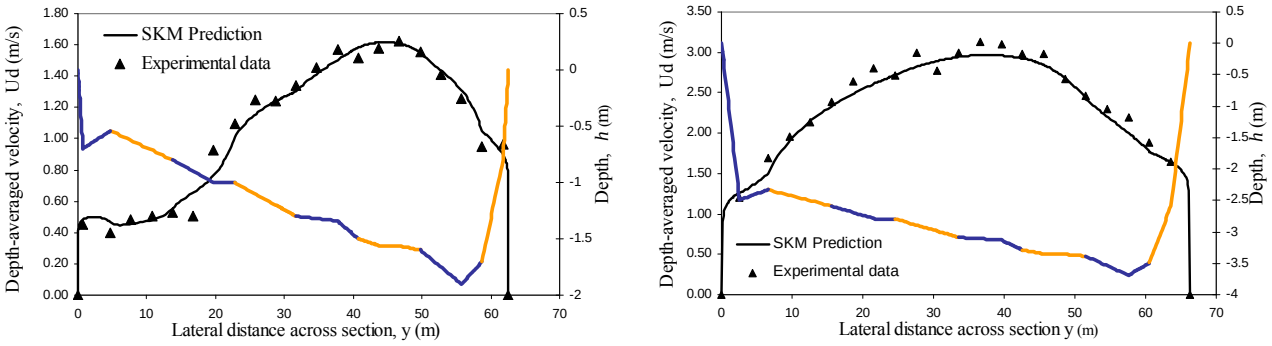

a) Colorado 01; h=1.900m b) Colorado 10; h=3.690m

Figure (5-31): Measured and simulated depth-averaged velocity distribution for River Colorado 04 (h=2.190m)

Colorado		01	02	03	04	05	06	07	08	09	10
T		62.56	62.74	62.85	63.17	63.21	63.35	63.80	64.64	65.26	66.29
h		1.90	1.98	2.04	2.19	2.21	2.28	2.49	2.90	3.20	3.69
T/h		32.93	31.62	30.81	28.84	28.60	27.79	25.58	22.30	20.41	17.97
Q ($m^3.s^{-1}$)		90.15	100.62	108.56	128.90	132.27	144.58	181.98	267.15	331.03	449.57
	f	0.1230	0.1278	0.1212	0.1228	0.0984	0.1233	0.1351	0.1622	0.1843	0.2127
Panel 1	λ	3.20	2.73	3.24	1.77	3.38	2.43	2.38	1.75	1.50	1.64
	Γ	3.27	3.08	3.06	2.56	3.16	3.15	3.17	3.15	3.12	2.65
	f	0.4351	0.4000	0.3741	0.3517	0.3304	0.2777	0.2226	0.1315	0.1322	0.1182
Panel 2	λ	1.01	2.14	2.68	1.86	1.69	1.58	2.47	1.14	2.81	1.62
	Γ	-3.15	-1.57	-3.36	-2.77	-2.25	-4.26	-4.23	-0.60	-2.98	-0.73
	f	0.2029	0.1891	0.1623	0.1584	0.1425	0.1232	0.0991	0.0318	0.0175	0.0379
Panel 3	λ	1.54	2.35	2.11	0.71	2.02	1.30	1.53	1.03	3.37	1.73
	Γ	1.20	1.40	2.93	0.62	3.73	4.29	1.63	4.32	0.51	2.03
	f	0.0906	0.0855	0.0805	0.0844	0.0697	0.0566	0.0559	0.0585	0.0513	0.0337
Panel 4	λ	4.39	4.05	4.30	4.17	4.20	3.13	3.54	1.91	2.08	1.68
	Γ	-2.87	-2.23	-2.46	-2.67	-3.54	-3.96	-2.46	-4.50	-2.77	-2.72
	f	0.0518	0.0456	0.0355	0.0290	0.0373	0.0333	0.0294	0.0280	0.0324	0.0250
Panel 5	λ	2.17	3.26	3.47	3.75	3.10	2.91	2.95	1.88	2.33	1.91
	Γ	3.14	1.80	3.41	1.96	1.18	3.70	0.62	1.39	2.50	1.94
	f	0.0593	0.0633	0.0546	0.0545	0.0466	0.0420	0.0324	0.0259	0.0107	0.0098
Panel 6	λ	2.72	3.64	2.96	2.24	3.41	2.68	3.75	3.32	2.43	3.66
	Γ	-3.46	-3.95	-3.28	-4.00	-2.48	-2.26	-3.52	-3.84	-1.78	-2.32
	f	0.0761	0.0752	0.0746	0.0957	0.0631	0.0644	0.0794	0.0803	0.0770	0.0819
Panel 7	λ	1.31	1.43	1.01	1.01	2.09	2.63	1.96	2.09	2.44	1.76
	Γ	1.32	2.40	1.49	1.09	4.00	1.78	1.23	2.23	2.32	3.38
	f	0.2350	0.2613	0.2041	0.2695	0.2972	0.3288	0.3177	0.2484	0.2850	0.2345
Panel 8	λ	2.90	3.78	3.80	3.12	3.48	1.86	1.37	2.25	3.49	2.41
	Γ	-1.45	-0.73	-0.31	-2.27	-2.04	-2.96	-2.58	-2.78	-1.89	-2.28

Table (5-17): Optimum parameter values for river Colorado dataset.

The Figures reveal that the mean velocity and discharge is well predicted throughout the whole range of flow depths. From the optimum values of SKM parameters in Table (5-17) it can be deduced that the lateral variation of friction follows a similar trend for all depths but the dimensionless eddy viscosity and secondary flow values are scattered and no explicit relationship can be found for their variation. This might be an indication of the independency of friction to panel structure, and dependency of interpretable lumped dimensionless eddy viscosity and secondary flow term values. Figures (5-32 & 5-33) show the lateral variation of friction against T/h and panel number, respectively. The following conclusions can be derived from these Figures:

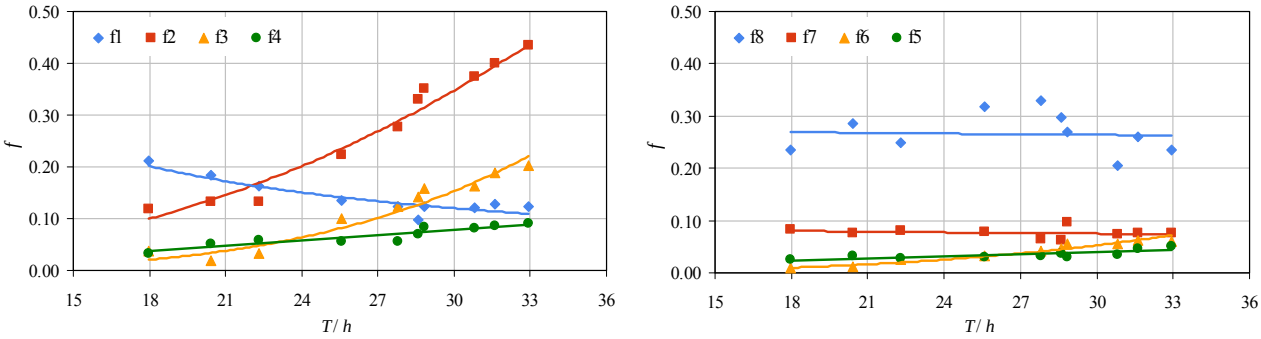

a) 1.90<*h*<2.21 b) 2.28<*h*<3.69

Figure (5-32): Friction factor vs. *T*/*h* for River Colorado.

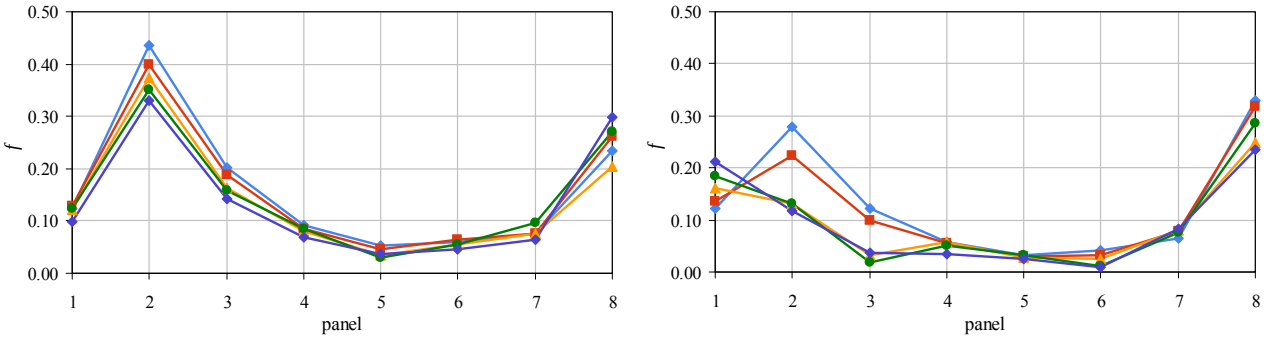

a) 1.90<*h*<2.21 b) 2.28<*h*<3.69

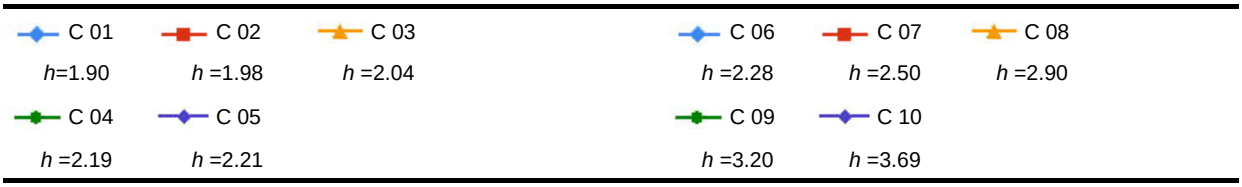

Figure (5-33): Friction factor vs. panel number for River Colorado.

1- The friction factor in the left side-wall panel decreases with the decrease of depth. Moreover, the variation of this parameter in the right side-wall panel seems to have no particular relation with depth. These observations might be a result of altering the dimensions of these two panels with depth changes.

2- Except for the first (utmost left) and last (utmost right) side-wall panels, the value of zonal friction in all panels increases with the increase in *T*/*h* (decrease of depth). This is similar to the observations of trapezoidal and rectangular channels.

3- As the right side-wall is approached the gradient of the variation of friction decreases. This might be related to the geometry of the cross-section.

4- For depths below 2.90m (C01-C07), the value of the friction factor increases suddenly from the first panel to its highest value at the second panel. The friction then drops to a value almost equal to f_1 in the third panel and then continues decreasing to the fifth panel where it obtains its lowest value. Again, it starts to increase gradually to its value in the seventh panel and finally increases suddenly to a value between 0.20 and 0.33 in the right side-wall panel.

5- For higher depths (h>2.90), the lateral variation of f follows a similar trend except for that in the second panel, the friction has a lower value than the first panel. As mentioned, this might be the effect of changing the first panel size with changes in depth.

5.4.4 River La Suela

Another river section where mean velocity measurements were available for various inbank depths was the River La Suela in Argentina (Figure (5-34)). This section of the river was approximately 25m wide, 2m deep with a reach-averaged longitudinal bed slope of 0.001355. It is noticeable that the measurements in this dataset were not as reliable as for the River Colorado: for many depths, the measured discharge was up to 25% different from its value calculated from integrating the measured velocity profile. Furthermore, the number and location of collected data points for different depths varied significantly. This might be due to the geometry or different seasonal vegetation at the time of performing the measurements.

Figure (5-34): River La Suela (McGahey, 2006).

The predictions of the calibrated SKM along with the measured velocity profile are provided in Appendix (IV.5.2). The Figures show good predictions of mean velocity and discharge throughout the whole range of flow depths. However, analyzing the optimum parameter

values, no specific trend could be observed for the variation of SKM parameters. Existence of various sources of uncertainty and also the assumed panel structure might be the reason behind this.

5.4.5 Other rivers

In addition to the River Colorado and the River La Suela, the calibration framework was applied to five other river sections: River Main at Bridge End Bridge (Myers & Lyness, 1989), River Severn at Montford Bridge (Knight, 1989b), River Trent, North Muskham (Knight, 1989b)), River Cuenca and River Tomebamba (McGahey, 2006). The first three rivers are inland rivers located in UK and the latter two are mountain rivers in Ecuador characterized by large boulders (approximately between 1 to1.3m in diameter) (McGahey, 2006). Other than the River Main, where measurements regarding two inbank flows were available, the remaining sections had only measurements for one inbank depth, making any generalized conclusions about the parameter variations impossible. The calibration results are provided in Appendix (IV.5.3). Again, the SKM simulates the measured data fairly well for all rivers. These promising results show the ability of SKM for simulating the flow over different sources of roughness (i.e. vegetation and boulders).

5.5 DISCUSSION

Accomplishing the multi-objective calibration of SKM for all available inbank channel and river datasets, an attempt was made to investigate the advantages of the proposed approach over previous calibration attempts. Furthermore, a cross-referencing analysis was performed to verify the obtained values of individual SKM parameters.

5.5.1 Advantages of the calibration approach

As mentioned in Section 2.6.5 a number of attempts had been previously made to calibrate SKM for inbank and overbank conditions using simple optimization techniques (e.g. exhausting search method, simple stochastic search method and visualization). In order to demonstrate the advantages of the multi-objective approach over previous calibration attempts, a comparison was made with two examples taken from Knight *et al*. (2007). Figure

(5-35) shows the depth averaged velocity and boundary shear stress distributions for two smooth homogeneous test cases along with the calculated values of the four objective functions (Eqs. 4-19 to 4-12).

Furthermore, the calibration results were compared with those of the CES model (McGahey, 2006) (which shares the same internal parameters with SKM) for two river test cases. Figure (5-36) shows this comparison. Figure (5-37) also compares the absolute errors in discharge prediction between SKM and CES results. It is observed that the predictions of the SKM calibrated with the NSGA-II algorithm, not only gives slightly better results in terms of both the general shape of the distributions and values of the objective functions, but is also an semi-automated process and does not rely on '*fitting by eye*'. This ability makes it suitable for applying it to many datasets with ease.

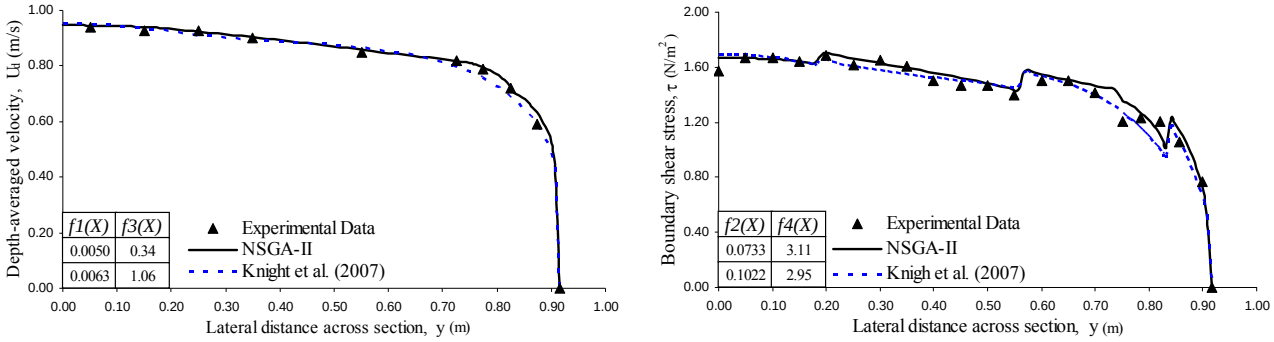

a) FCF 402 (2*b*/*h*=9.036)

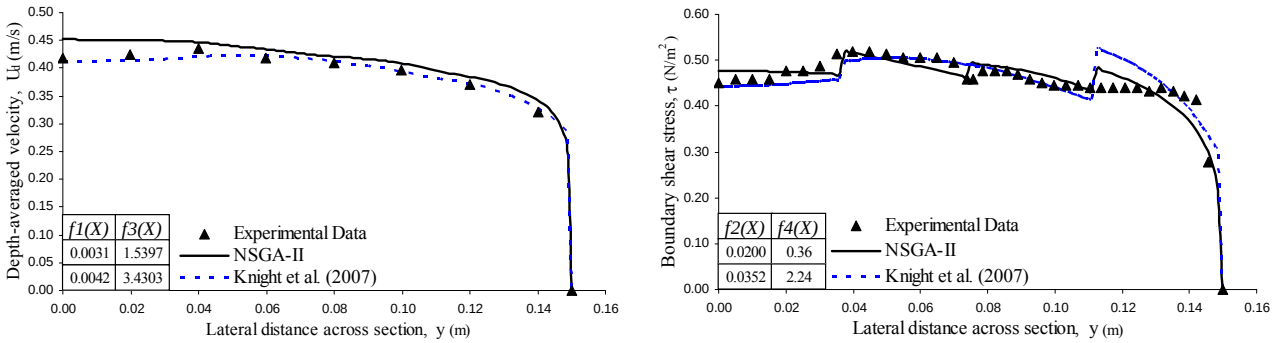

b) Yuen 008 (2*b*/*h*=2.00)

Figure (5-35): Comparing the predictions of the calibrated SKM with two examples taken from Knight *et al*. (2007).

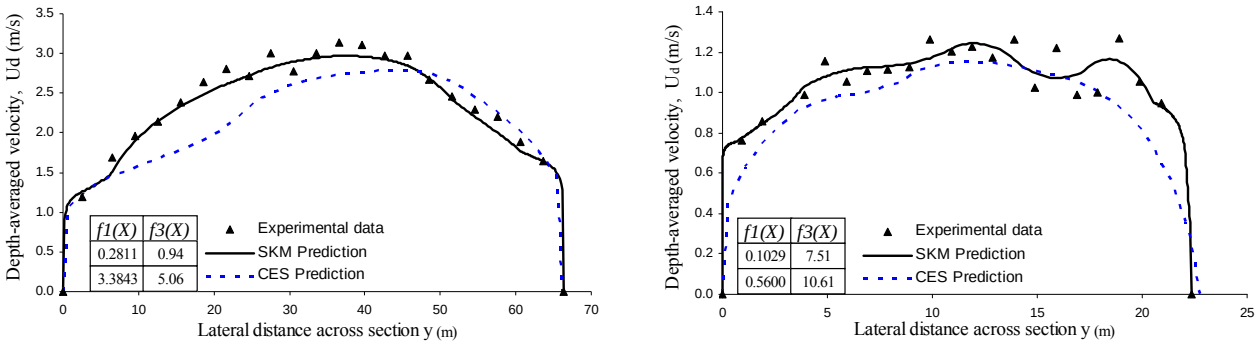

a) Colorado 10; depth 3.690m; Q_{data}=449.57 $m^3.s^{-1}$

b) La Suela 02; depth 1.28m; Q_{data}=21.11 $m^3.s^{-1}$

Figure (5-36): Comparing the predictions of the calibrated SKM with the calibrated CES (McGahey, 2006) for two river sections.

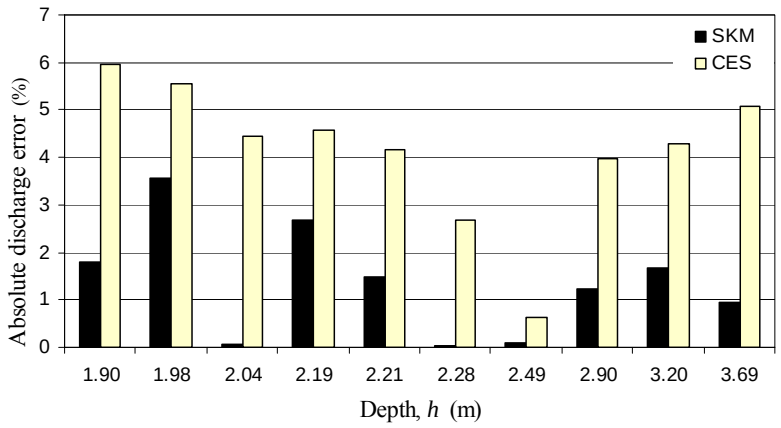

Figure (5-37): Comparing SKM and CES absolute errors in discharge predictions for different depths of River Colorado.

5.5.2 Friction factor

The lateral variation of the obtained optimum friction factors for both channels and rivers showed that the value of friction always increases in shallower regions. Assuming a constant value of k_s for the channel, this can be explained by using the Colebrook-White (1937) equation (Eq. 2.87).

Selecting the integration coefficients as C_{10}=12.27, C_{11}=3.09 and C_{12}=-2.03 (see Section 2.6.7 and Table (2-2)), and using an equivalent sand roughness of 0.05 mm, the averaged friction

values were calculated for all test cases of Yuen's data (Figure (5-38)). It is observed that for a constant bed slope, as the depth increases, R and Re increase and hence the value of f decreases. This conclusion can be extended to the value of zonal friction at shallow regions. Generally, as one moves towards the channel sidewall the velocity decreases and thus Re decreases and, as implied by Figure (5-38), the friction increases.

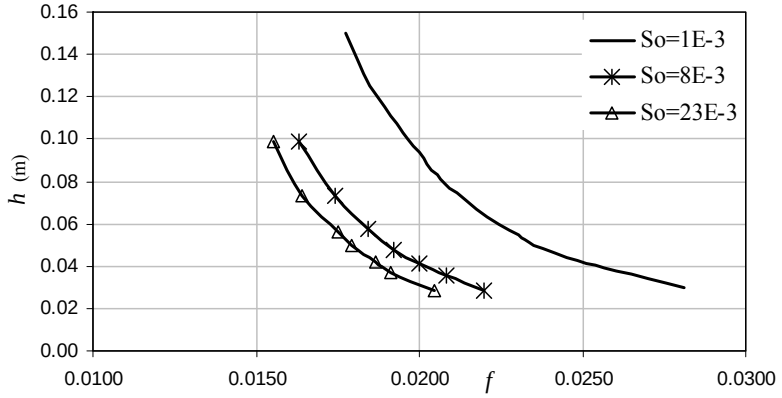

Figure (5-38): Variation of average friction factor with depth in Yuen's test cases

5.5.3 Dimensionless eddy viscosity

As shown for all investigated channels, the value of the dimensionless eddy viscosity did not appear to follow any specific pattern in the panels positioned in the constant depth region. This implies that the model is not sensitive to the value of this parameter in this region. In contrast, the model is sensitive to λ values in the side wall regions, and as a result the value of this parameter rapidly converges close to its final value during the optimization procedure.

Figure (5-39) shows the response surface of the first two objective functions in the parameter sub-space for a typical trapezoidal case. Here, only the value of λ in the side-wall regions (third and fourth panel) is changed and for the remaining parameters, their obtained optimum values are used. The analysis of these surfaces confirms previous findings by showing that the first objective function (predictions of mean velocity distribution) is not sensitive to either of the parameters, but for the second objective function (prediction of boundary shear stress) λ_4 converges to its optimum value (between 0.006 and 0.015 for different test cases) while λ_3 becomes more influential.

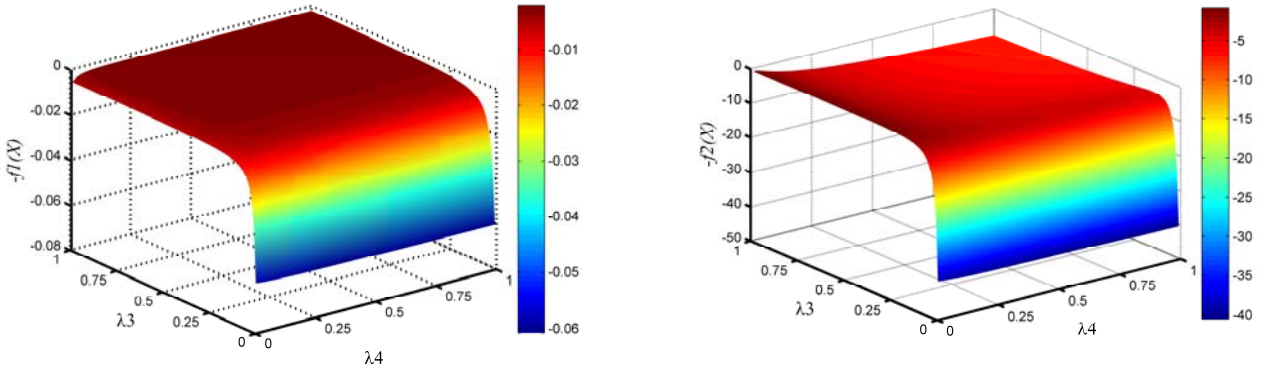

a) First objective function, $f_1(X)$ b) Second objective function, $f_2(X)$

Figure (5-39): Sensitivity of SKM to the values of λ_3 and λ_4 for Al-Hamid 05.

5.5.4 Secondary flow term

The following main conclusions were drawn from analyzing the variation of the secondary flow term in different datasets:

- Analyzing the clusters of solutions on the obtained Pareto front and cross-referencing the distributions of mean velocity and boundary shear of test cases in each dataset, the pattern of negative and positive values for Γ in adjacent panels was found as the optimum pattern for uniformly roughened trapezoidal channels. This agrees well with the findings of Knight *et al*. (2007) and justifies the optimum values found for Γ in the defined panels.
- For partially roughened channels (smooth bed and rough wall), the optimum sign pattern is completely reversed. This might be an indication of a change in the direction of the contra rotating secondary flow cells.
- Generally, higher values of Γ are found for the panels in the sidewall region. This implies high levels of circulation in these regions, which is consistent with the findings obtained from physical modelling (see Section 2.6.9).
- Boundary shear stress and velocity distributions were found to be more affected by the secondary currents and boundary roughness in differentially roughened channels than in uniformly roughened ones.

5.6 SUMMARY

Applying the calibration framework, the SKM was calibrated for a range of simple trapezoidal channels (Sections 5.2), rectangular channels (Section 5.3) and a few natural rivers (Section 5.4). Plotting the individual optimum model parameters against the panel number enabled the assessment of the lateral variation of each parameter. Furthermore, the effect of depth change on each parameter was studied by plotting the optimum model parameters versus P_b/P_w and versus T/h in channels and rivers, respectively. The major general findings can be summarized as follows:

- The value of the friction factor in shallower regions of channels and rivers is higher than its value in deeper regions.
- For the same channel geometry and bed slope, the increase in the mean depth causes the values of the local friction to decrease.
- The SKM is not sensitive to the dimensionless eddy viscosity, especially in flat bed regions.
- In trapezoidal channels, the optimum sign pattern of the secondary flow term is negative and positive in adjacent panels, which is in line with the assumptions made for choosing the panel structure.
- Generally, higher values of the secondary flow term are found for the panels in the sidewall region which implies high levels of circulation in these regions.
- A two panel structure (allocating 80% of half the symmetric channel width to the first panel and the remaining 20% to the second panel) seems to be the most suitable panel structure for modelling flows in rectangular channels.
- The SKM is capable of modelling flows in rivers with different roughnesses if an 8 panel structure is adopted.
- The calibration framework is applicable to complicated channel sections such as natural rivers.
- The values of the friction factor seem to be less dependent on the panel structure, while the depth-averaged lumped values of λ and Γ are highly affected by the panel structure. This emphasizes the importance of panel structure selection.

In Section 5.2.4 an attempt was made to generalize the calibrated parameter values of similar smooth trapezoidal channels by deriving relationships between the "*immeasurable*" parameters and the individual characteristics of channels (P_b/P_w). This enhances the capability of the model to be applied to any other similar channel. Once the calibration procedure is applied to a complete set of experiments, more accurate and useful rules can be generated.

After the calibration, a physical explanation was discovered for the friction factor. But it seems that due to the ill-posed conditions of the model, other parameters which are the result of time or space averaging might have lost some degree of interpretation. As the scope of this part of the research was limited to developing a calibration framework, a number of solutions and guidelines will be provided in Chapter 8 for overcoming this problem of lack of identifiability.

CHAPTER 6

GENETIC COMPUTATION: AN EFFICIENT TOOL FOR KNOWLEDGE DISCOVERY

6.1 INTRODUCTION

In Chapter 4, a multi-objective genetic algorithm (NSGA-II) was used to develop an effective calibration framework for the SKM model and its application to different channels and river sections with inbank flow was presented in Chapter 5. In this Chapter, a completely different application of evolutionary computation (EC) to a classic open channel flow problem is proposed: Genetic Programming (GP) (Section 3.4.4) is employed as an effective data mining tool in the procedure of developing a conceptual transparent model of the physical process of the free overfall (Section 2.7).

This chapter is composed of three main sections. The first section is devoted to the proposed methodology of the knowledge discovery process; data preprocessing, tuning the GP algorithm and model selection methodology are the subjects covered. The second section shows the results of applying the knowledge discovery process to experimental data extracted from earlier studies reported in the literature. This section introduces the free overfall problem and applies the knowledge discovery process to experimental data relating to three different cross-sectional shapes (i.e. flat bed circular channels, rectangular channels and trapezoidal channels). The section ends with investigating the applicability of the "best" fit model to channels with other cross-sections (i.e. inverted semi-circular, Δ-shaped, U-shaped and triangular). In the final section of the chapter, a critical discussion on this "best" model is developed further by performing a dimensional analysis on the free overfall problem and a dimensional reduction process on the experimental data.

6.2 METHODOLOGY

As mentioned in Chapter 3, the process of knowledge discovery consists of three main stages: data preprocessing, data mining and knowledge post-processing. In the following sections, detailed description of the actions undertaken in each of these stages will be provided.

6.2.1 Data preprocessing

The main action in this stage was integrating the data gathered from different sources into a suitable format. Initially, the variable units were all converted into SI units without applying any change to their scale (e.g. standardizing, normalizing or non-dimensionalizing). Then the entire data set was subjected to a cleaning process where errors (e.g. decimal displacement, rounding errors, and units) in the data were detected and corrected. Furthermore, inconsistent attributes such as friction were removed from the dataset and missing values (e.g. critical slope) were estimated and inserted where appropriate. Finally, among all original attributes, a set of suitable attributes were selected and the total dataset was then split into three disjointed subsets: training (66%), testing (23%) and validation data (11%), by means of uniform random sampling. The training data was used as inputs for the GP modelling process, the testing data for model selection and the validation data for evaluating the final selected model.

6.2.2 Tuning the GP algorithm

As stated in Chapter 3, GP is an efficient Data Mining tool based on the Darwinian theory of evolution. Starting with a number of random solutions, this technique tackles problems by improving the quality of the solutions by means of some natural variation operators. In its application to symbolic regression problems, this approach is able to develop a conceptual transparent (so-called white box) model of the physical process by searching through large amounts of data and detecting hidden or low-level patterns.

In this research, the Genetic programming lab (GPLAB) v.3 toolbox for Matlab (available from http://gplab.sourceforge.net) was used to evolve a relationship between the dependent (critical depth) and independent variables (end depth and other characteristics of the channel e.g. width, bed slope, end depth, etc.). Figure (6-1) shows the GPLAB algorithm structure.

For an in-depth description of this toolbox and its functions the reader is referred to GPLAB ver. 3 manual (http://gplab.sourceforge.net), and William and Northern (2008).

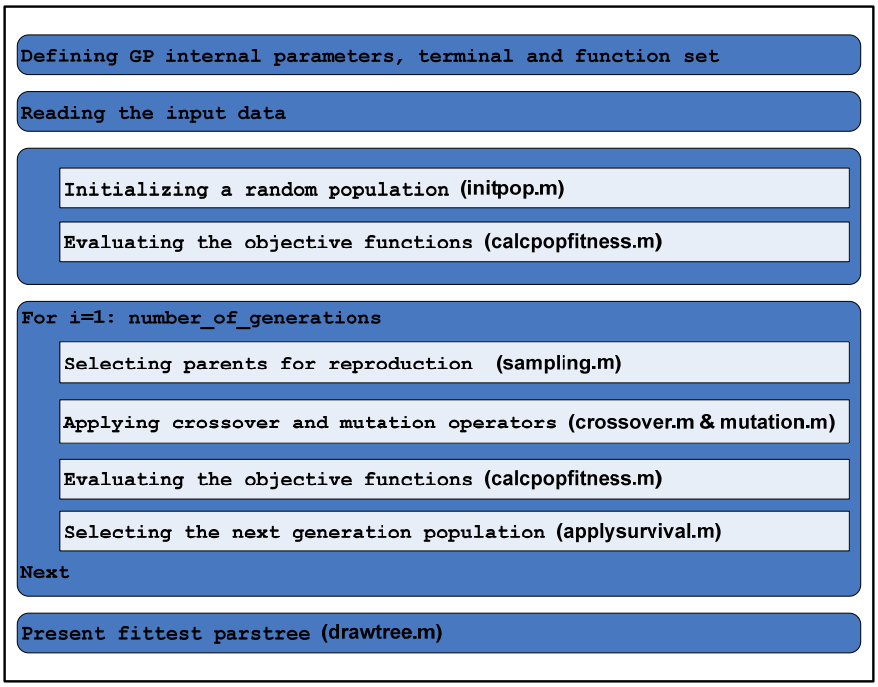

Figure (6-1): GPlab algorithm structure.

A number of standard arithmetic operators (i.e. plus, minus, times, divide, power, square root) and mathematical functions (i.e. exp, ln) were selected as the function set. In order to prevent the formation of any mathematical "*indeterminate forms*" and hence the termination of the algorithm, some of the original operators were substituted with their modified versions (Table (6-1)). The terminal set was selected based on the problem's characteristic. A preliminary analysis revealed that adding a random generated number to the terminal set would result in faster convergence. The sum of squared distances between the data points and their corresponding model predicted values was set as the fitness function.

Modified function	**MATLAB function**	**Input arguments**	**Output Arguments**
Division	mydivide	a, b	if b = 0, a else, a/b
Square root	mysqrt	a	if a <= 0, 0 else, sqrt(a)
Natural logarithm	mylog	a	If a = 0, 0 else, log (|a|)

Table (6-1): Modified operators and functions.

Based on similar applications of GP to symbolic regression problems in the literature (e.g. Keijzer, 2002; Keijzer *et al*., 2005; Aytek and Kisi, 2008) Ramped-half-and-half tree initialization method (Section 3.4.4.3), subtree crossover and mutation with variable probabilities (Section 3.4.4.5) were selected as the genetic operators. In addition, a modified tournament selection operator called Lexical tournament (Luke and Panait, 2002) was employed to control the tree size and consequently the complexity of the evolved symbolic expressions. This operator treats fitness as the primary objective and tree size as the secondary objective and has shown to be very effective in problems where many different individuals have the same fitness (Luke and Panait, 2001; 2002; Silva, 2005).

Similar to the method described in Section (4.4.4) a sensitivity analysis was performed in order to obtain a robust algorithm parameter set (Table (6-2)). In order to limit the effect of randomness on the results, by changing the seeding in each run, 50 independent runs of the GP algorithm were performed on the training data. Finally, the archive of solutions was searched and solely based on the value of the fitness function the top 100 potentially good models were selected.

Parameter	Value
Population size	75
Number of generations	100
Tree size restriction	10 nodes
Fitness function	Sum of squared distance
Tree Initialization method	Ramped-half-and-half
Genetic operators	Subtree Cross-over and Mutation
Operator probabilities	Variable (minimum equal to 0.20)
Selection method	Lexical tournament

Table (6-2): GP internal parameters and operators.

6.2.3 Model selection process

In the GP process, reaching optimum coefficient values for a symbolic expression requires the initial population to evolve through many generations and as such increases the computation time and memory requirements. To overcome this problem and to save computation time, a least square calculation was first performed on the training data to find the optimum coefficients for each of the models.

Evaluating what is meant by the concept of “best” can be both subjective and controversial. In the present context, the “best” model was evaluated by analyzing the complexity of the

model and its goodness of fit. To find this "best" model among the set of selected expressions, a combination of a subjective and an objective selection methodology was applied. In the subjective selection, the best 100 generated models were examined and the top 20 expressions were selected based on two criteria (Sharifi *et al*., 2009b&c):

1- *Complexity level*. The number and composition of functions and terminals along with the dimensions of the models were investigated to select simpler and dimensionally more correct models.

2- *Performance level*. The mean root of sum of squared error (MRSS) values were compared to select models with higher performance.

In order to gain a more complete picture of model performance, in the objective selection stage, two other fitness measures that are commonly reported in the literature, namely the root mean square of errors (RMSE) and coefficient of determination (CoD), were calculated for each expression on the training and testing data sets. The RMSE describes the average difference between experimental data and model predictions, while CoD is a measure of how much of the original uncertainty in the data is explained by the regression model (Weisberg, 1980). It was believed that a simultaneous assessment of these performance measures can provide a better insight on how thoroughly the model represents the system and hence a three step elimination strategy was followed to find the "best" model (Sharifi *et al*., 2009b):

1- Firstly, the expressions were sorted on the RMSE of the testing data and the 10 worst were detected. The expressions were then ranked on the CoD of testing data and the 10 worst were found. Any expression placed in any worst set was eliminated.

2- Secondly, for each of the remaining expressions, the RMSE related to training and testing data were summed and the total RMSE values were normalized between 0.0 and 1.0. The same procedure was then repeated with the CoD values. Afterwards, the normalized total RMSE was subtracted from the normalized total CoD and the expressions were sorted on this value. The normalization was done to ensure that both performance measures have the same range.

3- Finally, the computed values of the dependent variable from the top 5 remaining expressions were plotted against the measured values for both training and test data

and the deviation from the 45 degree line was inspected. The residual distribution of each expression was also plotted to investigate the degree of biasness. With the help of visual inspection and also judgment on the expression structure, a final elimination process was preformed to select the "best" expression.

6.3 FREE OVERFALL PROBLEM

In open channel flow, a free overfall is where the bottom of a channel drops suddenly, causing the flow to separate and form a free nappe. Based on various experiments in prismatic channels (Dey, 2002b), the end depth bears a unique relationship with the critical depth (h_c). The critical depth is an important concept in open channel flow since there exists a unique relationship between the depth of flow and the discharge. However, the location of the critical depth can vary with respect to discharge, whereas the location of the end depth is always fixed. Hence, if a relationship between h_e and h_c is provided, then the free overfall can be used as a simple flow measuring device (Sterling and Knight, 2001; Gupta *et al*., 1993). A review on the hydraulic aspects of the free overfall problem and previous attempts of solving this problem is provided in Section (2.7).

In this research, earlier work is extended, and Genetic Programming (GP) is applied as a data mining tool to solve this particular open channel flow problem. Various experimental data relating to several cases with different cross sections (i.e. rectangular, trapezoidal, circular, inverted semi-circular, Δ-shaped, U-shaped and triangular) were extracted from earlier studies reported in the literature and the methodology was applied to develop a conceptual transparent model of the physical process of the free overfall.

6.3.1 Circular channels with a flat bed

6.3.1.1 Introduction to the dataset

The first dataset used for the knowledge discovery process was the laboratory data from Sterling (1998). These experiments were undertaken in a 21.26 m long tilting channel with a working cross section of 610 mm wide by 365mm deep supported on hydraulic jacks that enabled the bed slope (S_0) to be varied. The experimental channel consisted of eight, 2 m

long plastic PVC pipe sections with an internal diameter (D) of 244 mm with a wall thickness of 3 mm. A 110 mm wide slot was cut in the crown of the pipe sections to provide access inside the pipe and make the measurements possible. A flat horizontal bed constructed from 9 mm thick PVC was added to the base of the circular pipe. Five series of experiments were carried out with five different bed thicknesses (t). For each test the brink depth (h_e) at the centerline was measured by means of a pointer gauge to an accuracy of ±0.1 mm and the discharge (Q) was measured via a calibrated orifice plate. The critical depth (h_c) was determined from $Q^2 / g = A^3 / T$ and the critical slope (S_c) was calculated using the average value of Manning's n. Figures (6-2 & 6-3) show the experimental setup and the geometry of the channels, respectively and Table (6-3) shows a summary of the experimental data. For further detailed information relating to the experiments, see Sterling (1998).

Series	Diameter (D) (m)	Bed thickness (t) (m)	Bed slope (S_0) (%)	Discharge (Q) ($l.s^{-1}$)	Brink depth (h_e) (m)
1	0.244	0.000	0.0	1.5 ~ 61.6	0.0197 ~ 0.1426
2	0.244	0.061	0.1	4.8 ~ 38.8	0.0217 ~ 0.0927
3	0.244	0.081	0.4	1.0 ~ 26.8	0.0080 ~ 0.0689
4	0.244	0.123	0.9	1.1 ~ 21.7	0.0074 ~ 0.0657
5	0.244	0.162	1.6	1.0 ~ 7.7	0.0091 ~ 0.0310

Table (6-3): Range of Sterling's (1998) experimental data.

Figure (6-2): University of Birmingham 22m long tilting flume and the circular PVC channel built inside (www.flowdata.bham.ac.uk).

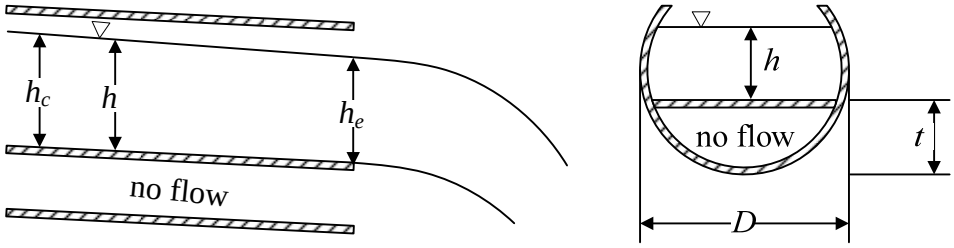

Figure (6-3): Geometry of circular channels with flat bed.

6.3.1.2 Modelling results

In the preprocessing stage (described in Section 6.2.1) a dataset was formed by integrating the 322 individual experiments within the 5 test series. Consequently, the total dataset was split into three separate subsets: training (66%), testing (23%) and validation data (11%), by means of uniform random sampling. The terminal set was chosen as {h_e, t, D, S_0, S_c, random number} and the GP algorithm was applied to the training data. An initial evaluation of the models considered to be "best", revealed that $\sqrt{S_0}$ was repeated in a large number of expressions and hence was one of the principal factors. In order to increase the efficiency of the algorithm, the terminal set was expanded to include the square root of the bed slope and critical slope. Fifty individual runs were performed and the results were evaluated to find the top 100 expressions. The subjective selection was then applied to find the least complex and best fit models (Table (6-4)). Finally, the best models were selected through the objective selection (Table (6-5)). Figure (6-4) shows the computed and measured values of the dependent variable (h_c) and the residual distribution of each expression for both training and test data.

No.	Expression	Training data			Test data		
		MRSS ($x10^{-4}$)	RMSE	CoD	MRSS ($x10^{-4}$)	RMSE	CoD
1	$h_c = h_e(e^{0.2471+S_0+1.5338\sqrt{S_0}})$	3.494	0.0749	0.9883	5.406	0.0726	0.9960
2	$h_c = h_e(e^{0.24+S_c+1.6706\sqrt{S_0}})$	3.564	0.0758	0.9878	5.508	0.0737	0.9958
3	$h_c = h_e e^{(0.1468+\sqrt{S_0})/0.6008}$	3.566	0.0758	0.9878	5.511	0.0735	0.9958
4	$h_c = 1.2769 h_e e^{1.6643\sqrt{S_0}}$	3.566	0.0758	0.9878	5.511	0.0735	0.9958
5	$h_c = h_e^{(1-\sqrt{S_c})}\sqrt{S_c}^{-\sqrt{S_0}}$	3.613	0.0992	0.9875	5.608	0.1003	0.9955
6	$h_c = h_e(e^{D+\sqrt{S_0}} + \sqrt{S_0})$	3.634	0.0767	0.9873	5.588	0.0743	0.9956
7	$h_c = h_e/(e^{(h_b)^2} - \sqrt{S_0} - 0.23602)$	3.670	0.0754	0.9873	5.940	0.0745	0.9953
8	$h_c = e^D h_e e^{2\sqrt{S_0}}$	3.706	0.0803	0.9890	5.293	0.0765	0.9963
9	$h_c = h_e/(e^{h_e-\sqrt{S_0}} - h_e - 0.23332)$	3.711	0.0758	0.9867	5.835	0.0748	0.9953
10	$h_c = h_e/(0.7680 - \sqrt{S_0})$	3.714	0.0754	0.9867	5.829	0.0742	0.9953
11	$h_c = h_e(e^{D+S_c+2\sqrt{S_0}})$	3.816	0.0815	0.9890	5.414	0.0779	0.9963
12	$h_c = e^D h_e D^{-\sqrt{S_0}}$	4.045	0.0784	0.9860	6.543	0.0771	0.9951
13	$h_c = h_e e^{\sqrt{\sqrt{S_0}+\sqrt{S_c}}}$	4.048	0.0802	0.9843	6.364	0.0803	0.9945
14	$h_c = 1.3039 h_e e^{(\sqrt{S_0}^{0.8782})}$	4.114	0.0790	0.9837	6.391	0.0782	0.9942
15	$h_c = (h_e/\sqrt{S_c}^{\sqrt{S_0}})^{0.94582}$	4.164	0.0895	0.9878	6.339	0.0847	0.9958
16	$h_c = h_e e^{(\sqrt{S_0}+0.28897)}$	4.374	0.0800	0.9816	6.985	0.0803	0.9934
17	$h_c = 1.2544 h_e e^{(\sqrt{S_0}+\sqrt{S_c})}$	4.405	0.0813	0.9813	7.084	0.0827	0.9932
18	$h_c = e^D h_e e^{(\sqrt{S_0}+\sqrt{S_c})}$	4.418	0.0831	0.9813	6.889	0.0849	0.9932
19	$h_c = e^D h_e(\sqrt{S_c} + e^{\sqrt{S_0}})$	4.462	0.0827	0.9806	7.042	0.0843	0.9929
20	$h_c = 1.37936 h_e S_c^{-S_0}$	4.501	0.0794	0.9806	7.275	0.0809	0.9929

Table (6-4): Selected expressions and the value of MRSS, RMSE and CoD for training and test data.

No.	Expression	Normalized Total		CoD_n - $RMSE_n$
		RMSE	CoD	
1	$h_c = h_e(e^{0.25+S_0+1.53\sqrt{S_0}})$	0.0000	0.6785	0.6785
3	$h_c = h_e e^{(0.15+\sqrt{S_0})/0.60}$	0.1959	0.4794	0.2835
4	$h_c = 1.28 h_e e^{1.66\sqrt{S_0}}$	0.1959	0.4794	0.2834
2	$h_c = h_e(e^{0.24+S_c+1.67\sqrt{S_0}})$	0.2210	0.4881	0.2671
8	$h_c = e^D h_e e^{2\sqrt{S_0}}$	1.0000	1.0000	0.0000
6	$h_c = h_e(e^{D+\sqrt{S_0}} + \sqrt{S_0})$	0.3820	0.2776	-0.1044
10	$h_c = h_e/(0.768 - \sqrt{S_0})$	0.2294	0.0000	-0.2294

Table (6-5): Normalized values of RMSE and CoD for the remaining expressions.

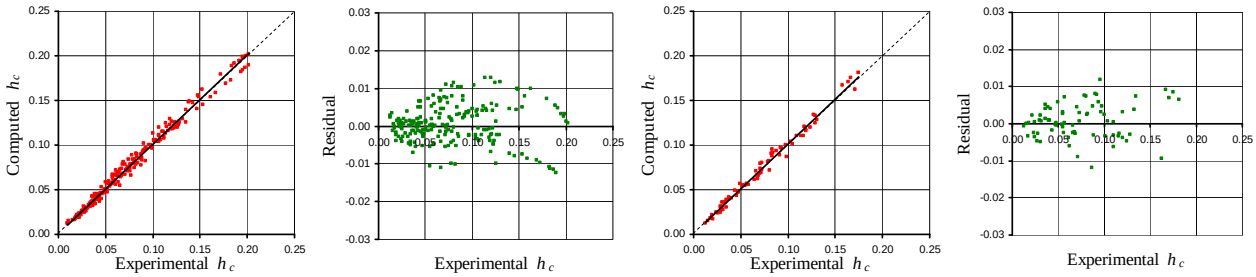

Training data Testing data

Exp. No (1) $h_c = h_e(e^{0.25+S_0+1.53\sqrt{S_0}})$

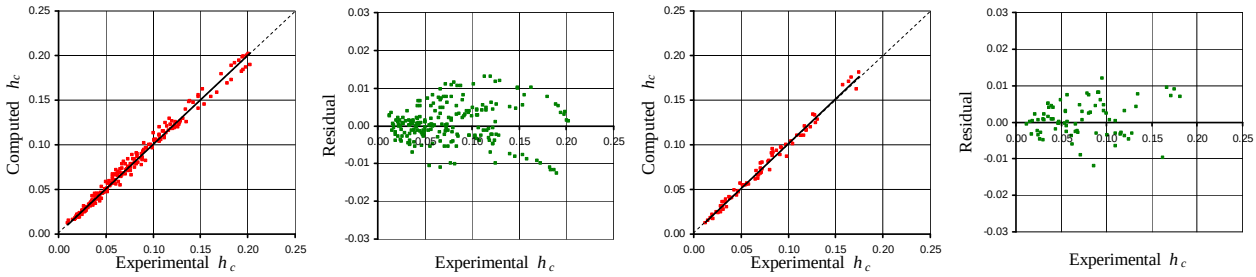

Training data Testing data

Exp. No (3) $h_c = h_e e^{(0.15+\sqrt{S_0})/0.60}$

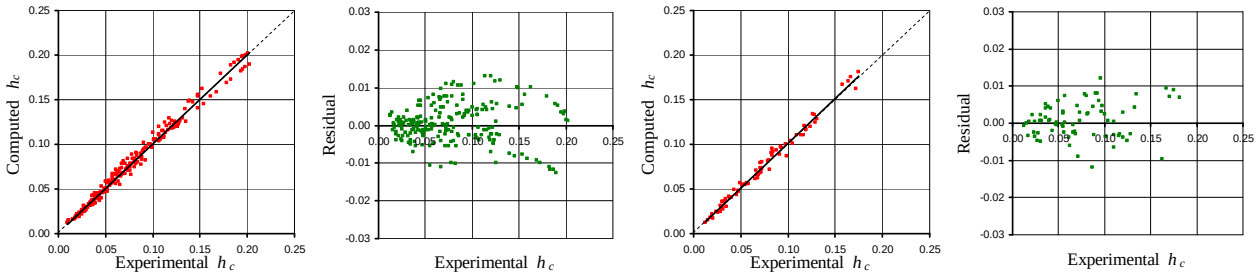

Training data Testing data

Exp. No (4) $h_c = 1.28 h_e e^{1.66\sqrt{S_0}}$

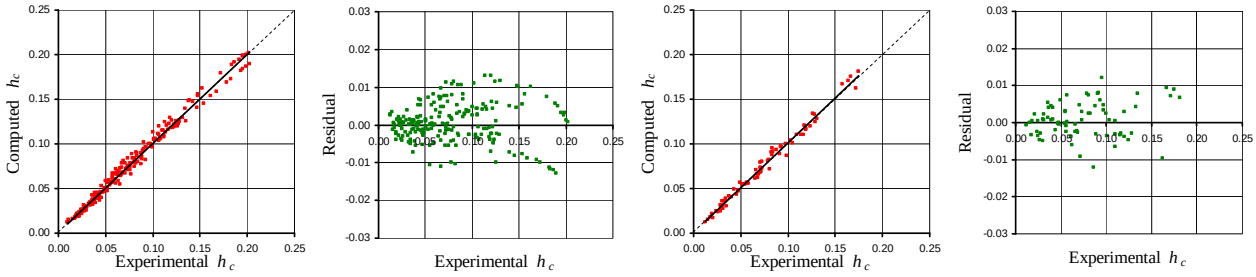

Training data Testing data

Exp. No (2) $h_c = h_e(e^{0.24+S_c+1.67\sqrt{S_0}})$

Figure (6-4): Performance of top 5 expressions on circular training and test data.

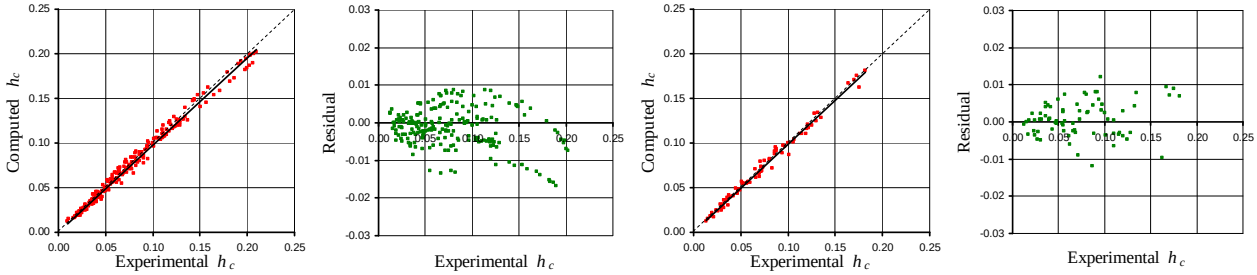

Training data Testing data

Exp. No (8) $h_c = e^D h_e e^{2\sqrt{S_0}}$

Figure (6-4): Continued.

Table (6-5) and Figure (6-4) show that all top 5 expressions fit the data from the training set extremely well, while the statistical performance on the set of the "unseen" test data, demonstrates that overfitting did not occur. This close performance on both sets of training and testing data implies that statistically, none of the expressions has any specific priority over others. Expressions 1, 3 and 4 express the critical depth as a function of end depth and bed slope and its only expression 2 that includes the critical slope. As measuring the critical slope accurately is difficult and requires the knowledge of the critical depth, expression 2 was discarded. Furthermore, although having the best overall performance, expression 1 was also discarded because of its relative complexity. A closer look at the expressions reveals that equations 3, 4 and 8 have the same structure and are only different in their coefficients. As a result, expression 4 ($h_c = 1.28 h_e e^{1.66\sqrt{S_0}}$) was selected as the most suitable model for calculating the critical depth.

6.3.1.3 Modelling validation

In order to validate the selected model, the fitness of the model was tested on another set of unseen data, namely the validation data. Figure (6-5) shows the performance of the selected expression ($h_c = 1.28 h_e e^{1.66\sqrt{S_0}}$) on the validation data. The CoD for this expression is 0.996 and the RMSE is 0.0685. This realistic estimate of future performance shows that the model is reliable and can be used for other cases.

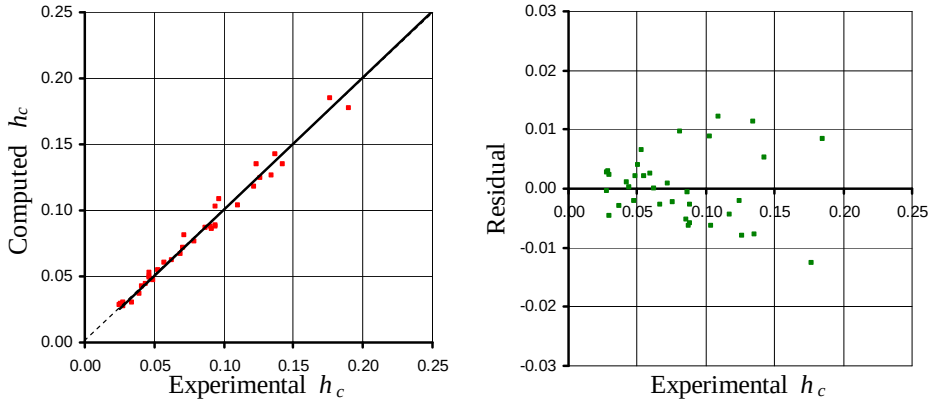

Exp. No (4) $h_c = 1.28 h_e e^{1.66\sqrt{S_0}}$

Figure (6-5): Performance of the selected expression structure on the validation dataset.

6.3.2 Rectangular free overfall

6.3.2.1 Introduction to the datasets

Following the work of Ledoux (1924), Rouse (1932; 1936; 1943) was perhaps the first to realize that the end depth of flow in a rectangular channel could be used as a simple flow measuring device. He started his experiments on a wide range of flat rectangular overfall in Karlsruhe University laboratory in 1932 and continued his research to investigate the effects of bed slope and Froude number on the end depth. Since then, because of its importance and also relatively simple laboratory setup, a large number of theoretical and experimental studies (e.g. Delleur *et al*., 1956; Rajaratnam and Muralidhar, 1968a&b; Ali and Sykes, 1972; Hager, 1983) have been carried out to understand the hydraulics of the end-depth problem and to determine the end-depth ratio ($EDR=h_e/h_c$) in rectangular channels.

Investigating various rectangular channels with different slopes and roughnesses, Delleur *et al*. (1956) found that the end-depth is independent of roughness but dependent on relative slope (S_o/S_c). However, Rajaratnam and Muralidhar, (1968a&b) discovered that the *EDR* in supercritical flow varies with the change of relative slope (S_o/S_c) and Froude number (Fr). Davis *et al*. (1998) undertook a similar experimental study and observed that the *EDR* was influenced by both slope and roughness and that the roughness had more effect at steeper slopes.

After a comprehensive search of the literature, seven different datasets (Rajaratnam and Muralidhar, 1968a&b; 1976; Davis *et al*., 1998; Ferro, 1999; Turan, 2002; Firat, 2004 and Kutlu, 2005) relating to measurements free overfalls in rectangular channels were obtained and integrated to form a database. The entire database consisted of a sub total of 354 individual experiments covering a wide range of rectangular channels with different bed slopes and flow regimes. Table (6-6) shows a summary of these datasets.

Series	Bed width (B) (m)	Bed slope (S_0) (%)	Discharge (Q) (ls^{-1})	End depth (h_e) (m)
Rajaratnam and Muralidhar (1968a&b)	0.46	0.00 ~ 2.88	31.43 ~ 67.32	0.0363 ~ 0.0957
Rajaratnam and Muralidhar (1976)	0.46	0.00 ~ 1.36	12.84 ~ 108.09	0.0183 ~ 0.1751
Davis *et al*. (1998)	0.295	0.30 ~ 0.20	0.44 ~ 14.01	0.0050 ~ 0.0365
Ferro (1999)	0.05 ~ 0.3	0.00	2.10 ~ 30.50	0.0167 ~ 0.0784
Turan (2002)	1.00	0.17 ~ 4.00	12.33 ~ 77.97	0.0101 ~ 0.0581
Firat (2004)	1.00	0.03 ~ 3.94	1.61 ~ 84.12	0.0038 ~ 0.0545
Kutlu (2005)	1.00	0.063 ~ 3.87	1.75 ~ 61.36	0.0046 ~ 0.0503

Table (6-6): Rectangular free overfall datasets.

6.3.2.2 Modelling results

In continuation of the knowledge discovery process undertaken on circular channels, the same modelling methodology was applied to the preprocessed rectangular database and the best suitable models were derived. The terminal set was chosen as {B, h_e, S_0, S_c, $S_0^{0.5}$, $S_c^{0.5}$, random number}. Table (6-7) shows the 5 top expressions after the objective selection and the values of different fitness measures on training and test data. Figure (6-6) illustrates the calculated and measured values of the critical depth along with the residual distributions for these expressions.

No.	Expression	Training data			Test data			Total	
		MRSS ($x10^{-4}$)	RMSE	CoD	MRSS ($x10^{-4}$)	RMSE	CoD	RMSE	CoD
1	$h_c = 1.35 h_e e^{2.05\sqrt{S_0}}$	2.927	0.0890	0.9738	5.203	0.0989	0.9803	0.1879	1.9541
2	$h_c = 1.48 h_e + h_e \sqrt{S_0}$	4.290	0.1230	0.9509	8.351	0.1573	0.9520	0.2803	1.9029
3	$h_c = 1.47 h_e + 0.15 S_0$	4.403	0.1242	0.9443	8.506	0.1386	0.9465	0.2628	1.8908
4	$h_c = 0.48 h_e + h_e e^{\sqrt{S_0}}$	4.208	0.1207	0.9525	8.182	0.1545	0.9538	0.2752	1.9063
5	$h_c = \sqrt{2h_e^2 + h_e S_0}$	3.769	0.1303	0.9580	7.164	0.1238	0.9637	0.2541	1.9217

Table (6-7): Value of MRSS, RMSE and CoD for rectangular training and test data.

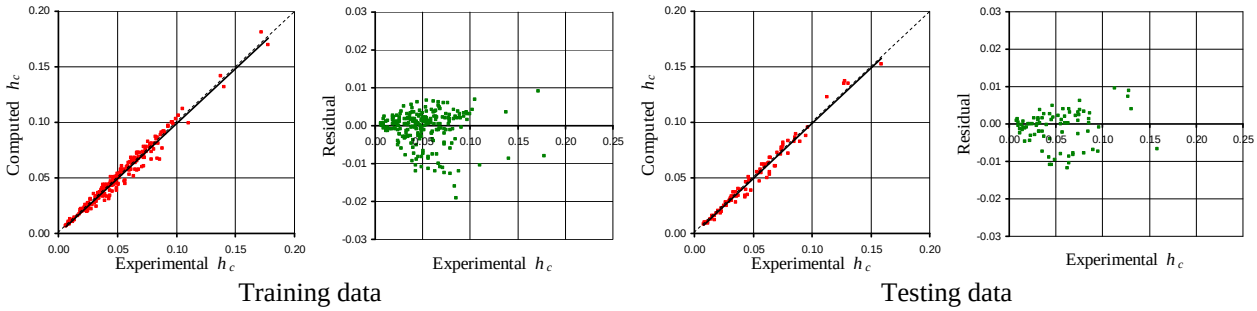

Training data Testing data

Exp. No (1) $h_c = 1.35 h_e e^{2.05\sqrt{S_0}}$

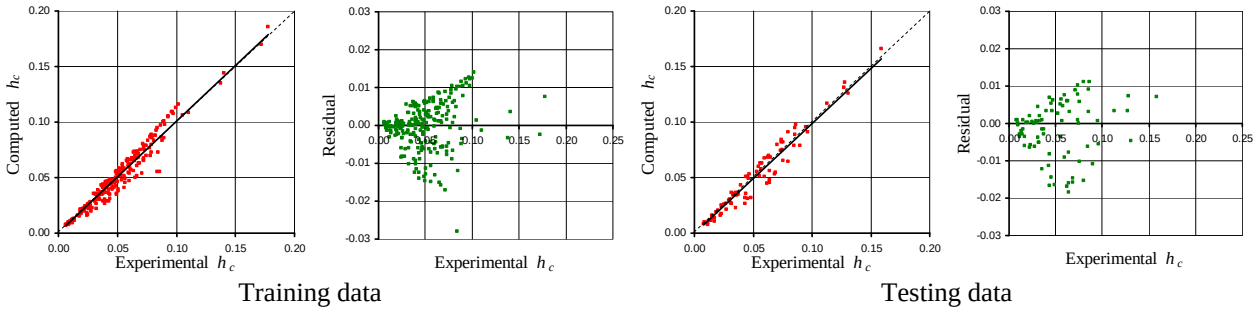

Training data Testing data

Exp. No (2) $h_c = 1.48 h_e + h_e\sqrt{S_0}$

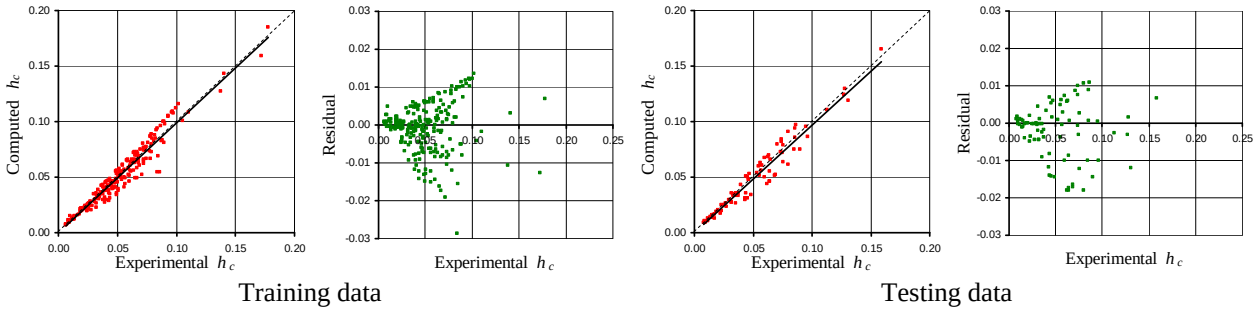

Training data Testing data

Exp. No (3) $h_c = 1.48 h_e + 0.15 S_0$

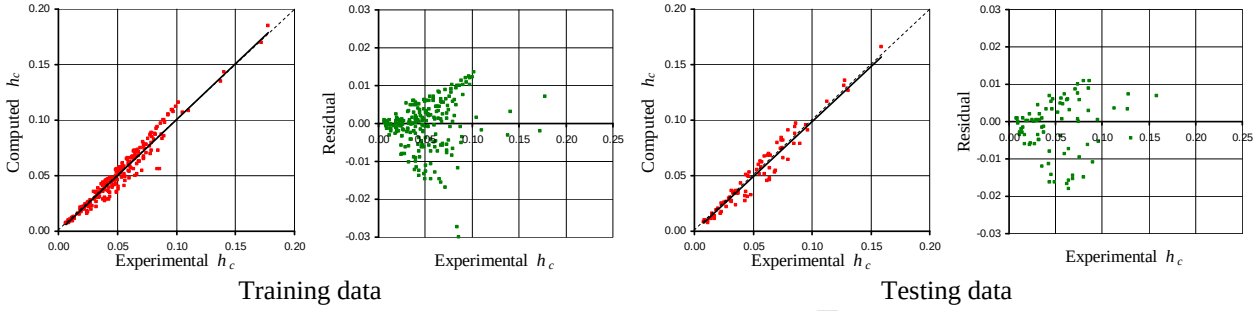

Training data Testing data

Exp. No (4) $h_c = 0.48 h_e + h_e e^{\sqrt{S_0}}$

Figure (6-6): Performance of top 5 expressions on rectangular training and test data.

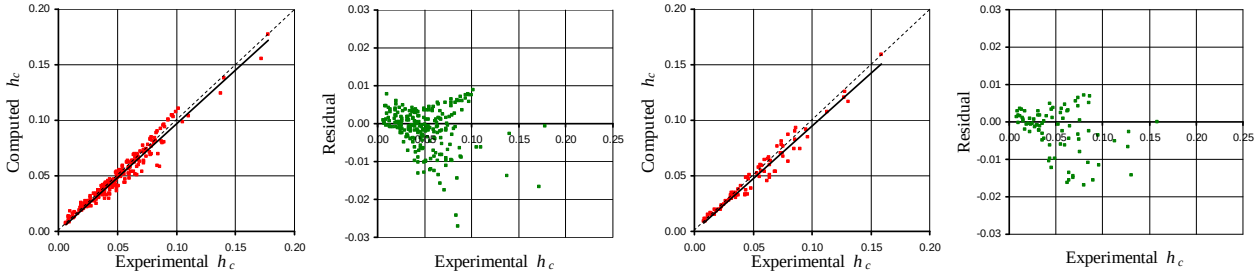

Training data Testing data

Exp. No (5) $h_c = \sqrt{2h_e^2 + h_e S_0}$

Figure (6-6): Continued.

It is interesting to note that in keeping with the above analysis, an expression of the form $h_c = \mathrm{A} h_e e^{\mathrm{B}\sqrt{S_0}}$ is found to be the simplest and most successful model at predicting the critical depth in rectangular free overfalls. In order to investigate the accuracy of this model for individual datasets, a least square regression was performed and the optimum coefficients of the expression were derived for each dataset. Table (6-8) shows the obtained coefficients along with the values of CoD, RMSE and MRSS. It can be seen that except for the dataset of Rajaratnam and Muralidhar (1968a & b), the model is relatively successful in simulating all other datasets. Furthermore, the examination of Tables (6-6) and (6-8) shows no immediate correlation between the coefficient values and available characteristics of the channels and flow.

Series	**A**	**B**	MRSS (x10^{-4})	RMSE	CoD
Rajaratnam and Muralidhar (1968a&b)	1.31	2.55	11.2619	1.4936	0.9156
Rajaratnam and Muralidhar (1976)	1.42	1.63	11.427	0.1030	0.9843
Davis *et al.* (1998)	1.10	2.96	4.4108	0.2424	0.9783
Ferro (1999)	1.33	2.87	1.7660	0.0238	0.9945
Turan (2002)	1.23	3.45	3.8150	0.0364	0.9897
Firat (2004)	1.35	2.46	3.6197	0.1016	0.9641
Kutlu (2005)	1.37	1.42	2.0409	0.0318	0.9923
All Data	1.32	2.31	2.4940	0.1240	0.9742

Table (6-8): The A and B coefficients in $h_c = \mathrm{A} h_e e^{\mathrm{B}\sqrt{S_0}}$, CoD, MRSS and RMSE for rectangular datasets.

6.3.3 Trapezoidal free overfall

6.3.3.1 Introduction to the datasets

Compared with the rectangular overfall, the investigations of the free overfall in channels with a trapezoidal cross section are small in number. The earliest significant study of this problem appears to be that of Diskin (1961). Subsequently, other researchers (e.g. Replogle, 1962; Rajaratnam and Muralidhar, 1970; Ali and Skyes, 1972; Subramanya and Keshavamurthy, 1987; Gupta *et al*., 1993) continued the research and studied the influence of roughness and slope. For example, Rajaratnam and Muralidhar (1970) observed that for the horizontal free overfall, the *EDR* is only a function of a non-dimensional length parameter, sh_c/B, and that the *EDR* increases from 0.705 to 0.758 as sh_c/B increases from 0 to about 9.0. Furthermore, in sloping channels, they found *EDR* to be a function of sh_c/B and the relative slope, S_o/S_c.

Five datasets (Diskin, 1961; Rajaratnam and Muralidhar, 1970; Keller and Fong, 1989; Yuen, 1989; Pagliara and Viti, 1995) relating to measurements in a wide range of trapezoidal free overfalls were derived from the literature. A summary of these data sets is shown in Table (6-9).

Series	Bed width (B) (m)	Side slope (s) 1:s = v:h	Bed slope (S_0) (%)	Discharge (Q) (ls^{-1})	End depth (h_e) (m)
Diskin (1961)	0.125 0.167	1.5 2.0	0.15	8.722 ~ 50.206	0.0399 ~ 0.1052
Rajaratnam and Muralidhar (1970)	0.0127 ~ 0.1016	0.17 ~ 1.00	0.00 ~ 6.73	0.878 ~ 44.288	0.0076 ~ 0.1676
Keller and Fong (1989)	0.150	1.00	0.067	6.130 ~ 23.190	0.0350 ~ 0.0779
Yuen (1989)	0.150 0.450	1.00	0.00 ~ 2.743	1.715 ~ 22.200	0.0144 ~ 0.0440 0.0098 ~ 0.0425
Pagliara and Viti (1995)	0.280 0.300	1.00	0.00 ~ 2.10	1.740 ~ 80.500	0.0100 ~ 0.1150

Table (6-9): Range of trapezoidal free overfall datasets.

6.3.3.2 Modelling results

Following the same modelling procedure as outlined above, the database of trapezoidal free overfall, which consisted of 336 individual experiments, was preprocessed and divided into training, testing and validation subsets. Selecting the GP terminal set as {b, s, h_e, S_0, S_c, $S_0^{0.5}$, $S_c^{0.5}$, random number}, the GP algorithm was run 50 times to generate models on the training

data. The subjective and objective model selection procedures were then performed to find the best models (Table (6-10)). Figure (6-7) illustrates the performance of these models on training and testing subsets. Again, it is observed that an expression of the form $h_c = \mathrm{A} h_e e^{\mathrm{B}\sqrt{S_0}}$ is found as one of the "best" expressions. The only model which can compete with this model in terms of performance is expression number 4 which due to the existence of the critical slope in its structure is an impractical expression. Table (6-11) also the shows the A and B coefficients for each individual dataset, obtained through regression.

No.	Expression	Training data			Test data			Total	
		MRSS ($\times 10^{-4}$)	RMSE	CoD	MRSS ($\times 10^{-4}$)	RMSE	CoD	RMSE	CoD
1	$h_c = 1.354 h_e e^{1.40\sqrt{S_0}}$	6.556	0.0813	0.9796	8.371	0.0785	0.9843	0.1598	1.9639
2	$h_c = 1.431 h_e + 0.280\sqrt{S_0}$	5.875	0.0956	0.9720	18.902	0.0810	0.9740	0.1766	1.946
3	$h_c = h_e + \sqrt{S_c}(\sqrt{h_e} + h_e \times \frac{S_0}{S_c})$	5.661	0.0898	0.9776	9.352	0.0868	0.9714	0.1766	1.949
4	$h_c = 1.419 h_e + 0.132 S_0^{0.75}$	5.770	0.0916	0.9726	8.529	0.0781	0.9755	0.1697	1.9481
5	$h_c = 1.384 h_e + \sqrt{S_0 . S_c}$	5.016	0.1030	0.9792	6.702	0.0803	0.9849	0.1833	1.9641

Table (6-10): Value of MRSS, RMSE and CoD for training and test data.

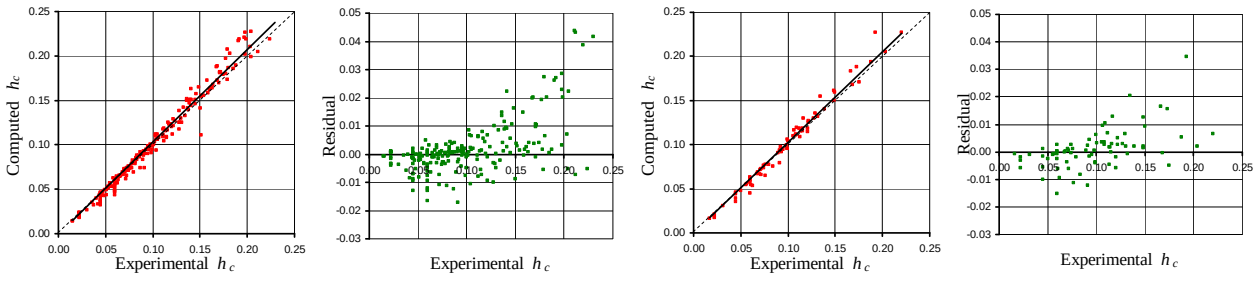

Training data Testing data

Exp. No (1) $h_c = 1.35 h_e e^{1.40\sqrt{S_0}}$

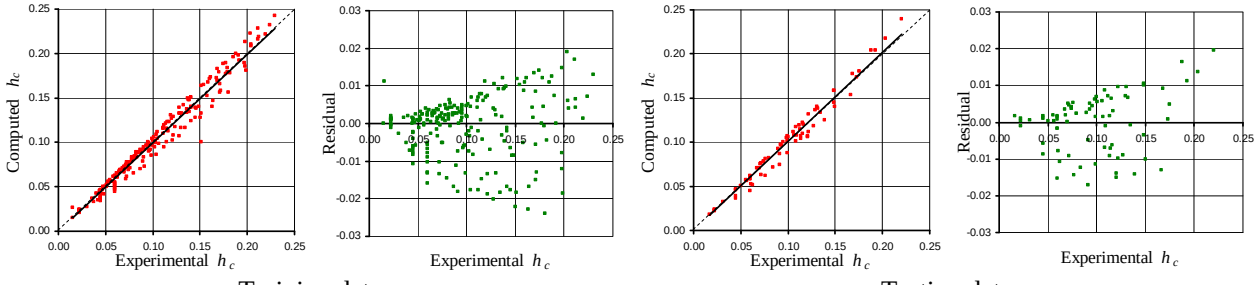

Training data Testing data

Exp. No (2) $h_c = 1.43 h_e + 0.28\sqrt{S_0}$

Figure (6-7): Performance of top 5 expressions on trapezoidal training and test data.

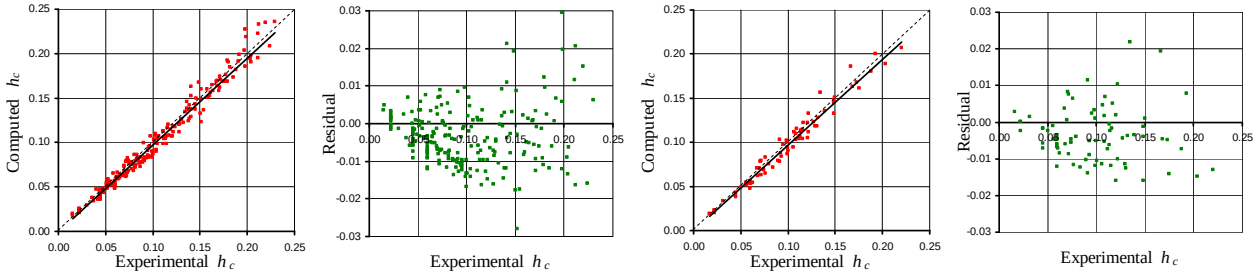

Training data Testing data

Exp. No (3) $h_c = h_e + \sqrt{S_c}\,(\sqrt{h_e} + h_e \times S_0 / S_c)$

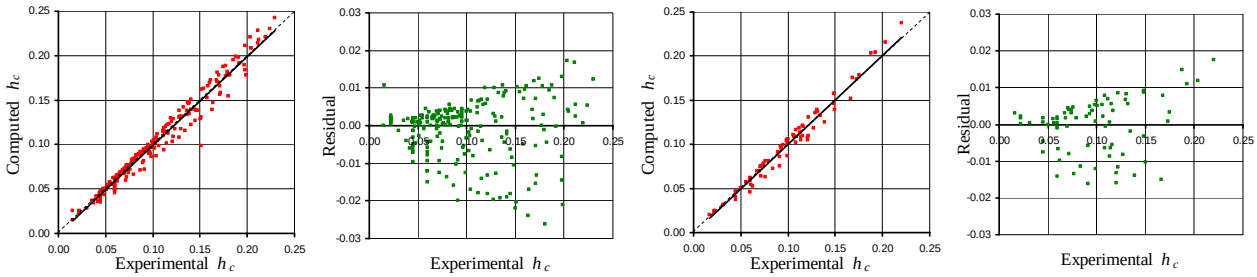

Training data Testing data

Exp. No (4) $h_c = 1.42h_e + 0.13S_0^{0.75}$

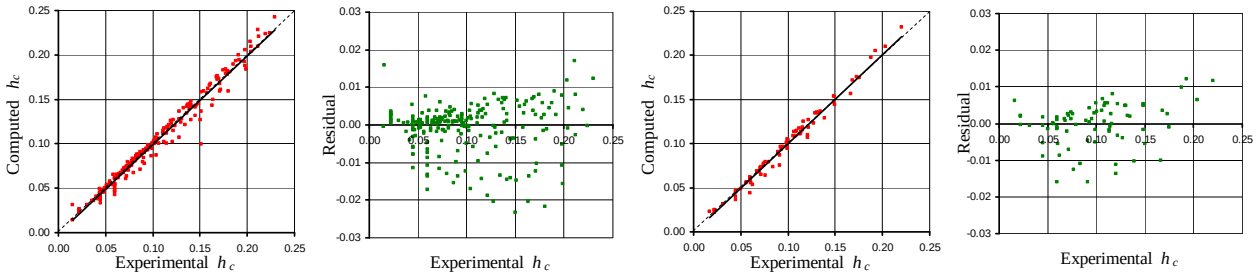

Training data Testing data

Exp. No (5) $h_c = 1.39h_e + \sqrt{S_0.S_c}$

Figure (6-7): Continued.

Series	A	B	MRSS (x10^{-4})	RMSE	CoD
Diskin (1961)	1.30	1.23	3.4089	0.0183	0.9929
Rajaratnam and Muralidhar (1970)	1.34	1.23	7.8027	0.0658	0.9717
Keller and Fong (1989)	1.32	2.00	2.2265	0.0171	0.9886
Yuen (1989)	1.25	3.11	3.8655	0.0623	0.9668
Pagliara and Viti (1995)	1.37	2.14	3.3729	0.0309	0.9971

Table (6-11): The A and B coefficients in $h_c = \mathrm{A}h_e e^{\mathrm{B}\sqrt{S_0}}$, Cod, RMSE and RMSE for trapezoidal datasets.

6.3.4 Channels with other cross sectional shapes

Compared to the studies of rectangular and trapezoidal free overfall, investigations of the free overfall in other channels are relatively few. Circular (Smith, 1962 and Rajaratnam and

Muralidhar, 1964a) parabolic and triangular (Diskin, 1961 Rajaratnam and Muralidhar, 1964b), egg-shaped (Biggiero, 1963 cited in Dey, 2002b), elliptic (Dey, 2001b), inverted semicircular (Dey, 2001c; Dey *et al*., 2004), U-shaped (Dey, 2003; 2005) and Δ-shaped (Dey and Kumar, 2002) channels are among the cross-sections which have been investigated.

The available experimental data relating to some of the mentioned channels (circular, inverted semi-circular, Δ-shaped, U-shaped and triangular) were extracted from earlier studies reported in the literature. Figure (6-8) illustrates the geometry of these cross-sections and Table (6-12) shows a summary of the datasets. The lack of sufficient data points in each set prevented accurate modelling using the methods outlined above. Hence, only the goodness of fit of the expression of the form $h_c = \mathrm{A} h_e e^{\mathrm{B}\sqrt{S_0}}$ was investigated. Table (6-13) shows the obtained optimum values of A and B coefficients (found through a least square regression) and the CoD and RMSE values for each data set. Furthermore, Figure (6-9) illustrates the calculated and measured values of the critical depth along with the residual distribution. Analyzing the results, it can be concluded that this expression is also suitable for channels with cross-sections other than circular, rectangular and trapezoidal.

Comparing Tables (6-5, 6-8 & 6-11) it is observed that the obtained "A" coefficient for all examined datasets lies in the range of 1.23 to 1.37 with only two exceptions being Rajaratnam and Muralidhar (1976) (A=1.42) and Davis *et al*. (1998) (A=1.1). This implies that the value of this coefficient might be independent of channel geometry and flow conditions and thus considering an average value of 1.30 for this coefficient for any cross-section will be a rational assumption.

Series	**Cross-section**	Length parameter (m)	Bed slope (S_0) (%)	Discharge (Q) ($l.s^{-1}$)	End depth (h_e) (m)
Smith (1962)	Circular	D: 0.1532	0.00	1.048~18.916	0.0210~0.1125
Rajaratnam and Muralidhar (1964)	Circular	D: 0.2032	0.00 ~ 5.53	1.019~28.147	0.0192~0.1040
Dey and Ravi Kumar (2002)	Δ-shaped	B: 0.12 ~ 0.18	0.00	0.787~17.824	0.0087~0.0740
Dey (2003)	U-Shaped	D: 0.07 ~ 0.13	0.00	0.729~0.73665	0.0221~0.2287
Dey *et al*. (2004)	Inverted semi-circular	D: 0.043 ~ 0.128	0.00 ~ 2.70	0.037~2.179	0.0029~0.0225
Ahmad (2006)	Triangular	s: 1	0.00 ~ 3.33	0.970~14.570	0.0370~0.1350

Table (6-12): Free overfall datasets in channels with other cross-sections.

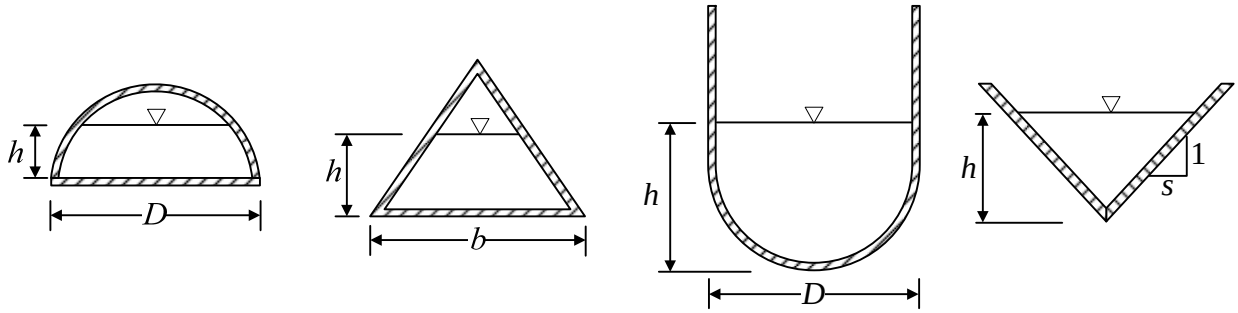

a) Inverted semi-circular b) Δ-shaped c) U-Shaped d) Triangular

Figure (6-8): Cross-section of other channels.

Series	**Cross-section**	**A**	**B**	CoD	RMSE
Smith (1962)	Circular	1.23	2.46	0.9839	0.0491
Rajaratnam and Muralidhar (1964)	Circular	1.38	1.71	0.9928	0.0057
Dey and Ravi Kumar (2002)	Δ-shaped	1.43	2.46	0.9983	0.0160
Dey (2003)	U-Shaped	1.38	2.46	0.9975	0.0318
Dey *et al*. (2004)	Inverted semi-circular	1.41	1.29	0.9839	0.0449
Ahmad (2006)	Triangular	1.19	1.15	0.9819	0.0412

Table (6-13): Performance of $h_c = \mathrm{A}h_e e^{\mathrm{B}\sqrt{S_0}}$ on other cross-sections.

6.3.5 Discussion

Finding a global expression for predicting the critical depth in channels with different cross sections and flow regimes, two separate analyses were performed to both verify the selected "best" expression and also investigate the underlying state of the expression's coefficients. First, using the Buckingham Pi theorem, a dimensional analysis was performed to investigate the general form of the relationship between the end-depth and critical depth. Then, a Principal Component Analysis (PCA) was performed on the available attributes of different datasets to define the principal variables of the problem. Furthermore, the performance of the obtained expression was compared to those of a number of proposed equations in the literature and an error analysis was done to find the maximum errors in predicting the discharge with using this equation.

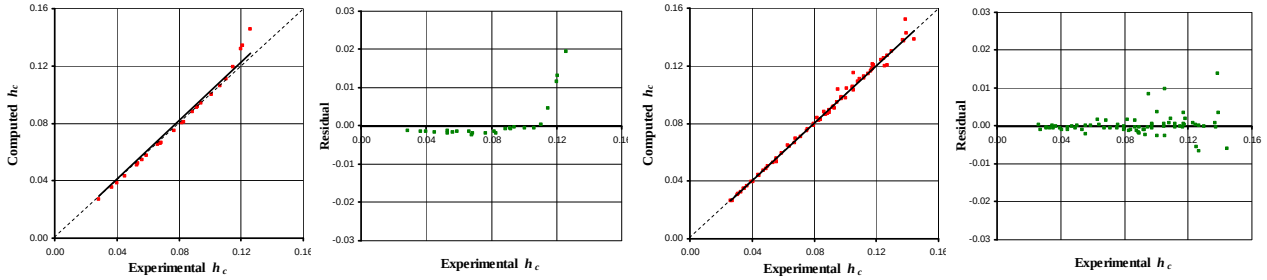

a) Circular (Smith, 1962)

b) Circular (Rajaratnam and Muralidhar, 1964)

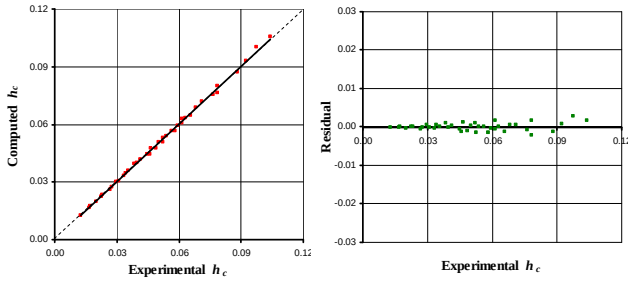

c) Δ-shaped (Dey and Kumar, 2002)

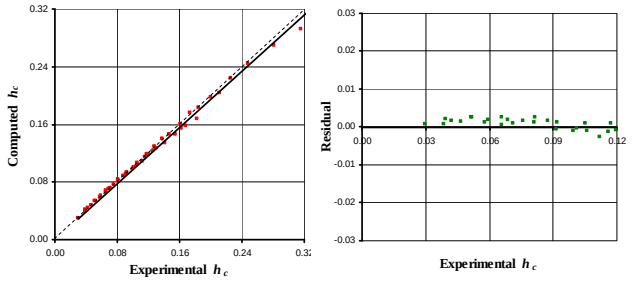

d) U-Shaped (Dey, 2003)

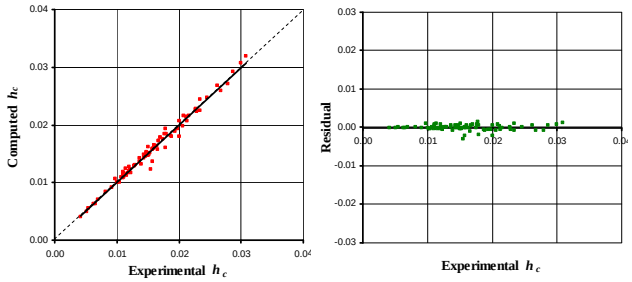

e) Inverted semi-circular (Dey *et al*., 2004)

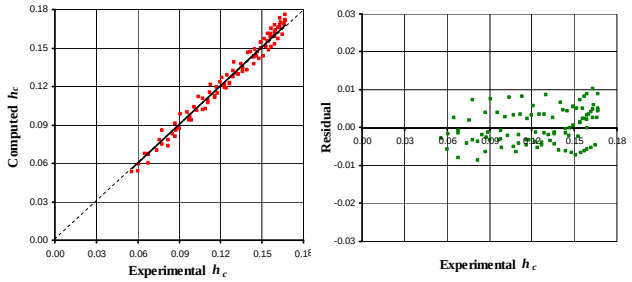

f) Triangular (Ahmad, 2006)

Figure (6-9): Performance of $h_c = \mathrm{A}h_e e^{\mathrm{B}\sqrt{S_0}}$ on other datasets.

6.3.5.1 Dimensional analysis

Dimensional analysis is a powerful tool for simplifying equations as well as clarifying the scaling behaviour of a system. In his Pi theorem, Buckingham (1914) showed that the original dimensional variables of a problem can be reconstructed into a set of dimensionless products using the constraints imposed upon them by their dimensions. According to this theorem, the original relationship between n variables represented by $f(x_1, x_2, ..., x_n) = 0$, can be transformed into a new function $\phi(\pi_1, \pi_2, ..., \pi_n)$ of n-m independent dimensionless

products (π_j) of the original variables (x_i). Here, m is the total number of fundamental dimensions of the original physical variables.

The dimensional analysis of the free overfall problem in different channels has been previously investigated by different researchers (e.g. Ferro, 2004; Firat, 2004). A similar dimensional analysis was performed to investigate the general form of the relationship between the end-depth and critical depth in rectangular free overfalls. Table (6-14) shows the variables which are thought to affect the behaviour of the flow at a free overfall. Therefore, a relationship in the form of $f(h_e, h_n, B, S_0, q, g, \mu, \rho, n) = 0$ can be considered for a free overfall.

Applying the Buckingham Pi technique, with q, h_n and ρ as the repeating variables, 6 dimensionless parameters were obtained:

$$\pi_1 = h_e / h_n,\ \pi_2 = B / h_n,\ \pi_3 = S_0, \pi_4 = n, \pi_5 = g h_n^3 / q^2 = \mathrm{Fr}^2, \pi_6 = \mu / q\rho = 1/\mathrm{Re} \quad (6\text{-}1)$$

Combining π_1 and π_5 a new dimensionless parameter can be formed:

$$\pi_7 = \pi_1 \times \pi_5^{1/3} = \frac{h_e}{h_n} \times \frac{h_n g^{1/3}}{q^{2/3}} = \frac{h_e}{\sqrt[3]{q^2/g}} = \frac{h_e}{h_c} \quad (6\text{-}2)$$

Substituting the simplified parameters, it can be concluded that:

$$EDR = \frac{h_e}{h_c} = f(l/h_n, S_0, n, \mathrm{Fr}, \mathrm{Re}) \quad (6\text{-}3)$$

This dimensional analysis implies that to be able to build an accurate model for predicting the critical depth or the end-depth ratio, in addition to the cross-section geometry, data regarding the uniform depth, channel roughness, Froude and Reynolds numbers should also be available.

Variable	***Symbol***	***Dimension***
End depth	h_e	L
Uniform flow depth	h_n	L
Channel width	B	L
Bed slope	S_0	-
Unit discharge	q	$L^3/T/L$
Gravitational acceleration	g	L/T^2
Dynamic viscosity	μ	M/LT
Density of water	ρ	M/L^3
Manning roughness parameter	n	-

Table (6-14): Variables affecting the behaviour of the free overfall

6.3.5.2 Dimensional reduction based on principal component analysis

Principal component analysis (PCA) (Johnson and Wichern, 1988) is an eigenvector-based multivariate analysis that produces a new set of variables (principal components) from the linear combination of the original variables. The first principal component tends to account for as a large degree of variability in the data as possible, while the second component accounts for less than the first but more than the third and so on. The goal of PCA is to identify the smallest number of components which can be used to summarize the data without a significant loss in information. In general, the number of principal components is equal to the number of original variables; however, for most of the datasets, the first few principal components account for most of the variance (as long as there is at least one dominant structure within the data). As a result, the rest of the principal components can be ignored with the minimal loss of information (for more details on PCA see Appendix (V))

Mardia *et al*. (1979) introduced a procedure for discarding redundant variables and selecting principal variables using principal component analysis. In this approach, the important characteristics (variables) of the dataset that contribute most to its variance are retained by ignoring the dominant variables of less important components. This variable elimination process can be summarized as follows:

1- First, the matrix of the normalized independent variables is formed.
2- The PCA is then applied to the normalized data and the variance explained by each of the corresponding principal components is calculated (see Figure (6-10)). Based on the results, the number of sufficient components for describing most of the variations (e.g. 90%) in the dataset is found.
3- The eigenvalue vector and the principal component coefficient matrix for the principal components are derived from PCA.
4- The coefficient matrix is searched and the variable that has the largest absolute coefficient value (most dominant variable) for the component with the smallest eigenvalue (least important component) is found and eliminated from the entire variable set.
5- PCA is again performed on the remaining variables and steps 3 to 5 are repeated.

6- This elimination process continues until the number of sufficient components (defined in step 2) remains. The remaining variables are the principal variables.

This method was implemented on the data set of rectangular, trapezoidal, and flat bed circular free overfall to obtain the principal variables. For rectangular channels, the set of variables was selected as $\{B, h_e, (h_e / B), S_0, S_c, \sqrt{S_0}, \sqrt{S_c}, (S_0 / S_c), \sqrt{(S_0 / S_c)}\}$. The PCA was then applied to the normalized variable matrix to determine the variance explained by each of the 9 components (Figure (6-10)). Based on this Figure, it can be argued that at least four principal components are required to describe more than 90% of the variability in the data. However, the first two components have an important role since they contain more than the 80% of the variability in the whole data set.

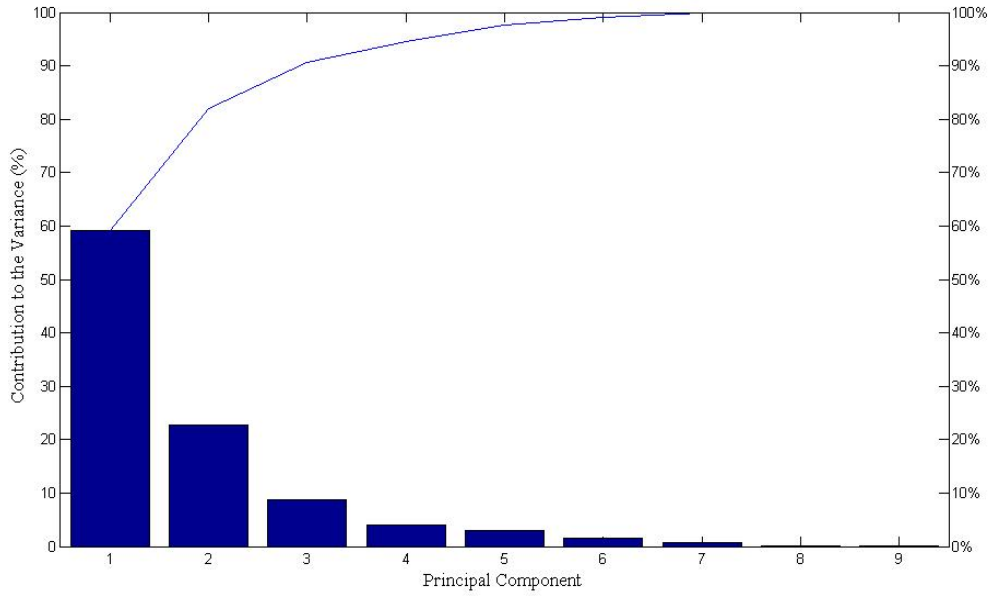

Figure (6-10): The percentage of total variability described by each principal component.

By visualizing the PCA results, it would be possible to analyze the role of each variable in the formation of the principal components. Figure (6-11) shows such a plot for the first two principal components. In this figure the lines indicate the effect of each of the original variables on the first and second principal component (principal components coefficients) and the dots show the locations of the mapped data in the surface of the first two principal components. Each of the nine original variables is represented by a vector. The length and

the direction of these vectors can indicate how the variables contribute in each of the principal components. For instance, it can be shown that the square root of the bed slope, $\sqrt{S_0}$, has the highest contribution in the formation of the first principal component while the channel bed width, *B*, has a major role in the formation of the second principal component. It is also observed that the vectors representing the variables and their square root (e.g. $S_c, \sqrt{S_c}$) overlap, which indicates the high correlation among these attributes. By considering such a plot for the last two principal components (the least important principal components), it would be possible to eliminate the variable that has the largest absolute principal components coefficients regarding the less important component.

Table (6-15) shows the principal component coefficient matrix for the principal components. It can be observed that the dominant variable for the last principal component is $\sqrt{(S_0 / S_c)}$. Removing this variable and continuing the elimination process for the reduced variable matrix, $B, h_e, \sqrt{S_0}, \sqrt{S_c}$ were found as the principal variables. Implementing the same procedure for trapezoidal and flat bed circular channels, $s, B, h_e, \sqrt{S_0}$ and $h_e, t.h_e / D, S_0, S_c$ were found as the principal variables, respectively. The results of this analysis verify the presence of h_e and $\sqrt{S_0}$ in the structure of the "best" expression and indicate that the two coefficients should be highly correlated with the geometry of the channel. It should be noted that this analysis was performed only on the available attributes of the datasets, and that the results could have been different if other variables (e.g. friction, Froude and Reynolds) were included. A more descriptive explanation of this elimination procedure is provided in Appendix (V.3).

variable	*Principal component*								
	I	***II***	***III***	***IV***	***V***	***VI***	***VII***	***VIII***	***IX***
B	-0.52	-0.75	-0.22	-0.26	-0.05	0.19	-0.07	0.02	-0.01
h_e	0.17	0.04	0.29	-0.86	-0.24	-0.29	0.00	-0.02	0.02
h_e/B	0.15	0.15	0.15	-0.24	0.08	0.91	0.20	0.05	-0.06
S_0	-0.48	0.35	0.29	0.02	-0.17	0.14	-0.67	0.22	0.13
S_c	0.02	-0.25	0.52	0.10	0.32	-0.13	0.09	0.61	-0.40
$\sqrt{S_0}$	-0.56	0.23	0.24	0.10	-0.33	-0.06	0.57	-0.22	-0.28
$\sqrt{S_c}$	0.05	-0.30	0.65	0.18	0.15	0.03	-0.01	-0.49	0.44
S_0 / S_c	-0.18	0.17	-0.05	-0.20	0.65	-0.05	-0.22	-0.47	-0.45
$\sqrt{S_0 / S_c}$	-0.32	0.23	-0.12	-0.19	0.50	-0.12	0.34	0.28	0.58

Table (6-15): Principal component coefficient matrix for rectangular free overfall data.

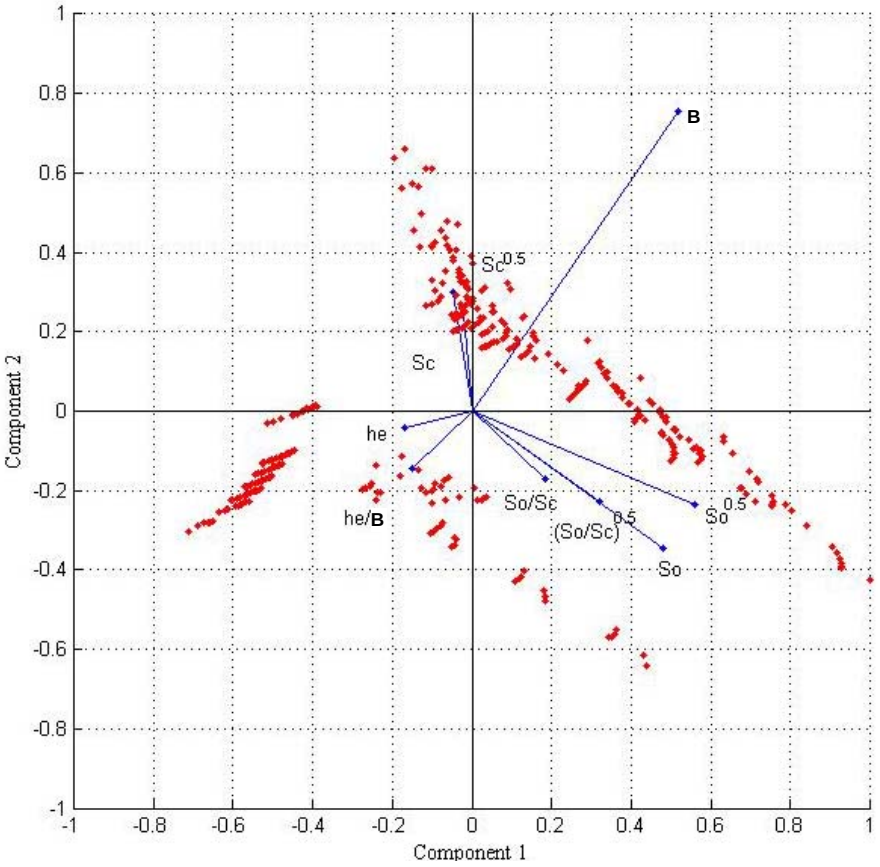

Figure (6-11): Visualization of the principal component coefficient matrix for the first two principal components.

6.3.5.3 Performance comparison

A number of expressions have been previously proposed by researchers for the prediction of the *EDR* in different channel sections (see Table (2-3)). Most of these expressions are derived for a particular bed slope and describe the *EDR* as a constant value (linear relationship between the h_e and the h_c) and hence, not applicable to all channels. However, there are a few more complex equations which relate the *EDR* to different parameters of the channel and flow and are more suitable for comparison.

Table (6-16) compares the obtained RMSE and CoD of $h_c = \mathrm{A} h_e e^{\mathrm{B}\sqrt{S_0}}$ with the equation proposed by Davis *et al*., (1998) on different rectangular free overfalls. Table (6-17) also shows the comparison of the performance of the proposed equation with Pagliara's (1995) equation for trapezoidal free overfalls. It can be seen that $h_c = \mathrm{A} h_e e^{\mathrm{B}\sqrt{S_0}}$ outperforms both equations for all datasets.

Series	$h_c = \mathrm{A} h_e e^{\mathrm{B}\sqrt{S_0}}$		$h_c = h_e / (0.77 - 2.05 S_0^{0.5})$	
	RMSE	CoD	RMSE	CoD
Rajaratnam and Muralidhar (1968a&b)	1.4936	0.9156	1.5233	0.7494
Rajaratnam and Muralidhar (1976)	0.1030	0.9843	0.1445	0.9333
Davis *et al*. (1998)	0.2424	0.9783	0.3559	0.9758
Ferro (1999)	0.0238	0.9945	0.0324	0.9945
Turan (2002)	0.0364	0.9897	0.0663	0.9822
Firat (2004)	0.1016	0.9641	0.1468	0.9523
Kutlu (2005)	0.0318	0.9923	0.1912	0.8909
All Data	0.1240	0.9742	0.1625	0.9513

Table (6-16): Comparison of the performance of the obtained expression with the equation proposed by Davis *et al.*, (1998) for rectangular datasets.

Series	$h_c = \mathrm{A} h_e e^{\mathrm{B}\sqrt{S_0}}$		$h_c = h_e / (0.705 + 0.029(m h_e / B))$	
	RMSE	CoD	RMSE	CoD
Diskin (1961)	0.0183	0.9929	0.0219	0.9876
Rajaratnam and Muralidhar (1970)	0.0658	0.9717	0.1741	0.8799
Keller and Fong (1989)	0.0171	0.9886	0.0106	0.9887
Yuen (1989)	0.0623	0.9668	0.2067	0.7965
Pagliara and Viti (1995)	0.0309	0.9971	0.1460	0.8972

Table (6-17): Comparison of the performance of the obtained expression with the equation proposed by Pagliara, (1995) for trapezoidal datasets.

6.3.5.4 The free overfall as a measuring device

The main aim of this chapter was to establish a definite relationship between the critical depth, h_c, and the end depth, h_e. Applying GP, an equation in the form of $h_c = \mathrm{A} h_e e^{\mathrm{B}\sqrt{S_0}}$ was found as a rigorous relationship which is valid in different channels and flow regimes. In this subsection, the effect that the variation of the calculated value of h_c has upon the discharge will be examined.

Rectangular channels

The critical depth can be evaluated using:

$$\frac{Q^2}{g} = \frac{A^3}{T} \tag{6-4}$$

which for a rectangular channel yields:

$$Q = \sqrt{gB^2 h_c} = g^{1/2} B h_c^{3/2} \tag{6-5}$$

hence:

$$dQ = 1.5 g^{1/2} B h_c^{1/2} dh_c \tag{6-6}$$

$$\frac{dQ}{Q} = \frac{1.5 g^{1/2} B h_c^{1/2} dh_c}{g^{1/2} B h_c^{3/2}} = 1.5 \frac{dh_c}{h_c} \tag{6-7}$$

For small percentages of error in the calculation of h_c, (dh_c / h_c), Eq. (6-7) can be used as an alternative to the direct calculation of error, to approximate the error in estimating the discharge. This equation implies that an error of x% in the estimation of h_c, results in a corresponding error of 1.5x% in the discharge. In the previous subsections, it was shown that the values of the "A" and "B" coefficients are related to the geometry of the channel and flow parameters, which cannot be identified in this stage of research. However, if proper constants values are chosen for the more reliable datasets (see Table (6.8)), the critical depth can be estimated with 5% of error. This yields a maximum error of about 7.5% for the discharge.

Trapezoidal channels

In the critical section of a trapezoidal channel, the discharge can be found by:

$$\frac{Q^2}{g} = \frac{A^3}{T} \quad \rightarrow Q^2 = g A^3 T^{-1} \tag{6-8}$$

where

$$A = (B + sh_c)h_c \text{ and } A' = B + 2sh_c = T \tag{6-9}$$

$$T = (B + 2sh_c) \text{ and } T' = 2s \tag{6-10}$$

Differentiating both sides of Eq. (6-8) yields:

$$2QdQ = g(3A'A^2T^{-1} - T'T^{-2}A^3)dh_c \tag{6-11}$$

$$\frac{dQ}{Q} = \frac{g(3A'A^2T^{-1} - T'T^{-2}A^3)dh_c}{2gA^3T^{-1}} \tag{6-12}$$

$$\frac{dQ}{Q} = \frac{1}{2}(\frac{3A'}{A} - \frac{T'}{T})dh_c \tag{6-13}$$

substituting Eqs. (6-9 & 6-10) in Eq. (6-13) and rearranging gives:

$$\frac{dQ}{Q} = \frac{1}{2}[\frac{3(B + 2sh_c)}{(B + 2h_c)h_c} - \frac{2s}{(B + 2sh_c)}]dh_c \tag{6-14}$$

$$\frac{dQ}{Q} = \frac{1}{2}[\frac{3(B + 2sh_c)}{(B + 2h_c)} - \frac{2s}{(B/h_c + 2s)}]\frac{dh_c}{h_c} \tag{6-15}$$

As it can be seen from Eq. (6-15), a totally different form of relationship between the error in critical depth and the error in discharge is found. This equation is implicit and implies that the range of the bed width, wall slope and the value of the critical depth itself influence the calculated error in discharge. Applying Eq. (6-15) to the range of the trapezoidal datasets (Table (6-9)) used in this research, it can be concluded that x% error in the estimation of h_c, would result in a maximum error of approximately 1.61x% in the discharge. Using $h_c = \mathrm{A}h_e e^{\mathrm{B}\sqrt{S_0}}$ with appropriate coefficients for the more reliable datasets results in approximating the critical depth with 6% error. Consequently, the error in the estimated discharge would be less than 10%.

Circular channels

Applying a similar analysis, the maximum error in estimating the discharge for circular channels is found to be less than 10%. The error analysis calculation for circular channels is available in Sterling (1998).

6.4 SUMMARY

In this chapter, Genetic Programming was used as a powerful knowledge discovery tool for solving a classic problem in open channel flow. Applying this tool and following a two-stage model selection procedure, a global transparent model in the form of $h_c = \mathrm{A} h_e e^{\mathrm{B}\sqrt{S_0}}$ (or $EDR = h_e / h_c = (1/\mathrm{A}) e^{-\mathrm{B}\sqrt{S_0}}$) was found as the most suitable and applicable expression for predicting critical depth and *EDR* in a wide range of channels. In addition to being dimensionally correct (Sharifi *et al.*, 2009b), this expression appears to be universal and can be applied to all common cross-section channel shapes and different flow regimes (subcritical and supercritical). Furthermore, its overall performance is better than any other proposed empirical relationship.

The knowledge discovery process by means of the Genetic Programming technique has brought us a step nearer to a better understanding of the free overfall problem. Although, the correct values of the two coefficients within the expression ($h_c = \mathrm{A} h_e e^{\mathrm{B}\sqrt{S_0}}$) still remain unknown, this equation can be confidently used after a simple calibration. At this stage, and based on the available measurements, not much can be said about these coefficients. In order to discover rules for defining these coefficients, which were shown to be related to the channel geometry, roughness, uniform depth Froude and Reynolds numbers, more experimental work is needed on various different channels.

CHAPTER 7

CONCLUSIONS

7.1 REVIEW OF MAIN GOALS

This thesis investigated the application of two Evolutionary Computation techniques to two different aspects of open channel flow:

- NSGA-II was used to build a three-phase calibration framework for the SKM. Measured data from various sources were used in conjunction with the framework to calibrate the SKM for inbank flows in open channels with simple rectangular and trapezoidal cross sections (Sections 5.2 & 5.3). In addition, the method has also been applied to a variety of natural river cross sections (Section 5.4). Finally, in the light of the calibration result, the lateral variations of optimal parameter values of f, λ and Γ were investigated.

- Genetic programming was used as an effective data mining tool to build a model induction methodology for knowledge discovery. The methodology was applied to various laboratory data and a conceptual global model for the physical process of the free overfall problem was obtained.

The results showed that Evolutionary Computation techniques can be applied effectively to the above. Furthermore, a clear advantage of using these techniques as opposed to classical methods was illustrated in both applications. The summary of the conclusions of this research are outlined below.

7.2 MULTI-OBJECTIVE CALIBRATION OF THE SKM FOR INBANK FLOW

7.2.1 General remarks

1- It has been shown that the multi-objective evolutionary algorithm implemented (NSGA-II) is a powerful tool for detailed critical analysis of lumped parameters within a RANS-based model, in supporting a considerably difficult model calibration problem (Chapters 4 and 5).

2- The methodology explained in this thesis can be used for addressing the calibration of other similar models in the field of hydroinformatics.

3- The calibration results revealed that SKM suffers from lack of identifiability and that various parameters sets can produce equally accepted outputs (Sections 4.4.6.3 and 4.5).

4- The application of simultaneous competing objective functions were found to be effective in reducing the uncertainty in parameter estimation (Section 4.4.1).

5- Being thoroughly tested on a variety of channels and rivers with inbank flow, the SKM was shown to be able to accurately predict the lateral distributions of depth-averaged velocity and boundary shear stress, as well as the overall discharge and $\%SF_w$ with the minimum of computational effort (Chapter 5 and Appendix IV).

6- The superiority of the proposed calibration framework over previous calibration approaches for the SKM was shown by comparing the predictions of mean velocity and boundary shear stress distribution using the calibrated parameter values (Section 5.5.1).

7- Guidance has been given relating to the trend and values of the three calibration coefficients, f, λ and Γ in each panel for rectangular and trapezoidal channels. The results will enable the user to both understand how these parameters interact and to model inbank flow for such geometries.

8- The panelling philosophy of Knight and co-workers (Knight *et al*., 2007) was shown to be acceptable for both smooth and rough trapezoidal channels.

9- Based on the available datasets, a two panel structure (allocating 80% of half the symmetric channel width to the first panel and the remaining 20% to the second panel) was found to be the most suitable panel structure for modelling flows in rectangular

channels (Section 5.3). This is in contrast with the modelling philosophies of Omran (2005) and Chlebeck (2009) which suggest 4 or 6 panels for half of the symmetric channel.

10- The SKM was shown to be capable of modelling flows in rivers with different roughnesses by adopting an 8 panel structure for the cross-section (see Section 5.4 and Appendix IV.5).

11- The values of the friction factor were found to be less dependent on the panel structure, while the depth-averaged lumped values of λ and Γ were highly affected by the panel structure. This might be due to the fact that these lumped parameters lose some degree of physical interpretation when averaged over time and depth and hence become dependent on the size and position of the panels.

7.2.2 Lateral variation of the friction factor

12- The value of the friction factor in shallower regions of channels and rivers was found to be higher than its value in deeper regions (Figures (5-4a), (5-10a) and (5-33a)).

13- For the same channel geometry and bed slope, the increase in the mean depth causes the values of the local friction to decrease (Figures (5-4b), (IV-10b), (IV-18b), (IV-24b), (5-17), (5-32a). This finding was justified by the Colebrook-White equation (Eq. 2.87) (Section 5.5.2).

14- Using laterally varied friction factor values within the model (see Section 5.2.2.2), was shown to result in smoother predictions of the shear stress distribution.

15- For smooth trapezoidal channels with aspect ratios between 7.5 and 30 (FCF Series 04 dataset), the friction factor linearly increases from the first to the third panel, then appears to remain constant or reduce before increasing to its highest value in the fifth panel (Figure (5-4a)).

16- For smooth trapezoidal channels with aspect ratios between 1.0 and 5.26 (Yuen's dataset), the friction factor increases almost linearly from the centerline of the channel towards the wall (Figure (5-10a)).

17- In smooth trapezoidal channels the value of the zonal friction factor in each panel was shown to increase with increase in the wetted perimeter ratio, P_b/P_w (Figures (5-4b), (IV-10b), (IV-18b) & (IV-24b)).

18- For differentially roughened trapezoidal channels, the value of the friction factor in the second bed panel, f_2, was slightly lower than in the first panel, f_1. In the rough wall region the value of f increases significantly from the bed-wall intersection, f_3, to its maximum at the channel edge, f_4 (Figures (5-17a) & (5-17b)).

19- In differentially roughened trapezoidal channels the values of the friction factors in the sloping sidewall region panels, f_3 and f_4, increase with an increase in the wetted perimeter ratio (Figures (5-17a) & (5-17b))

20- Generally, in the flat bed region of differentially and uniformly roughened trapezoidal channels, for same aspect ratios, larger values of f_1 and f_2 are found for channels with rougher walls. As the aspect ratio increases, the difference between the values of f_1 and f_2 in both types of channels decreases.

21- For uniformly roughened channels the friction factor in all panels were found to increase almost linearly with the increase in the wetted perimeter ratio, with an exception in the last panel where the friction factor remains more or less constant. (Figure (5-17c & d)).

22- The results of modelling a river section with different inbank depths revealed that the lateral variation of friction follows a similar trend for all depths (Figure (5-33)).

7.2.3 Lateral variation of the dimensionless eddy viscosity

23- In smooth trapezoidal channels, the value of the dimensionless eddy viscosity does not appear to follow any specific pattern in the panels positioned in the constant depth region (Figures (5-4c) & (5-10b)). This implies the insensitivity of the SKM to this parameter in this region. As the bed slope increases, the model becomes more sensitive to the value of this parameter in this region. A general value of 0.6 for this parameter was found to result in acceptable model predictions.

24- In the panels located on the sidewall region of smooth trapezoidal channels, the value of λ increases significantly as the wall is approached (Figures (5-4c) & (5-10b)).

25- In smooth trapezoidal channels, the values of λ increase linearly with the increase in the wetted perimeter ratio, P_b/P_w (Figures (5-4d), (IV-10d), (IV-18d) & (IV-24d)).

26- In partially roughened trapezoidal channels, the optimum values found for λ in the smooth bed region of channels are scattered. This implies that the model is not sensitive to λ in these smooth regions. On the other hand, the model is found to be very sensitive to the value of λ in the third and fourth panels.

27- In homogeneously roughened channels, the zonal dimensionless eddy viscosity, λ, increases with the increase in the wetted perimeter ratio, P_b/P_w (Figures (5-18c & 5-18d)).

7.2.4 Lateral variation of the secondary flow term

28- In smooth trapezoidal channels, the optimum sign pattern of the secondary flow term, Γ, alternates between negative and positive in adjacent panels. This is consistent with the assumptions made for choosing the panel structure and confirms the modelling philosophy of Knight *et al* (2007) (see Section 2.6.9.3).

29- Generally, higher values of the secondary flow term are found for the panels in the sidewall region which implies high levels of circulation in these regions.

30- In smooth trapezoidal channels, the absolute value of Γ in all the panels decreases by the increase in the wetted perimeter ratio, P_b/P_w (Figures (5-4f), (IV-10f), (IV-18f) & (IV-24f)).

31- In smooth trapezoidal channels with aspect ratios higher than 7.5, the secondary flow term, Γ, is initially negative in the first panel and then rises towards zero in all cases. The value of this parameter then increases slightly in the third panel to a value near 0.10 before decreasing to a negative value in the fourth panel. Finally, a maximum positive value is obtained in the fifth panel (Figure (5-4e)).

32- In trapezoidal channels with aspect ratios between 1.0 and 5.26, the secondary flow term, Γ, is initially negative in the first panel and then rises towards 0.15 in all cases. The value of this parameter then decreases to a negative value in the third panel. Finally, a maximum positive value is obtained in the forth panel (Figures (5-10c), (IV-10e), (IV-18e) & (IV-24e)).

33- In differentially roughened trapezoidal channels the best pattern for the sign of Γ is found to alternate between positive and negative values, i.e. it is opposite to that of smooth and uniformly roughened channels. This change in the sign of Γ can be interpreted as a change in the rotating direction of all the secondary flow cells.

34- The lateral variation of the absolute optimum values of Γ is similar in uniformly and partially roughened trapezoidal channels. The absolute value of Γ in the second panel of all cases again converges to a value near 0.25 which is slightly different from the smooth cases. The significant difference is that the maximum value of Γ for differentially roughened channels does not appear in the final panel (Figures (IV-30e), (IV-44e) & (IV-58e).

35- Modelling river sections with the suggested eight panel structure and evaluating the calibration results on the depth-averaged velocity distribution and discharge, results in scattered values for the secondary flow term (Table (5-17)).

7.3 THE FREE OVERFALL PROBLEM

36- It was shown that Genetic Programming is powerful and effective data mining tool which can be used for model induction purposes.

37- Applying this tool and following a two-stage model selection procedure, a global white box (transparent) model in the form of $h_c = \mathrm{A} h_e e^{\mathrm{B}\sqrt{S_0}}$ (or $EDR = h_e / h_c = (1/\mathrm{A}) e^{-\mathrm{B}\sqrt{S_0}}$) was found as the most suitable and applicable expression for predicting critical depth and *EDR* in a wide range of channels.

38- In addition to being dimensionally correct, this expression appears to be universal and can be applied to all common cross-section channel shapes and different flow regimes (subcritical and supercritical).

39- The overall performance of this model is better than any other proposed empirical relationship (Section 6.3.5.3).

40- Comparison of the optimum values of the A coefficients for different data sets revealed that the value of this coefficient might be independent of channel geometry and flow conditions. A global value of 1.30 was suggested to be suitable for the expression.

41- The overall structure of the found model was confirmed by Dimensional analysis and Principal Component Analysis.

42- It was also shown that the A and B coefficients of the expression should be related to the channel geometry, roughness, uniform depth, Froude and Reynolds numbers.

CHAPTER 8

RESEARCH LIMITATIONS AND RECOMMENDATIONS FOR FUTURE WORK

8.1 INTRODUCTION

Two different applications of Evolutionary Computation to open channel flow modelling were presented in this thesis. This chapter attempts to reiterate the gaps in knowledge, addresses the limitations of the work and suggest recommendations for the future work.

8.2 THE SKM MODEL

The analysis of the SKM revealed that this method is able to accurately model the flow in simple and complicated channel geometries. However, there are different sources of uncertainty which may influence the predictions of the model. The main sources of uncertainty in SKM modelling are:

- *Structure uncertainty*: the outputs of the SKM directly depend on the selected panel structure.
- *Perception uncertainty*: the time averaging and the spatial averaging of the lumped parameters within the model have caused these parameters to lose some degree of interpretation in the sense of being independently measurable.
- *Parameter estimation uncertainty*: the SKM system of equations is ill-posed in a sense that many sets of parameters would result in equally accepted model results.

The major part of this research was dedicated to overcome the overall uncertainty to some degree by building a robust evolutionary calibration framework to identify the model's

immeasurable parameters. To improve the modelling results and the applicability of SKM modelling, the following work is suggested to be undertaken on the SKM model:

- SKM should undergo uncertainty and structural identifiability analysis (Petersen, 2000), and the identified areas in the model domain which contribute to uncertainty should be modified.

- The structure of the panels should be examined in greater detail. A "roadmap" should be developed for the number and position of the panels by further studying of the secondary flows and the panel boundary conditions, and also conducting sensitivity analysis on various datasets.

- At rough boundaries, the boundary shear stress simulations are of poor quality, particularly at greater depths. This suggests that the use of a local friction factor f to relate the depth-averaged velocity and boundary shear stress (Eq. 2-51) may not be appropriate. An investigation should be made of alternative methods of boundary shear stress calculation.

- Generally, there are almost never sufficient calibration data to identify the spatially distributed parameters. The model calibration shows that further experimental work should be undertaken to investigate the effect of channel geometry and boundary roughness on the lateral variation of the SKM parameters and to quantify and detail the range for each parameter.

- SKM incorporates a spatially averaged secondary flow model Γ (Eq. 2-69), which provides the average effect of these circulations in each panel. Further study of the lateral and vertical components of velocity should be undertaken by conducting field measurements with using Acoustic Doppler Velocimeters and Acoustic Doppler Current Profiles. This would provide information on the number, position and intensity of the secondary flow cells and help developing the SKM.

8.3 THE CALIBRATION FRAMEWORK

Multi-objective calibration of a hydrodynamic model showed a challenging optimization problem. The following procedures are suggested towards improving the quality of multi-objective calibration:

- More constraints should be added to the optimization framework in order to improve convergence and ease the parameter identification process. This can be achieved by conducting further measurements and gaining knowledge on the range and quantities of the model parameters.
- Alternative fitness measures (RMSE, MRSS, etc.) should be incorporated in the algorithm and their efficiency on the convergence should be evaluated.
- Different genetic operators should be tested in the algorithm.
- The most suitable algorithm termination criteria should be defined.
- Alternative powerful multi-objective search algorithms, e.g. Multi-Objective Shuffled Complex Evolution Metropolis Algorithm (MOSCEM) (Vurgt *et al*., 2003) and LNSGA-II (Nazemi, 2008), should be tested in the framework.
- Advanced clustering techniques should be employed to identify similar Pareto solutions.
- Attempts should be made towards increasing the automation of the calibration framework.

Applying some modifications, the proposed calibration framework can be used for the parameter estimation of other models (including other hydrodynamic models). However, some fundamental work should be done beforehand:

- The basic question which is always asked in the context of modelling is “When is a model calibration good enough?” Methods and guidelines for robust and effective hydrodynamic model calibration should be proposed.
- The calibration framework should be tested and evaluated on other hydrodynamic models, and its weaknesses should be diagnosed.
- A guideline should be proposed for the selection of the NSGA-II internal parameters for hydrodynamic models.

8.4 THE FREE OVERFALL MODEL

Applying Genetic Programming and following a two-stage model selection procedure, a global transparent model in the form of $h_c = \mathrm{A} h_e e^{\mathrm{B}\sqrt{S_0}}$ (or $EDR = h_e / h_c = (1/\mathrm{A}) e^{-\mathrm{B}\sqrt{S_0}}$) was found as the most suitable and applicable expression for predicting critical depth and *EDR* in a wide range of channels. To be able to confidently use this model, the A and B coefficients should be predefined. Dimensional analysis and PCA showed that these coefficients should be related to the channel geometry, roughness, uniform depth, Froude and Reynolds numbers. Unfortunately, at the time of modelling due to the lack of measurements, these coefficients could not be defined. However, initial analysis revealed that "A" seems to be independent of the channel geometry and flow conditions. To obtain exact relationships for "A" and "B", experiments should be designed and conducted in various channels and accurate measurements of the mentioned attributes should be made. In the light of the obtained formulation of these coefficients, stronger steps can be taken towards knowledge discovery and understanding the probable physics behind the equation.

REFERENCES

Abril, J.B. and Knight, D.W. (2004) Stage-discharge prediction for rivers in flood applying a depth-averaged model. *Journal of Hydraulic Research*, IAHR, 42 (6): 616-629.

Ahmadi, G. (2005) *Particle transport and deposition in turbulent flows*, Course notes, Clarkson University, http://web2.clarkson.edu/projects/crcd/me637/downloads/637-09.pdf. Last accessed 15 May 2009.

Al-Hamid, A.A.I. (1991) *Boundary shear stress and velocity distributions in differentially roughened trapezoidal open channels*. PhD thesis, The University of Birmingham, Birmingham, UK.

Ali, K.H.M. and Sykes, A. (1972) Free-vortex theory applied to free overfall. *Journal of the Hydraulics Division,* ASCE, 98 (5): 973–979.

Anderson, J.D. (1997) *A history of aerodynamics and its impact on flying machines*. Cambridge University Press, Cambridge.

Anderson, M.V. (1967) Non-uniform flow in front of a free overfall. *Acta Polytechnic Scandinavia,* 42: 1–24.

Andreou, A.S., Georgopoulos, E.F. and Likothanassis, S.D. (2002) Exchange-rates forecasting: A hybrid algorithm based on genetically optimized adaptive neural networks. *Computational Economics,* Kluwer Academic Publishers, 20 (3): 191-210.

Aronica, G., Hankin, B. and Beven, K. (1998) Uncertainty and equifinality in calibrating distributed roughness coefficients in a flood propagation model with limited data. *Advances in Water Resources*, Elsevier, 22 (4): 349-365.

Aytek, A. and Kisi, O. (2008) A genetic programming approach to suspended sediment modelling. *Journal of Hydrology*, Elsevier, 351 (3-4): 288-298.

Babayan, A.V., Savic, D.A. and Walters, G.A. (2005) Multiobjective optimization for the least-cost design of water distribution systems under correlated uncertain parameters. *Proceedings of the 2005 World Water and Environmental Resources Congress*. [Ed. Walton, R.], Reston, United States.

Babovic, V. and Abbott, M.B. (1997a) The evolution of equation from hydraulic data, Part I: Theory. *Journal of Hydraulic Research*, IAHR, 35 (3): 397-410.

Babovic, V. and Abbott, M.B. (1997b) The evolution of equation from hydraulic data, Part II: Applications. *Journal of Hydraulic Research*, IAHR, 35 (3): 411-430.

References

Babovic, V. and Zhang, H. (2002) Modeling of vertical thermal structure using genetic programming. *The Seventh OMISAR Workshop on Ocean Models for the APEC Region (WOM-7)*, Singapour, 1:1-5.

Back, T., Fogel, D.B., Whitley, D. and Angeline, P.J. (1997a) Mutation. In Back, T., Fogel, D.B. & Michalewicz, Z. (Eds.) *Handbook of Evolutionary Computation*, IOP Publishing Ltd and Oxford University Press, Bristol and Oxford, C3.2:1–C3.2:14.

Back, T., Hammel, U. and Schwefel, H.P. (1997b) Evolutionary computation: comments on the history and current state. *IEEE Transactions on Evolutionary Computation*, IEEE, 1 (1): 3-17.

Back, T. and Schwefel, H.P. (1993) An overview of evolutionary algorithms for parameter optimization. *Evolutionary Computation*, MIT Press, 1 (1): 1-23.

Balachandar, R., Blakely, D. and Bugg, J. (2002) Friction velocity and power law velocity profile in smooth and rough shallow open channel flows. *Canadian Journal of Civil Engineering*, 29 (2): 256-266.

Barenblatt, G. (1993) Scaling laws for fully developed turbulent shear flows: Part 1. Basic hypothesis and analysis. *Journal of Fluid Mechanics*, Cambridge University Press, 248 513-520.

Barr, D.I.H. (1979) Osborne Reynolds' turbulent flow resistance formulae. *Proceedings Institution of Civil Engineers, Part 2*, 67: 743-750.

Batchelor, G.K. (1967) *An introduction to fluid dynamics*. Cambridge University Press, London.

Batchelor, G.K., Moffatt, H.K. and Worster, M.G. (2000) *Perspectives in fluid dynamics: a collective introduction to current research*. Cambridge University Press, Cambridge.

Bauer, S.W. and Graf, W.H. (1971) Free overfall as flow measuring device. *Journal of Irrigation and Drainage Division*, ASCE, 97 (1): 73–83.

Bekele, E.G. and Nicklow, J.W. (2007) Multi-objective automatic calibration of SWAT using NSGA-II. *Journal of Hydrology*, Elsevier, 341 (3-4): 165-176.

Beven, K. (2004) Does an interagency meeting in Washington imply uncertainty? *Hydrological Processes*, 18 (9): 1747-1750.

Beven, K. (2006) A manifesto for the equifinality thesis. *Journal of Hydrology*, Elsevier, 320 (1-2): 18-36.

Beven, K. and Binley, A. (1992) The future of distributed models: model calibration and uncertainty prediction. *Hydrological Processes*, 6 (3): 279-298.

Beven, K. and Freer, J. (2001) Equifinality, data assimilation, and uncertainty estimation in mechanistic modelling of complex environmental systems using the GLUE methodology. *Journal of Hydrology*, Elsevier Science, 249 (1-4): 11-29.

References

Bhallamudi, S.M. (1994) End depth in trapezoidal and exponential channels. *Journal of Hydraulic Research,* IAHR, 32 (2): 219-232.

Bilgil, A. (2005) Correlation and distribution of shear stress for turbulent flow in a smooth rectangular open channel. *Journal of Hydraulic Research,* IAHR, 43 (2): 165-173.

Bishop, C.M. (2006) *Pattern recognition and machine learning*. Springer Link, Singapour.

Blashfield, R. and Aldenderfer, M. (1978) The Literature on Cluster Analysis. *Multivariate Behavioral Research,* 13 (3): 271-295.

Bousmar, D. and Zech, Y. (2004) Velocity distribution in non-prismatic compound channels. *Water Management,* 157 (2): 99-108.

Bradshaw, P. (1971) *An introduction to turbulence and its measurement*. Pergamon Press, Oxford.

Bradshaw, P. and Huang, G.P. (1995) The law of the wall in turbulent flow. *Proceedings of the Royal Society of London, Series A (Mathematical and Physical Sciences),* 451 (1941): 165-188.

Brundrett, E. and Baines, W.D. (1964) The production and diffusion of vorticity in duct flow. *Journal of Fluid Mechanics,* Cambridge University Press, 19 (03): 375-394.

Carrera, J. and Neuman, S.P. (1986) Estimation of aquifer parameters under transient and steady state conditions. II. Uniqueness, stability, and solution algorithms. *Water Resources Research,* 22 (2): 211-227.

Caruana, R.A. and Schaffer, J.D. (1988) Representation and hidden bias: Gray vs. binary coding for genetic algorithms. *Proceedings of 5th International Conference on Machine Learning,* Los Altos, CA, 153-162.

Castillo, F., Kordon, A. and Smits, G. (2006) Robust Pareto front genetic programming parameter selection based on design of experiments and industrial data. In Rick, L.R., Soule, T. & Worzel, B. (Eds.) *Genetic Programming Theory and Practice IV.* Springer, Ann Arbor.

Charbonneau, P. (1995) Genetic algorithms in astronomy and astrophysics. *The Astrophysical Journal Supplement Series,* 101 (2): 309-334.

Chaudhry, M.H. (1993) *Open-Channel Flow*. Prentice-Hall Inc., New York.

Chellapilla, K. and Fogel, D.B. (2001) Evolving an expert checkers playing program without using human expertise. *IEEE Transactions on Evolutionary Computation,* Institute of Electrical and Electronics Engineers Inc., 5 (4): 422-428.

Chen, C.L. (1991) Unified theory on power laws for flow resistance. *Journal of Hydraulic Engineering,* ASCE, 117 (3): 371-389.

Chen, S.H., Jakeman, A.J. and Norton, J.P. (2008) Artificial Intelligence techniques: An introduction to their use for modelling environmental systems. *Mathematics and Computers in Simulation*, 78 (2-3): 379-400.

Chen, S.H. and Liao, C.C. (2005) Agent-based computational modeling of the stock price-volume relation. *Information Sciences*, Elsevier, 170 (1): 75-100.

Cheng, C.T., Zhao, M.Y., Chau, K.W. and Wu, X.Y. (2006) Using genetic algorithm and TOPSIS for Xinanjiang model calibration with a single procedure. *Journal of Hydrology*, 316 (1-4): 129-140.

Chiu, C.L. (1987) Entropy and probability concepts in hydraulics. *Journal of Hydraulic Engineering*, ASCE, 113 (5): 583-600.

Chiu, C.L. (1989) Velocity distribution in open channel. *Journal of Hydraulic Engineering*, ASCE, 115 (5): 576-594.

Chlebek, J. (2009) *Modelling of simple prismatic channels with varying roughness using the SKM and a study of flows in smooth non-prismatic channels with skewed floodplains*. PhD thesis, University of Birmingham, Birmingham, UK.

Chlebek, J. and Knight, D.W. (2006) A new perspective on sidewall correction procedures, based on SKM modeling. *Proceedings of the International Conference on Fluvial Hydraulics (River Flow 2006)*. [Eds. Ferreira, R.M.L., Alves, E.C.T.L., Leal, J.G.A.B. & Cardoso, A.H.], Lisbon, Portugal, 1: 135-144.

Chow, V.T. (1959) *Open-channel hydraulics*. McGraw-Hill, New York.

Christensen, B. and Fredsoe, J. (1998) *Bed shear stress distribution in straight channels with arbitrary cross section*. Lyngby, Denmark, Institute of Hydrodynamics and Hydraulic Engineering, Technical University of Denmark, 77.

Clausnitzer, B. and Hager, W.H. (1997) Outflow characteristics from circular pipe. *Journal of Hydraulic Engineering*, ASCE, 123 (10): 914-917.

Coello, C.A.C. (1999) A comprehensive survey of evolutionary-based multiobjective optimization techniques. *Knowledge and Information Systems*, Springer-Verlag, 1 (3): 269-308.

Coello, C.A.C. (2006) Twenty years of evolutionary multi-objective optimization: A historical view of the field. *IEEE Computational Intelligence Magazine*, IEEE, 1 (1): 23-68.

Cohen, I.M., Kundu, P.K. and Hu, H.H. (2004) *Fluid mechanics*. 3rd edition, Elsevier Science & Technology, San Diego, California.

Coles, D. (1956) The law of the wake in the turbulent boundary layer. *Journal of Fluid Mechanics*, Cambridge University Press, 1: 191-226.

Coley, D.A. (1999) *An introduction to genetic algorithms for scientists and engineers*. World Scientific Publishing, Singapore.

Cunge, J.A. and Erlich, M. (1999) Hydroinformatics in 1999: what is to be done? *Journal of Hydroinformatics,* IWA Publishing, 1 (1): 21-31.

Cunge, J.A., Holly, F.M. and Verway, A. (1980) *Practical aspects of computational river hydraulics*. The Pitman Press, Bath, UK.

Davidson, P.A. (2004) *Turbulence: An introduction for scientists and engineers*. Oxford University Press, New York.

Davis, A.C., Ellett, B.G.S. and Jacob, R.P. (1998) Flow measurement in sloping channels with rectangular free overfall. *Journal of Hydraulic Engineering,* ASCE, 124 (7): 760-763.

Davis, L. (1991) *Handbook of genetic algorithms*. Van Nostrand Reinhold, New York.

De Cacueray, N., Hargreaves, D.M. and Morvan, H.P. (2009) A computational study of shear stress in smooth rectangular channels. *Journal of Hydraulic Research,* IAHR, 47 (1): 50-57.

De Jong, K.A. (1975) *Analysis of the behavior of a class of genetic adaptive systems*. PhD thesis, University of Michigan, Ann Arbor, USA.

De Jong, K.A. (2006) *Evolutionary Computation: A unified approach*. MIT Press, Cambridge, MA.

Deb, K. (1997) Limitations of evolutionary computation methods. In Back, T., Fogel, D.B. & Michalewicz, Z. (Eds.) *Hand book of evolutionary computation.* Tylor & Francis group, Oxon, B2.9.1-B2.9.2.

Deb, K. (1999) Multi-objective genetic algorithms: problem difficulties and construction of test problems. *Evolutionary Computation,* MIT Press, 7 (3): 205-230.

Deb, K. and Agrawal, R.B. (1995) Simulated binary crossover for continuous search space. *Complex Systems,* Complex Systems Publications, 9 (2): 115-148.

Deb, K. and Agrawal, S. (1998) Understanding interactions among genetic algorithm parameters. In Banzhaf, W. & Reeves, C. (Eds.) *Foundations of Genetic Algorithms* Morgan Kaufmann, San Francisco, CA, 265-286.

Deb, K., Agrawal, S., Pratab, A. and Meyarivan, T. (2000) A fast elitist non-dominated sorting genetic algorithm for multi-objective optimization: NSGA-II. *Proceedings of the Parallel Problem Solving from Nature VI Conference*. [Eds. Schoenauer, M., Deb, K., Rudolph, G.u.,Yao, X., Lutton, E., Merelo, J.J. & Schwefel, H.P.], Paris, France, 849-858.

Deb, K. and Kumar, A. (1995) Real-coded genetic algorithms with simulated binary crossover: studies on multimodal and multiobjective problems. *Complex Systems,* Complex Systems Publications, 9 (6): 431-454.

References

Deb, K., Pratap, A., Agarwal, S. and Meyarivan, T. (2002) A fast and elitist multiobjective genetic algorithm: NSGA-II. *IEEE Transactions on Evolutionary Computation*, IEEE, 6 (2): 182-197.

DEFRA/EA (2003) *Reducing uncertainty in river flood conveyance, Roughness Review*, HR Wallingford, UK, Project W5A- 057.

Delleur, J.W., Dooge, J.C.I. and Gent, K.W. (1956) Influence of slope and roughness on the free overfall. *Journal of the Hydraulics Division*, ASCE, 82 (4): 30–35.

Dey, S. (1998) End depth in circular channels. *Journal of Hydraulic Engineering*, ASCE, 124 (8): 856-863.

Dey, S. (2001a) EDR in circular channels. *Journal of Irrigation and Drainage Engineering*, 127 (2): 110-112.

Dey, S. (2001b) Flow measurement by the end-depth method in inverted semicircular channels. *Flow Measurement and Instrumentation*, Elsevier, 12 (4): 253–258.

Dey, S. (2001c) Flow metering by end-depth method in elliptic channels. *Dam Engineering*, 12 (1): 5-19.

Dey, S. (2002a) Free overfall in circular channels with flat base: a method of open channel flow measurement. *Flow Measurement and Instrumentation*, Elsevier, 13 (5-6): 209-221.

Dey, S. (2002b) Free overfall in open channels: state-of-the-art review. *Flow Measurement and Instrumentation*, Elsevier, 13 (5-6): 247–264.

Dey, S. (2003) Overfall in U-shaped channels. *Journal of Engineering Mechanics*, American Society of Civil Engineers, 129 (3): 358-362.

Dey, S. (2005) End depth in U-shaped channels: A simplified approach. *Journal of Hydraulic Engineering*, ASCE, 131 (6): 513-516.

Dey, S. and Kumar, B.R. (2002) Hydraulics of free overfall in Delta-shaped channels. *Sadhana - Academy Proceedings in Engineering Sciences*, Indian Academy of Sciences, 27 (3): 353-363.

Dey, S., Kumar, D.N. and Singh, D.R. (2004) End-depth in inverted semicircular channels: Experimental and theoretical studies. *Nordic Hydrology*, Nordic Association of Hydrology, 35 (1): 73-79.

Diskin, M.H. (1961) The end depth at a drop in trapezoidal channels. *Journal of the Hydraulics Division*, ASCE, 87 (4): 11–32.

Drazin, P.G. and Riley, N. (2006) *The Navier-Stokes equations: a classification of flows and exact solutions*. Cambridge University Press, Cambridge.

Duan, Q., Sorooshian, S. and Gupta, V. (1992) Effective and efficient global optimization for conceptual rainfall-runoff models. *Water Resources Research,* American Geophysical Union, 28 (4): 1015-1031.

Einstein, H.A. (1942) Formulas for transportation of bed load. *Transactions of the American Society of Civil Engineers,* ASCE, 68 (8, Part 2): 561-577.

Elder, J.W. (1959) The dispersion of marked fluid in turbulent shear flow. *Journal of Fluid Mechanics,* Cambridge University Press, 5 (4): 544-560.

Engelund, F. (1964) Flow resistance and hydraulic radius. *Acta Polytechnica Scandinavica: Civil Engineering and Building,* 24: 532-543.

Ervine, D.A., Babaeyan-Koopaei, K. and Sellin, R.H.J. (2000) Two-dimensional solution for straight and meandering overbank flows. *Journal of Hydraulic Engineering,* ASCE, 126 (9): 653-669.

Farina, M. (2001) *Cost-effective evolutionary strategies for Pareto optimal front approximation in multiobjective shape design optimization of electromagnetic devices*. PhD thesis, University of Pavia, Pavia, Italy.

Ferro, V. (1992) Flow measurement with rectangular free overfall. *Journal of Irrigation and Drainage Engineering,* ASCE, 118 (6): 956-964.

Ferro, V. (1999) Theoretical end-depth-discharge relationship for free overfall. *Journal of Irrigation and Drainage Engineering,* ASCE, 125 (1): 40-44.

Ferro, V. (2004) Discussion of "Free overfall in inverted semicircular channels" by S. Dey. *Journal of Hydraulic Engineering,* ASCE, 130 (11): 1126-1128.

Finnemore, E.J. and Franzini, J.B. (2002) *Fluid mechanics with engineering applications*. 10th edition, McGraw-Hill, Boston.

Finnie, J.I. and Jeppson, R.W. (1991) Solving turbulent flows using finite elements. *Journal of Hydraulic Engineering,* ASCE, 117 (11): 1513-1530.

Firat, C.E. (2004) *Effect of roughness on flow measurements in sloping rectangular channels with free overfall*. MSc thesis, The middle east technical university, Ankara, Turkey.

Fischer, H.B. and Calif, M.P. (1967) *Transverse mixing in a sand bed channel*. U.S Geological Survey Professional Paper 575-D.

Flintham, T.P. and Carling, P.A. (1988) Prediction of mean bed and wall boundary shear in uniform and compositely rough channels. *Proceedings of the International Conference on River Regime*, Oxon, UK, 267-286.

Flury, B. (1988) *Common principal components and related multivariate models*. John Wiley, New York.

Fogel, L.J., Owens, A.J. and Walsh, M.J. (1966) *Artificial intelligence through simulated evolution*. John Wiley, New York.

Fonseca, C.M. and Fleming, P.J. (1995) An overview of evolutionary algorithms in multiobjective optimization. *Evolutionary Computation,* 3: 1-16.

Fonseca, C.M. and Fleming, P.J. (1998) Multiobjective optimization and multiple constraint handling with evolutionary algorithms - Part II: application example. *IEEE Transactions on Systems, Man, and Cybernetics Part A: Systems and Humans,* IEEE, 28 (1): 38-47.

Franchini, M. and Galeati, G. (1997) Comparing several genetic algorithm schemes for the calibration of conceptual rainfall run-off models. *Hydrological Sciences,* 42 (3): 357-379.

Freer, J., Beven, K. and Ambroise, B. (1996) Bayesian estimation of uncertainty in runoff prediction and the value of data: an application of the GLUE approach. *Water Resources Research,* 32 (7): 2161-2173.

Freitas, A.A. (1998) On objective measures of rule surprisingness. *Proceedings of the Second European Conference on the Principles of Data Mining and Knowledge Discovery (PKDD'98)*, Nantes, France, 1-9.

Freitas, A.A. (1999) On rule interestingness measures. *Knowledge-Based Systems,* Elsevier, 12 (5-6): 309-315.

Freitas, A.A. (2002) A survey of evolutionary algorithms for data mining and knowledge discovery. In Ghosh, A. & Tsutsui, S. (Eds.) *Advances in Evolutionary Computation: Theory and Applications.* Springer-Verlag, 819-845.

Gessner, F.B. (1973) The origin of secondary flow in turbulent flow along a corner. *Journal of Fluid Mechanics,* Cambridge University Press, 58 (1): 1-25.

Ghosh, A. and Dehuri, S.N. (2004) Evolutionary algorithms for multi-criterion optimization: A survey. *International Journal of Computing and Information Science,* 2 (1): 38-57.

Ghosh, A. and Jain, L.C. (2005) *Evolutionary Computation in Data Mining*. Springer-Verlag, Berlin.

Ghosh, S.N. and Roy, N. (1970) Boundary shear distribution in open channel flow. *Journal of the Hydraulics Division,* ASCE, 96 (4): 967-994.

Gillet, V.J., Khatib, W., Willett, P., Fleming, P.J., et al. (2002) Combinatorial library design using a multiobjective genetic algorithm. *Journal of Chemical Information and Computer Sciences,* American Chemical Society, 42 (2): 375-385.

Giro, R., Cyrillo, M. and Galvo, D.S. (2002) Designing conducting polymers with genetic algorithms, *Chemical Physics Letters*, 700: 283-288.

Glover, R.E. (1964) Dispersion of dissolved or suspended materials in flowing streams. *U.S. Geological Survey*, Professional Paper 433-B.

Gnanadesikan, R. (1977) *Methods for statistical data analysis of multivariate observations*. John Wiley and Sons Inc., New Jersey.

Goldberg, D.E. (1989) *Genetic Algorithms in search, optimization, and machine learning*. Addison-Wesley, Boston.

Goldberg, D.E. and Deb, K. (1991) A comparison of selection schemes used in genetic algorithms. In Rawlins, G.E. (Ed.) *Foundations of genetic algorithms*. Morgan Kaufmann, San Mateo, California, 69-93.

Goldberg, D.E., Deb, K. and Clark, J.H. (1992) Genetic algorithms, noise, and the sizing of populations. *Complex Systems*, 6 (4): 333-362.

Goncharov, V.N. (1964) *Dynamics of channel flow*. Israel Program for Scientific Translations, Jerusalem.

Guo, J. and Julien, P.Y. (2005) Shear stress in smooth rectangular open-channel flows. *Journal of Hydraulic Engineering*, ASCE, 131 (1): 30-37.

Guo, Y. (2005) Numerical modeling of free overfall. *Journal of Hydraulic Engineering*, ASCE, 131 (2): 134-138.

Guo, Y., L., Z. and Zhang, J. (2006) Numerical simulation of free overfall in a rough channel. *Proceedings of European Conference on Computational Fluid Dynamics*, Egmond Aan Zee, The Netherlands.

Gupta, H.V., Beven, K.J. and Wagener, T. (2005) Model calibration and uncertainty estimation. In Anderson, M.G. (Ed.) *Encyclopedia of hydrologic sciences*. Wiley, Chichester.

Gupta, H.V., Sorooshian, S. and Yapo, P.O. (1998) Toward improved calibration of hydrologic models: Multiple and noncommensurable measures of information. *Water Resources Research*, 34 (4): 751-763.

Gupta, R.D., Jamil, M. and Mohsin, M. (1993) Discharge prediction in smooth trapezoidal free overfall - (positive, zero and negative slopes). *Journal of Irrigation & Drainage Engineering*, ASCE, 119 (2): 215-224.

Guyon, I., Matic, N. and Vapnik, V. (1996) Discovering informative patterns and data cleaning. In Fayyad, U.M., Piatetsky-Shapiro, G., Smyth, P. & Uthurusamy, R. (Eds.) *Advances in Knowledge Discovery and Data Mining*. AAAI/MIT Press, 181-203.

Hager, W.H. (1983) Hydraulics of the plane overfall. *Journal of Hydraulic Engineering*, ASCE, 109 (2): 1683–1697.

Hager, W.H. and Hutter, K. (1984) On pseudo-uniform flow in open channel hydraulics. *Acta Mechanica*, Springer-Verlag, 53 (3): 183-200.

Harik, G., Cantu-Paz, E., Goldberg, D.E. and Miller, B.L. (1997) The gambler's ruin problem, genetic algorithms, and the sizing of populations. *Fourth International Conference on Evolutionary Computation (ICEC '97)*, New York, NY, USA, 7-12.

Henderson, F.M. (1966) *Open channel flow*. Macmillan Publishing, New York.

Hirschen, K. and Schafer, M. (2006) A study on evolutionary multi-objective optimization for flow geometry design. *Computational Mechanics*, Springer Verlag, 37 (2): 131-141.

Holland, J.H. (1962) Outline for a logical theory of adaptive systems. *Journal of the Association for Computing Machinery*, 3 297-314.

Holland, J.K. (1975) *Adaptation in Natural and Artificial Systems*. MIT Press, USA.

Holley, E.R. and Abraham, G. (1973) Laboratory studies on transverse mixing in rivers. *Journal of Hydraulic Research*, IAHR, 11 (3): 219-253.

Hunter, N.M., Bates, P.D., Neelz, S., Pender, G., et al. (2008) Benchmarking 2D hydraulic models for urban flooding. *Proceedings of the Institution of Civil Engineers: Water Management*, Thomas Telford Services Ltd, 161 (1): 13-30.

Ikeda, S. (1981) Self-formed straight channels in sandy beds. *Journal of the Hydraulics Division*, ASCE, 107 (HY4 Proc. Paper, 16195): 389-406.

Jaeger, C. (1957) *Engineering Fluid Mechanics*. Blackie, London.

Johnson, R.A. and Wichern, D.W. (1988) *Applied Multivariate Statistical Analysis*. 2nd edition, Printice-Hall Publications, New Jersey.

Johnson, R.W. (1998) *The handbook of fluid dynamics*. CRC Press, Springer-Verlag, USA.

Jolliffe, I.T. (1986) *Pincipal component analysis*. Springer, New York.

Jones, W.P. and Launder, B.E. (1973) Prediction of low-Reynolds-number phenomena with a 2-equation model of turbulence. *International Journal of Heat & Mass Transfer*, 16 1119-1125.

Kazemipour, A.K. and Apelt, C.J. (1980) Shape effects on resistance to flow in smooth rectangular channels. *Research Report Series - University of Queensland, Department of Civil Engineering*, CE9.

Keijzer, M. (2002) *Scientific discovery using genetic programming*. PhD thesis, Technical University of Denmark, Kongens Lyngby, Denmark.

Keijzer, M. (2004) Scaled symbolic regression. *Genetic Programming and Evolvable Machines*, Kluwer Academic Publishers, 5 (3): 259-269.

Keijzer, M. and Babovic, V. (1999) Dimensionally aware genetic programming. *Proceedings of the Genetic and Evolutionary Computation Conference*. [Eds. Banzhaf, W., Daida, J.,

Eiben, A.E., Garzon, M.H., Honavar, V., Jakiela, M. & Smith, R.E.], Orlando, Florida, USA, 2: 1069-1076.

Keijzer, M., Baptist, M., Babovic, V. and Uthurburu, J.R. (2005) Determining equations for vegetation induced resistance using genetic programming. *Proceedings of the 2005 conference on Genetic and evolutionary computation*, Washington DC, USA, 1999-2006.

Keller, R.J. and Fong, S.S. (1989) Flow measurement with trapezoidal free overfall. *Journal of Irrigation and Drainage Engineering,* ASCE, 115 (1): 125-136.

Khare, V., Yao, X. and Deb, K. (2003) Performance scaling of multi-objective evolutionary algorithms. *Proceedings of the Second International Conference on Evolutionary Multi-Criterion Optimization, EMO 2003. (Lecture Notes in Computer Science Vol.2632)*. [Eds. Fonseca, C.M., Fleming, P.J., Zitzler, E. & Deb, K.], Berlin, Germany, 376-390.

Khatibi, R.H., Williams, J.J.R. and Wormleaton, P.R. (1997) Identification problem of open-channel friction parameters. *Journal of Hydraulic Engineering,* ASCE, 123 (12): 1078-1088.

Khodashenas, S.R., El Kadi, A.K. and Paquier, A. (2008) Boundary shear stress in open channel flow: A comparison among six methods. *Journal of Hydraulic Research,* IAHR, 46 (5): 598-609.

Khodashenas, S.R. and Paquier, A. (1999) Geometrical method for computing the distribution of boundary shear stress across irregular straight open channels. *Journal of Hydraulic Research,* IAHR, 37 (3): 381-388.

Kirkby, M.J. (1996) A role for theoretical models in geomorphology? *The Scientific Nature of Geomorphology: Proceedings of the 27th Binghamton Symposium in Geomorphology*. [Eds. Rhoads, B.L. & Thorn, C.E.], New York, 257–272.

Kirkgöz, M.S. (1989) Turbulent velocity profiles for smooth and rough open channel flow. *Journal of Hydraulic Engineering,* ASCE, 115 (11): 1543-1561.

Klemettinen, M., Mannila, H., Ronkainen, P., Toivonen, H., et al. (1994) Finding interesting rules from large sets of discovered association rules. *Proceeding of 3rd International Conference on Information and Knowledge Management*, Gaithersburg, Maryland, 401-407.

Knight, D.W. (1981) Boundary shear stress in smooth and rough channels. *Journal of the Hydraulics Division,* ASCE, 107 (7): 839–851.

Knight, D.W. (1985) Advances in river engineering. *Proceedings of the International Symposium on Advances in Water Engineering*. [Ed. Tebbutt, T.H.Y.], Birmingham, UK, 278-288.

Knight, D.W. (1989a) Hydraulics of flood channels. In Beven, K. (Ed.) *Floods: Hydrological, sedimentological and geomorphological implications* John Wiley & Sons, 83-105.

Knight, D.W. (1989b) *River channels and floodplains, Final Report for Severn Trent Water Authority*. Severn-Trent Water Authority.

Knight, D.W. (1992) *SERC Flood Channel Facility experimental data - Phase A, Vols. 1-15*. School of Civil Engineering, The University of Birmingham,

Knight, D.W. and Abril, B. (1996) Refined calibration of a depth-averaged model for turbulent flow in a compound channel. *Proceedings of the Institution of Civil Engineers, Water, Maritime and Energy Division,* 118 (3): 151-159.

Knight, D.W. and Demetriou, J.D. (1983) Flood plain and main channel flow interaction. *Journal of Hydraulic Engineering,* ASCE, 109 (8): 1073-1092.

Knight, D.W., Demetriou, J.D. and Hamed, M.E. (1984a) Boundary shear in smooth rectangular channels. *Journal of Hydraulic Engineering,* ASCE, 110 (4): 405-422.

Knight, D.W., Demetriou, J.D. and Hamed, M.E. (1984b) Stage discharge relationships for compound channels, in Channels and Control Structures *Proceedings of the 1st International Conference on Hydraulic Design in Water Resources Engineering: Channels and Channel Control Structures*. [Ed. Smith, K.V.H.], Southampton, 4.15-14.36.

Knight, D.W. and Macdonald, J.A. (1979) Hydraulic resistance of artificial strip roughness. *Journal of the Hydraulics Division,* ASCE, 105 (6): 675-690.

Knight, D.W., McGahey, C., Lamb, R. and Samuels, P.G. (2009) *Practical channel hydraulics – roughness, conveyance and afflux*. Taylor & Francis, (in Press).

Knight, D.W., Omran, M. and Tang, X. (2007) Modeling depth-averaged velocity and boundary shear in trapezoidal channels with secondary flows. *Journal of Hydraulic Engineering,* ASCE, 133 (1): 39-47.

Knight, D.W. and Patel, H.S. (1985) Boundary shear in smooth rectangular ducts. *Journal of Hydraulic Engineering,* ASCE, 111 (1): 29-47.

Knight, D.W., Patel, H.S., Demetriou, J.D. and Hamed, M.E. (1983) Boundary shear stress distributions in open channel and closed conduit flows. *Proceedings of Euromech 156 - The Mechanics of Sediment Transport*. [Eds. Sumer, B.M. & Muller, A.], Istanbul, Turkey, 33-40.

Knight, D.W. and Sellin, R.H.J. (1987) The SERC Flood Channel Facility. *Journal of the Institution of Water and Environmental Management,* 1 198-204.

Knight, D.W. and Shiono, K. (1990) Turbulence measurements in a shear layer region of a compound channel. *Journal of Hydraulic Research,* IAHR, 28 (2): 175- 196.

Knight, D.W. and Shiono, K. (1996) River channel and floodplain hydraulics. In Anderson, M.G., Walling, D.E. & Bates, P.D. (Eds.) *Floodplain Processes.* J.Wiley & Sons, 139-181.

Knight, D.W., Yuen, K.W.H. and Al-Hamid, A.A.I. (1994) Boundary shear stress distributions in open channel flow. In Beven, K., Chatwin, P. & Millbank, J. (Eds.) *Physical Mechanisms of Mixing and Transport in the Environment.* John Wiley & Sons, 51-87.

Koza, J. (1990) *Genetic programming: A paradigm for genetically breeding populations of computer programs to solve problems*. Department of Computer Science, Stanford University, STAN-CS-90-1314.

Koza, J.R. (1992) *Genetic Programming: On the Programming of Computers by Means of Natural Selection*. MIT Press, Cambridge, MA, USA.

Koza, J.R. and Andre, D. (1996) Classifying Protein Segments as Transmembrane Domains Using Architecture-Altering Operations in Genetic Programming. In Angeline, P.J. & Kinnear Jr., K.E. (Eds.) *Advances in Genetic Programming 2*. MIT Press, Cambridge, MA, USA, 155-176.

Kutlu, I. (2005) *Scrutinizing Rectangular Free overfall*. MSc thesis, Middle East Technical University, Ankara, Turkey.

Lahanas, M., Baltas, D. and Zamboglou, N. (2003) A hybrid evolutionary algorithm for multi-objective anatomy-based dose optimization in high-dose-rate brachytherapy. *Physics in Medicine and Biology*, Institute of Physics Publishing, 48 (3): 399-415.

Lambert, M.F. and Sellin, R.H.J. (1996) Discharge prediction in straight compound channels using the mixing length concept. *Journal of Hydraulic Research,* IAHR, 34 (3): 381-394.

Langley, P. and Zytkow, J.M. (1989) Data-driven approaches to empirical discovery. *Artificial Intelligence*, 40 (1-3): 283-312.

Lau, Y.L. and Krishnappan, B.G. (1977) Transverse dispersion in rectangular channels. *Journal of the Hydraulics Division,* ASCE, 103 (10): 1173-1189.

Lean, G.H. and Weare, T.J. (1979) Modeling two-dimensional circulating flow. *Journal of the Hydraulics Division,* ASCE, 105 (1): 17-26.

Ledoux, J.W. (1925) Open End Flume Water Meter based on Exponential Equation. *Engineering News Record*, September 25.

Legates, D.R. and McCabe Jr, G.J. (1999) Evaluating the use of 'goodness-of-fit' measures in hydrologic and hydroclimatic model validation. *Water Resources Research*, American Geophysical Union, 35 (1): 233-241.

Leslie, D.C. (1973) *Developments in the theory of turbulence*. Oxford science publications, Oxford.

Liu, Y., Zhou, C. and Ye, W.J. (2005) A fast optimization method of using nondominated sorting genetic algorithm (NSGA-II) and 1-nearest neighbor (1NN) classifier for numerical model calibration. *IEEE International Conference on Granular Computing*. 2: 544-549.

Lobo, F. (2000) *The parameter-less genetic algorithm: Rational and automated parameter selection for simplified genetic algorithm operation*. PhD thesis, Universidade de Lisboa, Lisbon, Portugal.

Luke, S. and Panait, L. (2001) A survey and comparison of tree generation algorithms. *Proceedings of the Genetic and Evolutionary Computation Conference (GECCO-2001)*. [Ed. Spector, L., Goodman, E. D., Wu, A., Langdon, W. B., Voigt, H.M., Gen, M., Sen, S., Dorigo, M., Pezeshk, S., Garzon, M. H. & Burke, E.], San Francisco, California, USA, 81-88.

Luke, S. and Panait, L. (2002) Lexicographic parsimony pressure. *Proceedings of GECCO-2002*. [Eds. Langdon, W.B., Cantu-Paz, E., Mathias, K., Roy, R., Davis, D., Poli, R., Balakrishnan, K., Honavar, V., Rudolph, G. & Wegener, J.] 829-836.

Lundgren, H. and Jonsson, I.G. (1964) Shear and velocity distribution in shallow channels. *Journal of the Hydraulics Division,* ASCE, 90 (1): 1-21.

Madsen, H. (2000) Automatic calibration of a conceptual rainfall-runoff model using multiple objectives. *Journal of Hydrology,* Elsevier Science, 235 (3-4): 276-288.

Marchi, E. (1993) On the free overfall. *Journal of Hydraulic Research,* IAHR, 31 (6): 777-790.

Mardia, K.V., Kent, J.T. and Bibby, J.M. (1979) *Multivariate analysis, probability and mathematical statistics*. Academic Press, New York.

Marko, K.A. and Hampo, R.J. (1990) Application of genetic programming to control of vehicle systems, New York, NY, USA, 191-195.

Massey, B.S. (1998) *Mechanics of fluids*. 6th edition, Chapman and Hall, London.

McGahey, C. (2006) *A practical approach to estimating the flow capacity of rivers*. PhD thesis, The Open University, UK.

McGahey, C., Knight, D.W. and Samuels, P.G. (2009) Advice, methods and tools for estimating channel roughness. *Proceedings of the Institution of Civil Engineers: Water Management,* (in Press).

McGahey, C., Samuels, P.G. and Knight, D.W. (2006) A practical approach to estimating the flow capacity of rivers-Application and analysis. *Proceedings of the International Conference on Fluvial Hydraulics (River Flow 2006)*. [Eds. Ferreira, R.M.L., Alves, E.C.T.L., Leal, J.G.A.B. & Cardoso, A.H.], Lisbon, Portugal, 1: 303-312.

McGahey, C., Samuels, P.G., Knight, D.W. and O'Hare, M.T. (2008) Estimating river flow capacity in practice. *Journal of Flood Risk Management,* Wiley InterScience, 1 (1): 23-33.

Melling, A. and Whitelaw, J.H. (1976) Turbulent flow in a rectangular duct. *Journal of Fluid Mechanics,* Cambridge University Press, 78 289-315.

Michaelwicz, Z. (1992) *Genetic Algorithms + Data Structures = Evolution programs*. 3rd edition, Springer-Verlag, New York.

Michalewicz, Z. (1996) Heuristic methods for evolutionary computation techniques. *Journal of Heuristics,* Kluwer Academic Publishers, 1 (2): 177-206.

Mitchell, M. (1999) *Bioinformatics: An introduction to genetic algorithms*. MIT press, Massachusets.

Mohapatra, P.K., Murty Bhallamudi, S. and Eswaran, V. (2001) Numerical study of flows with multiple free surfaces. *International Journal for Numerical Methods in Fluids,* John Wiley and Sons, Ltd., 36 (2): 165-184.

Morvan, H., Knight, D., Wright, N., Tang, X. and Crossley, A. (2008) The concept of roughness in fluvial hydraulics and its formulation in 1D, 2D and 3D numerical simulation models. *Journal of Hydraulic Research,* International Association of Hydraulic Engineering Research, 46 (2): 191-208.

Muller, A. and Studerus, X. (1979) Secondary flow in open channel. *Congress of International Associations for Hydraulic Research*, Italy, 189-222.

Myers, W.R.C. and Lynness, J.F. (1989) *Flow resistance in rivers with floodplains, final report on recearch grant GR/D/45437*. University of Ulster, grant GR/D/45437.

Nazemi, A. (2008) *A novel evolutionary-based regional modelling framework for prediction in ungauged basins*. PhD thesis, University of Birmingham, Birmingham, UK.

Nazemi, A., Xin, Y. and Chan, A.H. (2006) Extracting a set of robust Pareto-optimal parameters for hydrologic models using NSGA-II and SCEM. *Proceedings of 2006 IEEE Congress on Evolutionary Computation (CEC'06)*, Vancouver, Canada, 6792-6799.

Nezu, I. (2005) Open-channel flow turbulence and its research prospect in the 21st century. *Journal of Hydraulic Engineering,* 131 (4): 229-246.

Nezu, I. and Nakagawa, H. (1993) *Turbulence in open-channel flows*. IAHR Monograph Series, A. A. Balkema, Rotterdam.

Nezu, I. and Rodi, W. (1985) Experimental study on secondary currents in open channel flow. *Proceeding of 21st IAHR Congress*, Melbourne, Australia, 2: 115-119.

Ng, A.W.M. and Perera, B.J.C. (2003) Selection of genetic algorithm operators for river water quality model calibration. *Engineering Applications of Artificial Intelligence,* Elsevier Ltd, 16 (5-6): 529-541.

Nokes, R.I. and Wood, I.R. (1988) Vertical and Lateral Turbulent Dispersion: Some Experimental Results. *Journal of Fluid Mechanics,* Cambridge University Press, 187 373-394.

Obayashi, S., Sasaki, D., Takeguchi, Y. and Hirose, N. (2000) Multiobjective evolutionary computation for supersonic wing-shape optimization. *IEEE Transactions on Evolutionary Computation,* IEEE, 4 (2): 182-187.

Odgaard, A.J. (1984) Shear-induced secondary currents in channel flows. *Journal of Hydraulic Engineering,* ASCE, 110 (7): 996-1004.

Olivero, M., Aguirre-Pey, J. and Moncada, A. (1999) Shear stress distribution in rectangular channels. *Proceeding of XXVIII IAHR Congress,* Graz, Austria, papers on CD-ROM, pp. 6.

Omran, M.N. (2005) *Modelling stage-discharge curves, velocity and boundary shear stress distributions in natural and artificial channls using a depth averaged model*. PhD thesis, University of Birmingham, Birmingham, UK.

Osyczka, A. (2002) *Evolutionary algorithms for single and multi-criteria design optimization.* Physica-Verlag, Heidelberg,, New York.

Ozturk, H.U. (2005) *Discharge predictions using ANN in sloping rectangular channels with free overfall*. MSc thesis, Middle East technical University, Ankara, Turkey.

Pagliara, S. (1995) Discussion on "End depth in trapezoidal and exponential channels" by S. Murty Bhallamudi. *Journal of Hydraulic Research,* IAHR, 33 (2): 283–286.

Pagliara, S. and Viti, C. (1995) Discussion on "Discharge prediction in smooth trapezoidal free overfall" by R. D. Gupta, M. Jamil and M. Moshin. *Journal of Irrigation and Drainage Engineering,* ASCE, 121 (1): 128-130.

Pal, M. and Goel, A. (2006) Prediction of the end-depth ratio and discharge in semi-circular and circular shaped channels using support vector machines. *Flow Measurement and Instrumentation,* Elsevier Ltd, 17 (1): 49-57.

Pal, M. and Goel, A. (2007) Estimation of discharge and end depth in trapezoidal channel by support vector machines. *Water Resources Management,* 21 (10): 1763-1780.

Patel, V.C. (1965) Calibration of the Preston tube and limitations on its use in pressure gradients. *Journal of Fluid Mechanics,* Cambridge University Press, 23 185-208.

Perera, B.J.C. and Siriwardene, N.R. (2006) Selection of genetic algorithm operators for urban drainage model parameter optimisation. *Mathematical and Computer Modelling,* Elsevier, 44 (5-6): 415-429.

Perkins, H.J. (1970) The formation of streamwise vorticity in turbulent flow. *Journal of Fluid Mechanics,* Cambridge University Press, 44 (04): 721-740.

Petersen, B. (2000) *Calibration, identifiability and optimal experimental design of activated sludge models*. PhD thesis thesis, Ghent University, Ghent, Belgium.

Pizzuto, J.E. (1991) A numerical model for calculating the distributions of velocity and boundary shear stress across irregular straight open channels. *Water Resources Research,* 27 (9): 2457-2466.

Poli, R., Langdon, W.B. and McPhee, N.F. (2008) *A field guide to genetic programming*. Lulu.com Publisher, www.gp-field-guide.org.uk

Powell, M.A. (1995) Metrology and mathematics in ancient Mesopotamia. In Sasson, M. (Ed.) *Civilizations of the ancient Near East.* Scribners, New York, 1941-1958.

Preston, J.H. (1954) The Determination of Turbulent Skin Friction by Means of Pitot Tubes. *Journal of the Royal Aeronautical Society,* 58 109-121.

Price, R.K. and Jemberie, A.A. (2005) The application of hydroinformatics. In Knight, D.W. & Shamseldin, A.Y. (Eds.) *River basin modelling for flood risk mitigation.* Taylor & Francis/Balkema, London, IK, 109-126.

Pyle, D. (1999) *Data Preparation for Data Mining*. Morgan Kaufmann, San Francisco.

Raghuwanshi, M.M. and Kakde, O.G. (2006) Survey on multiobjective evolutionary and real coded genetic Algorithms. *8th Asia Pacific Symposium on Intelligent and Evolutionary Systems*, Cairns, Queensland, Australia, 11: 150–161.

Raikar, R.V., Nagesh Kumar, D. and Dey, S. (2004) End depth computation in inverted semicircular channels using ANNs. *Flow Measurement and Instrumentation,* Elsevier Ltd, 15 (5-6): 285-293.

Rajaratnam, N. and Muralidhar, D. (1964a) End depth for circular channels. *Journal of the Hydraulics Division,* ASCE, 90 (2): 99-119.

Rajaratnam, N. and Muralidhar, D. (1964b) End depth for exponential channels. *Journal of the Irrigation and Drainage Division,* ASCE, 90 (1): 17-39.

Rajaratnam, N. and Muralidhar, D. (1968a) Characteristics of rectangular free overfall. *Journal of Hydraulic Research,* IAHR, 6 (3): 233–258.

Rajaratnam, N. and Muralidhar, D. (1968b) The rectangular free overfall. *Journal of the Hydraulics Division,* ASCE, 94 (3): 849–850.

Rajaratnam, N. and Muralidhar, D. (1969) Boundary shear stress distribution in rectangular open channels. *La Houille Blanche,* 24 (6): 603-609.

Rajaratnam, N. and Muralidhar, D. (1970) The trapezoidal free overfall. *Journal of Hydraulic Research,* IAHR, 8 (4): 419–447.

Rajaratnam, N. and Muralidhar, D. (1976) Roughness effect of rectangular free overfall. *Journal of the Hydraulics Division,* ASCE, 102 (5): 559-614.

Ramamurthy, A.S., Qu, J. and Vo, D. (2006) VOF model for simulation of a free overfall in trapezoidal channels. *Journal of Irrigation and Drainage Engineering,* ASCE, 132 (4): 425-428.

Reed, P., Kollat, J.B. and Devireddy, V.K. (2007) Using interactive archives in evolutionary multiobjective optimization: A case study for long-term groundwater monitoring design. *Environmental Modelling and Software*, Elsevier Ltd, 22 (5): 683-692.

Replogle, J.A. (1962) Discussion on "End depth at a drop in trapezoidal channels" by M.H. Diskin. *Journal of the Hydraulics Division,* ASCE, 88 (2): 161–165.

Reynolds, A.J. (1974) *Turbulent flow in engineering*. John Wiley & Sons, Great Britain.

Rezaei, B. (2006) *Overbank flow in compound channels with prismatic and non prismatic floodplains*. PhD thesis, University of Birmingham, Birmingham, UK.

Rhodes, D.G. and Knight, D.W. (1995) Lateral shear in wide compound duct. *Journal of Hydraulic Engineering,* ASCE, 121 (11): 829-832.

Rodi, W. (1995) Turbulence models and their application in hydraulics: a state-of-the-art review, third edition. *Applied Mechanics Reviews,* ASME, 48 (3): 33.

Rodriguez-Fernandez, M., Balsa-Canto, E., Egea, J.A. and Banga, J.R. (2007) Identifiability and robust parameter estimation in food process modeling: application to a drying model. *Journal of Food Engineering,* Elsevier, 83 (3): 374-383.

Romanowicz, R.J., Beven, K.J. and Tawn, J. (1996) Bayesian calibration of flood inundation models. In Anderson, M.G. & Walling, D.E. (Eds.) *Floodplain Processes*. Wiley, Chichester, 333-360.

Rothlauf, F. (2006) *Representations for Genetic and Evolutionary Algorithms*. Springer-Verlag, Berlin Heidelberg.

Rouse, H. (1936) Discharge characteristics of the free overfall. *Civil Engineering,* ASCE, 6 (4): 257-260.

Rouse, H. (1943) Discussion on "Energy loss at the base of a free overfall" by W.L. Moore. *Transactions of ASCE,* ASCE, 108: 1383-1387.

Rouse, H. (1946) *Elementary mechanics of fluids*. John Wiley and Sons, New York.

Rouse, H. (1959) *Advanced mechanics of fluids*. Wiley & Sons, New York.

Rouse, H. (1965) Critical analysis of open-channel resistance. *Journal of the Hydraulics Division,* ASCE, 91 (HY4, Part 1): 1-25.

Ryan, C., Collins, J.J. and O Neill, M. (1998) Grammatical evolution: Evolving programs for an arbitrary language. *Proceedings of the 1st European Workshop on Genetic Programming, EuroGP'98,* Paris, France, 1391: 83-83.

Sambridge, M. and Gallagher, K. (1993) Earthquake hypocenter location using genetic algorithms. *Bulletin of the Seismological Society of America*, 83 (5): 1467-1467.

Samuels, P.G. (1988) Lateral shear layers in compound channels. *Proceedings of the International Conference on Fluvial Hydraulics*, Budapest, Hungary.

Samuels, P.G. (1989) Some analytical aspects of depth averaged flow models. *Proceedings of the International Conference on Hydraulic and Environmental Modelling of Coastal, Estuarine and River Waters*, Bradford, UK,

Sarkar, D. and Modak, J.M. (2006) Optimal design of multiproduct batch chemical plant using NSGA-II. *Asia-Pacific Journal of Chemical Engineering*, John Wiley and Sons Ltd, 1 (1-2): 13-20.

Sastry, K. (2007) *Genetic algorithms and genetic programming for multiscale modeling: Applications in materials science and chemistry and advances in scalability*. PhD thesis, University of Illinois at Urbana-Champaign, Illinois, USA.

Sato, S., Otori, K., Takizawa, A., Sakai, H., et al. (2002) Applying genetic algorithms to the optimum design of a concert hall. *Journal of Sound and Vibration*, Academic Press, 258 (3): 517-526.

Sayre, W.W. and Chamberlain, A.R. (1964) Exploratory laboratory study of lateral turbulent diffusion at the surface of an alluvial channel. *U.S. Geological Survey*, Circular 484.

Schaffer, J.D. (1985) Multiple objective optimization with vector evaluated genetic algorithms. *Proceedings of the First International Conference on Genetic Algorithm and their Applications*, 93-100.

Scheuren, J.M., de Waroux, O.P., Below, R., Guha-Sapir, D., et al. (2008) *Annual disaster statistical review: The numbers and trends 2007*, Brussels, CRED based on the : EM-DAT: The OFDA/CRED, International Disaster Database.

Schlichting, H. (1979) *Boundary Layer Theory*. 7th edition, McGraw-Hill, London.

Sharifi, S., Knight, D.W. and Sterling, M. (2008) Modelling flow using SKM and a multi-objective evolutionary algorithm. *RiverFlow 2008*. [Eds. Altinakar, M.S., Kokpinar, M.A., Aydin, I., Cokgar, S. & Kirkgoz, S.], Cesme, Turkey, 3: 2149-2158.

Sharifi, S., Knight, D.W. and Sterling, M. (2009a) A novel application of a multi-objective evolutionary algorithm in open channel flow modelling. *Journal of Hydroinformatics*, IWA Publishing, 11 (1): 31-50.

Sharifi, S., Sterling, M. and Knight, D.W. (2009b) End-Depth Ratio Prediction in Rectangular and Trapezoidal Channels Using Genetic Programming. *Proceedings of 17th UK Conference on Computational Mechanics ACME 2009*. [Ed. Sansour, C.], Nottingham, UK, 105-108.

Sharifi, S., Sterling, M., and Knight, D.W. (2009c) Prediction of End-Depth Ratio in Open Channels Using Genetic Programming, *Journal of Hydroinformatic* (in Press).

Sharma, S.K. and Irwin, G.W. (2003) Fuzzy coding of genetic algorithms. *IEEE Transactions on Evolutionary Computation,* IEEE, 7 (4): 344-355.

Shiono, K. and Knight, D.W. (1988) Two-dimensional analytical solution for a compound channel. *Proceedings of the 3rd International Symposium on Refined Flow Modelling and Turbulence Measurements,* Tokyo, Japan, 503-510.

Shiono, K. and Knight, D.W. (1990) Mathematical models of flow in two or multi stage straight channels. *Proceedings of the Conference on River Flood Hydraulics*. [Ed. White, W.R.], Wallingford, 229-238.

Shiono, K. and Knight, D.W. (1991) Turbulent open-channel flows with variable depth across the channel. *Journal of Fluid Mechanics,* Cambridge University Press, 222 617-646.

Sigaud, O. and Wilson, S.W. (2007) Learning classifier systems: a survey. *Soft Computing,* Springer-Verlag, 11 (11): 1065-1078.

Silberschatz, A. and Tuzhilin, A. (1996) What makes patterns interesting in knowledge discovery systems. *IEEE Transactions on Knowledge and Data Engineering,* IEEE, 8 (6): 970-974.

Silva, S. (2005) *GPLAB: A genetic programming toolbox for MATLAB.* http://gplab.sourceforge.net.

Simoudis, E., Livezey, B. and Kerber, R. (1996) Integrating inductive and deductive reasoning for data mining. In Fayyad, U.M., Piatetsky-Shapiro, G., Smyth, P. & Uthurusamy, R. (Eds.) *Advances in Knowledge Discovery and Data Mining.* AAAI/MIT Press, 353-373.

Smith, C.D. (1962) Brink depth for a circular channel. *Journal of the Hydraulics Division,* ASCE, 88 (6): 125–134.

Smith, L.I. (2002) *A tutorial on principal components analysis,* University of Otago, www.cs.otago.ac.nz/cosc453/student_tutorials/principal_components.pdf.

Solomatine, D.P. and Ostfeld, A. (2008) Data-driven modelling: Some past experiences and new approaches. *Journal of Hydroinformatics,* IWA Publishing, 10 (1): 3-22.

Southwell, R.V. and Vaisey, G. (1943) Relaxation methods applied to engineering problems. VIII. Plane-potential problems involving specified normal gradients. *Proceedings of the Royal Society of London, Series A (Mathematical and Physical Sciences),* 182 129-151.

Spooner, J. and Shiono, K. (2003) Modelling of meandering channels for overbank flow. *Proceedings of the Institution of Civil Engineers: Water and Maritime Engineering,* Thomas Telford Services Ltd, 156 (3): 225-233.

Steinley, D. (2006) K-means clustering: A half-century synthesis. *British Journal of Mathematical & Statistical Psychology,* British Psychological Society, 59 1-34.

Sterling, M. (1998) *A study of boundary shear stress, flow resistance and the free overfall in open channels with a circular cross-section*. PhD thesis, University of Birmingham, Birmingham, UK.

Sterling, M. and Knight, D.W. (2001) The free overfall as a flow measuring device in a circular channel. *Proceedings of the Institution of Civil Engineers: Water, Maritime and Energy*, Thomas Telford Services Ltd., 148 (4): 235-243.

Streeter, V.L. (1985) *Fluid mechanics*. 8th edition, McGraw-Hill, New York.

Subramanya, K. and Keshavamurthy, K. (1987) End depth in a trapezoidal channel. *Journal of Institution of Engineers (India)*, 67 (C16): 343–346.

Sumner, N.R., Fleming, P.M. and Bates, B.C. (1997) Calibration of a modified SFB model for twenty-five Australian catchments using simulated annealing. *Journal of Hydrology*, Elsevier Science, 197 (1-4): 166-188.

Sun, D., Benekohal, R. and Waller, S. (2003) Multi-objective traffic signal timing optimization using non-dominated sorting genetic algorithm II, Lecture Notes in Computer Science. *Genetic and Evolutionary Computation - GECCO 2003*. Springer-Verlag, Berlin, 210-210.

Tan, K.C., Lee, T.H. and Khor, E.F. (2002) Evolutionary algorithms for multi-objective optimization: Performance assessments and comparisons. *Artificial Intelligence Review*, Kluwer Academic Publishers, 17 (4): 253-290.

Tennekes, H. and Lumley, J.L. (1997) *A first course in turbulence*. M.I.T. Press, Cambridge, Massachusetts.

TFFF (1963) Friction factor in open channels, Report of the ASCE Task Force. *Journal of Hydraulic Engineering*, ASCE, 89 (2): 97–143.

Tominaga, A., Nezu, I., Ezaki, K. and Nakagawa, H. (1989) Three-dimensional turbulent structure in straight open channel flows. *Journal of Hydraulic Research*, IAHR, 27 (1): 149-173.

Tracy, H.J. and Lester, C.M. (1961) Resistance coefficients and velocity distribution, smooth rectangular channel. *U.S. Geological Survey*, Water-supply paper 1592-A: 1-18.

Tran, K.D. (2005) Elitist Non-Dominated Sorting GA-II (NSGA-II) as a parameter-less multi-objective genetic algorithm. *Proceedings of IEEE Southeast Conference*, Piscataway, NJ, United States, 359-367.

Turan, C. (2002) *Experimental studies on free overfall*. MSc Thesis thesis, Middle East Technical University, Ankara, Turkey.

USBR (2001) *Water Measurement Manual*. Washington DC, U.S. Bureau of Reclamation, U.S Government Printing Office.

Versteeg, H.K. and Malalasekera, W. (1995) *An introduction to computational fluid dynamics: The finite volume method approach*. Longman Scientific and Technical, Malaysia.

Vidal, J.P., Moisan, S., Faure, J.B. and Dartus, D. (2005) Towards a reasoned 1D river model calibration. *Journal of Hydroinformatics,* IWA Publishing, 7 (2): 91-104.

Vreugdenhil, C.B. and Wijbenga, J.H.A. (1982) Computation of flow patterns in rivers. *Journal of the Hydraulics Division,* ASCE, 108 (11): 1296-1310.

Vrugt, J.A., Gupta, H.V., Bastidas, L.A., Bouten, W. and Soroushian, S. (2003) Effective and efficient algorithm for multiobjective optimization of hydrologic models. *Water Resources Research,* American Geophysical Union, 39 (8): SWC51-SWC519.

Wagener, T. and Gupta, H.V. (2005) Model identification for hydrological forecasting under uncertainty. *Stochastic Environmental Research and Risk Assessment,* 19 (6): 378-387.

Wagener, T., Wheater, H.S. and Gupta, H.V. (2003) Identification and evaluation of watershed models. In Duan, Q., Sorooshian, S., Gupta, H.V., Rousseau, A. & Turcotte, R. (Eds.) *Advances in calibration of watershed models. AGU Monograph.* American Geophysical Union, Washington, USA, 29-47.

Wagener, T., Wheater, T. and Gypta, H.V. (2004) *Rainfall-runoff modelling in gauaged and ungauaged catchments*. Imperial College Press, London, UK.

Wang, Q.J. (1991) The genetic algorithm and its application to calibrating conceptual rainfall-runoff models. *Water Resources Research,* 27 (9): 2467-2471.

Wardlaw, R. and Sharif, M. (1999) Evaluation of genetic algorithms for optimum reservoir system operation. *Journal of Water Resources Planning and Management,* ASCE, 125 (1): 25-33.

Webel, G. and Schatzmann, M. (1984) Transverse mixing in open channel flow. *Journal of Hydraulic Engineering,* ASCE, 110 (4): 423-435.

Weisberg, S. (1980) *Applied linear regression*. Wiley, New York.

Weise, T. (2009) *Global optimization algorithms - theory and application*. ebook, www.it-weise.de/projects/book.pdf. Last accessed 1 May 2009.

Wheater, H.S., Wagener, T. and McIntyre, N. (2007) Calibration, uncertainty, and regional analysis of conceptual rainfall-runoff models. In Wheater, H., Sorooshian, S. & Sharma, K.D. (Eds.) *Hydrological Modelling in Arid and Semi-Arid Areas.* Cambridge University Press.

White, F.M. (1999) *Fluid mechanics*. 4th edition, McGraw-Hill, Boston.

William, E. and Northern, J. (2008) Genetic Programming Lab (GPLab) tool set version 3.0, Region 5 Conference, IEEE, Kansas City, MO, United states, 1-6.

Wormleaton, P.R. (1988) Determination of discharge in compound channels using the dynamic equation for lateral velocity distribution. *Proceedings of the International Conference on Fluvial Hydraulics*, Budapest, Hungary, 98-103.

Wormleaton, P.R. (1996) Floodplain secondary circulation as a mechanism for flow and shear stress redistribution in straight compound channels. In Ashworth, Bennett, Best, and McLelland (Ed.) *Coherent flow structures in open channels.* Wiley, New York, 581–608.

Yang, S.Q., Tan, S.K. and Lim, S.Y. (2004) Velocity distribution and dip-phenomenon in smooth uniform open channel flows. *Journal of Hydraulic Engineering,* ASCE, 130 (12): 1179-1186.

Yang, S.Q. and Lim, S.Y. (1997) Mechanism of energy transportation and turbulent flow in a 3D channel. *Journal of Hydraulic Engineering,* ASCE, 123 (8): 684-692.

Yang, S.Q. and Lim, S.Y. (2005) Boundary shear stress distributions in trapezoidal channels. *Journal of Hydraulic Research,* IAHR, 43 (1): 98-102.

Yang, S.Q., Lim, S.Y., Guo, J. and Julien, P.Y. (2006) Discussion of "shear stress in smooth rectangular open-channel flows" by J. Guo and P.Y. Julien. *Journal of Hydraulic Engineering,* ASCE, 132 (6): 629-631.

Yapo, P.O., Gupta, H.V. and Sorooshian, S. (1998) Multi-objective global optimization for hydrologic models. *Journal of Hydrology*, Elsevier Science, 204 (1-4): 83-97.

Yardimci, A. (2007) A survey on use of soft computing methods in medicine, Porto, Portugal, 4669 LNCS: 69-79.

Yen, B.C. (1991) Hydraulic resistance in open channels. In Yen, B.C. (Ed.) *Channel Flow: Centennial of Manning's Formula.* Water Resources Publications, Littleton, CO., 1-135.

Yen, B.C. (2002) Open channel flow resistance. *Journal of Hydraulic Engineering*, ASCE, 128 (1): 20-39.

Yotsukura, N., Fischer, H.B. and Sayre, W.W. (1970) Measurement of mixing characteristics of the Missouri River between Sioux City, Iowa, and Plattsmouth, Nebraska. *U.S. Geological Survey*, Water Supply paper 1899-G.

Yuen, K.W.H. (1989) *A study of boundary shear stress, flow resistance and momentum transfer in open channels with simple and compound trapezoidal cross sections*. PhD thesis, University of Birmingham, Birmingham, UK.

Yuen, K.W.H. and Knight, D.W. (1990) Critical flow in a two stage channel. *Proceedings of the International Conference on River Flood Hydraulics*. [Ed. White, W.R.], Wallingford, UK, 267-276.

Zelinka, I., Oplatkova, Z. and Nolle, L. (2005) Analytic programming - symbolic regression by means of arbitrary evolutionary algorithms. *International Journal of Simulation: Systems, Science &amp, Technology,* United Kingdom Simulation Society, 6 (9): 44-56.

Zheng, Y. and Jin, Y.C. (1998) Boundary shear in rectangular ducts and channels. *Journal of Hydraulic Engineering*, ASCE, 124 (1): 86-89.

Zitzler, E., Deb, K. and Thiele, L. (1999) *Comparison of multiobjective evolutionary algorithms: Empirical results.* Computer Engineering and Networks Laboratory (TIK), Swiss Federal Institute of Technology (ETH) Zurich, Technical Report 70,.

BIBLIOGRAPHY

Biggiero, V. (1963) Sul tracciamento del profili delle vene liquide. *Proceedings of Convegno di Idraulica*. Pisa, Italy, 1-19.

Boussinesq, J. (1877) Théorie de l'Écoulement Tourbillant, Mem. *Présentés par Divers Savants Acad. Sci. Inst. Fr.*, 23:46-50.

Buckingham, E. (1914) On physically similar systems: Illustrations of the use of dimensional equations. *Physical Review N.S.*, IV: 345-376.

Ciray, C. (1970) On Wall-Shear Stress Determination, *Journal of Pure Applied Sciences*, METU, 3:41-54

Colebrook C.F. and White C.M. (1937) Experiments with fluid friction in roughened pipes, *Proceedings of the Royal Society*, A161, 367.

Collins, J. (1959) Darwin's impact on philosophy. *Thoughts*, 34:185-248

Darcy H. (1857) Experimental Research Relating to the Movement of Water in Pipes, *Mallet-Bachelier*, Paris.

Darwin, C. (1859) *On the origin of species by means of natural selection, or the preservation of favored races in the struggle for life*, 1st edition, John Murray, London, UK.

Edgeworth, F.Y. (1881) *Mathematical psychics: An essay on the application of mathematics to the moral sciences*. Kegan Paul, London.

Hampel, C.G. (1963), Explanations and predictions by covering laws, In B. Baumrin (Ed.) *Philosophy of Science*, The Delaware seminar, John Wiley, 107-133

Johnson, W. (1942) The importance of side-wall friction in bed-load investigation. *Civil Engineering*, 12:329-331.

Keulegan, G.H. (1938) Laws of turbulent flow in open channels. *Journal of Research of the National Bureau of Standards*, 21(RP1151): 707-741.

Kolmogorov, A.N. (1941) Local structure of turbulence in an incompressible fluid for very large Reynolds numbers. In Friedlander, S.K. & Topper, L. (Eds.) *Turbulence: Classic Papers on Statistical Theory*. Interscience Publishers, New York.

Kolmogorov, A.N. (1941) The local structure of turbulence in incompressible viscous fluids at very large Reynolds numbers, *Dokl. Akad. Nauk. SSSR*, 30: 301-305

Ledoux, J. W. (1924) Open end flume water meter based on exponential equation, *Engineering News Record*, September 25.

Leighly, J. B. (1932) Toward a theory of the morphologic significance of turbulence in the flow of water in streams. *Geography*, University of California Publications, 6(1): 1-22.

Markland, E. (1965) Calculation of flow at a free overfall by relaxation method. *Proceedings of Institution of Civil Engineers*. 31:71-78.

Meyer-Peter, E. and Müller, R. (1948) Formulas for bed-load transport. *Proceedings of the 2nd Meeting*, IAHR, Stockholm, Sweden, 39-64.

Moody, M.L. (1947) An approximate formula for pipe friction factors. *Transactions of ASME*, 69:1005.

Nikuradse, J. (1926) *Untersuchungen uber die geschwindigkeits verteilung in turbulenten stromungen*. PhD Thesis, Gottingen, VDI Forsch,

Nikuradse J. (1933) Translates to: Laws of flow in rough pipes, Verein deutscher Ingenieure, *Forschubgsheft*, No. 361, Berlin.

Pareto, V. (1897) Cours d'economie politique, *Rouge et Cie*, Paris.

Prandtl, L. (1921) Applications of Modern Hydrodynamics to Aeronautics, *NASA*, Report No. 116.

Prandtl, L. (1925) Bericht uber untersuchungen zur ausgebildete Turbulenz, Z. angew. *Math. Mech.*, 5:136–139.

Prandtl, L. (1926) Uber die ausgebildete turbulenz, Verh. *2nd Intl Kong. Fur Tech. Mech*., Zurich [English translation, NACA Tech. Memo. 435]

Prandtl, L. (1932) Meteorologische Anwendungen der Strömungslehre, *Beitr. Phys. Frei. tmos*., 18: 188-202.

Prandtl, L. (1933) Neuere Ergebnisse der Turbulenzforschung, *Z. Ver. Deut. Ing*. 77, 105-114

Rechenberg, I. (1965) Cybernetic solution path of an experimental problem. Library Translation 1122, *Royal Aircraft Establishment*, Farnborough, UK.

Reynolds O., (1883) An experimental investigation of the circumstances which determine whether the motion of water shall be direct or sinuous, and of the law of resistance in parallel channels. *Philosophical Transactions of the Royal Society*.

Reynolds O., (1884) On the two manners of motion of water. *Royal Institution Proceedings.*

Richardson, L.F. (1922) Weather prediction by numerical process. Cambridge University Press, Cambridge.

Rouse, H. (1932), *Verteilung der hydraulischen energie bei einem lotrechten absturz*, Thesis, TU Karlsruhe, Germany, (in German).

Rouse, H. (1936) Discharge characteristics of the free overfall. *Civil Engineering*, 6 (4): 257-260.

Saint-Venant de B. (1843) Note a joindre au Memoire sur la dynamique des fluides, Comptes-rendus hebdomadaires des Seances de l'Acadamie des Sciences, Vol. 17.

Van Leer, B.R. (1922) The California Pipe Method of Water Measurement, *Engineering News Record*, August 3.

Van Leer, B.R. (1924) The California Pipe Method of Water Measurement, *Engineering News Record*, August 21.

Vanoni, V.A. and Brooks, N.H., (1957) Laboratory studies of the roughness and suspended load of alluvial streams, Sedimentation Lab., *California Institute of Technology*, Report E-68, Pasadena, USA.

Weisbach J. (1845) *Lehrbuch der ingenieur- und maschinen-mechanik*, Braunschwieg.

Zegzhda A.P. (1938) Theory of similarity and methods of design of models for hydraulic engineering, *Teoriia*, Gosstroiizdat, Leningrad.

WORLD WIDE WEB

CES, (2008) Conveyance Estimation System. http://www.river-conveyance.net. Last accessed 15 May 2009.

Flow Database at the University of Birmingham (2009). http://flowdata.bham.ac.uk. Last accessed 20 May 2009.

GPlab (2009) A Genetic Programming toolbox for MATLAB. http://gplab.sourceforge.net. Last accessed 20 April 2009

APPENDIX II

SKM MATRIX APPROACH

II.1 FOUR PANEL TRAPEZOIDAL CHANNEL

1- SKM matrix approach for a four panel trapezoidal channel

$0 \le y \le b/2$ $\qquad U_d^1 = [A_1 e^{\gamma_1 y} + A_2 e^{-\gamma_1 y} + k_1]^{1/2}$

$b/2 \le y \le b$ $\qquad U_d^2 = [A_3 e^{\gamma_2 y} + A_4 e^{-\gamma_2 y} + k_2]^{1/2}$

$b \le y \le b + b'/2$ $\qquad U_d^3 = [A_5 \xi_3^{\alpha_3} + A_6 \xi_3^{-(\alpha_3+1)} + \omega_3 \xi_3 + \eta_3]^{1/2}$

$b + b'/2 \le y \le b + b'$ $\qquad U_d^4 = [A_7 \xi_4^{\alpha_4} + A_8 \xi_4^{-(\alpha_4+1)} + \omega_4 \xi_4 + \eta_4]^{1/2}$

Boundary Conditions:

1- $U_d^4\big|_{\xi_4=0} = 0 \rightarrow \quad A_8 = 0 \quad$ or $\quad \eta_4 = 0$

2- $U_d^3\big|_{\xi_3=H/2} = U_d^4\big|_{\xi_4=H/2} \rightarrow$

$$A_5(H/2)^{\alpha_3} + A_6(H/2)^{-(\alpha_3+1)} + \omega_3(H/2) + \eta_3 = A_7(H/2)^{\alpha_4} + A_8(H/2)^{-(\alpha_4+1)} + \omega_4(H/2) + \eta_4$$

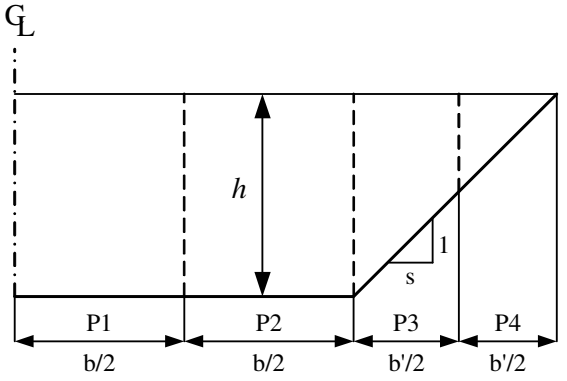

Figure (II-1): 4 panel structure

Appendix II – SKM Matrix Approach

3- $\mu_3 \left.\frac{\partial U_d^3}{\partial y}\right|_{\xi_3=H/2} = \mu_4 \left.\frac{\partial U_d^4}{\partial y}\right|_{\xi_4=H/2} \rightarrow$

$$\mu_3\left[A_5\alpha_3(H/2)^{\alpha_3-1} - A_6(\alpha_3+1)(H/2)^{-(\alpha_3+2)} + \omega_3\right] = \mu_4\left[A_7\alpha_4(H/2)^{\alpha_4-1} - A_8(\alpha_4+1)(H/2)^{-(\alpha_4+2)} + \omega_4\right]$$

4- $U_d^2\big|_{y=b} = U_d^3\big|_{\xi=H} \rightarrow \quad A_3e^{\gamma_2 b} + A_4e^{-\gamma_2 b} + k_2 = A_5H^{\alpha_3} + A_6H^{-(\alpha_3+1)} + \omega_3 H + \eta_3$

5- $\mu_2 \left.\frac{\partial U_d^2}{\partial y}\right|_{y=b} = \mu_3 \left.\frac{\partial U_d^3}{\partial y}\right|_{\xi=H} \rightarrow \quad -\mu_2\gamma_2 s\left[A_3e^{\gamma_2 b} - A_4e^{-\gamma_2 b}\right] = \mu_3\left[A_5\alpha_3H^{\alpha_3-1} - A_6(\alpha_3+1)H^{-(\alpha_3+2)} + \omega_3\right]$

6- $U_d^1\big|_{y=b/2} = U_d^2\big|_{y=b/2} \rightarrow \quad A_1e^{\gamma_1(b/2)} + A_2e^{-\gamma_1(b/2)} + k_1 = A_3e^{\gamma_2(b/2)} + A_4e^{-\gamma_2(b/2)} + k_2$

7- $\mu_1 \left.\frac{\partial U_d^1}{\partial y}\right|_{y=b/2} = \mu_2 \left.\frac{\partial U_d^2}{\partial y}\right|_{y=b/2} \rightarrow \quad \mu_1(A_1\gamma_1e^{\gamma_1(b/2)} - A_2\gamma_1e^{-\gamma_1(b/2)}) = \mu_2(A_3\gamma_2e^{\gamma_2(b/2)} - A_4\gamma_2e^{-\gamma_2(b/2)})$

8- $\left.\frac{\partial U_d^1}{\partial y}\right|_{y=0} = 0 \rightarrow A_1\gamma_1e^0 - A_2\gamma_1e^0 = 0 \quad \rightarrow A_1\gamma_1 - A_2\gamma_1 = 0 \quad \rightarrow A_1 = A_2$

$$\begin{bmatrix} 1 & -1 & 0 & 0 & 0 & 0 & 0 & 0 \\ 0 & 0 & 0 & 0 & 0 & 0 & 0 & 1 \\ 0 & 0 & 0 & 0 & (H/2)^{\alpha_3} & (H/2)^{-(\alpha_3+1)} & -(H/2)^{\alpha_4} & -(H/2)^{-(\alpha_4+1)} \\ 0 & 0 & 0 & 0 & \mu_3\alpha_3(H/2)^{(\alpha_3-1)} & -\mu_3(\alpha_3+1)(H/2)^{-(\alpha_3+2)} & -\mu_4\alpha_4(H/2)^{(\alpha_4-1)} & \mu_4(\alpha_4+1)(H/2)^{-(\alpha_4+2)} \\ 0 & 0 & e^{\gamma_2 b} & e^{-\gamma_2 b} & -H^{\alpha_3} & -H^{-(\alpha_3+1)} & 0 & 0 \\ 0 & 0 & -\mu_2\gamma_2 s e^{\gamma_2 b} & \mu_2\gamma_2 s e^{-\gamma_2 b} & -\mu_3\alpha_3H^{(\alpha_3-1)} & \mu_3(\alpha_3+1)H^{-(\alpha_3+2)} & 0 & 0 \\ e^{\gamma_1(b/2)} & e^{-\gamma_1(b/2)} & -e^{\gamma_2(b/2)} & -e^{-\gamma_2(b/2)} & 0 & 0 & 0 & 0 \\ \mu_1\gamma_1e^{\gamma_1(b/2)} & -\mu_1\gamma_1e^{-\gamma_1(b/2)} & -\mu_2\gamma_2e^{\gamma_2(b/2)} & \mu_2\gamma_2e^{-\gamma_2(b/2)} & 0 & 0 & 0 & 0 \end{bmatrix} \times \begin{bmatrix} A_1 \\ A_2 \\ A_3 \\ A_4 \\ A_5 \\ A_6 \\ A_7 \\ A_8 \end{bmatrix} = \begin{bmatrix} 0 \\ 0 \\ (H/2)(\omega_4-\omega_3)+\eta_4-\eta_3 \\ \mu_4\omega_4 - \mu_3\omega_3 \\ \omega_3H + \eta_3 - k_2 \\ \mu_3\omega_3 \\ k_2 - k_1 \\ 0 \end{bmatrix} \quad \text{II-2}$$

II.2 FIVE PANEL TRAPEZOIDAL CHANNEL

$0 \le y \le b/4$ $\qquad U_d^1 = [A_1 e^{\gamma_1 y} + A_2 e^{-\gamma_1 y} + k_1]^{1/2}$

$b/4 \le y \le 3b/4$ $\qquad U_d^2 = [A_3 e^{\gamma_2 y} + A_4 e^{-\gamma_2 y} + k_2]^{1/2}$

$3b/4 \le y \le b$ $\qquad U_d^3 = [A_5 e^{\gamma_3 y} + A_6 e^{-\gamma_3 y} + k_3]^{1/2}$

$b \le y \le b + b'/2$ $\qquad U_d^4 = [A_7 \xi_4^{\alpha_4} + A_8 \xi_4^{-(\alpha_4+1)} + \omega_4 \xi_4 + \eta_4]^{1/2}$

$b + b'/2 \le y \le b + b'$ $\qquad U_d^5 = [A_9 \xi_5^{\alpha_5} + A_{10} \xi_5^{-(\alpha_5+1)} + \omega_5 \xi_5 + \eta_5]^{1/2}$

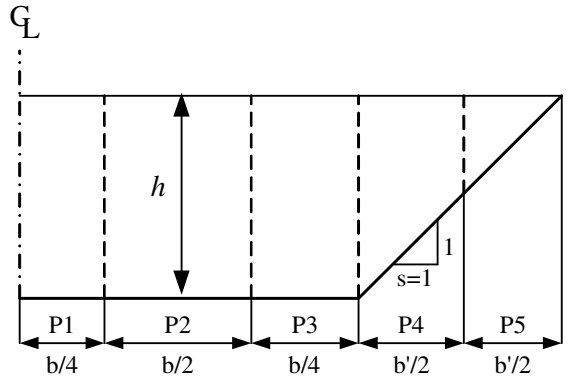

Figure (II-2): 5 panel structure

Boundary Conditions:

1- $U_d^5\big|_{\xi_5=0} = 0 \rightarrow \quad A_{10} = 0 \quad \text{or} \quad \eta_5 = 0$

2- $U_d^4\big|_{\xi_4=H/2} = U_d^5\big|_{\xi_5=H/2} \rightarrow$

$$A_7(H/2)^{\alpha_4} + A_8(H/2)^{-(\alpha_4+1)} + \omega_4(H/2) + \eta_4 = A_9(H/2)^{\alpha_5} + A_{10}(H/2)^{-(\alpha_5+1)} + \omega_5(H/2) + \eta_5$$

Appendix II – SKM Matrix Approach

3- $\mu_4 \left.\frac{\partial U_d^4}{\partial y}\right|_{\xi_4=H/2} = \mu_5 \left.\frac{\partial U_d^5}{\partial y}\right|_{\xi_5=H/2} \rightarrow \quad \mu_4\left[A_7\alpha_4(H/2)^{\alpha_4-1} - A_8(\alpha_4+1)(H/2)^{-(\alpha_4+2)} + \omega_4\right] = \mu_5\left[A_9\alpha_5(H/2)^{\alpha_5-1} - A_{10}(\alpha_5+1)(H/2)^{-(\alpha_5+2)} + \omega_5\right]$

4- $\left.U_d^3\right|_{y=b} = \left.U_d^4\right|_{\xi_4=H} \rightarrow \quad A_5 e^{\gamma_3 b} + A_6 e^{-\gamma_3 b} + k_3 = A_7 H^{\alpha_4} + A_8 H^{-(\alpha_4+1)} + \omega_4 H + \eta_4$

5- $\mu_3 \left.\frac{\partial U_d^3}{\partial y}\right|_{y=b} = \mu_4 \left.\frac{\partial U_d^4}{\partial y}\right|_{\xi_4=H} \rightarrow \quad -\mu_3\gamma_3 s\left[A_5 e^{\gamma_3 b} - A_6 e^{-\gamma_3 b}\right] = \mu_4\left[A_7\alpha_4 H^{\alpha_4-1} - A_8(\alpha_4+1)H^{-(\alpha_4+2)} + \omega_4\right]$

6- $\left.U_d^2\right|_{y=3b/4} = \left.U_d^3\right|_{y=3b/4} \rightarrow \quad A_3 e^{\gamma_2(3b/4)} + A_4 e^{-\gamma_2(3b/4)} + k_2 = A_5 e^{\gamma_3(3b/4)} + A_6 e^{-\gamma_3(3b/4)} + k_3$

7- $\mu_2 \left.\frac{\partial U_d^2}{\partial y}\right|_{y=3b/4} = \mu_3 \left.\frac{\partial U_d^3}{\partial y}\right|_{y=3b/4} \rightarrow \quad \mu_2(A_3\gamma_2 e^{\gamma_2(3b/4)} - A_4\gamma_2 e^{-\gamma_2(3b/4)}) = \mu_3(A_5\gamma_3 e^{\gamma_3(3b/4)} - A_6\gamma_3 e^{-\gamma_3(3b/4)})$

8- $\left.U_d^1\right|_{y=b/4} = \left.U_d^2\right|_{y=b/4} \rightarrow \quad A_1 e^{\gamma_1(b/4)} + A_2 e^{-\gamma_1(b/4)} + k_1 = A_3 e^{\gamma_2(b/4)} + A_4 e^{-\gamma_2(b/4)} + k_2$

9- $\mu_1 \left.\frac{\partial U_d^1}{\partial y}\right|_{y=b/4} = \mu_2 \left.\frac{\partial U_d^2}{\partial y}\right|_{y=b/4} \rightarrow \quad \mu_1(A_1\gamma_1 e^{\gamma_1(b/4)} - A_2\gamma_1 e^{-\gamma_1(b/4)}) = \mu_2(A_3\gamma_2 e^{\gamma_2(b/4)} - A_4\gamma_2 e^{-\gamma_2(b/4)})$

10- $\left.\frac{\partial U_d^1}{\partial y}\right|_{y=0} = 0 \rightarrow A_1\gamma_1 e^0 - A_2\gamma_1 e^0 = 0 \quad \rightarrow A_1\gamma_1 - A_2\gamma_1 = 0 \quad \rightarrow A_1 = A_2$

Appendix II – SKM Matrix Approach

$$
\begin{bmatrix}
-1 & 1 & 0 & 0 & 0 & 0 & 0 & 0 & 0 & 0 \\
0 & 0 & 0 & 0 & 0 & 0 & 0 & 0 & 0 & 1 \\
0 & 0 & 0 & 0 & 0 & 0 & (\frac{H}{2})^{\alpha_4} & (\frac{H}{2})^{-(\alpha_4+1)} & -(\frac{H}{2})^{\alpha_5} & -(\frac{H}{2})^{-(\alpha_5+1)} \\
0 & 0 & 0 & 0 & 0 & 0 & \mu_4\alpha_4(\frac{H}{2})^{\alpha_4-1} & -\mu_4(\alpha_4+1)(\frac{H}{2})^{-(\alpha_4+2)} & -\mu_5\alpha_5(\frac{H}{2})^{\alpha_5-1} & \mu_5(\alpha_5+1)(\frac{H}{2})^{-(\alpha_5+2)} \\
0 & 0 & 0 & 0 & e^{\gamma_3 b} & e^{-\gamma_3 b} & -H^{\alpha_4} & -H^{-(\alpha_4+1)} & 0 & 0 \\
0 & 0 & 0 & 0 & -\mu_3\gamma_3 s e^{\gamma_3 b} & \mu_3\gamma_3 s e^{-\gamma_3 b} & -\mu_4\alpha_4 H^{(\alpha_4-1)} & \mu_4(\alpha_4+1)H^{-(\alpha_4+2)} & 0 & 0 \\
0 & 0 & e^{\gamma_2(3b/4)} & e^{-\gamma_2(3b/4)} & -e^{\gamma_3(3b/4)} & -e^{-\gamma_3(3b/4)} & 0 & 0 & 0 & 0 \\
0 & 0 & \mu_2\gamma_2 e^{\gamma_2(3b/4)} & -\mu_2\gamma_2 e^{-\gamma_2(3b/4)} & -\mu_3\gamma_3 e^{\gamma_3(3b/4)} & \mu_3\gamma_3 e^{-\gamma_3(3b/4)} & 0 & 0 & 0 & 0 \\
e^{\gamma_1(b/4)} & e^{-\gamma_1(b/4)} & -e^{\gamma_2(b/4)} & -e^{-\gamma_2(b/4)} & 0 & 0 & 0 & 0 & 0 & 0 \\
\mu_1\gamma_1 e^{\gamma_1(b/4)} & -\mu_1\gamma_1 e^{-\gamma_1(b/4)} & -\mu_2\gamma_2 e^{\gamma_2(b/4)} & \mu_2\gamma_2 e^{-\gamma_2(b/4)} & 0 & 0 & 0 & 0 & 0 & 0
\end{bmatrix}
$$

$$
\times
\begin{bmatrix} A_1 \\ A_2 \\ A_3 \\ A_4 \\ A_5 \\ A_6 \\ A_7 \\ A_8 \\ A_9 \\ A_{10} \end{bmatrix}
=
\begin{bmatrix}
0 \\ 0 \\ (\frac{H}{2})(\omega_5-\omega_4)+\eta_5-\eta_4 \\ \mu_5\omega_5-\mu_4\omega_4 \\ \omega_4 H+\eta_4-k_3 \\ \mu_4\omega_4 \\ k_3-k_2 \\ 0 \\ k_2-k_1 \\ 0
\end{bmatrix}
$$

II.3 16 PANEL RIVER SECTION

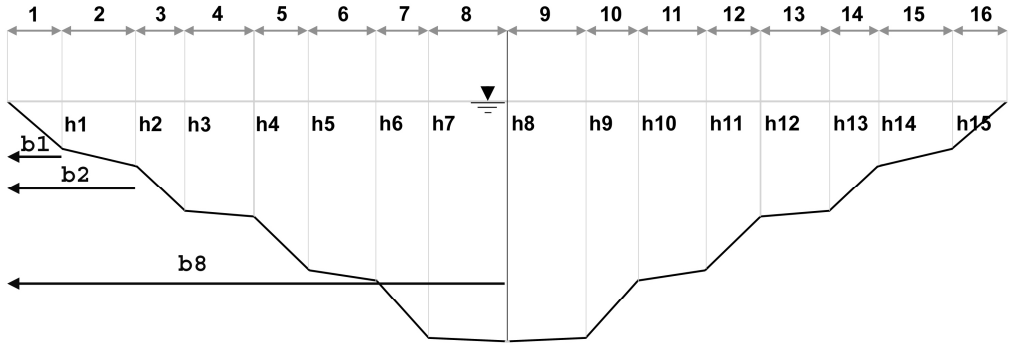

Table (II-3): 16 panel structure

$$U_d^{(1)} = \left[A_{11}\xi_1^{\alpha_1} + A_{12}\xi_1^{-(\alpha_1+1)} + \omega_1\xi_1 + \eta_1 \right]^{1/2}$$

$$U_d^{(2)} = \left[A_{21}\xi_2^{\alpha_2} + A_{22}\xi_2^{-(\alpha_2+1)} + \omega_2\xi_2 + \eta_2 \right]^{1/2}$$

$$U_d^{(3)} = \left[A_{31}e^{\gamma_3 y} + A_{32}e^{-\gamma_3 y} + k_3 \right]^{1/2}$$

$$U_d^{(4)} = \left[A_{41}e^{\gamma_4 y} + A_{42}e^{-\gamma_4 y} + k_4 \right]^{1/2}$$

$$U_d^{(5)} = \left[A_{51}\xi_5^{\alpha_5} + A_{52}\xi_5^{-(\alpha_5+1)} + \omega_5\xi_5 + \eta_5 \right]^{1/2}$$

$$U_d^{(6)} = \left[A_{61}\xi_6^{\alpha_6} + A_{62}\xi_6^{-(\alpha_6+1)} + \omega_6\xi_6 + \eta_6 \right]^{1/2}$$

$$U_d^{(7)} = \left[A_{71}e^{\gamma_7 y} + A_{72}e^{-\gamma_7 y} + k_7 \right]^{1/2}$$

$$U_d^{(8)} = \left[A_{81}e^{\gamma_8 y} + A_{82}e^{-\gamma_8 y} + k_8 \right]^{1/2}$$

$$U_d^{(9)} = \left[A_{91}e^{\gamma_9 y} + A_{92}e^{-\gamma_9 y} + k_9 \right]^{1/2}$$

$$U_d^{(10)} = \left[A_{101}e^{\gamma_{10} y} + A_{102}e^{-\gamma_{10} y} + k_{10} \right]^{1/2}$$

$$U_d^{(11)} = \left[A_{111}\xi_{11}^{\alpha_1} + A_{112}\xi_{11}^{-(\alpha_{11}+1)} + \omega_{11}\xi_{11} + \eta_{11} \right]^{1/2}$$

$$U_d^{(12)} = \left[A_{121}\xi_{12}^{\alpha_{12}} + A_{122}\xi_{12}^{-(\alpha_{12}+1)} + \omega_{12}\xi_{12} + \eta_{12} \right]^{1/2}$$

$$U_d^{(13)} = \left[A_{131}e^{\gamma_{13} y} + A_{132}e^{-\gamma_{13} y} + k_{13} \right]^{1/2}$$

$$U_d^{(14)} = \left[A_{141}e^{\gamma_{14} y} + A_{142}e^{-\gamma_{14} y} + k_{14} \right]^{1/2}$$

$$U_d^{(15)} = \left[A_{151}\xi_{15}^{\alpha_{15}} + A_{152}\xi_{15}^{-(\alpha_{15}+1)} + \omega_{15}\xi_{15} + \eta_{15} \right]^{1/2}$$

$$U_d^{(16)} = \left[A_{161}\xi_{16}^{\alpha_{16}} + A_{162}\xi_{16}^{-(\alpha_{16}+1)} + \omega_{16}\xi_{16} + \eta_{16} \right]^{1/2}$$

Appendix II – SKM Matrix Approach

Boundary conditions

1- $U_d^{(1)}\Big|_{\xi_1=0}=0 \rightarrow U_d^{(1)}=\left[A_{11}\xi_1^{\alpha_1}+A_{12}\xi_1^{-(\alpha_1+1)}+\omega_1\xi_1+\eta_1\right]^{1/2}\Big|_{\xi_1=0}=0 \rightarrow A_{11}\xi_1^{\alpha_1}+\omega_1\xi_1+\eta_1=0\ ,\ A_{12}=0$

2- $U_d^{(1)}|_{\xi_1=h_1}=U_d^{(2)}|_{\xi_2=h_1} \rightarrow \left[A_{11}\xi_1^{\alpha_1}+A_{12}\xi_1^{-(\alpha_1+1)}+\omega_1\xi_1+\eta_1\right]^{1/2}|_{\xi_1=h_1}=\left[A_{21}\xi_2^{\alpha_2}+A_{22}\xi_2^{-(\alpha_2+1)}+\omega_2\xi_2+\eta_2\right]^{1/2}|_{\xi_2=h_1}$

$\rightarrow A_{11}h_1^{\alpha_1}+A_{12}h_1^{-(\alpha_1+1)}-A_{21}h_1^{\alpha_2}-A_{22}h_1^{-(\alpha_2+1)}=\omega_2h_1+\eta_2-\omega_1h_1-\eta_1$

3- $\mu_1\dfrac{dU_d^{(1)}}{dy}\Big|_{\xi_1=h_1}=\mu_2\dfrac{dU_d^{(2)}}{dy}\Big|_{\xi_2=h_1} \rightarrow -\dfrac{\mu_1\left[A_{11}\alpha_1h_1^{\alpha_1-1}-A_{12}(\alpha_1+1)h_1^{-(\alpha_1+2)}+\omega_1\right]}{2s_1\left[A_{11}h_1^{\alpha_1}+A_{12}h_1^{-(\alpha_1+1)}+\omega_1h_1+\eta_1\right]^{1/2}}=-\dfrac{\mu_2\left[A_{21}\alpha_2h_1^{\alpha_2-1}-A_{22}(\alpha_2+1)h_1^{-(\alpha_2+2)}+\omega_2\right]}{2s_2\left[A_{21}h_1^{\alpha_2}+A_{22}h_1^{-(\alpha_2+1)}+\omega_2h_1+\eta_2\right]^{1/2}}$

$\rightarrow -\mu_1s_2A_{11}\alpha_1h_1^{\alpha_1-1}+\mu_1s_2A_{12}(\alpha_1+1)h_1^{-(\alpha_1+2)}+\mu_2s_1A_{21}\alpha_2h_1^{\alpha_2-1}-\mu_2s_1A_{22}(\alpha_2+1)h_1^{-(\alpha_2+2)}=-\mu_2s_1\omega_2+\mu_1s_2\omega_1$

4- $U_d^{(2)}|_{\xi_2=h_2}=U_d^{(3)}|_{y=b_2} \rightarrow \left[A_{21}\xi_2^{\alpha_2}+A_{22}\xi_{22}^{-(\alpha_2+1)}+\omega_2\xi_2+\eta_2\right]^{1/2}|_{\xi_2=h_2}=\left[A_{31}e^{\gamma_3y}+A_{32}e^{-\gamma_3y}+k_3\right]^{1/2}|_{y=b_2}$

$\rightarrow A_{21}h_2^{\alpha_2}+A_{22}h_2^{-(\alpha_2+1)}-A_{31}e^{\gamma_3b_2}-A_{32}e^{-\gamma_3b_2}=-\omega_2h_2-\eta_2+k_3$

5- $\mu_2\dfrac{dU_d^{(2)}}{dy}\Big|_{\xi_2=h_2}=\mu_3\dfrac{dU_d^{(3)}}{dy}\Big|_{y=b_2} \rightarrow -\dfrac{\mu_2\left[A_{21}\alpha_2h_2^{\alpha_2-1}-A_{22}(\alpha_2+1)h_2^{-(\alpha_2+2)}+\omega_2\right]}{2s_2\left[A_{21}h_2^{\alpha_2}+A_{22}h_2^{-(\alpha_2+1)}+\omega_2h_2+\eta_2\right]^{1/2}}=\dfrac{\mu_3\gamma_3\left[A_{31}e^{\gamma_3b_2}-A_{32}e^{-\gamma_3b_2}\right]}{2\left[A_{31}e^{\gamma_3b_2}+A_{32}e^{-\gamma_3b_2}+k_3\right]^{1/2}}$

$\rightarrow -\mu_2\left[A_{21}\alpha_2h_2^{\alpha_2-1}-A_{22}(\alpha_2+1)h_2^{-(\alpha_2+2)}+\omega_2\right]=\mu_3\gamma_3s_2\left[A_{31}e^{\gamma_3b_2}-A_{32}e^{-\gamma_3b_2}\right]$

$$\rightarrow -\mu_2 A_{21}\alpha_2 h_2^{\alpha_2-1} + \mu_2 A_{22}(\alpha_2+1)h_2^{-(\alpha_2+2)} - \mu_3\gamma_3 s_2 A_{31}e^{\gamma_3 b_2} + \mu_3\gamma_3 s_2 A_{32}e^{-\gamma_3 b_2} = \mu_2\omega_2$$

6- $U_d^{(3)}|_{y=b_3} = U_d^{(4)}|_{y=b_3} \rightarrow \left[A_{31}e^{\gamma_3 y} + A_{32}e^{-\gamma_3 y} + k_3\right]^{1/2}|_{y=b_3} = \left[A_{41}e^{\gamma_4 y} + A_{42}e^{-\gamma_4 y} + k_4\right]^{1/2}|_{y=b_3} \rightarrow A_{31}e^{\gamma_3 b_3} + A_{32}e^{-\gamma_3 b_3} - A_{41}e^{\gamma_4 b_3} - A_{42}e^{-\gamma_4 b_3} = k_4 - k_3$

7- $\mu_3 \frac{dU_d^{(3)}}{dy}\Big|_{y=b_3} = \mu_4 \frac{dU_d^{(4)}}{dy}\Big|_{y=b_3} \rightarrow \frac{\mu_3\gamma_3\left[A_{31}e^{\gamma_3 b_3} - A_{32}e^{-\gamma_3 b_3}\right]}{2\left[A_{31}e^{\gamma_3 b_3} + A_{32}e^{-\gamma_3 b_3} + k_3\right]^{1/2}} = \frac{\mu_4\gamma_4\left[A_{41}e^{\gamma_4 b_3} - A_{42}e^{-\gamma_4 b_3}\right]}{2\left[A_{41}e^{\gamma_4 b_3} + A_{42}e^{-\gamma_4 b_3} + k_4\right]^{1/2}}$

$$\rightarrow \mu_3\gamma_3 A_{31}e^{\gamma_3 b_3} - \mu_3\gamma_3 A_{32}e^{\gamma_3 b_3} - \mu_4\gamma_4 A_{41}e^{\gamma_4 b_3} + \mu_4\gamma_4 A_{42}e^{\gamma_4 b_3} = 0$$

8- $U_d^{(4)}|_{y=b_4} = U_d^{(5)}|_{\xi_5=h_4} \rightarrow \left[A_{41}e^{\gamma_4 y} + A_{42}e^{-\gamma_4 y} + k_4\right]^{1/2}|_{y=b_4} = \left[A_{51}\xi_5^{\alpha_5} + A_{52}\xi_5^{-(\alpha_5+1)} + \omega_5\xi_5 + \eta_5\right]^{1/2}|_{\xi_5=h_4}$

$$\rightarrow A_{41}e^{\gamma_4 b_4} + A_{42}e^{-\gamma_4 b_4} - A_{51}h_4^{\alpha_5} - A_{52}h_4^{-(\alpha_5+1)} = \omega_5 h_4 + \eta_5 - k_4$$

9- $\mu_4 \frac{dU_d^{(4)}}{dy}\Big|_{y=b_4} = \mu_5 \frac{dU_d^{(5)}}{dy}\Big|_{\xi_5=h_4} \rightarrow \frac{\mu_4\gamma_4\left[A_{41}e^{\gamma_4 b_4} - A_{42}e^{-\gamma_4 b_4}\right]}{2\left[A_{41}e^{\gamma_4 b_4} + A_{42}e^{-\gamma_4 b_4} + k_4\right]^{1/2}} = -\frac{\mu_5\left[A_{51}\alpha_5 h_4^{\alpha_5-1} - A_{52}(\alpha_5+1)h_4^{-(\alpha_5+2)} + \omega_5\right]}{2s_5\left[A_{51}h_4^{\alpha_5} + A_{52}h_4^{-(\alpha_5+1)} + \omega_5 h_5 + \eta_5\right]^{1/2}}$

$$\rightarrow \mu_4\gamma_4 s_5\left[A_{41}e^{\gamma_4 b_4} - A_{42}e^{-\gamma_4 b_4}\right] = -\mu_5\left[A_{51}\alpha_5 h_4^{\alpha_5-1} - A_{52}(\alpha_5+1)h_4^{-(\alpha_5+2)} + \omega_5\right]$$

$$\rightarrow \mu_4\gamma_4 s_5 A_{41}e^{\gamma_4 b_4} - \mu_4\gamma_4 s_5 A_{42}e^{-\gamma_4 b_4} + \mu_5 A_{51}\alpha_5 h_4^{\alpha_5-1} - \mu_5 A_{52}(\alpha_5+1)h_4^{-(\alpha_5+2)} = -\mu_5\omega_5$$

10- ….

APPENDIX III

MATLAB IMPLEMENTATION OF NSGA-II

III.1 INPUT

```
function [B H S ss YU UD YT TT Qt]=innput(temp1)

% This function contains the inputs for a typical test case:
% Yuen 406 (2b/h=7.04 h=0.2131)
% temp1 is a temporary variable

DATTA=[0.075 0.07299 23.3700e-3 1];

B=DATTA(1);      % half of channel width
H=DATTA(2);      % channel depth
S=DATTA(3);      % channel slope
ss=DATTA(4);     % side slope ss(H):1(V)

Qt=39.0;         % total discharge (lit/s)

% YU is the lateral coordinates of depth-averaged velocity data (m)
% UD is the relative depth-averaged velocity (m/s)

YU=[0.0000  0.0200  0.0400  0.0600  0.0800  0.1000  0.1200  0.1400
0.1480];
UD=[2.5883  2.5687  2.5225  2.4899  2.3749  2.2098  2.0198  1.4395
0.0000];

% YT is the lateral coordinates of bed shear stress data (m)
% UD is the relative bed shear stress (N/m^2)
YT=[0.0000  0.0050  0.0100  0.0150  0.0200  0.0250  0.0300  0.0350
0.0400...
    0.0450  0.0500  0.0550  0.0600  0.0650  0.0700  0.0740  0.0757
0.0785...
    0.0821  0.0856  0.0891  0.0927  0.0997  0.1068  0.1139  0.1210
0.1280...
    0.1351  0.1422  0.1480];
TT=[11.1883 11.2800 11.3372 11.4402 11.5973 11.6600 11.8409 11.8922
11.9675...
    11.9476 11.9363 11.9647 11.7868 12.1876 11.2184 9.9693  9.9693
11.3558...
    11.5773 11.5216 11.3944 11.1295 10.6580 10.0651 9.8064  9.6417
9.2615...
    8.2118  5.7539  0.0000];
```

III.2 INITIAL_POPULATION.M

```
function [f min max]= initial_population(N,B,H,S,ss,YU,YT,UD,TT)
% This function generates the initial population set
% N is the Population size
% B,H,S,ss,YU,YT,UD,TT are the data related to the experimental test case
V = 12;     % number of decision variables
O = 2;      % number of objectives
K = V + O;
%% Defining the range for all the decision variables.
% min is a vector with the lower bounds of all variables
% mix is a vector with the upper bounds of all variables
for i=1:V/3
    % the range for friction (f)
    min((i-1)*3+1)=0.01;
    max((i-1)*3+1)=0.50;
    % the range for dimensionless eddy viscosity (Lamda)
    min((i-1)*3+2)=0.05;
    max((i-1)*3+2)=1.50;
    % the range for secondary term (Gamma)
    min((i-1)*3+3)=-1.50;
    max((i-1)*3+3)=1.50;
end

%% Initialize the decision variables and evaluating the objective functions
for i = 1 : N
    % Initialize the decision variables
    for j = 1 : V
        f(i,j) = min(j) + (max(j) - min(j))*rand(1);
    end
%   Evaluate evaluating the objective functions
    f(i,V + 1: K) = evaluate_objective(f(i,:),B,H,S,ss,YU,YT,UD,TT);
end
```

III.3 EVALUATE_OBJECTIVE.M

```
function f = evaluate_objective(x,B,H,S,ss,YU,YT,UD,TT)
% This function evaluates the objective functions
% x is the decision variables
% B,H,S,ss,YU,YT,UD,TT are the data related to the experimental test case

%% SKM is first used to find the calculated values of depth-averaged
velocity and bed shear stress at positions where experimental measurements
are available
[Ud,To]=SKM(B,H,S,ss,YU,YT,x(1,1),x(1,2),x(1,3),x(1,4),x(1,5),x(1,6),x(1,7)
...
    ,x(1,8),x(1,9),x(1,10),x(1,11),x(1,12));

%% The objective functions are evaluated by calculating the sum of squared
errors
err1=(Ud-UD).^2;
err2=(To-TT).^2;
f(1)=sum(err1);
f(2)=sum(err2);
```

III.4 SKM.M

```
function
[Ud,To]=SKM(B,H,S,ss,YU,YT,f1,La1,Ga1,f2,La2,Ga2,f3,La3,Ga3,f4,La4,Ga4)
% This function calculates the depth-averaged velocity and bed shear stress
% at defined lateral positions using SKM
% B,H,S,ss,YU,YT are the data related to the experimental test case
% f is the friction
% La is the dimension less eddy viscosity
% Ga is the secondary flow term

%% Arranging SKM inputs
h(1:4)=H;               % channel depth
S0(1:4)=S;              % bed slope
BP=ss*H;                % width of sloping section
f=[f1 f2 f3 f4];
La=[La1 La2 La3 La4];
Ga=[Ga1 Ga2 Ga3 Ga4];

%% Calculating SKM variables (Beta,k,Nu,Mu,alpha,omega,eta)
Beta=Ga./(9.81*1000.*h.*S0);
k =8*9.81.*S0.*h./f.*(1-Beta);
Nu=((2./La).^0.5).*((f/8).^0.25).*(1./h);
Mu=La.*(f./8).^0.5;
alfa=-0.5+0.5.*(1+ss*(1+ss^2)^0.5./La.*(8.*f).^0.5).^0.5;
omega=9.81*S./((1+ss^2)^0.5/ss.*f./8-La./ss^2.*(f./8).^0.5);
eta=-Ga./((1+ss^2)^0.5/ss*1000.*f./8);

%% Calculating the variable matrix (X)
X=ones(8,8);

X(1,1)=1;
X(1,2)=-1;
X(1,3:8)=0;

X(2,1:7)=0;
X(2,8)=1;

X(3,1:4)=0;
X(3,5)=(H/2)^alfa(1,3);
X(3,6)=(H/2)^(-1*(alfa(1,3)+1));
X(3,7)=-1*(H/2)^alfa(1,4);
X(3,8)=-1*(H/2)^(-1*(alfa(1,4)+1));

X(4,1:4)=0;
X(4,5)=Mu(1,3)*alfa(1,3)*(H/2)^(alfa(1,3)-1);
X(4,6)=-Mu(1,3)*(alfa(1,3)+1)*(H/2)^(-1*(alfa(1,3)+2));
X(4,7)=-Mu(1,4)*alfa(1,4)*(H/2)^(alfa(1,4)-1);
X(4,8)=Mu(1,4)*(alfa(1,4)+1)*(H/2)^(-1*(alfa(1,4)+2));

X(5,1:2)=0;
X(5,3)=exp(Nu(1,2)*B);
X(5,4)=exp(-1*Nu(1,2)*B);
X(5,5)=-1*H^alfa(1,3);
X(5,6)=-1*H^(-1*(alfa(1,3)+1));
X(5,7:8)=0;
```

```
X(6,1:2)=0;
X(6,3)=-1*Mu(1,2)*Nu(1,2)*ss*exp(Nu(1,2)*B);
X(6,4)=Mu(1,2)*Nu(1,2)*ss*exp(-1*Nu(1,2)*B);
X(6,5)=-1*Mu(1,3)*alfa(1,3)*H^(alfa(1,3)-1);
X(6,6)=Mu(1,3)*(alfa(1,3)+1)*H^(-1*(alfa(1,3)+2));
X(6,7:8)=0;


X(7,1)=exp(Nu(1,1)*(B/2));
X(7,2)=exp(-1*Nu(1,1)*(B/2));
X(7,3)=-exp(Nu(1,2)*(B/2));
X(7,4)=-exp(-1*Nu(1,2)*(B/2));
X(7,5:8)=0;

X(8,1)=Mu(1,1)*Nu(1,1)*exp(Nu(1,1)*(B/2));
X(8,2)=-Mu(1,1)*Nu(1,1)*exp(-1*Nu(1,1)*(B/2));
X(8,3)=-Mu(1,2)*Nu(1,2)*exp(Nu(1,2)*(B/2));
X(8,4)=Mu(1,2)*Nu(1,2)*exp(-1*Nu(1,2)*(B/2));
X(8,5:8)=0;

%% Introducing the coefficient matrix (C)
C(1,1)=0;
C(2,1)=0;
C(3,1)=(H/2)*(omega(1,4)-omega(1,3))+eta(1,4)-eta(1,3);
C(4,1)=Mu(1,4)*omega(1,4)-Mu(1,3)*omega(1,3);
C(5,1)=omega(1,3)*H+eta(1,3)-k(1,2);
C(6,1)=Mu(1,3)*omega(1,3);
C(7,1)=k(1,2)-k(1,1);
C(8,1)=0;

%% Calculating the A coefficient matrix
A=X\C;

%% Calculating depth-averaged velocity (Ud)
y=YU;
for i=1:length(YU);
    if y(1,i)<(B/2)
        Ud(1,i)=real((A(1,1)*exp(Nu(1,1)*y(1,i))+A(2,1)*exp(-1*Nu(1,1)*...
            y(1,i))+k(1,1))^0.5);
    else
        if y(1,i)<(B)
            Ud(1,i)=real((A(3,1)*exp(Nu(1,2)*y(1,i))+A(4,1)*exp(-
1*Nu(1,2)...
                *y(1,i))+k(1,2))^0.5);
        else
            if y(1,i)<(B+BP/2)
                kessi=H-(y(1,i)-B)/ss;
                Ud(1,i)=real((A(5,1)*kessi^alfa(1,3)+A(6,1)*kessi^(-1*...
                    (alfa(1,3)+1))+omega(1,3)*kessi+eta(1,3))^0.5);
            else
                kessi=H-(y(1,i)-B)/ss;
                Ud(1,i)=real((A(7,1)*kessi^alfa(1,4)+A(8,1)*kessi^(-1*...
                    (alfa(1,4)+1))+omega(1,4)*kessi+eta(1,4))^0.5);
            end
        end
    end
end
```

```
%% Caclulating bed shear stress (To)
y=YT;

for i=1:length(YT);
    if y(1,i)<(B/2)
        Udd(1,i)=real((A(1,1)*exp(Nu(1,1)*y(1,i))+A(2,1)*exp(-1*Nu(1,1)*...
            y(1,i))+k(1,1))^0.5);
        To(1,i)=real(1000.*f(1,1)/8.*Udd(1,i).^2);
    else
        if y(1,i)<(B)
            Udd(1,i)=real((A(3,1)*exp(Nu(1,2)*y(1,i))+A(4,1)*exp(-
1*Nu(1,2)...
                *y(1,i))+k(1,2))^0.5);
            To(1,i)=real(1000.*f(1,2)/8.*Udd(1,i).^2);
        else
            if y(1,i)<(B+BP/2)
                kessi=H-(y(1,i)-B)/ss;
                Udd(1,i)=real((A(5,1)*kessi^alfa(1,3)+A(6,1)*kessi^(-1*...
                    (alfa(1,3)+1))+omega(1,3)*kessi+eta(1,3))^0.5);
                To(1,i)=real(1000.*f(1,3)/8.*Udd(1,i).^2);
            else
                kessi=H-(y(1,i)-B)/ss;
                Udd(1,i)=real((A(7,1)*kessi^alfa(1,4)+A(8,1)*kessi^(-1*...
                    (alfa(1,4)+1))+omega(1,4)*kessi+eta(1,4))^0.5);
                To(1,i)=real(1000.*f(1,4)/8.*Udd(1,i).^2);
            end
        end
    end
end
```

III.5 NON_DOMINATION_SORT.M

```
function f = non_domination_sort(x)
% This function sorts the current population based on non-domination.
% All individuals in the first front are given a rank of 1, the second
front individuals are assigned rank 2 and so on. After assigning the rank
the crowding in each front is calculated.

[N,M] = size(x);
M = 2;
V = 12;
front = 1;

F(front).f = [];
individual = [];
for i = 1 : N
    % Number of individuals that dominate this individual
    individual(i).n = 0;
    % Individuals which this individual dominate
    individual(i).p = [];
    for j = 1 : N
        dom_less = 0;
        dom_equal = 0;
        dom_more = 0;
        for k = 1 : M
            if (x(i,V + k) < x(j,V + k))
                dom_less = dom_less + 1;
            elseif (x(i,V + k) == x(j,V + k))
                dom_equal = dom_equal + 1;
            else
                dom_more = dom_more + 1;
            end
        end
        if dom_less == 0 & dom_equal ~= M
            individual(i).n = individual(i).n + 1;
        elseif dom_more == 0 & dom_equal ~= M
            individual(i).p = [individual(i).p j];
        end
    end
    if individual(i).n == 0
        x(i,M + V + 1) = 1;
        F(front).f = [F(front).f i];
    end
end
% Find the subsequent fronts
while ~isempty(F(front).f)
   Q = [];
   for i = 1 : length(F(front).f)
       if ~isempty(individual(F(front).f(i)).p)
            for j = 1 : length(individual(F(front).f(i)).p)
                individual(individual(F(front).f(i)).p(j)).n = ...
                    individual(individual(F(front).f(i)).p(j)).n - 1;
                if individual(individual(F(front).f(i)).p(j)).n == 0
                    x(individual(F(front).f(i)).p(j),M + V + 1) = ...
                        front + 1;
                    Q = [Q individual(F(front).f(i)).p(j)];
                end
```

```
            end
        end
    end
    front =  front + 1;
    F(front).f = Q;
end

[temp,index_of_fronts] = sort(x(:,M + V + 1));
for i = 1 : length(index_of_fronts)
    sorted_based_on_front(i,:) = x(index_of_fronts(i),:);
end
current_index = 0;
% Find the crowding distance for each individual in each front
for front = 1 : (length(F) - 1)
    objective = [];
    distance = 0;
    y = [];
    previous_index = current_index + 1;
    for i = 1 : length(F(front).f)
        y(i,:) = sorted_based_on_front(current_index + i,:);
    end
    current_index = current_index + i;
    % Sort each individual based on the objective
    sorted_based_on_objective = [];
    for i = 1 : M
        [sorted_based_on_objective, index_of_objectives] = ...
            sort(y(:,V + i));
        sorted_based_on_objective = [];
        for j = 1 : length(index_of_objectives)
            sorted_based_on_objective(j,:) = y(index_of_objectives(j),:);
        end
        f_max = ...
            sorted_based_on_objective(length(index_of_objectives), V + i);
        f_min = sorted_based_on_objective(1, V + i);
        y(index_of_objectives(length(index_of_objectives)),M + V + 1 +
i)...
            = Inf;
        y(index_of_objectives(1),M + V + 1 + i) = Inf;
         for j = 2 : length(index_of_objectives) - 1
            next_obj  = sorted_based_on_objective(j + 1,V + i);
            previous_obj  = sorted_based_on_objective(j - 1,V + i);
            if (f_max - f_min == 0)
                y(index_of_objectives(j),M + V + 1 + i) = Inf;
            else
                y(index_of_objectives(j),M + V + 1 + i) = ...
                     (next_obj - previous_obj)/(f_max - f_min);
            end
         end
    end
    distance = [];
    distance(:,1) = zeros(length(F(front).f),1);
    for i = 1 : M
        distance(:,1) = distance(:,1) + y(:,M + V + 1 + i);
    end
    y(:,M + V + 2) = distance;
    y = y(:,1 : M + V + 2);
    z(previous_index:current_index,:) = y;
end
f = z();
```

III.6 TOURNAMENT.M

```
function f = tournament(chromosome,pool_size,tour_size)
% This function selects the parents for reproduction
% The selection is based on tournament selection.
% chromosome is the current generation population from which the
individuals are selected to

[pop,variables] = size(chromosome);
rank = variables - 1;
distance = variables;

for i = 1 : pool_size
    for j = 1 : tour_size
        candidate(j) = round(pop*rand(1));
        if candidate(j) == 0
            candidate(j) = 1;
        end
        if j > 1
            while ~isempty(find(candidate(1 : j - 1) == candidate(j)))
                candidate(j) = round(pop*rand(1));
                if candidate(j) == 0
                    candidate(j) = 1;
                end
            end
        end
    end
    for j = 1 : tour_size
        c_obj_rank(j) = chromosome(candidate(j),rank);
        c_obj_distance(j) = chromosome(candidate(j),distance);
    end
    min_candidate = ...
        find(c_obj_rank == min(c_obj_rank));
    if length(min_candidate) ~= 1
        max_candidate = ...
        find(c_obj_distance(min_candidate) ==
max(c_obj_distance(min_candidate)));
        if length(max_candidate) ~= 1
            max_candidate = max_candidate(1);
        end
        f(i,:) = chromosome(candidate(min_candidate(max_candidate)),:);
    else
        f(i,:) = chromosome(candidate(min_candidate(1)),:);
    end
end
```

III.7 GENETIC_OPERATOR .M

```
function f = genetic_operator ...
(parent_population,Pc,muc,Pm,mum,B,H,S,ss,YU,YT,UD,TT,min,max)
% This function is utilized to produce offsprings from parent chromosomes
% by applying Simulated Binary Crossover (SBX) and Polynomial mutation.

% parent_population is the set of selected chromosomes.
% Pc is the probability of crossover
% muc is the distribution index for crossover
% mum - distribution index for mutation
% B,H,S,ss,YU,YT,UD,TT are the data related to the experimental test case
% min - a vector of lower bounds for the corresponding decsion variables
% max - a vector of upper bounds for the corresponding decsion variables

[N,ttemp] = size(parent_population);
clear 'ttemp'

M = 2;      % number of objectives
V = 12;     % number of variables
p = 1;

was_crossover = 0;
was_mutation = 0;
for i = 1 : N
    if rand(1) < Pc
        child_1 = [];
        child_2 = [];
        parent_1 = round(N*rand(1));
        if parent_1 < 1
            parent_1 = 1;
        end
        parent_2 = round(N*rand(1));
        if parent_2 < 1
            parent_2 = 1;
        end
        while
isequal(parent_population(parent_1,:),parent_population(parent_2,:))
            parent_2 = round(N*rand(1));
            if parent_2 < 1
                parent_2 = 1;
            end
        end
        parent_1 = parent_population(parent_1,:);
        parent_2 = parent_population(parent_2,:);
        for j = 1 : V
            % SBX (Simulated Binary Crossover)
            u(j) = rand(1);
            if u(j) <= 0.5
                bq(j) = (2*u(j))^(1/(muc+1));
            else
                bq(j) = (1/(2*(1 - u(j))))^(1/(muc+1));
            end
            child_1(j) = ...
                0.5*(((1 + bq(j))*parent_1(j)) + (1 - bq(j))*parent_2(j));
            child_2(j) = ...
                0.5*(((1 - bq(j))*parent_1(j)) + (1 + bq(j))*parent_2(j));
```

```
            % Make sure that the mutation does not result in variables out
            of the search space.
            if child_1(j) > max(j)
                child_1(j) = max(j);
            elseif child_1(j) < min(j)
                child_1(j) = min(j);
            end
            if child_2(j) > max(j)
                child_2(j) = max(j);
            elseif child_2(j) < min(j)
                child_2(j) = min(j);
            end
        end
        child_1(:,V + 1: M + V) =
evaluate_objective(child_1,B,H,S,ss,YU,YT,UD,TT);
        child_2(:,V + 1: M + V) =
evaluate_objective(child_2,B,H,S,ss,YU,YT,UD,TT);
        was_crossover = 1;
        was_mutation = 0;
    else
        parent_3 = round(N*rand(1));
        if parent_3 < 1
            parent_3 = 1;
        end
        child_3 = parent_population(parent_3,:);
        for j = 1 : V
           r(j) = rand(1);
           if r(j) < 0.5
               delta(j) = (2*r(j))^(1/(mum+1)) - 1;
           else
               delta(j) = 1 - (2*(1 - r(j)))^(1/(mum+1));
           end
           child_3(j) = child_3(j) + delta(j);
         % Make sure that the mutation does not result in variables out of
         % the search space.
          if child_3(j) > max(j);
               child_3(j) = max(j);
           elseif child_3(j) < min(j)
               child_3(j) = min(j);
           end
        end
        child_3(:,V + 1: M + V) =
evaluate_objective(child_3,B,H,S,ss,YU,YT,UD,TT);
        was_mutation = 1;
        was_crossover = 0;
    end
    if was_crossover
        child(p,:) = child_1;
        child(p+1,:) = child_2;
        was_cossover = 0;
        p = p + 2;
    elseif was_mutation
        child(p,:) = child_3(1,1 : M + V);
        was_mutation = 0;
        p = p + 1;
    end
end
f = child;
```

III.6 SELECT.M

```
function f  = select(inter_pop,pop)
% This function replaces the parents based on rank and crowding distance.
% inter_pop is the intermediate population
% pop is the number of population

[N,V] = size(inter_pop);
M = 2;
V = 12;

% Get the index for the population sort based on the rank
[temp,index] = sort(inter_pop(:,M + V + 1));

% Now sort the individuals based on the index
for i = 1 : N
    sorted_chromosome(i,:) = inter_pop(index(i),:);
end

% Find the maximum rank in the current population
max_rank = max(inter_pop(:,M + V + 1));

% Start adding each front based on rank and crowing distance until the
% whole population is filled.
previous_index = 0;
for i = 1 : max_rank
    current_index = max(find(sorted_chromosome(:,M + V + 1) == i));
    if current_index > pop
        remaining = pop - previous_index;
        temp_pop = ...
            sorted_chromosome(previous_index + 1 : current_index, :);
        [temp_sort,temp_sort_index] = ...
            sort(temp_pop(:, M + V + 2),'descend');
        for j = 1 : remaining
            f(previous_index + j,:) = temp_pop(temp_sort_index(j),:);
        end
        return;
    elseif current_index < pop
        f(previous_index + 1 : current_index, :) = ...
            sorted_chromosome(previous_index + 1 : current_index, :);
    else
        f(previous_index + 1 : current_index, :) = ...
            sorted_chromosome(previous_index + 1 : current_index, :);
        return;
    end
    previous_index = current_index;
end
```

APPENDIX IV

SKM PREDICTIONS OF DEPTH-AVERAGED VELOCITY AND BOUNDARY SHEAR STRESS

IV.1 FCF DATA

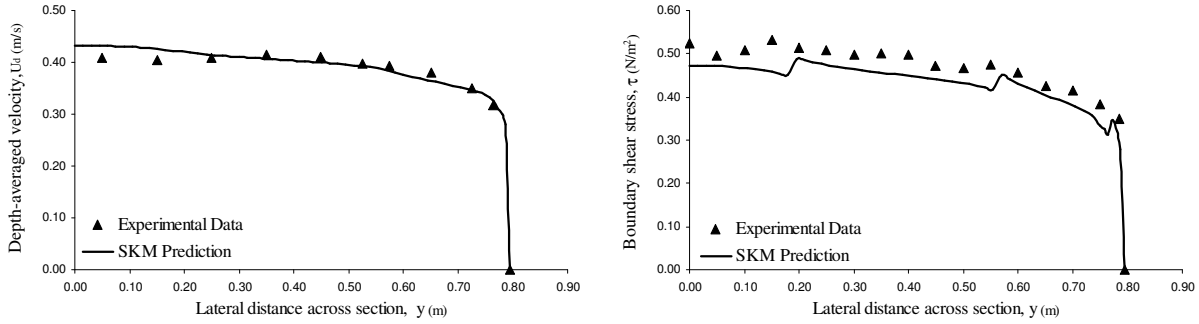

Figure (IV-1): FCF 0501; depth 0.0486m; Q_{data}=29.90 l.s^{-1}; Q_{SKM}=27.60 l.s^{-1}

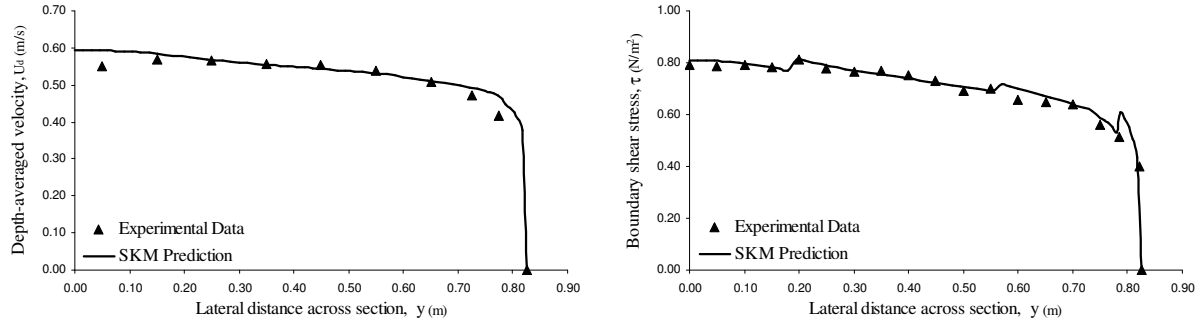

Figure (IV-2): FCF 7501; depth 0.0755m; Q_{data}=64.00 l.s^{-1}; Q_{SKM}=64.20 l.s^{-1}

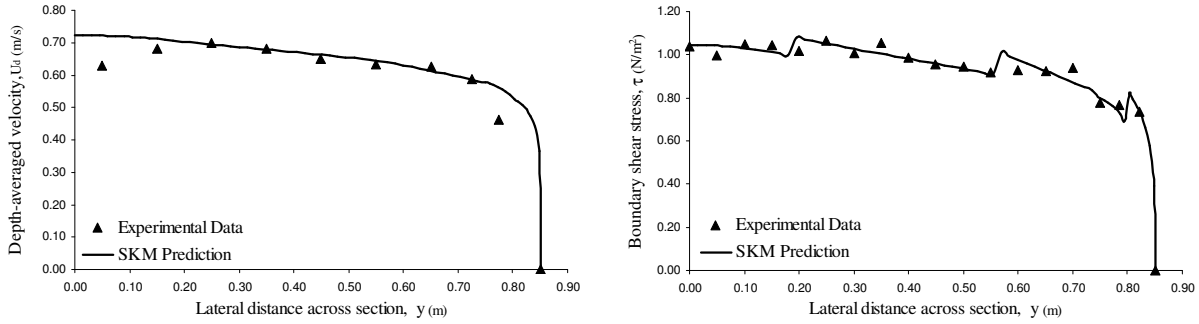

Figure (IV-3): FCF 1002; depth 0.1009m; Q_{data}=103.5 l.s^{-1}; Q_{SKM}=105.40 l.s^{-1}

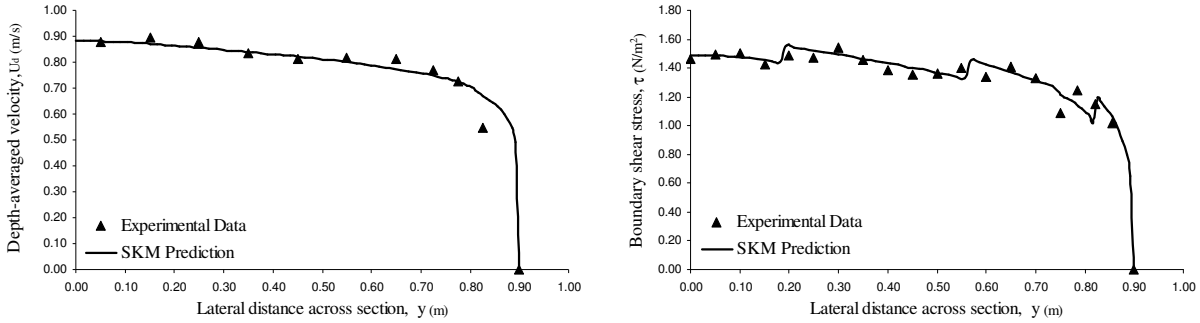

Figure (IV-4): FCF 1502; depth 0.1488m; Q_{data}=202.3 l.s^{-1}; Q_{SKM}=200.60 l.s^{-1}

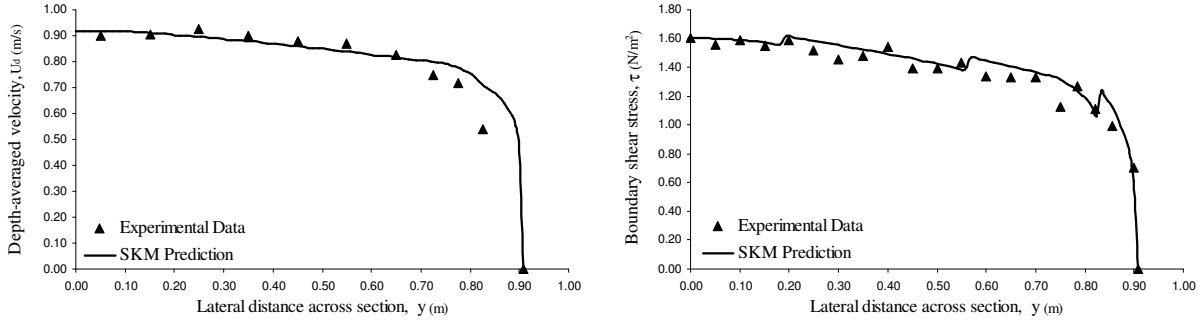

Figure (IV-5): FCF 0401; depth 0.1580m; Q_{data}=223.70 l.s^{-1}; Q_{SKM}=222.40 l.s^{-1}

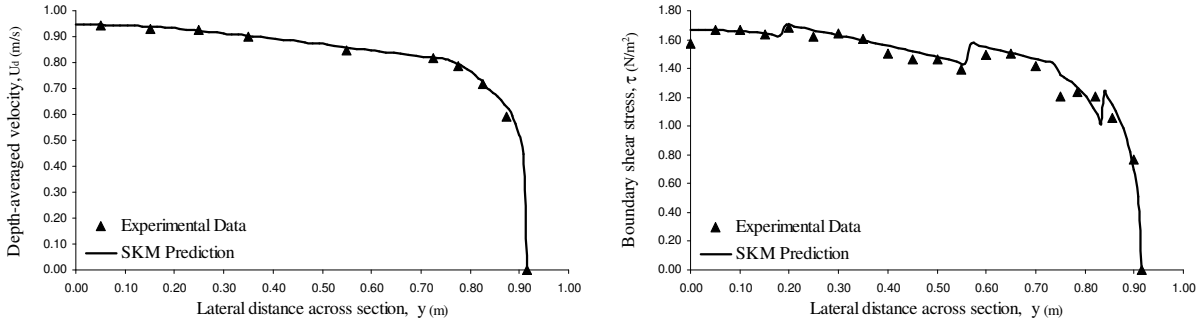

Figure (IV-6): FCF 0402; depth 0.1662m; Q_{data}=241.40 l.s^{-1}; Q_{SKM}=240.60 l.s^{-1}

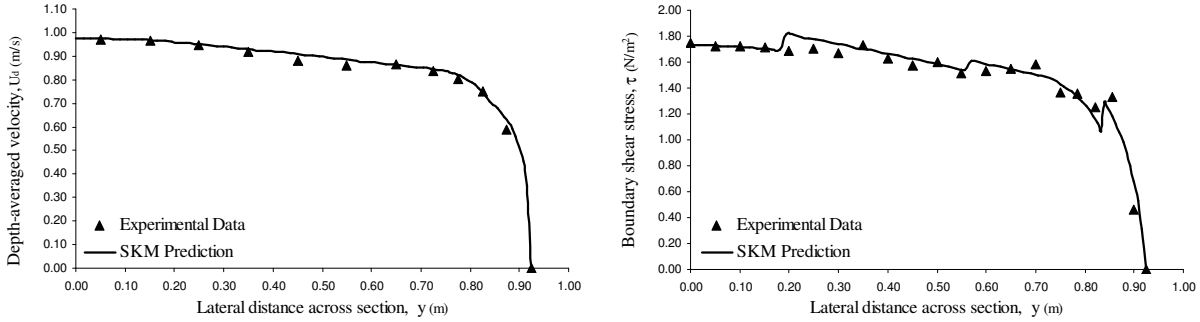

Figure (IV-7): FCF 0403; depth 0.1753m; Q_{data}=262.30 l.s^{-1}; Q_{SKM}=261.40 l.s^{-1}

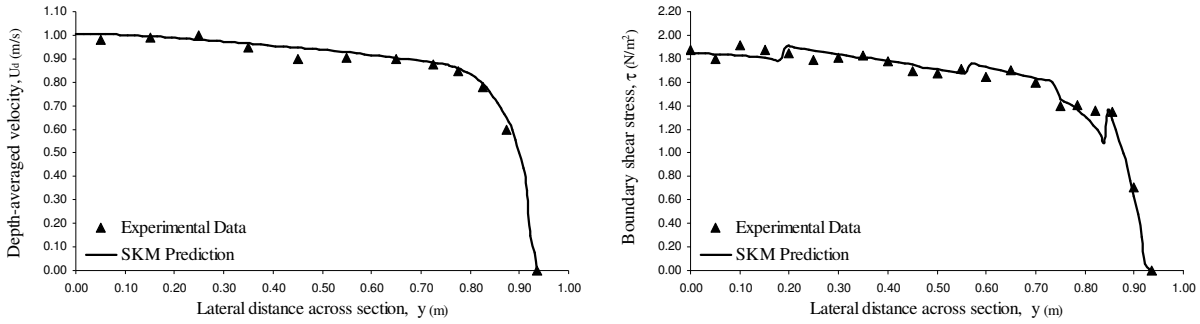

Figure (IV-8): FCF 0404; depth 0.1869m; Q_{data}=290.90 l.s^{-1}; Q_{SKM}=290.50 l.s^{-1}

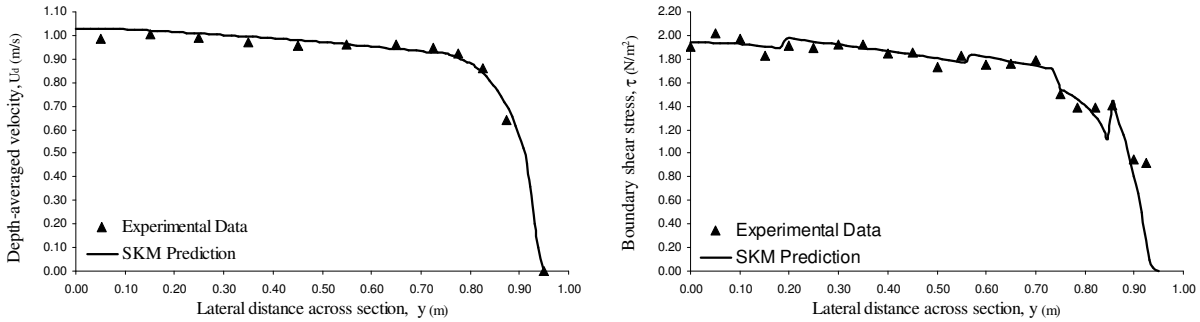

Figure (IV-9): FCF 0405; depth 0.1992m; Q_{data}=324.00 l.s^{-1}; Q_{SKM}=321.20 l.s^{-1}

IV.2 YUEN'S DATA

IV.2.1 Yuen Series 1 (S_0=1.000x10^{-3})

Yuen test case		004	006	008	010	013	014	016
$2b/h$		3.00	2.50	2.00	1.80	1.50	1.40	1.00
P_b/P_w		1.06	0.88	0.71	0.64	0.53	0.50	0.35
Panel 1	f	0.0199	0.0189	0.0187	0.0181	0.0170	0.0166	0.0159
	λ	1.08	1.35	1.29	1.30	0.79	1.05	1.07
	Γ	-0.50	-0.52	-0.54	-0.55	-0.57	-0.63	-0.72
Panel 2	f	0.0231	0.0218	0.0207	0.0198	0.0182	0.0177	0.0171
	λ	0.49	0.45	0.38	0.30	0.28	0.24	0.16
	Γ	0.16	0.15	0.13	0.14	0.15	0.15	0.12
Panel 3	f	0.0244	0.0235	0.0221	0.0210	0.0200	0.0194	0.0185
	λ	0.86	0.84	0.84	0.84	0.82	0.77	0.71
	Γ	-0.15	-0.25	-0.36	-0.42	-0.55	-0.62	-0.64
Panel 4	f	0.0283	0.0268	0.0250	0.0244	0.0228	0.0222	0.0210
	λ	1.57	1.55	1.50	1.47	1.47	1.44	1.36
	Γ	0.71	0.72	0.79	0.82	0.89	0.93	0.96

Table (IV-1): The optimal parameter values in different panels of Yuen's series 1 data.

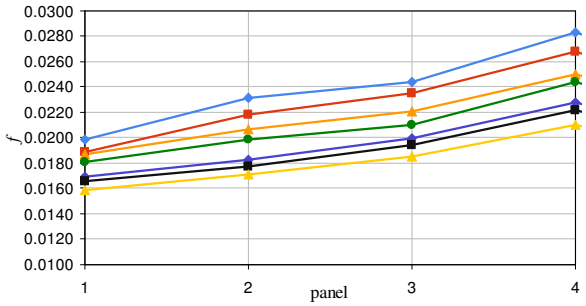

a) Friction factor vs. panel number

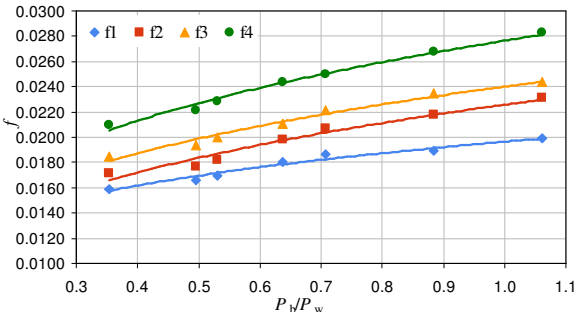

b) Friction factor vs. P_b/P_w

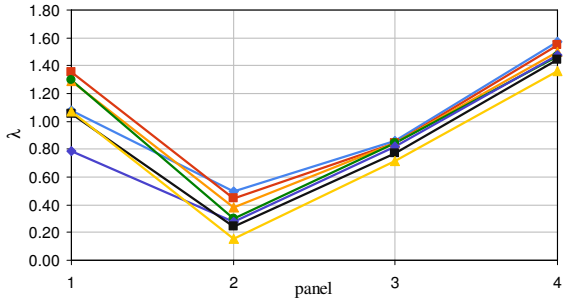

c)Dimensionless eddy viscosity vs. panel

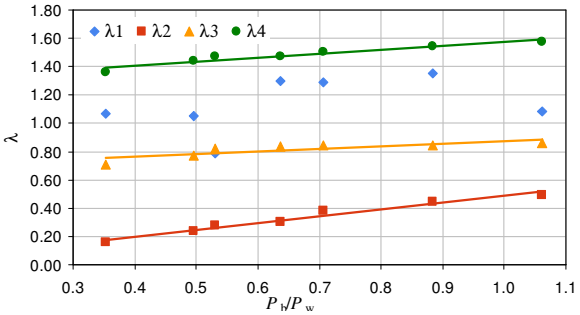

d) Dimensionless eddy viscosity vs. P_b/P_w

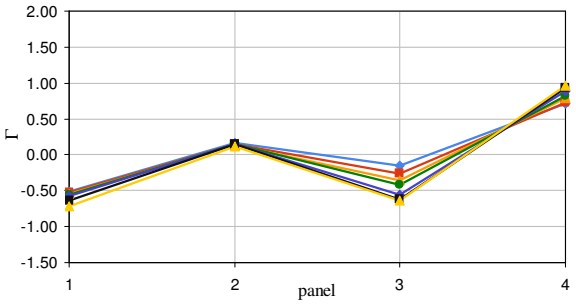

e) Secondary flow term vs. panel number

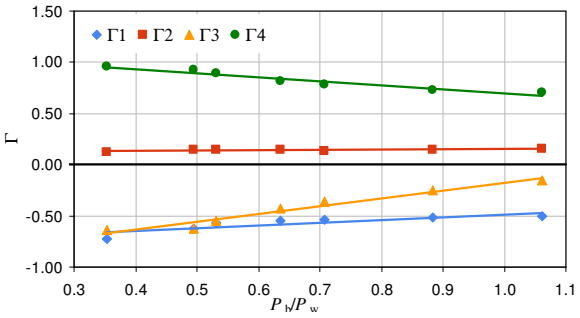

f) Secondary flow term vs. P_b/P_w

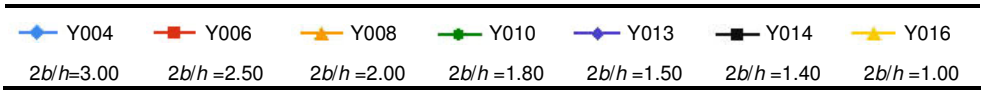

Figure (IV-10): Variation of the friction factor, dimensionless eddy viscosity and secondary flow term against the panel number and wetted perimeter ratio (P_b/P_w) for Yuen's series 1 ($1.0<2b/h<3.0$ and $S_0=1.000\text{x}10^{-3}$)

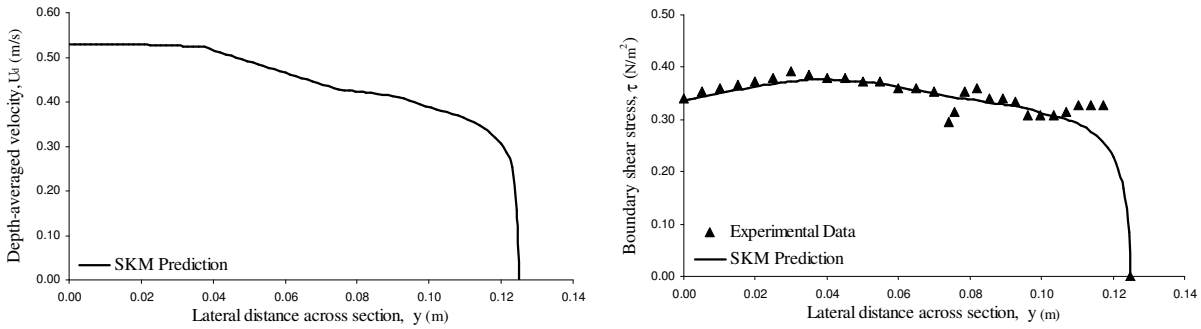

Figure (IV-11): Yuen 004; depth 0.0500 m; $Q_{data}=3.5$ l.s^{-1}; $Q_{SKM}=3.49$ l.s^{-1}

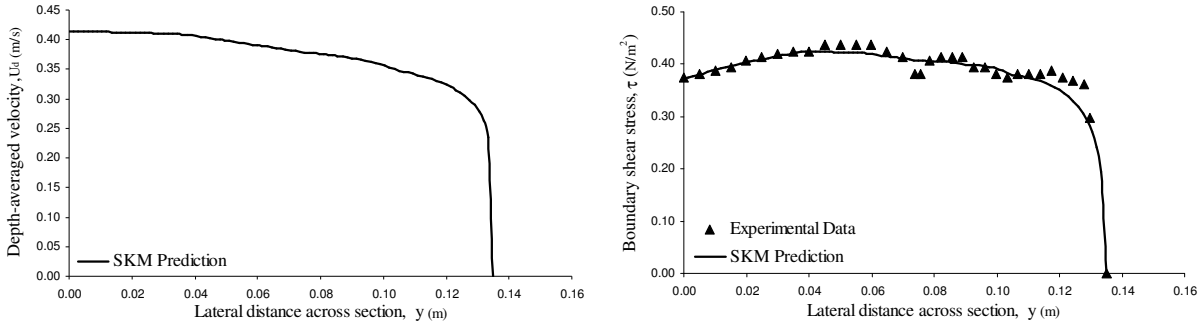

Figure (IV-12): Yuen 006; depth 0. 0600 m; Q_{data}=4.65 l.s^{-1}; Q_{SKM}=4.82 l.s^{-1}

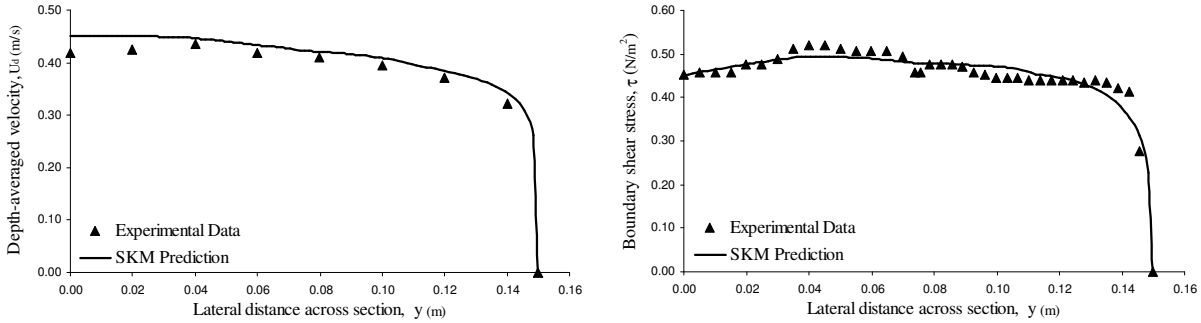

Figure (IV-13): Yuen 008; depth 0.0750 m; Q_{data}=7.00 l.s^{-1}; Q_{SKM}=7.11 l.s^{-1}

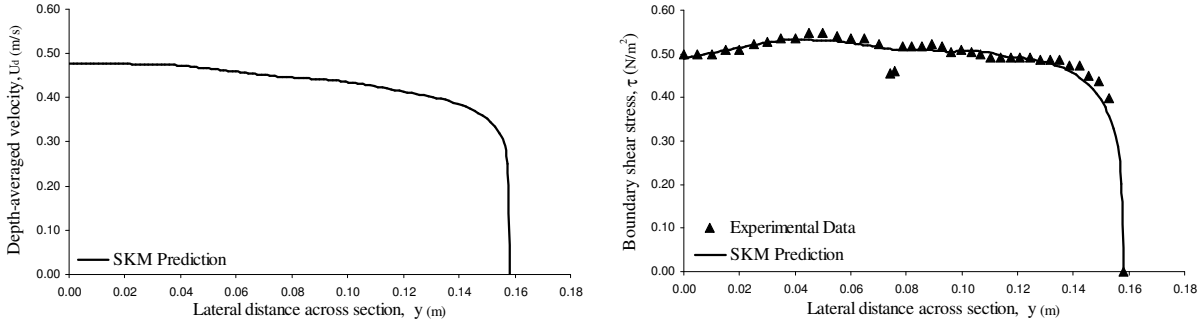

Figure (IV-14): Yuen 010; depth 0.0833 m; Q_{data}=8.55 l.s^{-1}; Q_{SKM}=8.63 l.s^{-1}

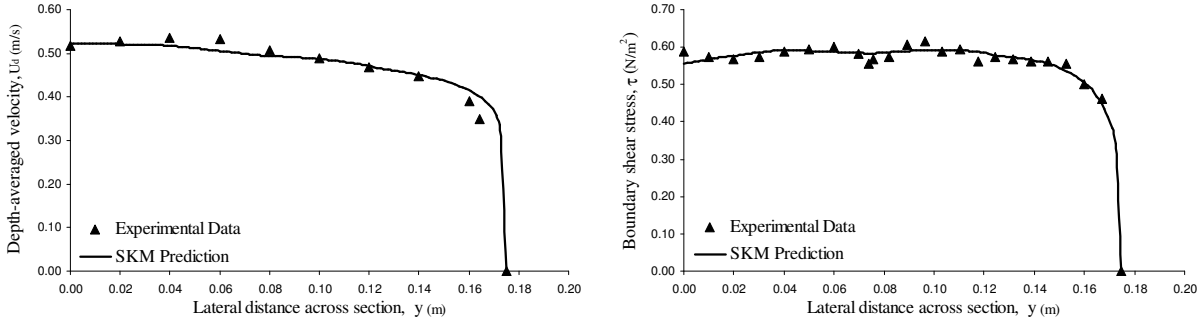

Figure (IV-15): Yuen 013; depth 0.100 m; Q_{data}=12.00 l.s^{-1}; Q_{SKM}=12.21 l.s^{-1}

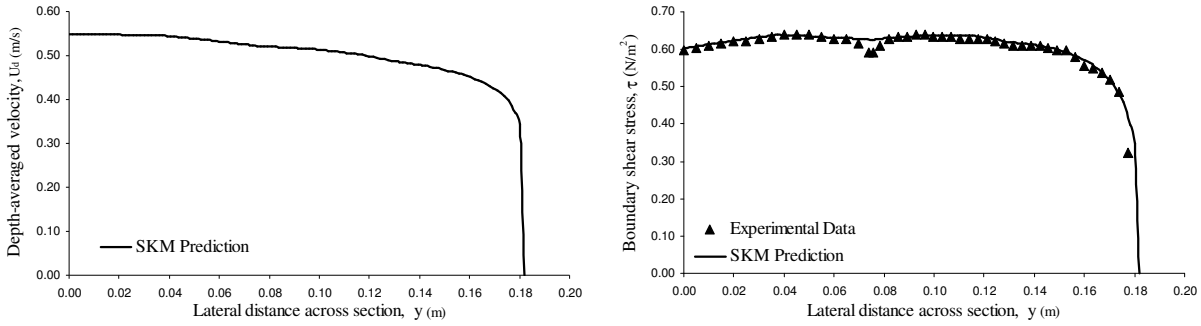

Figure (IV-16): Yuen 014; depth 0.1071 m; Q_{data}=13.70 l.s^{-1}; Q_{SKM}=14.12 l.s^{-1}

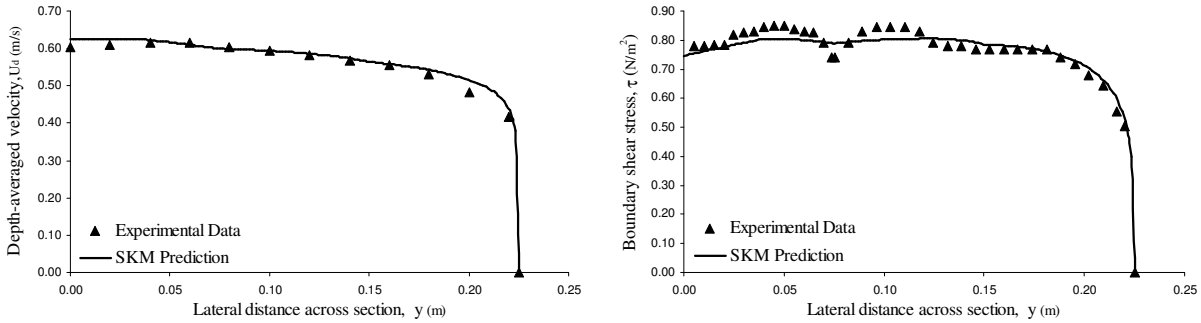

Figure (IV-17): Yuen 016; depth 0.150 m; Q_{data}=26.30 l.s^{-1}; Q_{SKM}=26.26 l.s^{-1}

IV.2.2 Yuen Series 3 (S_0=8.706x10^{-3})

Yuen test case		201	203	205	206	207
$2b/h$		5.26	3.67	2.61	2.05	1.52
P_b/P_w		1.86	1.30	0.92	0.73	0.54
Panel 1	f	0.0180	0.0165	0.0164	0.0150	0.0144
	λ	0.98	0.62	0.77	0.55	0.78
	Γ	-0.35	-0.53	-0.65	-0.79	-0.96
Panel 2	f	0.0208	0.0183	0.0168	0.0162	0.0157
	λ	0.15	0.14	0.12	0.11	0.11
	Γ	0.32	0.23	0.22	0.22	0.20
Panel 3	f	0.0240	0.0203	0.0188	0.0179	0.0167
	λ	0.50	0.39	0.32	0.29	0.24
	Γ	-0.67	-0.67	-0.78	-0.89	-1.14
Panel 4	f	0.0250	0.0221	0.0205	0.0194	0.0185
	λ	0.67	0.60	0.53	0.49	0.40
	Γ	1.04	1.30	1.57	1.70	1.80

Table (IV-2): The optimal parameter values in different panels of Yuen's series 3 data.

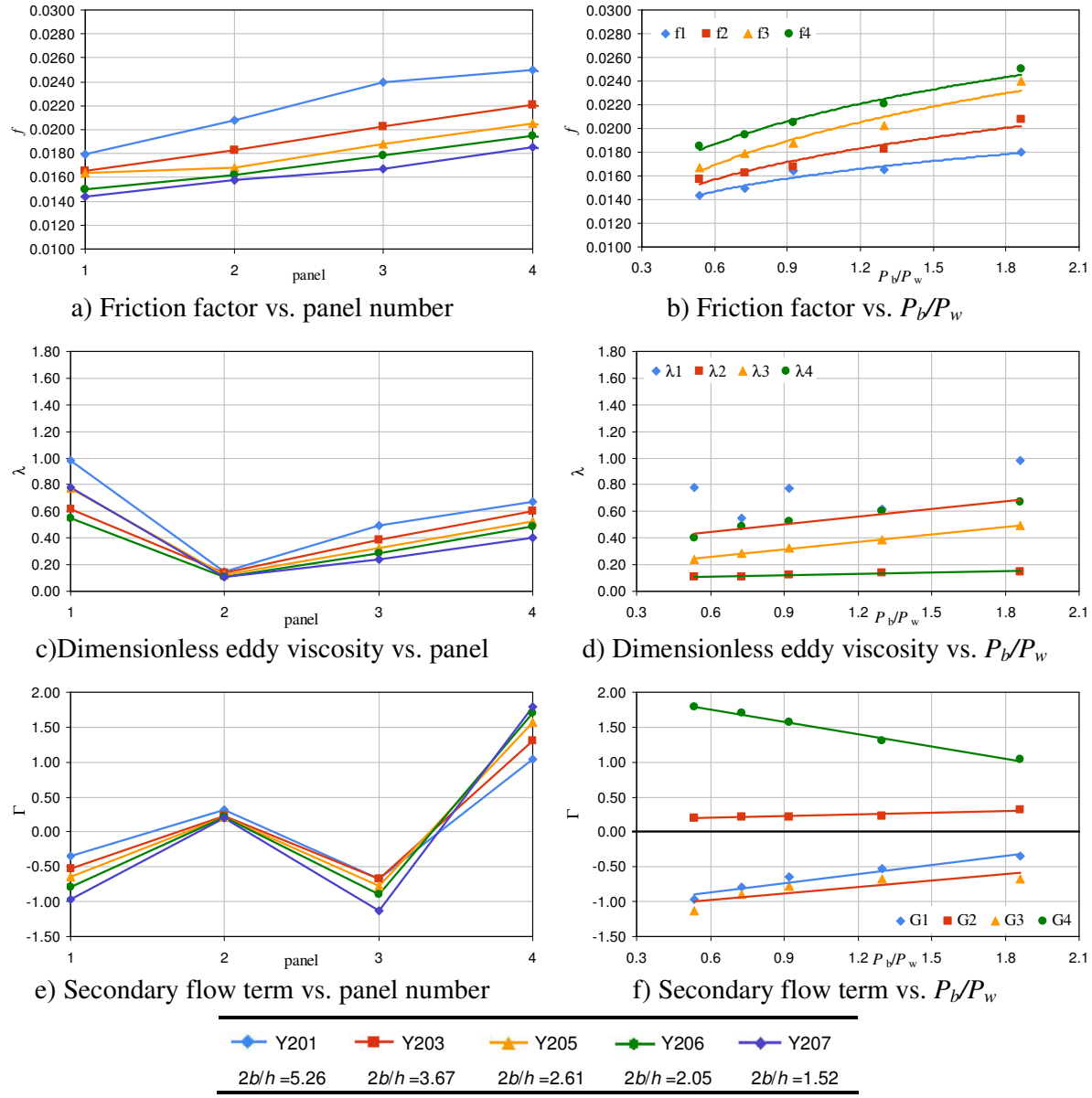

a) Friction factor vs. panel number

b) Friction factor vs. P_b/P_w

c)Dimensionless eddy viscosity vs. panel

d) Dimensionless eddy viscosity vs. P_b/P_w

e) Secondary flow term vs. panel number

f) Secondary flow term vs. P_b/P_w

Figure (IV-18): Variation of the friction factor, dimensionless eddy viscosity and secondary flow term against the panel number and wetted perimeter ratio (P_b/P_w) for Yuen's series 3 ($1.52<2b/h<5.26$ and $S_0=8.706\text{x}10^{-3}$)

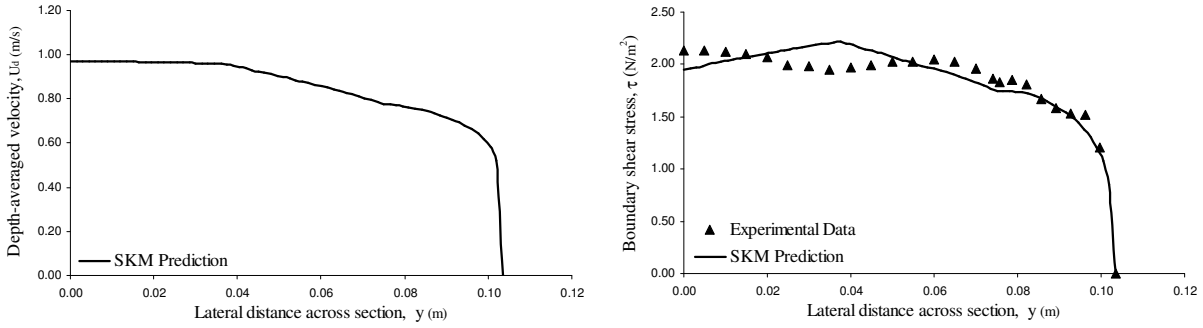

Figure (IV-19): Yuen 201; depth 0.285 m; $Q_{data}=4.70$ l.s^{-1}; $Q_{SKM}=4.47$ l.s^{-1}

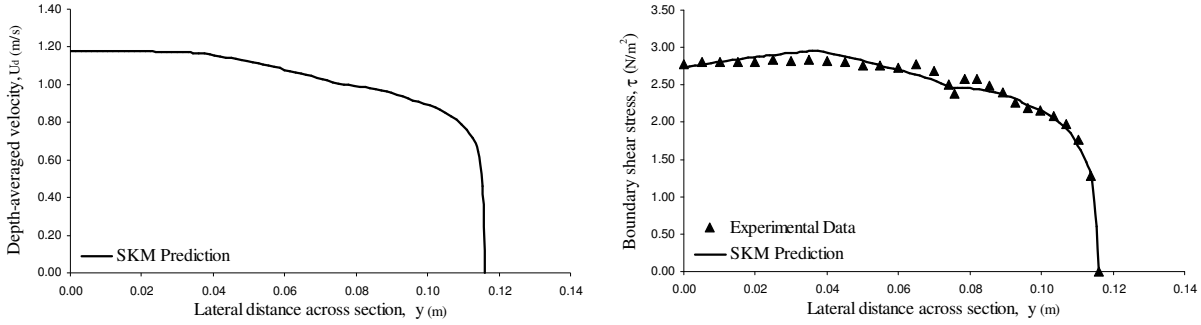

Figure (IV-20): Yuen 203; depth 0.409 m; Q_{data}=8.68 l.s^{-1}; Q_{SKM}=8.39 l.s^{-1}

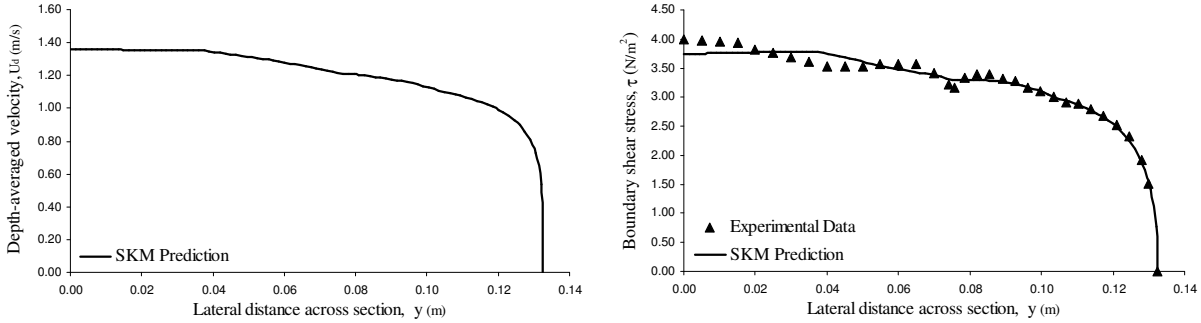

Figure (IV-21): Yuen 205; depth 0.575 m; Q_{data}=15.60 l.s^{-1}; Q_{SKM}=14.84 l.s^{-1}

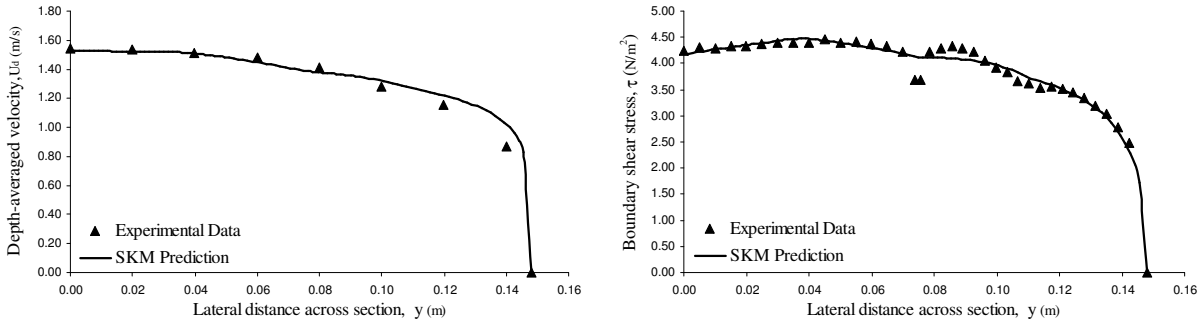

Figure (IV-22): Yuen 206; depth 0.730 m; Q_{data}=23.90 l.s^{-1}; Q_{SKM}= l.s^{-1}

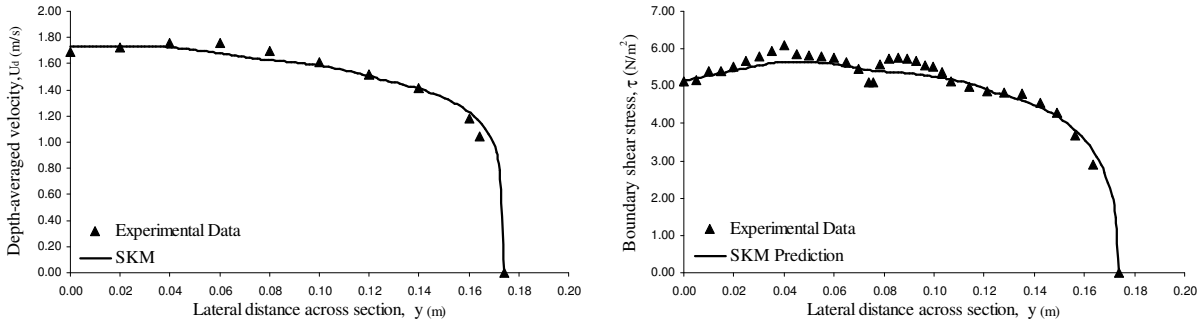

Figure (IV-23): Yuen 207; depth 0.990 m; Q_{data}=41.10 l.s^{-1}; Q_{SKM}=39.28 l.s^{-1}

IV.2.3 Yuen Series 5 (S_0=23.370x10^{-3})

Yuen test case		401	403	405	406	407
$2b/h$		5.26	3.57	2.65	2.05	1.52
P_b/P_w		1.86	1.26	0.94	0.73	0.54
Panel 1	f	0.0159	0.0157	0.0150	0.0144	0.0136
	λ	0.75	0.68	0.72	0.64	0.64
	Γ	-0.74	-0.82	-0.88	-0.97	-1.10
Panel 2	f	0.0184	0.0176	0.0160	0.0157	0.0149
	λ	0.14	0.14	0.15	0.12	0.12
	Γ	0.10	0.20	0.13	0.18	0.18
Panel 3	f	0.0218	0.0191	0.0174	0.0167	0.0159
	λ	0.31	0.27	0.25	0.22	0.20
	Γ	-1.00	-1.10	-1.16	-1.30	-1.41
Panel 4	f	0.0253	0.0219	0.0198	0.0185	0.0176
	λ	0.43	0.41	0.35	0.31	0.30
	Γ	1.35	1.58	1.72	1.91	1.98

Table (IV-3): The optimal parameter values in different panels of Yuen's series 5 data.

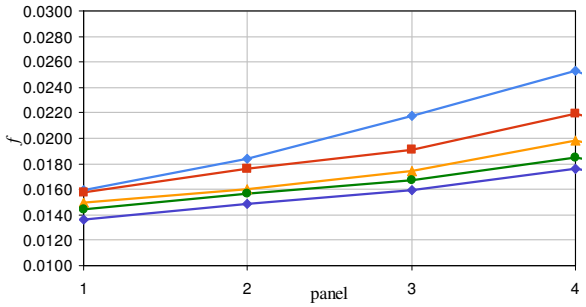

a) Friction factor vs. panel number

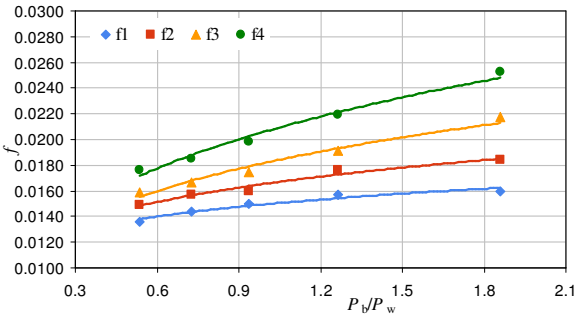

b) Friction factor vs. P_b/P_w

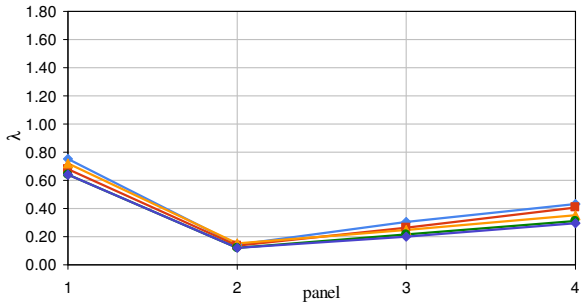

c)Dimensionless eddy viscosity vs. panel

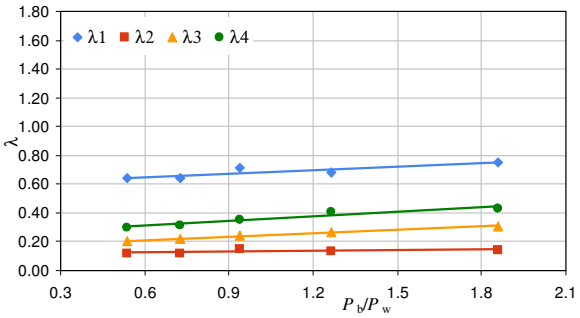

d) Dimensionless eddy viscosity vs. P_b/P_w

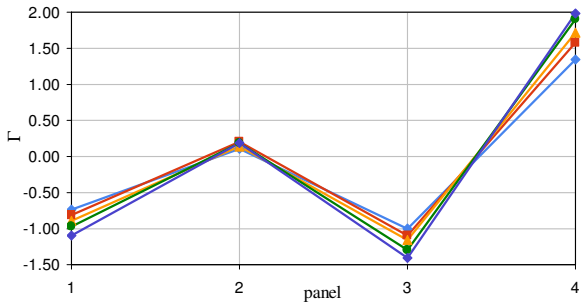

e) Secondary flow term vs. panel number

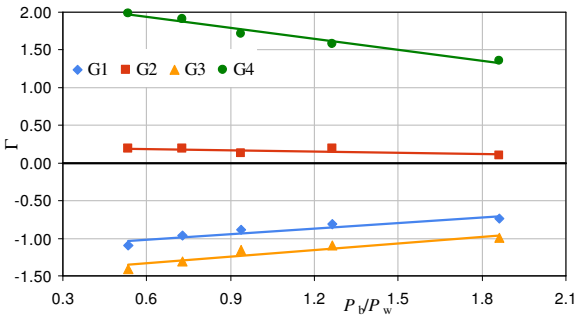

f) Secondary flow term vs. P_b/P_w

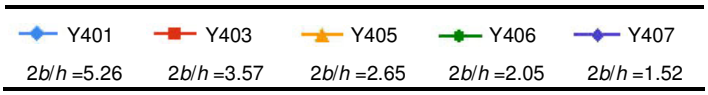

Figure (IV-24): Variation of the friction factor, dimensionless eddy viscosity and secondary flow term against the panel number and wetted perimeter ratio (P_b/P_w) for Yuen's series 5 ($1.52<2b/h<5.26$ and $S_0=23.37\text{x}10^{-3}$)

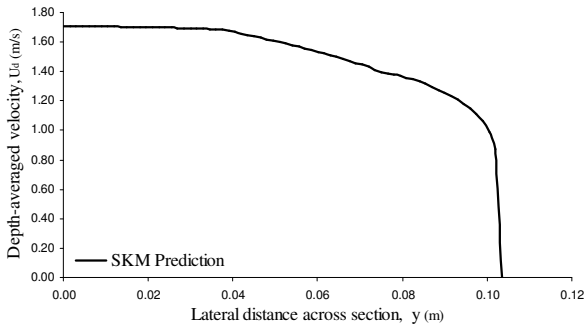

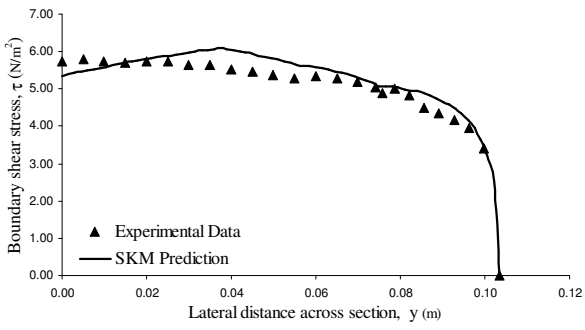

Figure (IV-25): Yuen 401; depth 0.0285 m; $Q_{data}=8.10$ l.s^{-1}; $Q_{SKM}=7.91$ l.s^{-1}

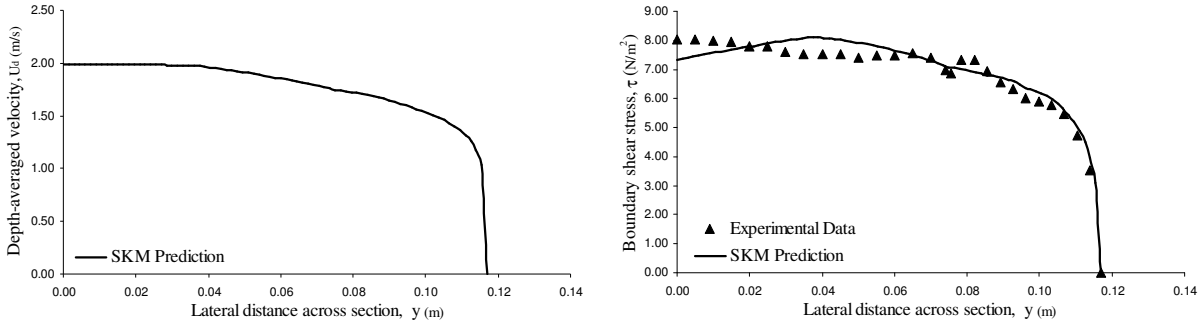

Figure (IV-26): Yuen 403; depth 0.0420 m; Q_{data}=15.33 l.s^{-1}; Q_{SKM}=14.78 l.s^{-1}

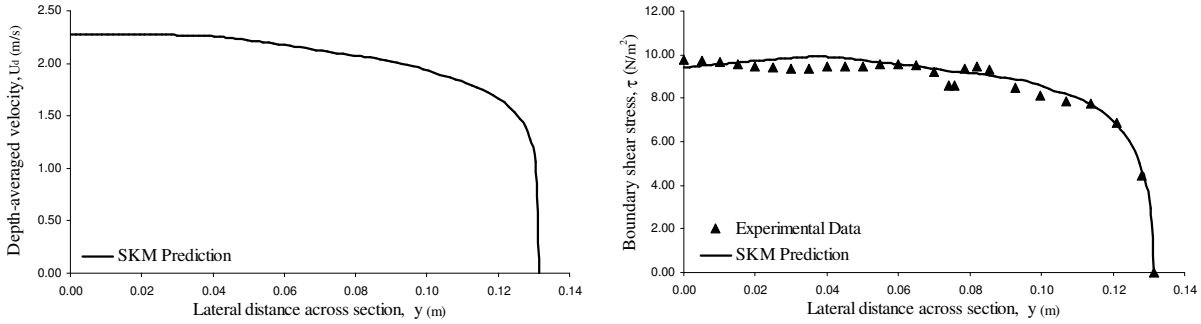

Figure (IV-27): Yuen 405; depth 0.0565 m; Q_{data}=25.55 l.s^{-1}; Q_{SKM}=24.61 l.s^{-1}

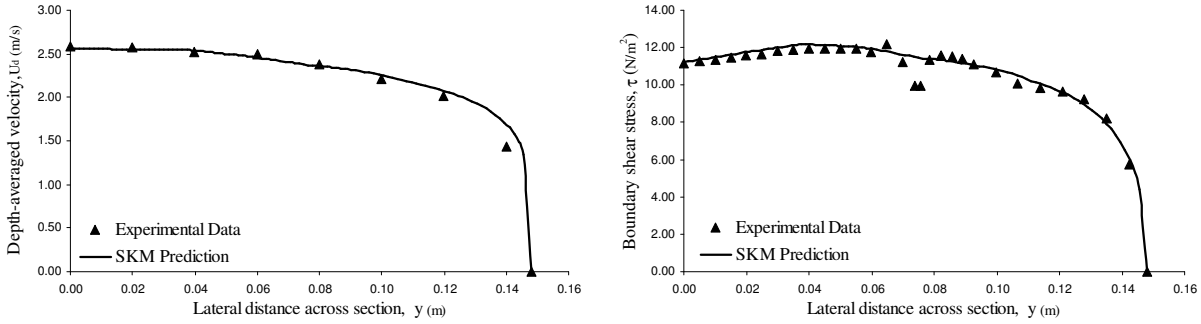

Figure (IV-28): Yuen 406; depth 0.0730 m; Q_{data}=39.00 l.s^{-1}; Q_{SKM}=38.44 l.s^{-1}

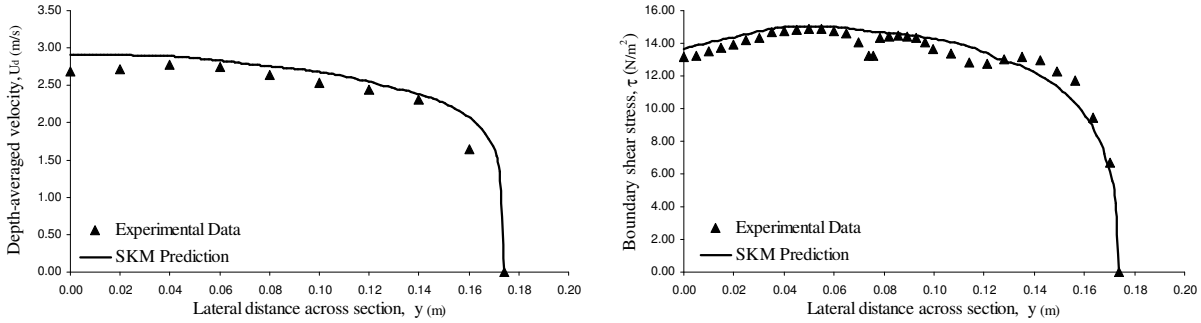

Figure (IV-29): Yuen 407; depth 0.0990 m; Q_{data}=66.30 l.s^{-1}; Q_{SKM}=66.13 l.s^{-1}

IV.3 AL-HAMID'S DATA

IV.3.1 Smooth Bed and R1 on the Walls

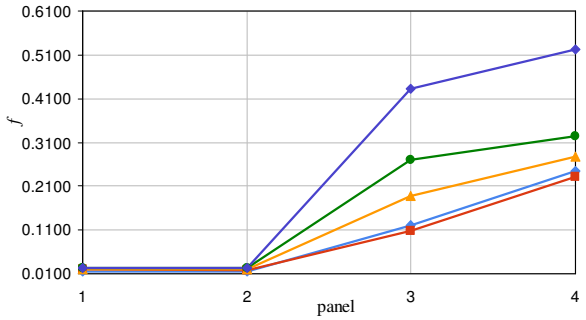

a) Friction factor vs. panel number (0.85<2*b*/*h*<2.49)

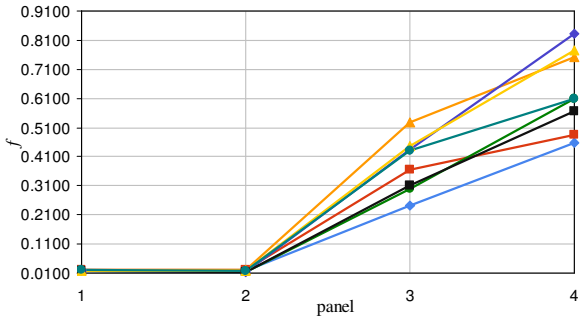

b) Friction factor vs. panel number (3.01<2*b*/*h*<9.99)

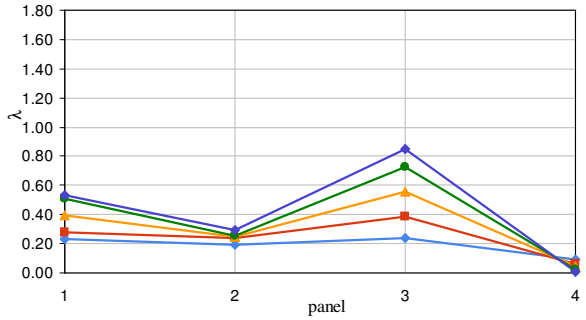

c) Dimensionless eddy viscosity vs. panel number (0.85<2*b*/*h*<2.49)

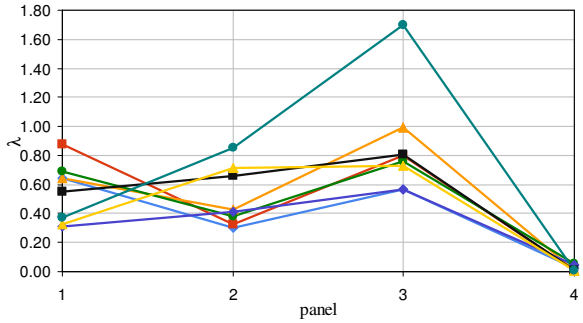

d) Dimensionless eddy viscosity vs. panel number (3.01<2*b*/*h*<9.99)

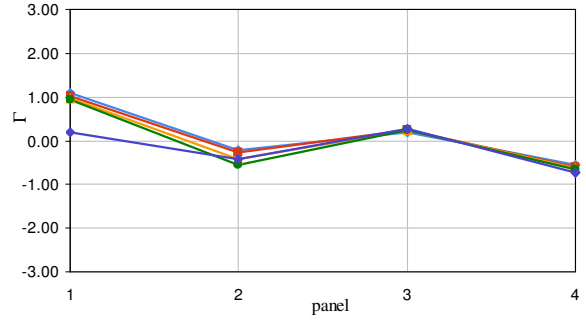

e) Secondary flow term vs. panel number (0.85<2*b*/*h*<2.49)

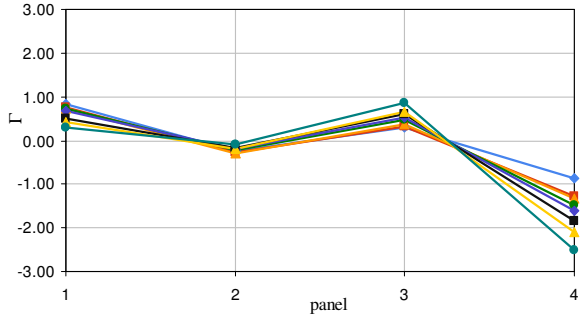

e) Secondary flow term vs. panel number (3.01<2*b*/*h*<9.99)

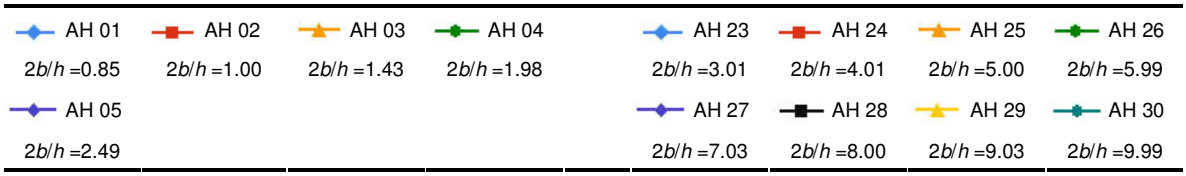

Figure (IV-30): Variation of the friction factor, dimensionless eddy viscosity and secondary flow term against the panel number for Al-Hamid's trapezoidal channels with smooth bed and R1 on the wall (S_o=3.920x10^{-3})

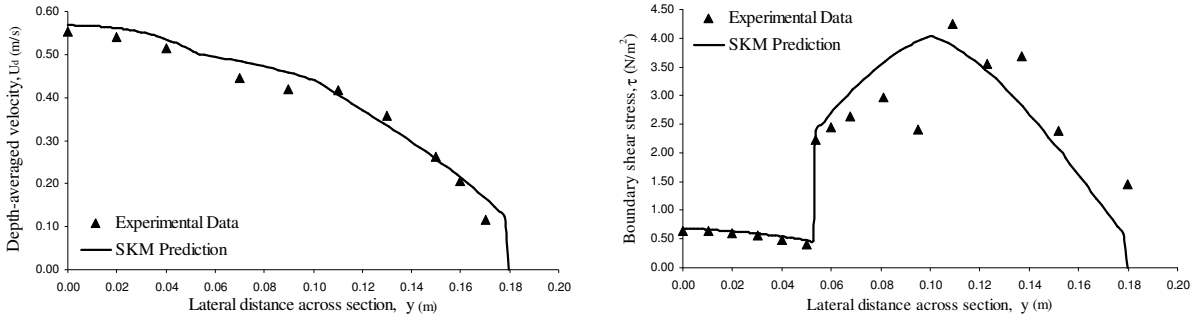

Figure (IV-31): Al-Hamid 01; depth 0.126 m;
Q_{data}=13.69 l.s^{-1}; Q_{SKM}=13.04 l.s^{-1}; %SFw$_{data}$=94.70; %SFw$_{SKM}$=93.99

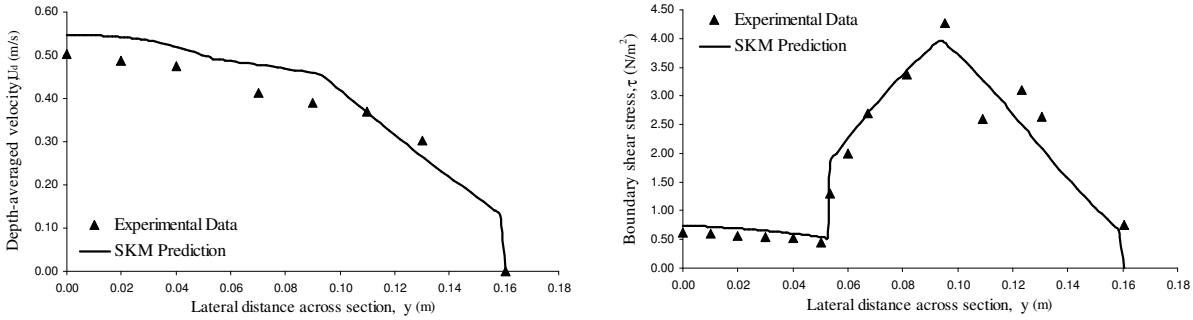

Figure (IV-32): Al-Hamid 02; depth 0.107 m;
Q_{data}=9.99 l.s^{-1}; Q_{SKM}=10.10 l.s^{-1}; %SFw$_{data}$=93.33; %SFw$_{SKM}$=91.51

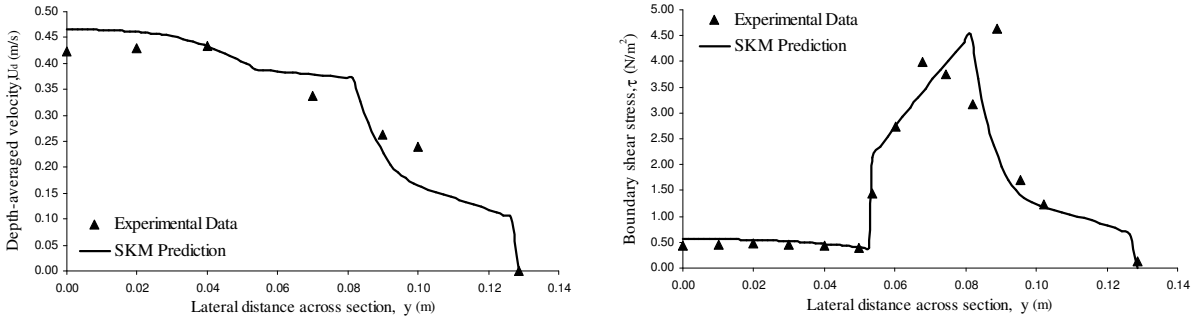

Figure (IV-33): Al-Hamid 03; depth 0.075 m;
Q_{data}=5.15 l.s^{-1}; Q_{SKM}=4.96 l.s^{-1}; %SFw$_{data}$=90.99; %SFw$_{SKM}$=89.73

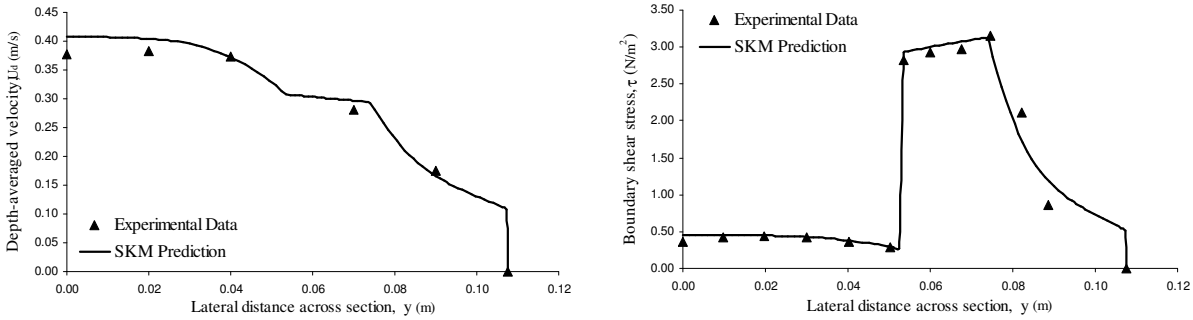

Figure (IV-34): Al-Hamid 04; depth 0.054 m;
Q_{data}=2.91 l.s^{-1}; Q_{SKM}=2.86 l.s^{-1}; %SFw$_{data}$=87.38; %SFw$_{SKM}$=86.96

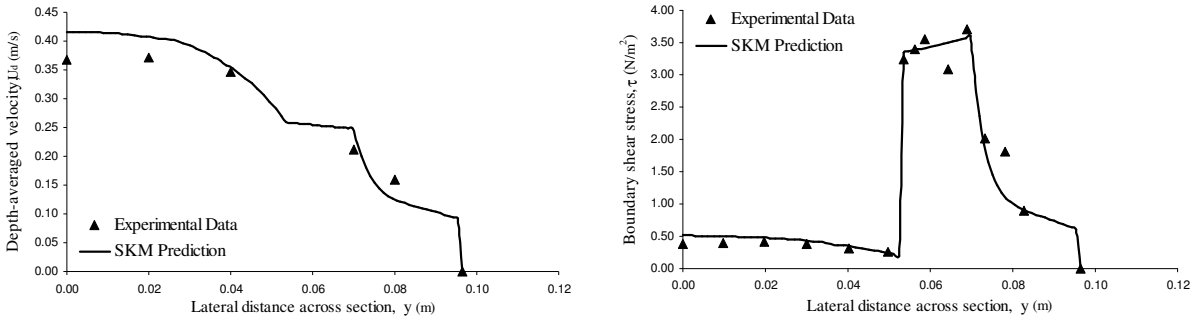

Figure (IV-35): Al-Hamid 05; depth 0.043 m;
Q_{data}=2.01 l.s^{-1}; Q_{SKM}=2.05 l.s^{-1}; %SFw$_{data}$=84.69; %SFw$_{SKM}$=84.60

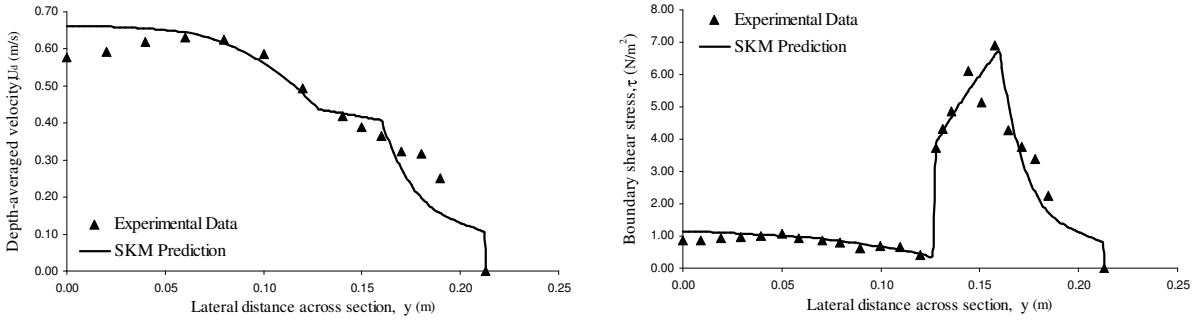

Figure (IV-36): Al-Hamid 23; depth 0.085 m;
Q_{data}=15.53 l.s^{-1}; Q_{SKM}=15.18 l.s^{-1}; %SFw$_{data}$=81.14; %SFw$_{SKM}$=78.48

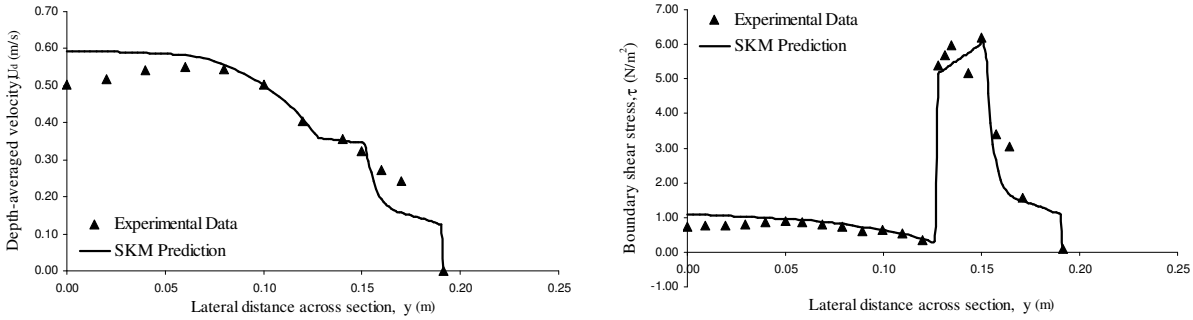

Figure (IV-37): Al-Hamid 24; depth 0.064 m;
Q_{data}=9.68 l.s^{-1}; Q_{SKM}=9.79 l.s^{-1}; %SFw$_{data}$=76.65; %SFw$_{SKM}$=73.25

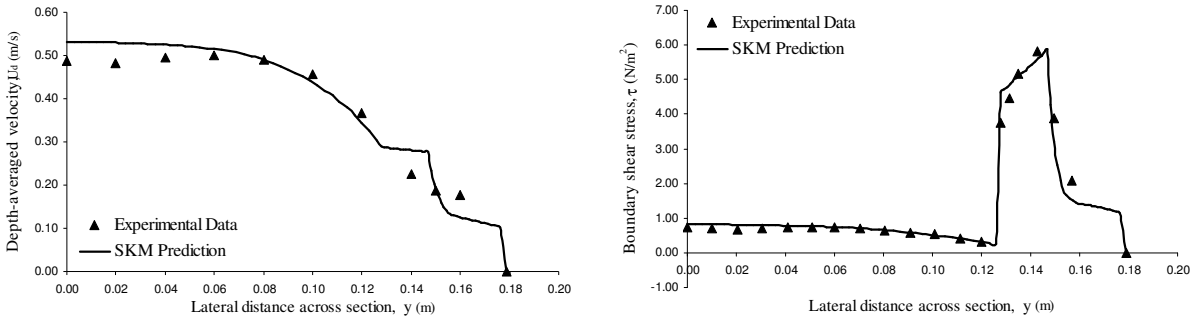

Figure (IV-38): Al-Hamid 25; depth 0.051 m;
Q_{data}=6.71 l.s^{-1}; Q_{SKM}=6.72 l.s^{-1}; %SFw$_{data}$=73.65; %SFw$_{SKM}$=72.40

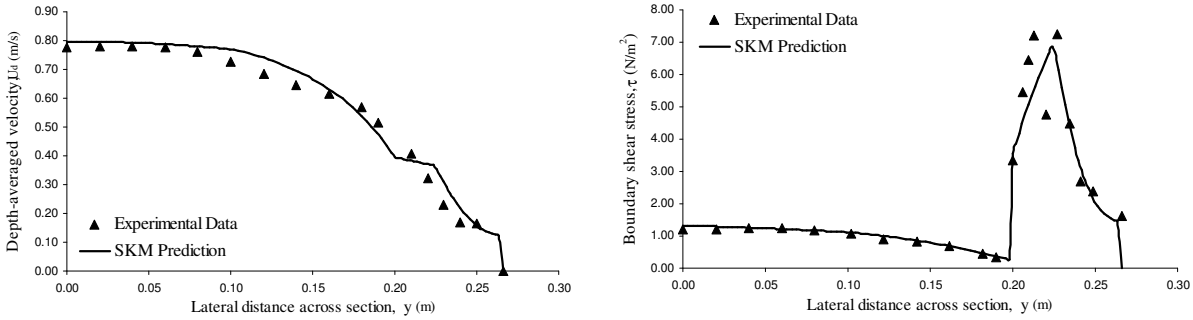

Figure (IV-39): Al-Hamid 26; depth 0.067 m;
Q_{data}=20.05 l.s^{-1}; Q_{SKM}=20.14 l.s^{-1}; %SFw$_{data}$=67.81; %SFw$_{SKM}$=64.85

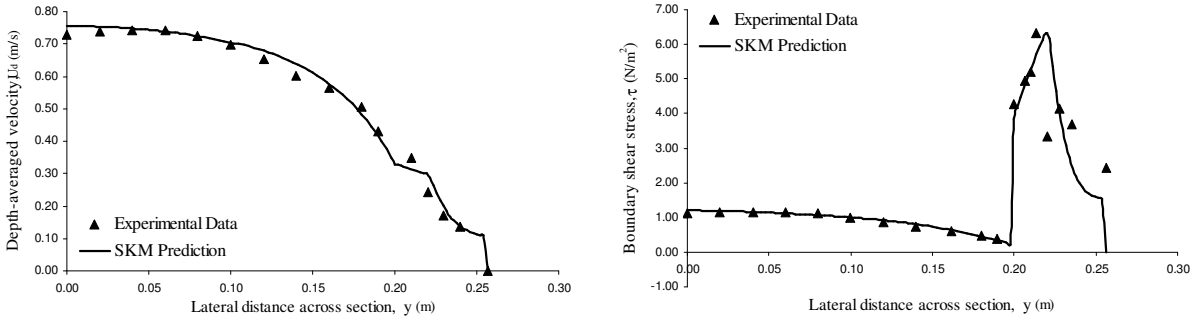

Figure (IV-40): Al-Hamid 27; depth 0.057 m;
Q_{data}=15.76 l.s^{-1}; Q_{SKM}=15.61 l.s^{-1}; %SFw$_{data}$=64.04; %SFw$_{SKM}$=61.46

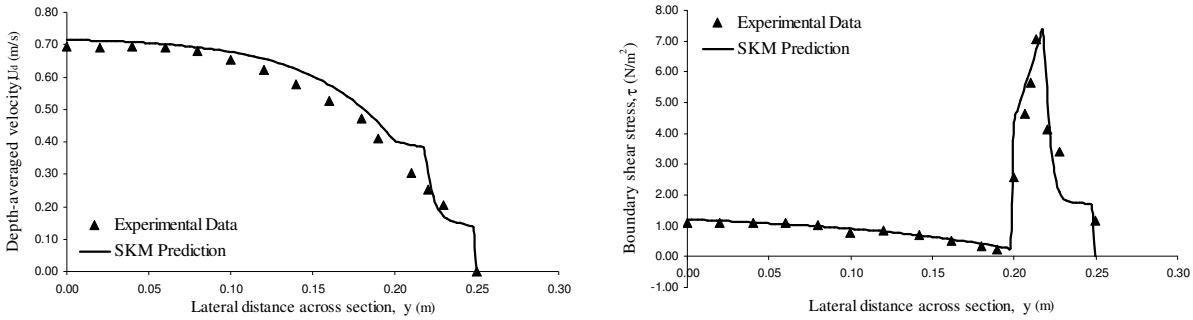

Figure (IV-41): Al-Hamid 28; depth 0.050 m;
Q_{data}=12.99 l.s^{-1}; Q_{SKM}=13.40 l.s^{-1}; %SFw$_{data}$=61.50; %SFw$_{SKM}$=61.49

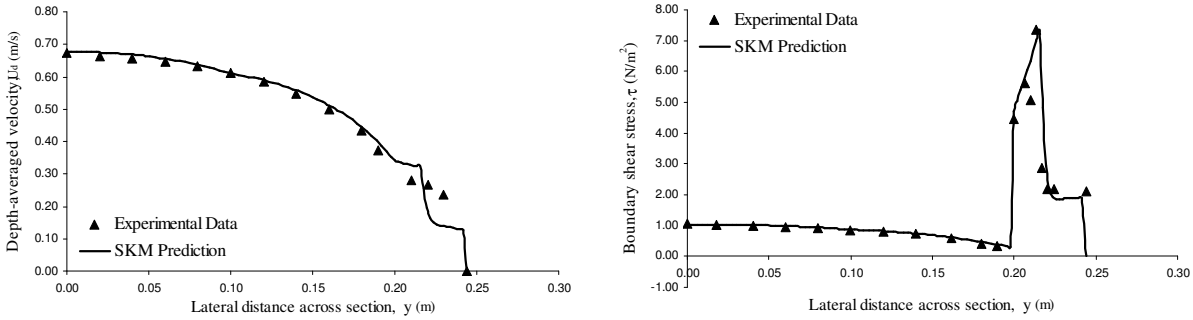

Figure (IV-42): Al-Hamid 29; depth 0.044 m;
Q_{data}=10.83 l.s^{-1}; Q_{SKM}=10.76 l.s^{-1}; %SFw$_{data}$=57.90; %SFw$_{SKM}$=57.97

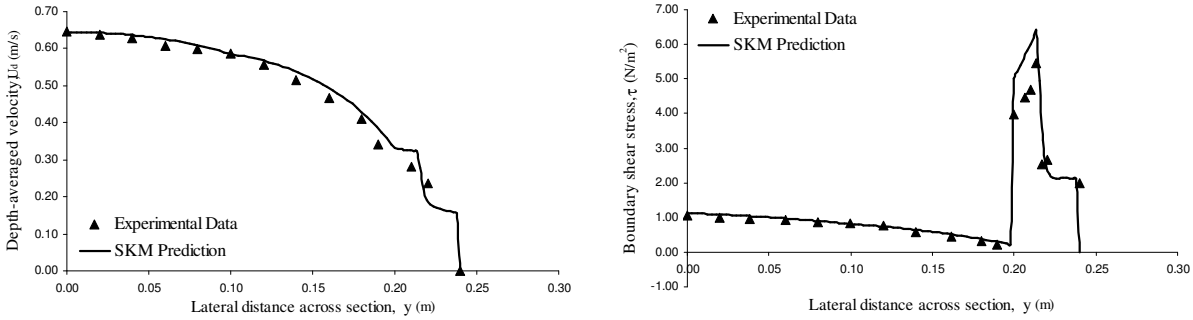

Figure (IV-43): Al-Hamid 30; depth 0.040 m;
Q_{data}=9.30 l.s^{-1}; Q_{SKM}=9.31 l.s^{-1}; %SFw$_{data}$=56.34; %SFw$_{SKM}$=56.67

IV.3.2 Smooth Bed and R2 on the Walls

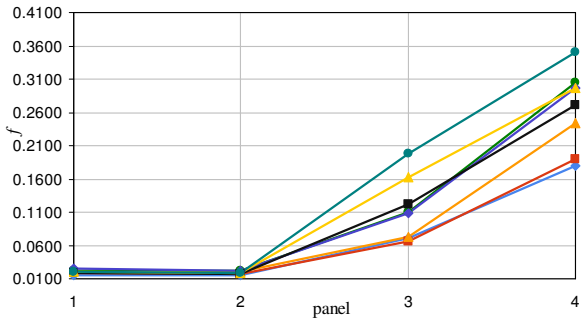

a) Friction factor vs. panel number ($0.85<2b/h<4.49$, $S_0=3.920\text{x}10^{-3}$)

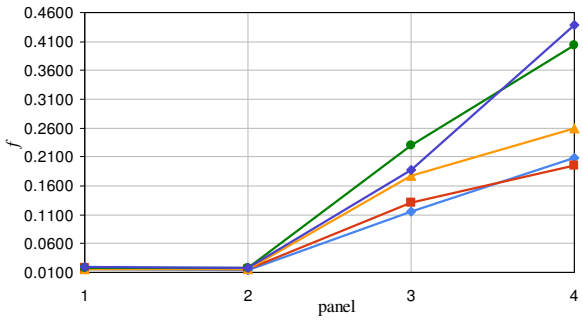

b) Friction factor vs. panel number ($3.01<2b/h<9.99$, $S_0=1.935\text{x}10^{-3}$)

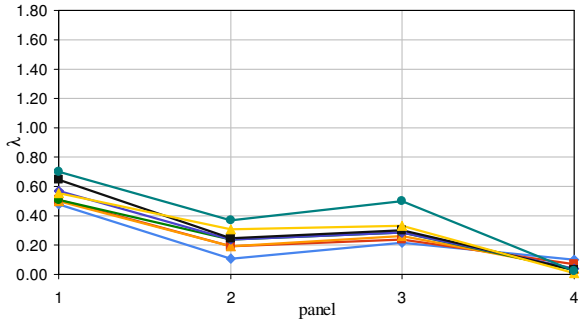

c) Dimensionless eddy viscosity vs. panel number ($0.85<2b/h<4.49$, $S_0=3.920\text{x}10^{-3}$)

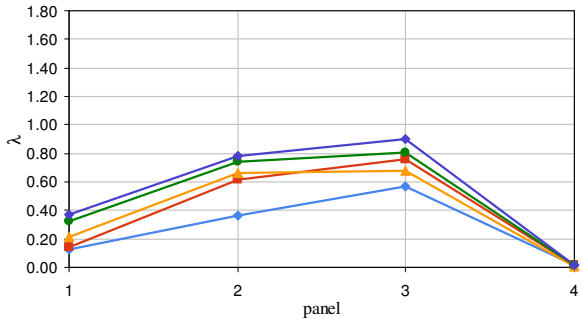

d) Dimensionless eddy viscosity vs. panel number ($3.01<2b/h<9.99$, $S_0=1.935\text{x}10^{-3}$)

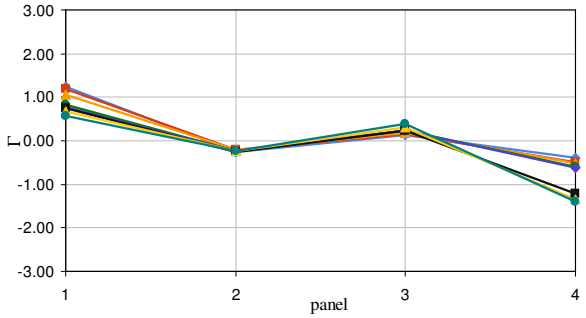

e) Secondary flow term vs. panel number ($0.85<2b/h<4.49$, $S_0=3.920\text{x}10^{-3}$)

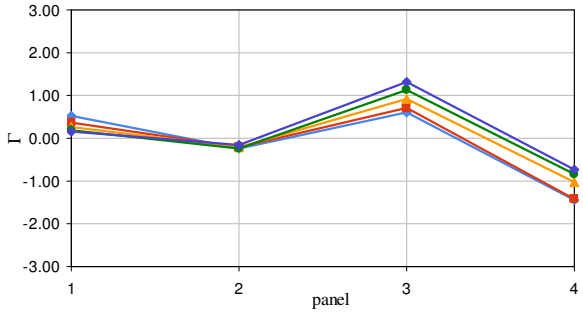

e) Secondary flow term vs. panel number ($3.01<2b/h<9.99$, $S_0=1.935\text{x}10^{-3}$)

AH 09	AH 10	AH 11	AH 12	AH 31	AH 32	AH 33	AH 24
$2b/h$=0.85	$2b/h$ =1.00	$2b/h$ =1.50	$2b/h$ =2.00	$2b/h$ =5.99	$2b/h$ =7.01	$2b/h$ =8.01	$2b/h$ =8.96
AH 13	AH 17	AH 18	AH 19	AH 35			
$2b/h$ =2.51	$2b/h$ =3.00	$2b/h$ =4.00	$2b/h$ =4.99	$2b/h$ =10.01			

Figure (IV-44): Variation of the friction factor, dimensionless eddy viscosity and secondary flow term against the panel number for Al-Hamid's trapezoidal channels with smooth bed and R2 on the wall

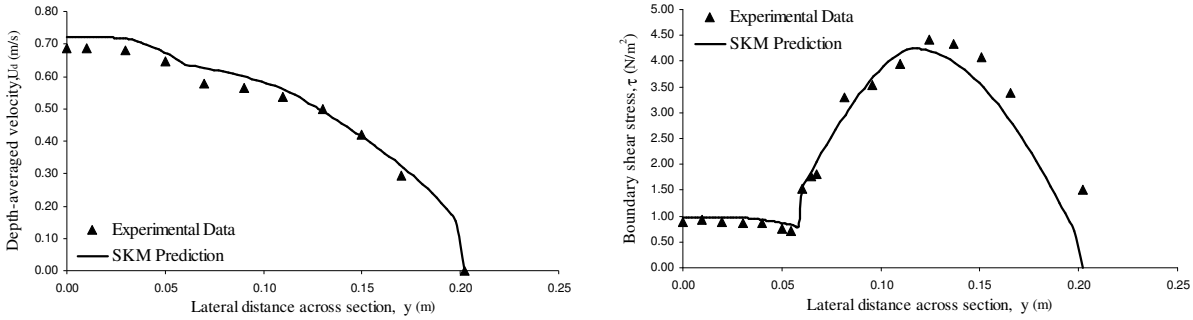

Figure (IV-45): Al-Hamid 09; depth 0.1426 m;
Q_{data}=21.95 l.s^{-1}; Q_{SKM}=21.21 l.s^{-1}; %SFw$_{data}$=92.87; %SFw$_{SKM}$=92.11

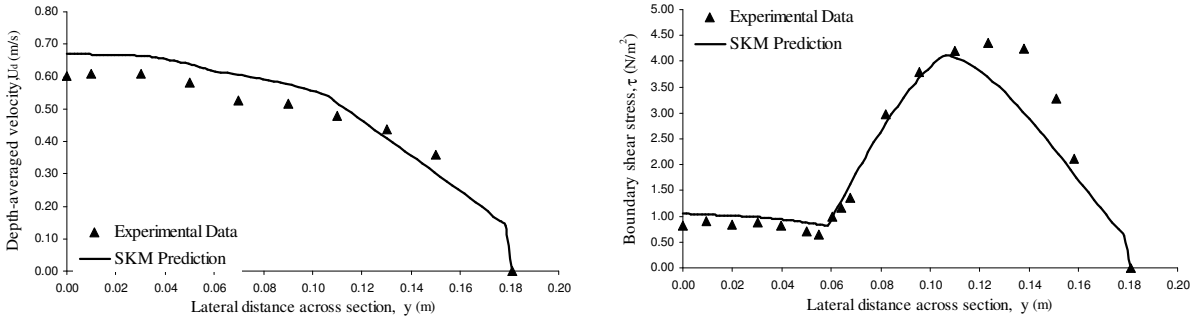

Figure (IV-46): Al-Hamid 10; depth 0.121 m;
Q_{data}=15.91 l.s^{-1}; Q_{SKM}=15.81 l.s^{-1}; %SFw$_{data}$=91.16; %SFw$_{SKM}$=89.68

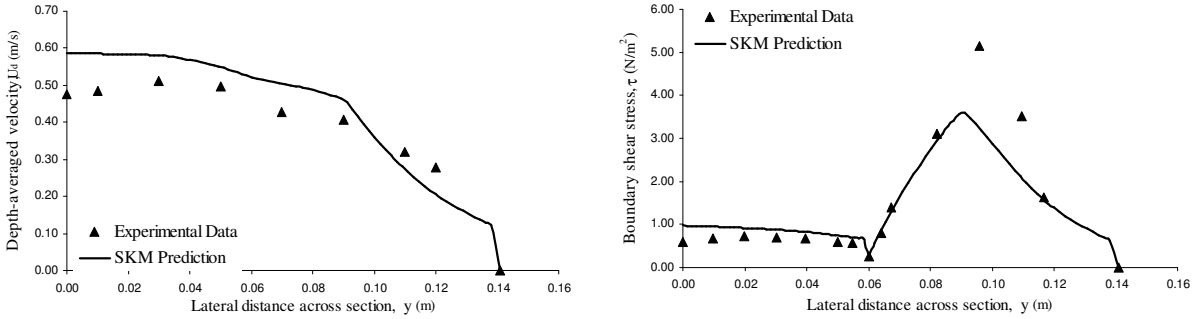

Figure (IV-47): Al-Hamid 11; depth 0.081 m;
Q_{data}=7.38 l.s^{-1}; Q_{SKM}=7.75 l.s^{-1}; %SFw$_{data}$=87.36; %SFw$_{SKM}$=83.21

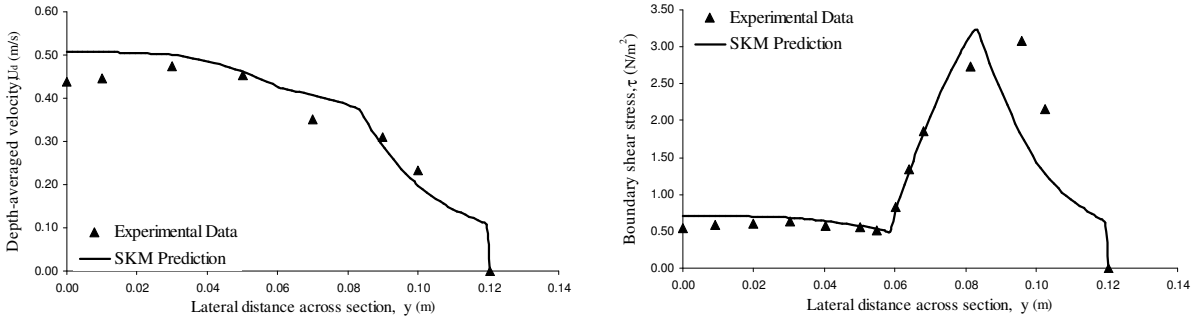

Figure (IV-48): Al-Hamid 12; depth 0.060 m;
Q_{data}=4.48 l.s^{-1}; Q_{SKM}=4.56 l.s^{-1}; %SFw$_{data}$=82.73; %SFw$_{SKM}$=81.07

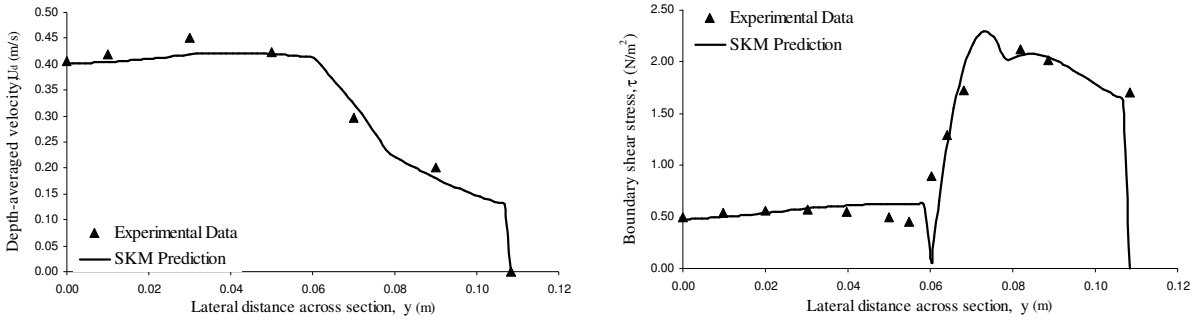

Figure (IV-49): Al-Hamid 13; depth 0.048 m;
Q_{data}=3.11 l.s^{-1}; Q_{SKM}=2.92 l.s^{-1}; %SFw$_{data}$=79.59; %SFw$_{SKM}$=80.58

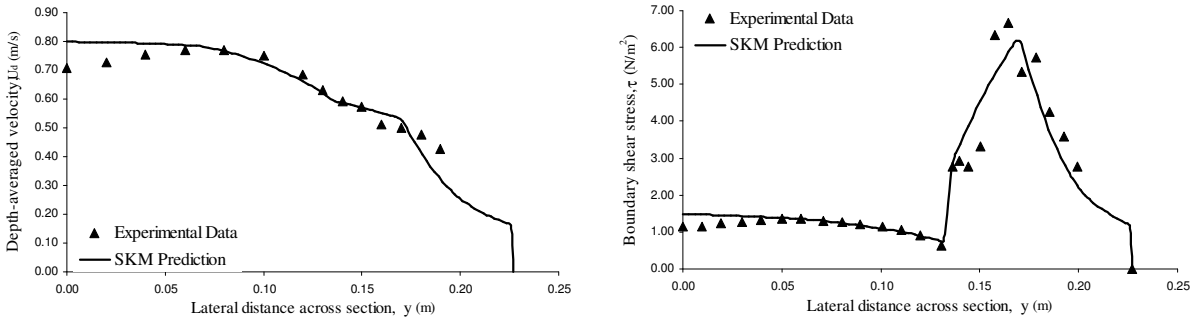

Figure (IV-50): Al-Hamid 17; depth 0.091 m;
Q_{data}=22.25 l.s^{-1}; Q_{SKM}=21.75 l.s^{-1}; %SFw$_{data}$=74.68; %SFw$_{SKM}$=74.34

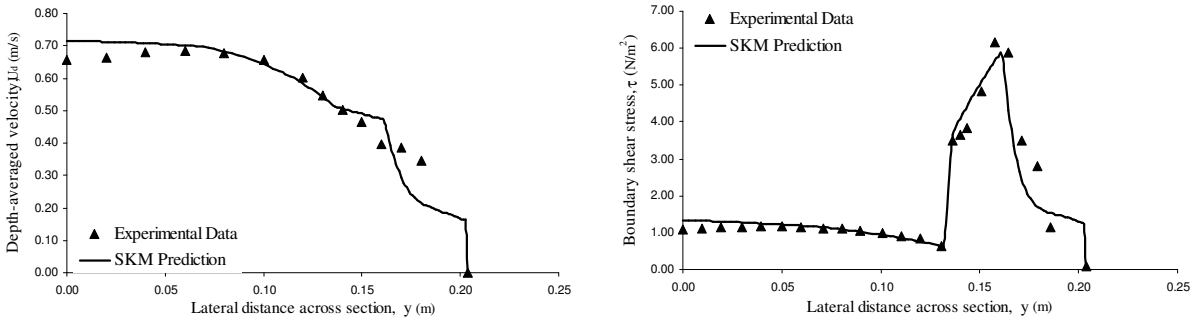

Figure (IV-51): Al-Hamid 18; depth 0.068 m;
Q_{data}=14.09 l.s^{-1}; Q_{SKM}=13.86 l.s^{-1}; %SFw$_{data}$=68.32 ; %SFw$_{SKM}$=68.01

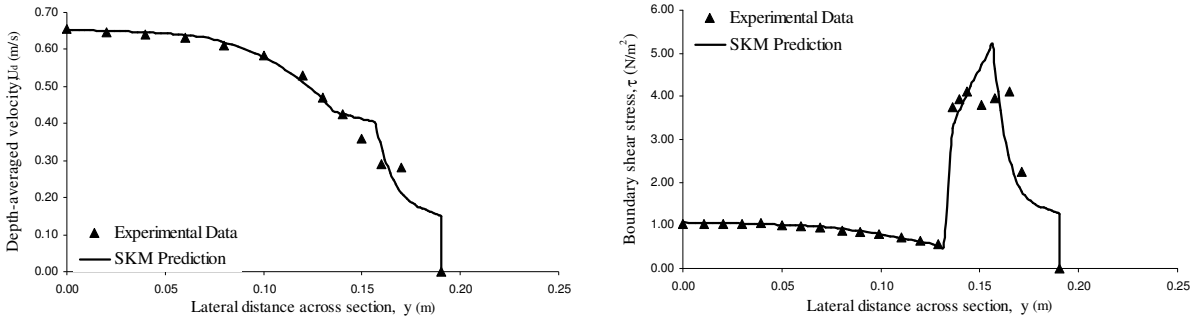

Figure (IV-52): Al-Hamid 19; depth 0.055 m;
Q_{data}=10.00 l.s^{-1}; Q_{SKM}=9.79 l.s^{-1}; %SFw$_{data}$=64.36; %SFw$_{SKM}$=65.05

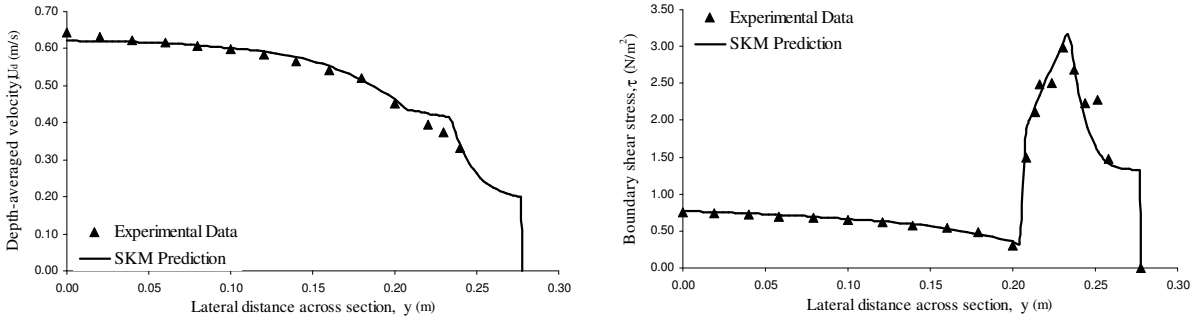

Figure (IV-53): Al-Hamid 31; depth 0.070 m;
Q_{data}=18.47 l.s^{-1}; Q_{SKM}=18.25 l.s^{-1}; %SFw$_{data}$=59.66; %SFw$_{SKM}$=60.97

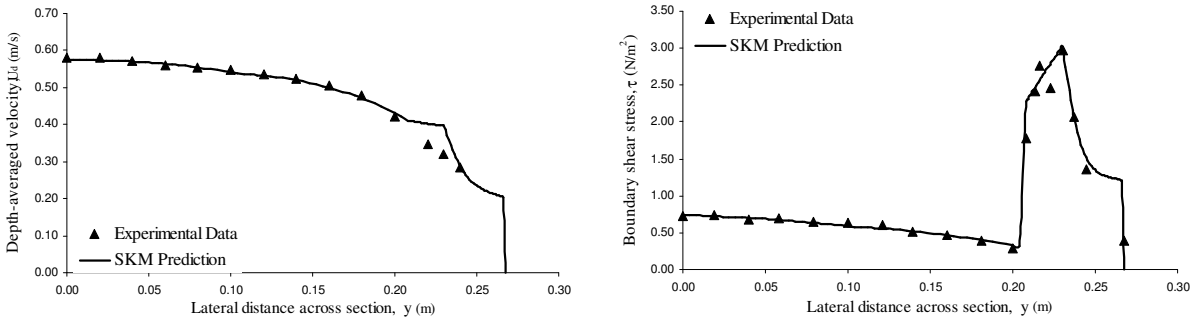

Figure (IV-54): Al-Hamid 32; depth 0.059 m;
Q_{data}=14.30 l.s^{-1}; Q_{SKM}=14.13 l.s^{-1}; %SFw$_{data}$=55.56; %SFw$_{SKM}$=58.85

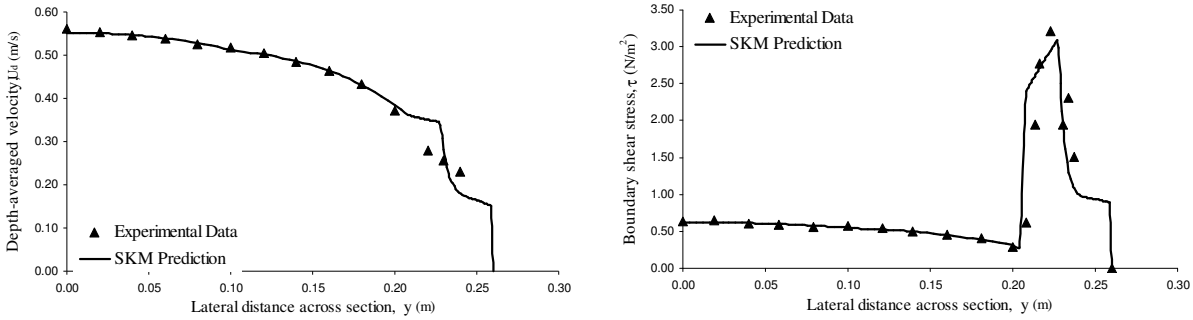

Figure (IV-55): Al-Hamid 33; depth 0.052 m;
Q_{data}=11.53 l.s^{-1}; Q_{SKM}=11.44 l.s^{-1}; %SFw$_{data}$=52.22; %SFw$_{SKM}$=54.97

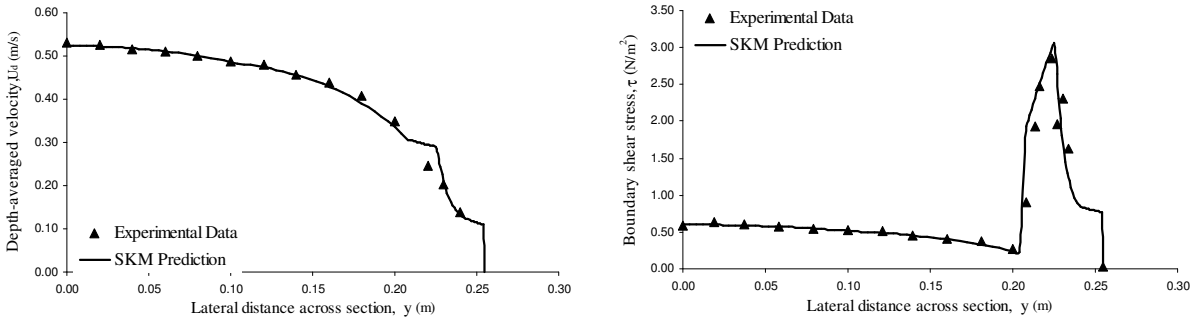

Figure (IV-56): Al-Hamid 34; depth 0.046 m;
Q_{data}=9.61 l.s^{-1}; Q_{SKM}=9.44 l.s^{-1}; %SFw$_{data}$=49.99; %SFw$_{SKM}$=51.88

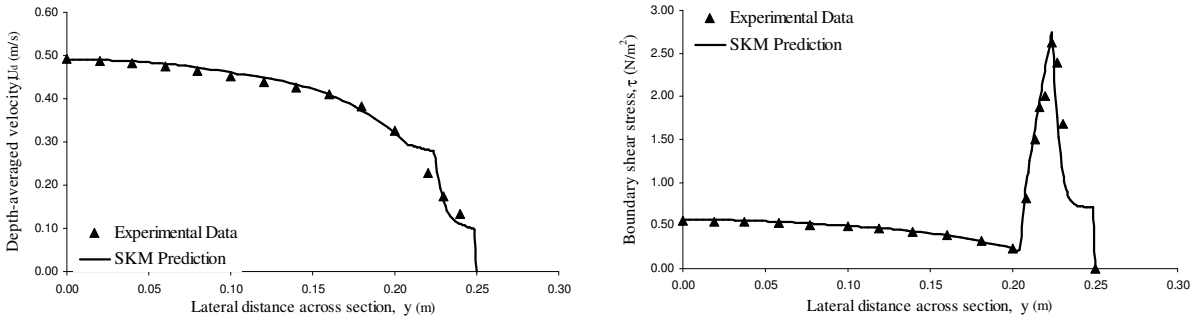

Figure (IV-57): Al-Hamid 35; depth 0.042 m;
Q_{data}=8.03 l.s^{-1}; Q_{SKM}=7.95 l.s^{-1}; %SFw$_{data}$=46.91; %SFw$_{SKM}$=44.71

IV.3.2 Rough Bed and Rough Walls

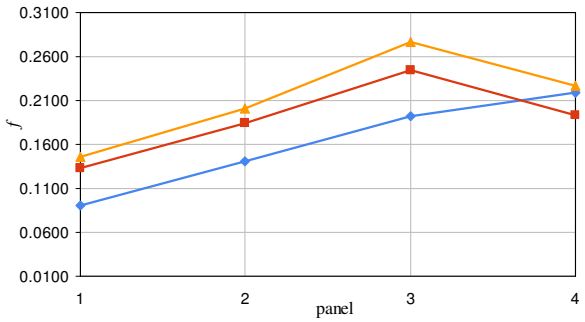

a) Friction factor vs. panel number

R1 (1.49<2*b*/*h*<2.50, S_0=3.920x10^{-3})

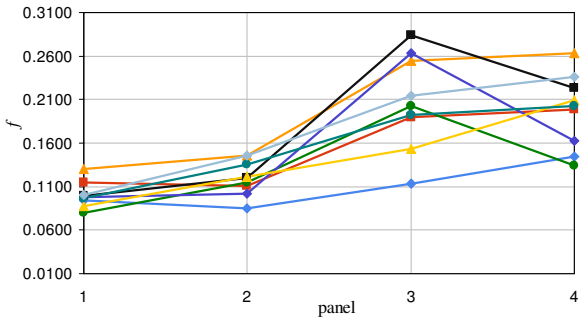

b) Friction factor vs. panel number

R2 (1.50<2*b*/*h*<9.98, S_0=1.935 & 4.03x10^{-3})

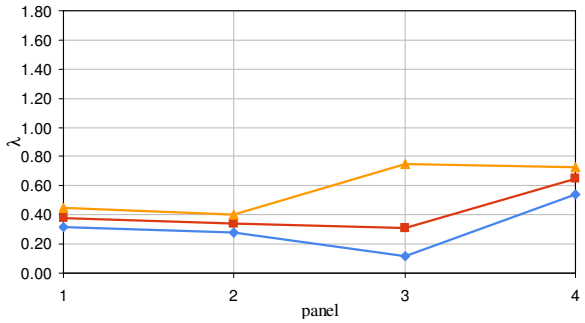

c) Dimensionless eddy viscosity vs. panel

R1 (1.49<2*b*/*h*<2.50, S_0=3.920x10^{-3})

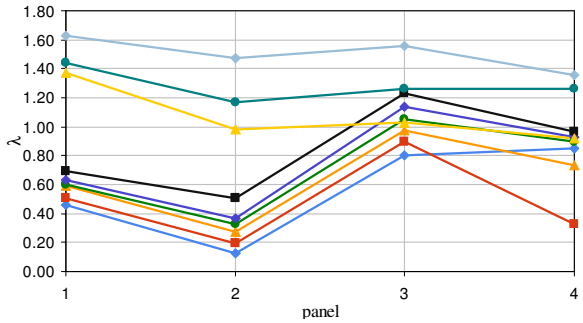

d) Dimensionless eddy viscosity vs. panel

R2 (1.50<2*b*/*h*<9.98, S_0=1.935 & 4.03x10^{-3})

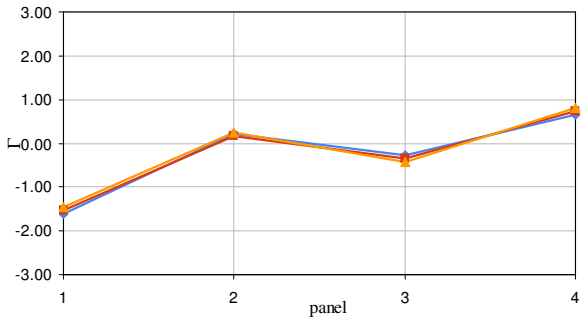

e) Secondary flow term vs. panel number

R1 (1.49<2*b*/*h*<2.50, S_0=3.920x10^{-3})

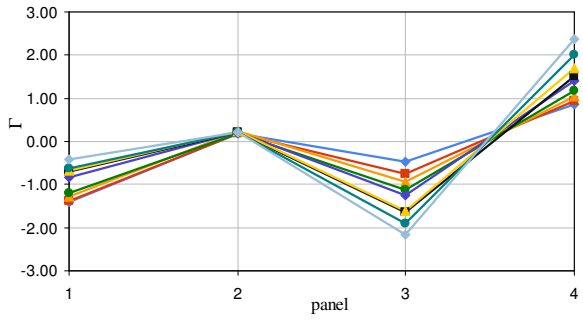

e) Secondary flow term vs. panel number

R2 (1.50<2*b*/*h*<9.98, S_0=1.935 & 4.03x10^{-3})

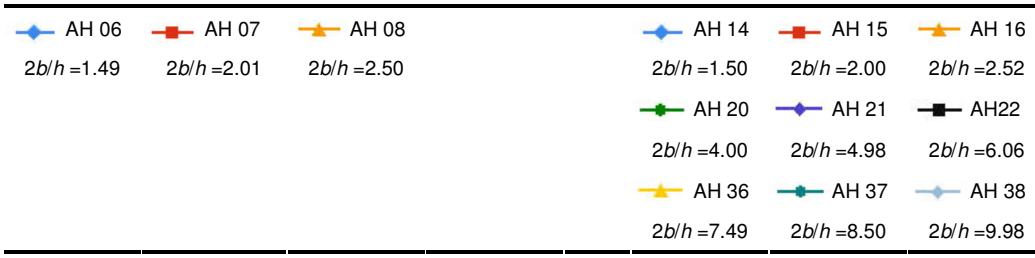

Figure (IV-58): Variation of the friction factor, dimensionless eddy viscosity and secondary flow term against the panel number for Al-Hamid's trapezoidal channels with rough bed and wall.

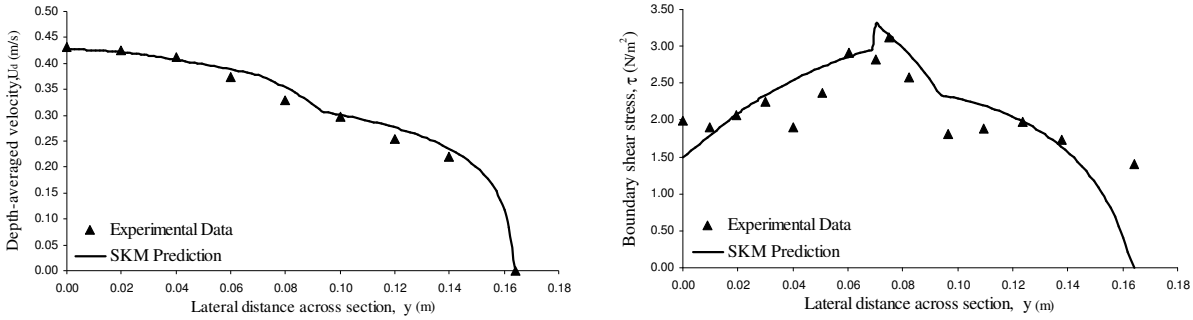

Figure (IV-59): Al-Hamid 06; depth 0.094 m;
Q_{data}=8.02 l.s^{-1}; Q_{SKM}=7.75 l.s^{-1}; %SFw$_{data}$=64.09; %SFw$_{SKM}$=61.34

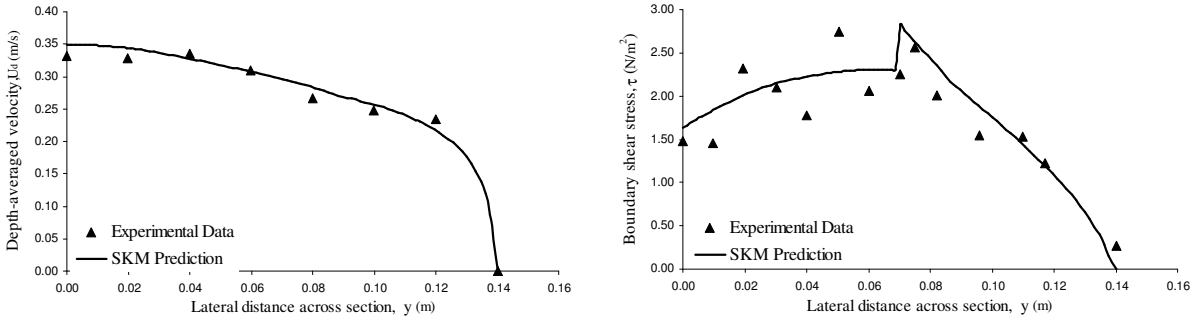

Figure (IV-60): Al-Hamid 07; depth 0.070 m;
Q_{data}=4.43 l.s^{-1}; Q_{SKM}=4.37 l.s^{-1}; %SFw$_{data}$=52.13; %SFw$_{SKM}$=51.03

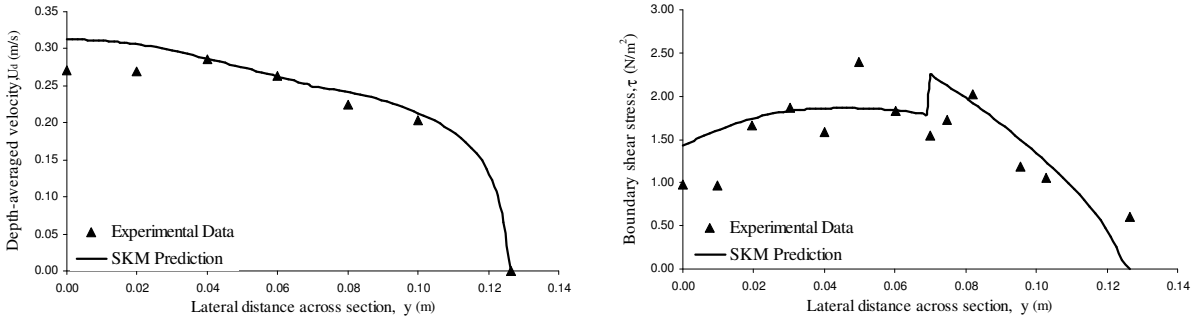

Figure (IV-61): Al-Hamid 08; depth 0.056 m;
Q_{data}=2.82 l.s^{-1}; Q_{SKM}=2.9 l.s^{-1}; %SFw$_{data}$=47.89; %SFw$_{SKM}$=46.04

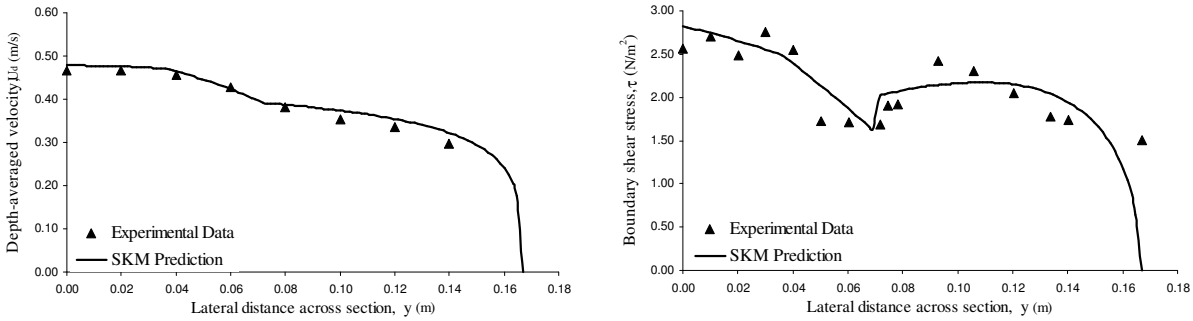

Figure (IV-62): Al-Hamid 14; depth 0.095 m;
Q_{data}=9.50 l.s^{-1}; Q_{SKM}=9.29 l.s^{-1}; %SFw$_{data}$=62.93; %SFw$_{SKM}$=60.33

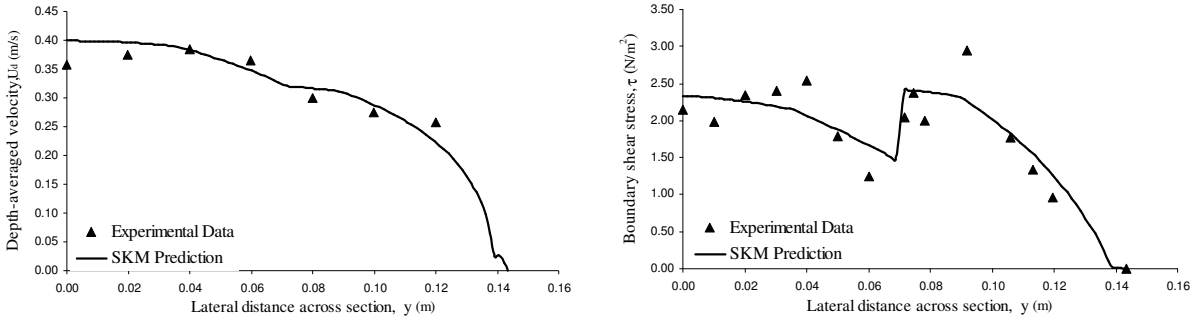

Figure (IV-63): Al-Hamid 15; depth 0.072 m;
Q_{data}=5.33 l.s^{-1}; Q_{SKM}=5.40 l.s^{-1}; %SFw$_{data}$=53.88; %SFw$_{SKM}$=55.80

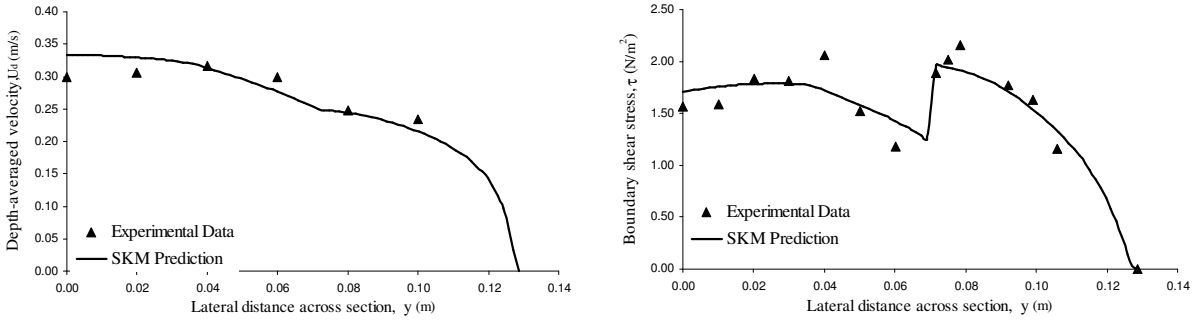

Figure (IV-64): Al-Hamid 16; depth 0.057 m;
Q_{data}=3.31 l.s^{-1}; Q_{SKM}=3.15 l.s^{-1}; %SFw$_{data}$=49.01; %SFw$_{SKM}$=47.43

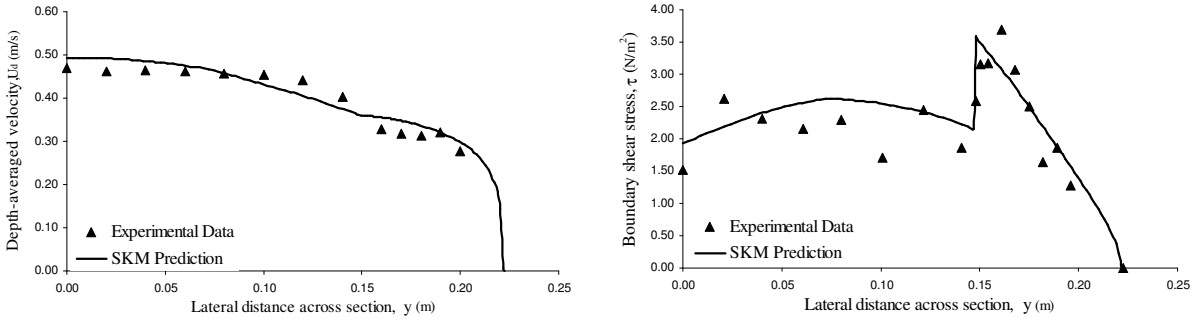

Figure (IV-65): Al-Hamid 20; depth 0.074 m;
Q_{data}=11.78 l.s^{-1}; Q_{SKM}=11.52 l.s^{-1}; %SFw$_{data}$=38.18; %SFw$_{SKM}$=36.56

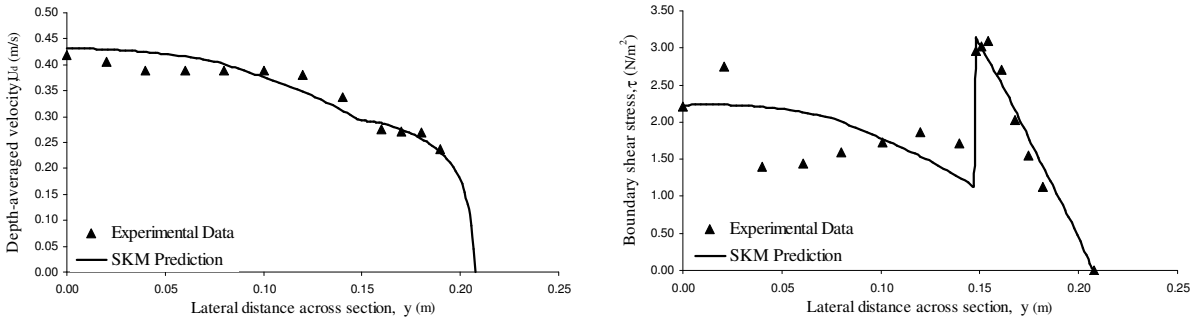

Figure (IV-66): Al-Hamid 21; depth 0.060 m;
Q_{data}=7.86 l.s^{-1}; Q_{SKM}=7.72 l.s^{-1}; %SFw$_{data}$=32.12; %SFw$_{SKM}$=31.80

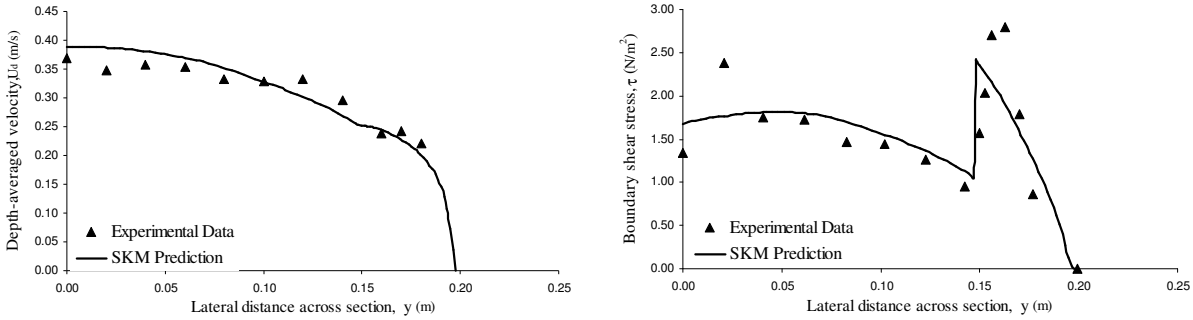

Figure (IV-67): Al-Hamid 22; depth 0.050 m;
Q_{data}=5.58 l.s^{-1}; Q_{SKM}=5.54 l.s^{-1}; %SFw$_{data}$=29.03; %SFw$_{SKM}$=28.36

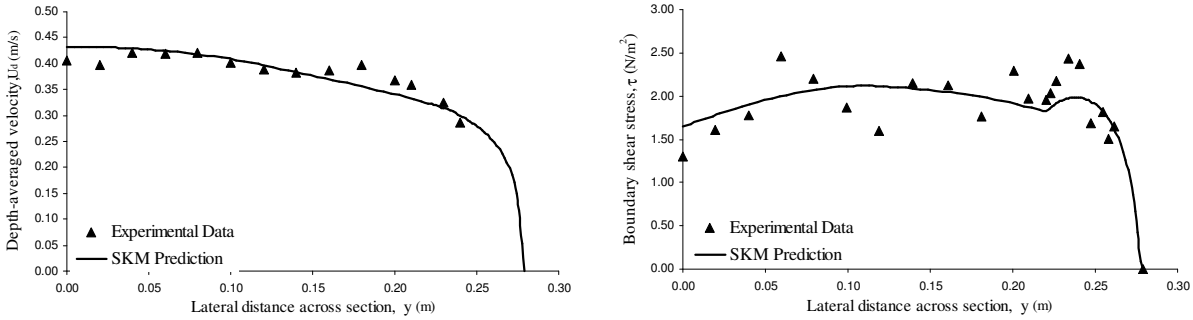

Figure (IV-68): Al-Hamid 36; depth 0.059 m;
Q_{data}=11.43 l.s^{-1}; Q_{SKM}=11.11 l.s^{-1}; %SFw$_{data}$=24.12; %SFw$_{SKM}$=23.57

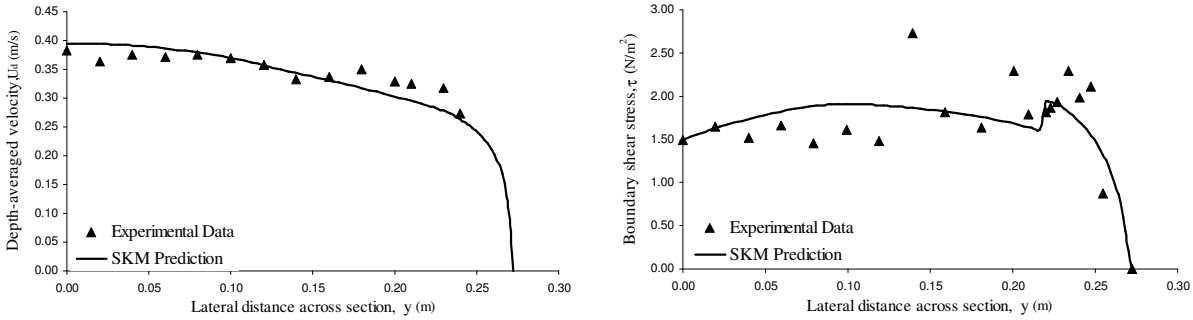

Figure (IV-69): Al-Hamid 37; depth 0.052 m;
Q_{data}=9.01 l.s^{-1}; Q_{SKM}=8.75 l.s^{-1}; %SFw$_{data}$=21.15; %SFw$_{SKM}$=20.90

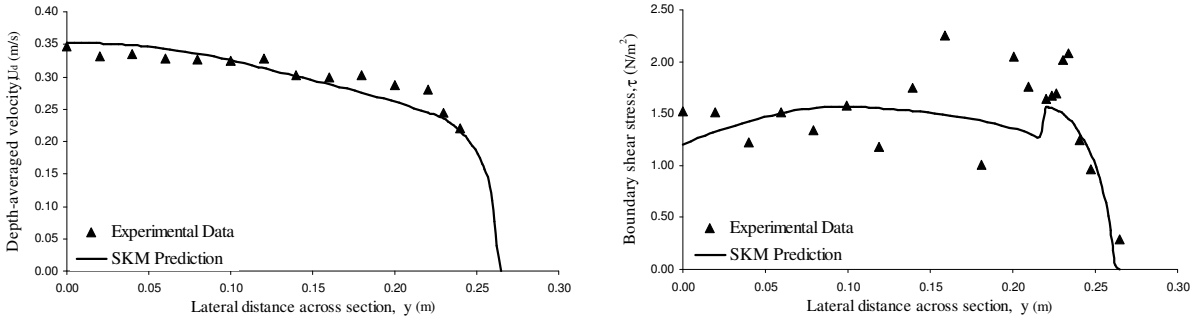

Figure (IV-70): Al-Hamid 38; depth 0.044 m;
Q_{data}=6.66 l.s^{-1}; Q_{SKM}=6.46 l.s^{-1}; %SFw$_{data}$=18.08; %SFw$_{SKM}$=17.65

IV.4 RECTANGULAR DATA

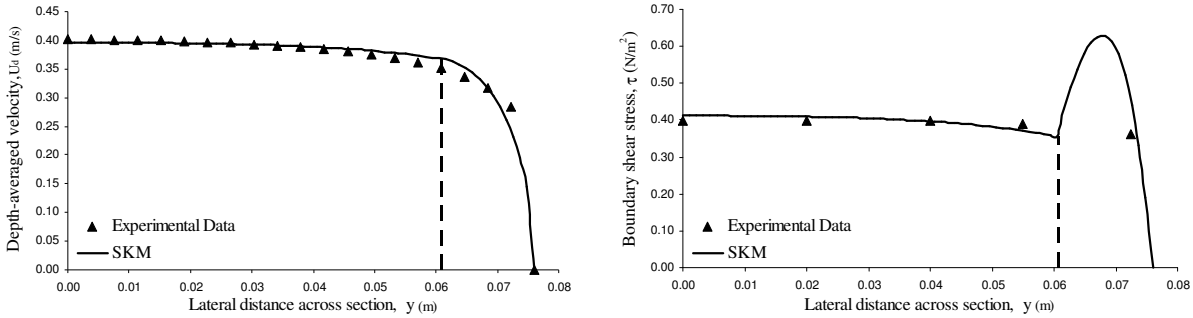

Figure (IV-71): DWK01; depth 0.0858 m; Q_{data}=4.80 l.s^{-1}; Q_{SKM}=4.78 l.s^{-1}

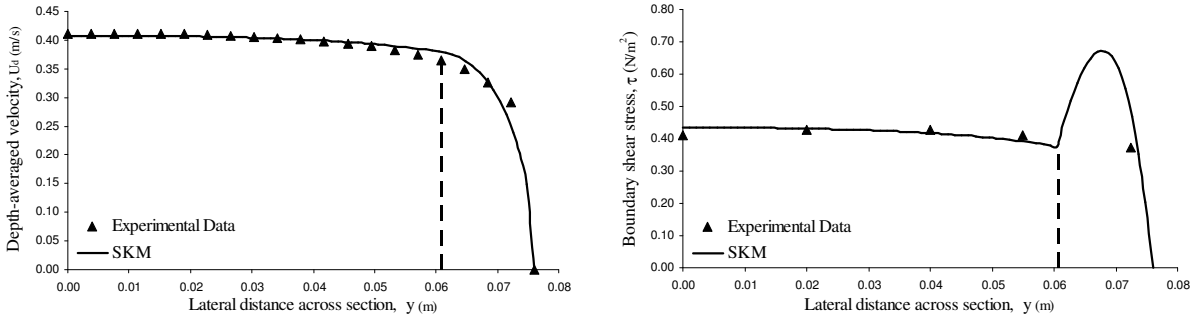

Figure (IV-72): DWK02; depth 0.0970 m; Q_{data}=5.60 l.s^{-1}; Q_{SKM}=5.57 l.s^{-1}

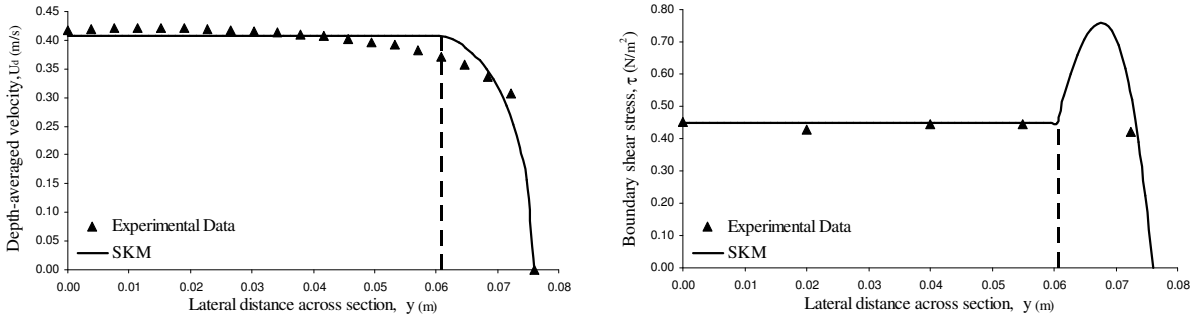

Figure (IV-73): DWK03; depth 0.1026 m; Q_{data}=6.07 l.s^{-1}; Q_{SKM}=6.03 l.s^{-1}

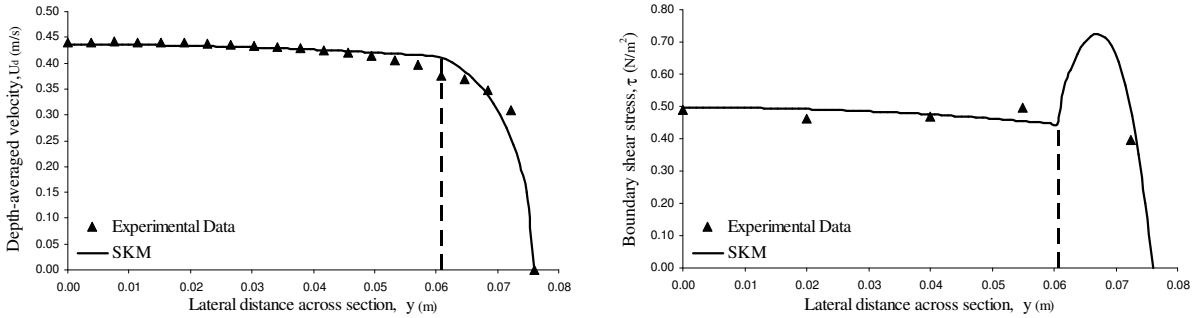

Figure (IV-74): DWK04; depth 0.1136 m; Q_{data}=7.00 l.s^{-1}; Q_{SKM}=6.94 l.s^{-1}

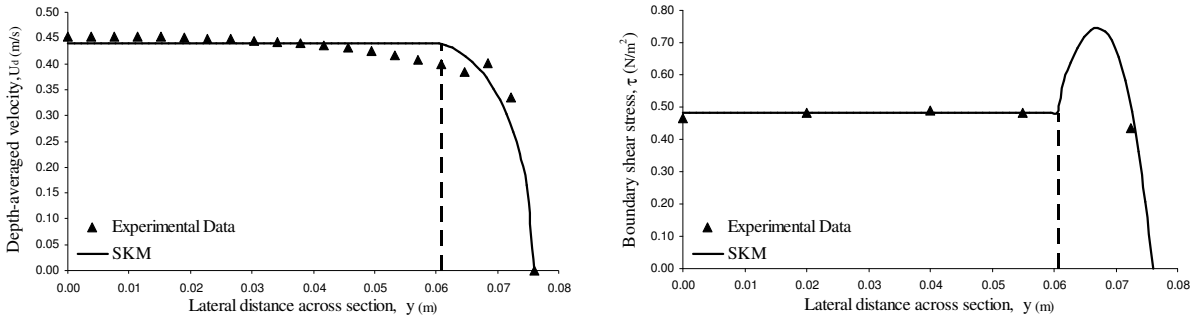

Figure (IV-75): DWK05; depth 0.1259 m; Q_{data}=8.00 l.s^{-1}; Q_{SKM}=7.96 l.s^{-1}

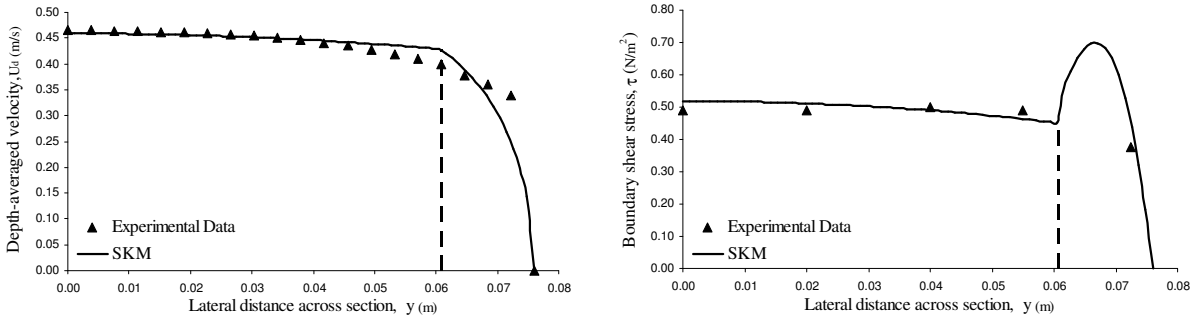

Figure (IV-76): DWK06; depth 0.1530 m; Q_{data}=9.85 l.s^{-1}; Q_{SKM}=9.73 l.s^{-1}

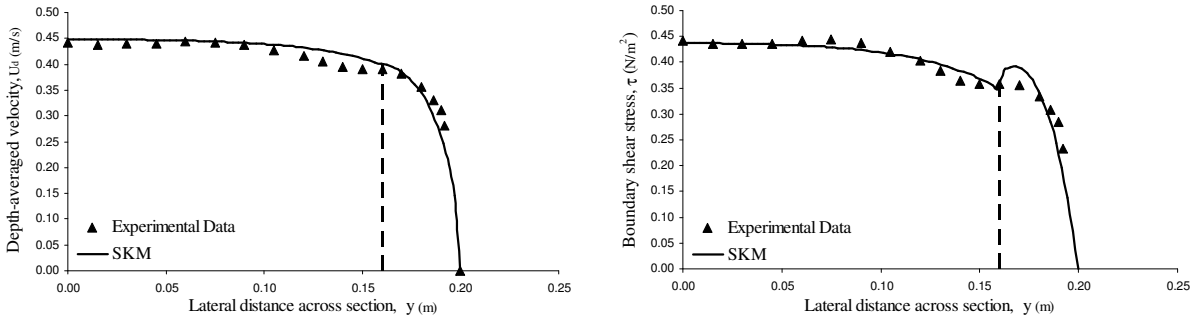

Figure (IV-77): AP1001; depth 0.0683 m; Q_{data}=9.85 l.s^{-1}; Q_{SKM}=10.70 l.s^{-1}

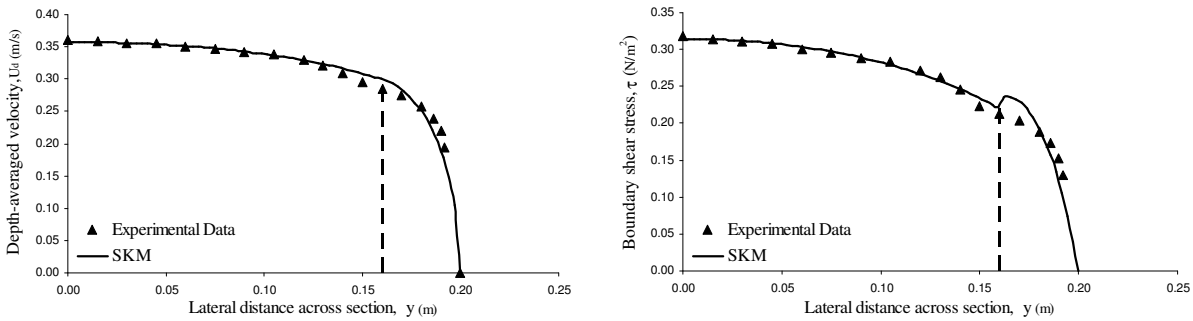

Figure (IV-78): AP1002; depth 0.0499 m; Q_{data}=5.81 l.s^{-1}; Q_{SKM}=6.30 l.s^{-1}

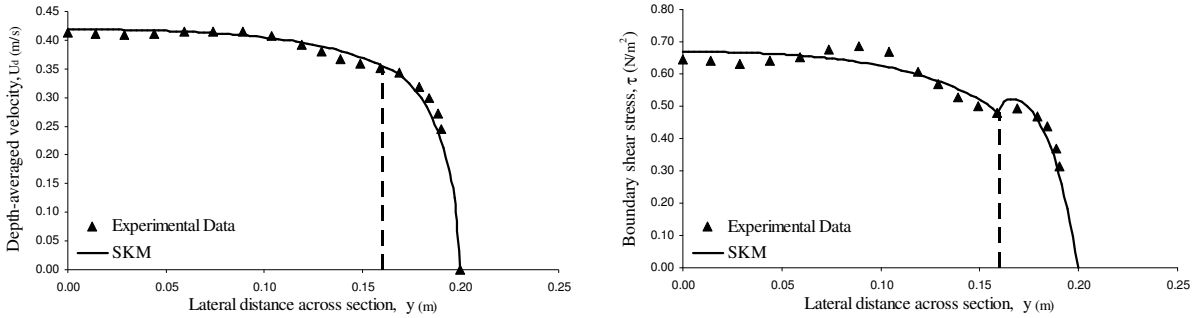

Figure (IV-79): AP1601; depth 0.0663 m; Q_{data}=9.25 l.s^{-1}; Q_{SKM}=9.94 l.s^{-1}

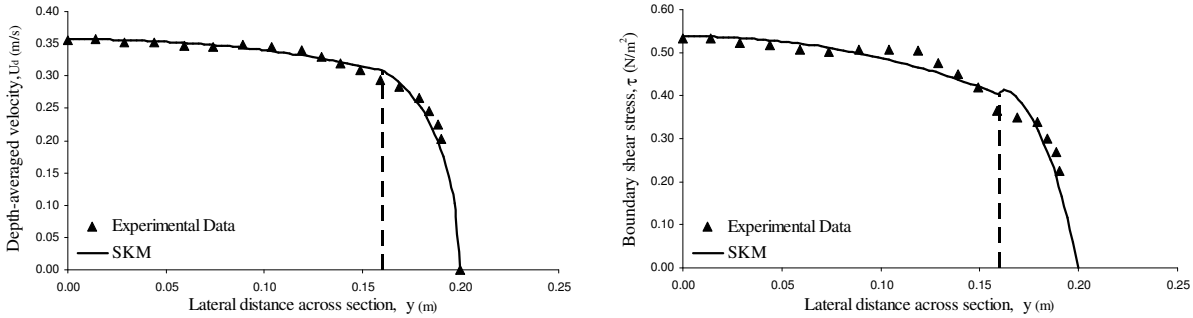

Figure (IV-80): AP1602; depth 0.0496 m; Q_{data}=5.87 l.s^{-1}; Q_{SKM}=6.29 l.s^{-1}

IV.5 RIVERS WITH INBANK FLOW

IV.5.1 River Colorado

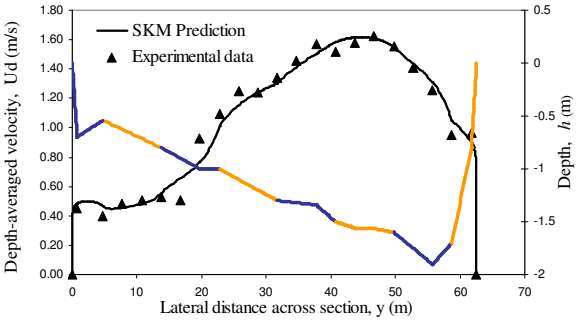

Figure (IV-81): Colorado 01; depth 1.900m; Q_{data}=90.15 m^3.s^{-1}; Q_{SKM}=88.52m^3.s^{-1}

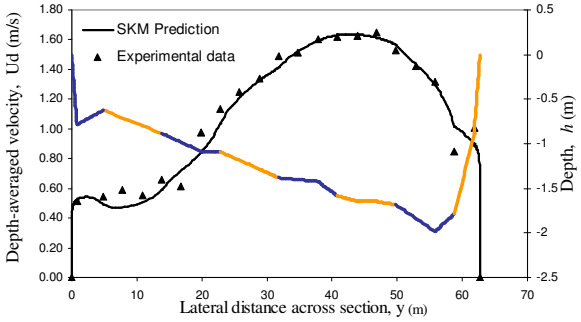

Figure (IV-82): Colorado 02; depth 1.984m; Q_{data}=100.62 m^3.s^{-1}; Q_{SKM}=97.05 m^3.s^{-1}

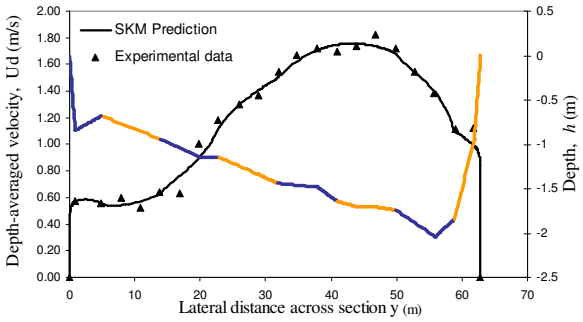

Figure (IV-83): Colorado 03; depth 2.040m; Q_{data}=108.56 $m^3.s^{-1}$; Q_{SKM}=108.48 $m^3.s^{-1}$

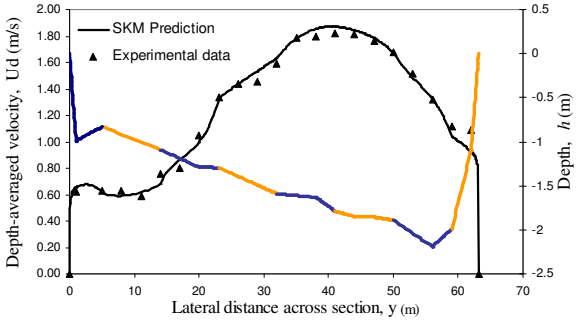

Figure (IV-84): Colorado 04; depth 2.190m; Q_{data}=128.90 $m^3.s^{-1}$; Q_{SKM}=125.44 $m^3.s^{-1}$

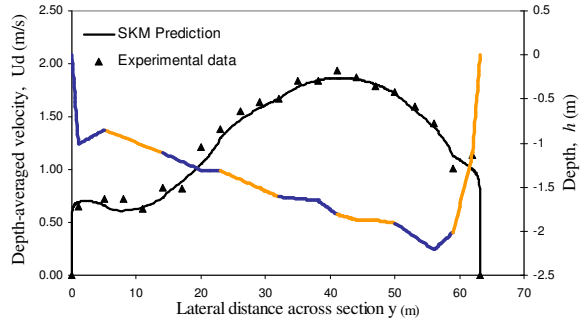

Figure (IV-85): Colorado 05; depth 2.210m; Q_{data}=132.27 $m^3.s^{-1}$; Q_{SKM}=130.30 $m^3.s^{-1}$

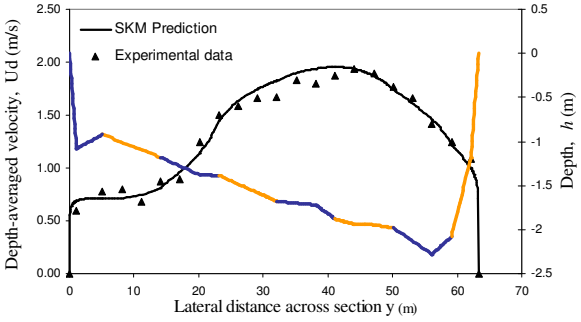

Figure (IV-86): Colorado 06; depth 2.280m; Q_{data}=144.58 $m^3.s^{-1}$; Q_{SKM}=144.53 $m^3.s^{-1}$

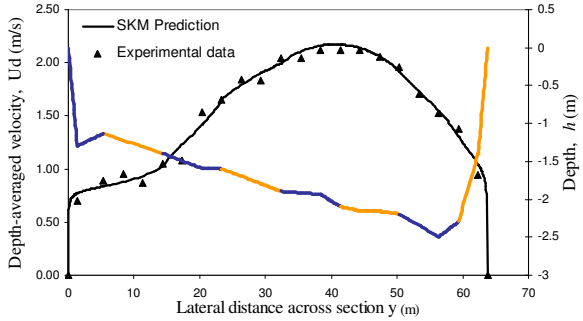

Figure (IV-87): Colorado 07; depth 2.494m; Q_{data}=181.98 $m^3.s^{-1}$; Q_{SKM}=182.14 $m^3.s^{-1}$

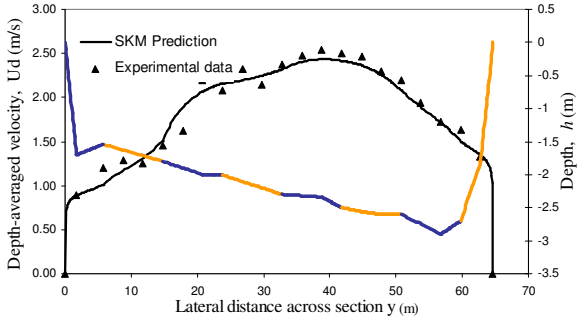

Figure (IV-88): Colorado 08; depth 2.899m; Q_{data}=267.15 $m^3.s^{-1}$; Q_{SKM}=263.87 $m^3.s^{-1}$

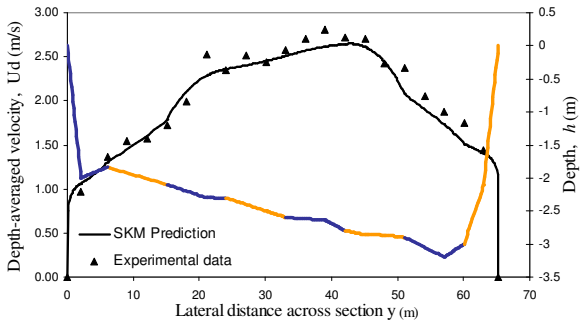

Figure (IV-89): Colorado 09; depth 3.198m; Q_{data}=331.03 $m^3.s^{-1}$; Q_{SKM}=325.46 $m^3.s^{-1}$

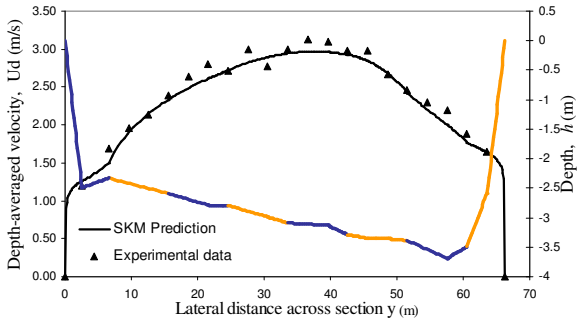

Figure (IV-90): Colorado 10; depth 3.690m; Q_{data}=449.57 $m^3.s^{-1}$; Q_{SKM}=453.78 $m^3.s^{-1}$

IV.5.2 RIVer La Suela

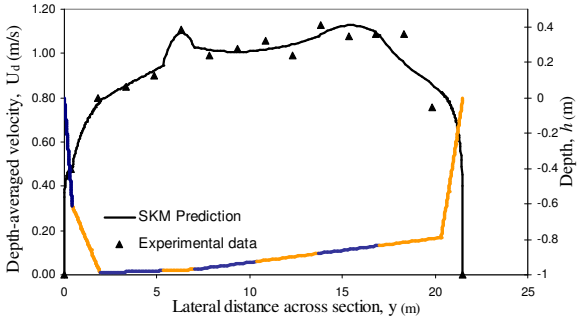

Figure (IV-91): La Suela 01; depth 0.99m; Q_{data}=15.30 $m^3.s^{-1}$; Q_{SKM}=17.91 $m^3.s^{-1}$

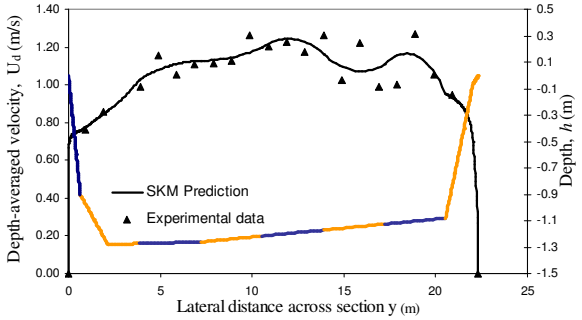

Figure (IV-92): La Suela 02; depth 1.28m; Q_{data}=21.11 $m^3.s^{-1}$; Q_{SKM}=26.92 $m^3.s^{-1}$

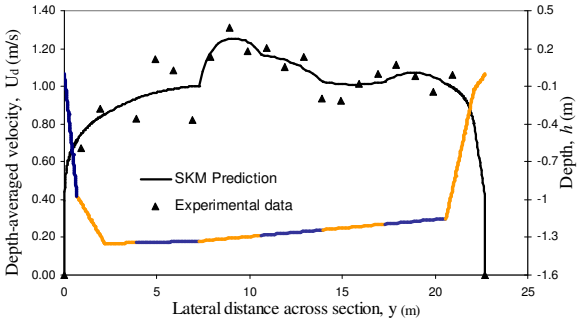

Figure (IV-93): La Suela 03; depth 1.35m; Q_{data}=21.31 $m^3.s^{-1}$; Q_{SKM}=27.22 $m^3.s^{-1}$

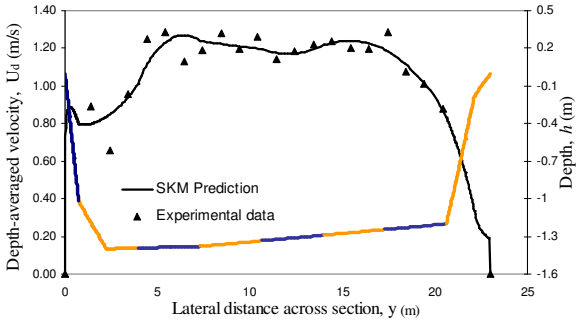

Figure (IV-94): La Suela 04; depth 1.40m; Q_{data}=27.87 $m^3.s^{-1}$; Q_{SKM}=30.44 $m^3.s^{-1}$

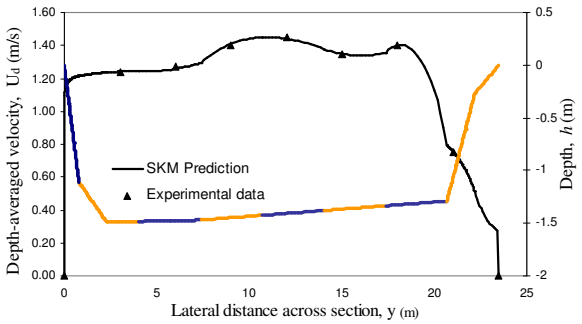

Figure (IV-95): La Suela 05; depth 1.49m; Q_{data}=33.96 $m^3.s^{-1}$; Q_{SKM}=38.27 $m^3.s^{-1}$

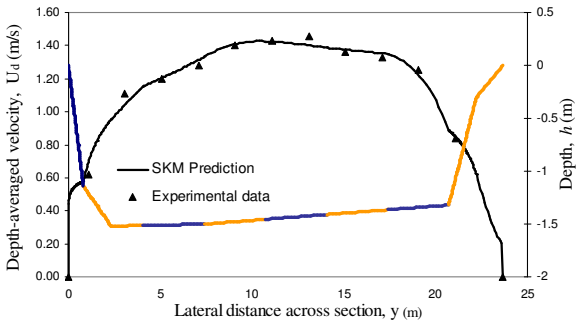

Figure (IV-96): La Suela 06; depth 1.52m; Q_{data}=35.75 $m^3.s^{-1}$; Q_{SKM}=37.24 $m^3.s^{-1}$

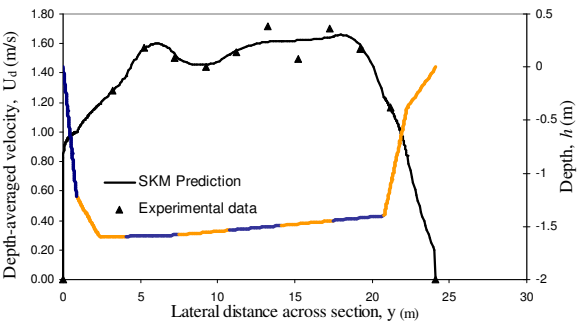

Figure (IV-97): La Suela 07; depth 1.60m; Q_{data}=42.60 $m^3.s^{-1}$; Q_{SKM}=47.24 $m^3.s^{-1}$

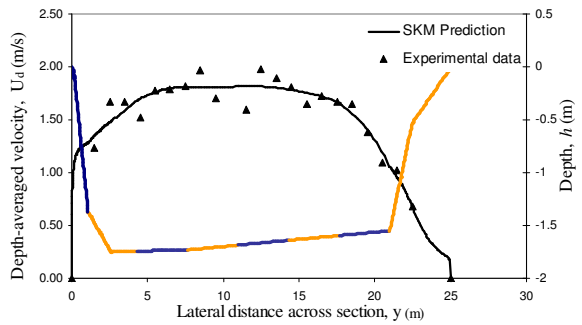

Figure (IV-98): La Suela 08; depth 1.75m; Q_{data}=49.30 $m^3.s^{-1}$; Q_{SKM}=57.99 $m^3.s^{-1}$

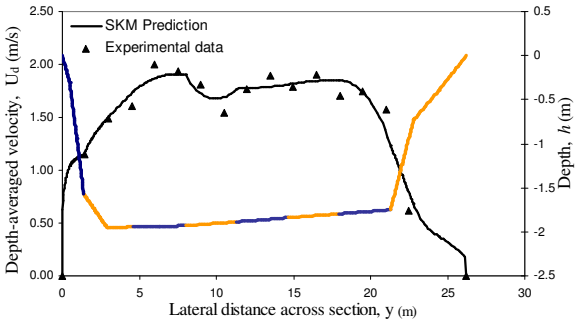

Figure (IV-99): La Suela 09; depth 1.95m; Q_{data}=59.79 $m^3.s^{-1}$; Q_{SKM}=67.54 $m^3.s^{-1}$

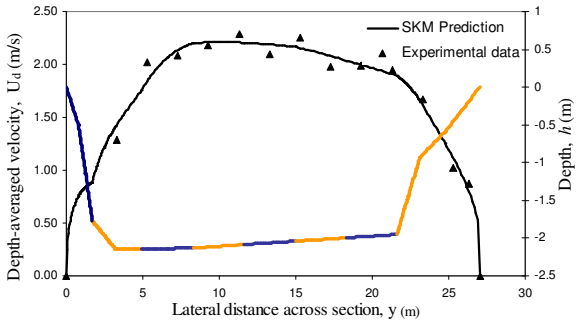

Figure (IV-100): La Suela 10; depth 2.15m; Q_{data}=83.41 $m^3.s^{-1}$; Q_{SKM}=89.06 $m^3.s^{-1}$

IV.5.3 Other River Sections

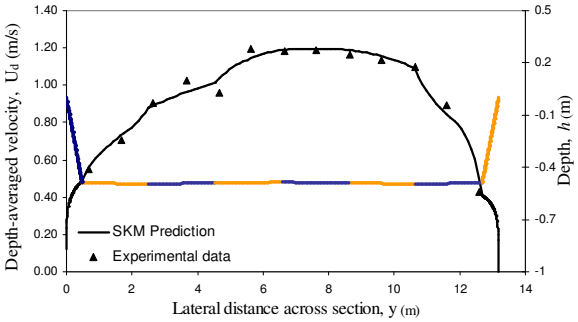

Figure (IV-101): River Main at Bridge End; depth 0.49m; Q_{data}=6.03$m^3.s^{-1}$; Q_{SKM}=6.03$m^3.s^{-1}$

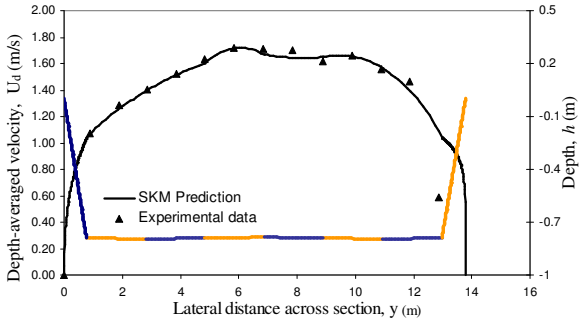

Figure (IV-102): River Main at Bridge End; depth 0.79m; Q_{data}=14.82$m^3.s^{-1}$; Q_{SKM}=15.16$m^3.s^{-1}$

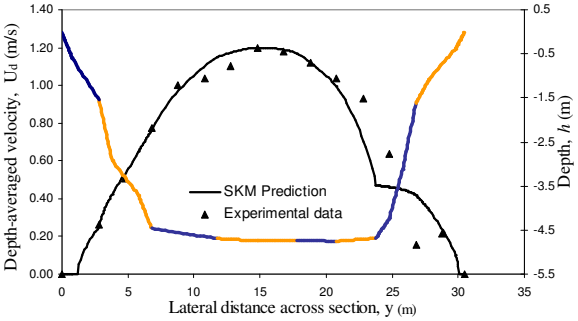

Figure (IV-103): River Severn at Montford; depth 4.753m; Q_{data}=98.3$m^3.s^{-1}$; Q_{SKM}=96.12$m^3.s^{-1}$

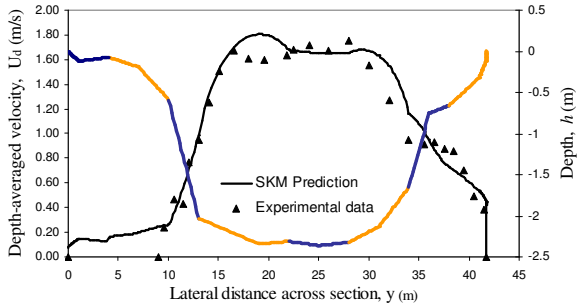

Figure (IV-104): River Trent at Yoxall; Depth 2.360m; Q_{data}=82.59 $m^3.s^{-1}$; Q_{SKM}=83.48$m^3.s^{-1}$

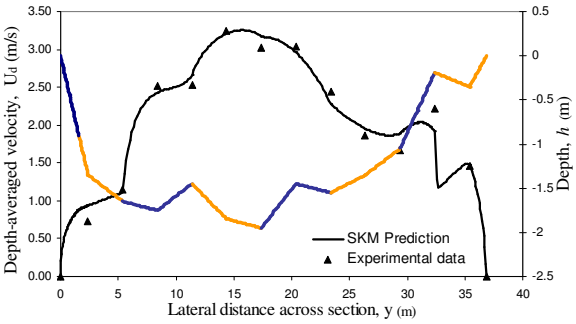

Figure (IV-105): River Cuenca Ecuador; depth 1.95m; Q_{data}=135.470 $m^3.s^1$; Q_{SKM}=125.625 $m^3.s^{-1}$

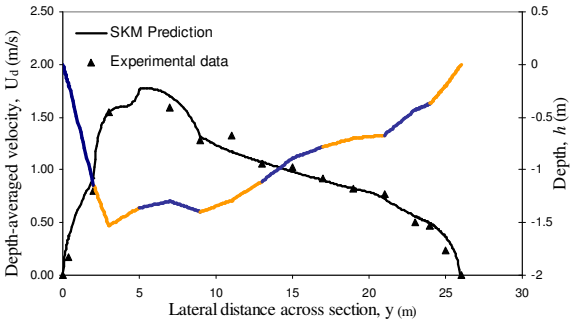

Figure (IV-106): River Tomebamba, Ecuador; depth 1.53m; Q_{data}=29.22 $m^3.s^{-1}$; Q_{SKM}=29.23 $m^3.s^{-1}$

APPENDIX V

STATISTICAL PROCEDURES

V.1 INTRODUCTION

In this Appendix, two statistical procedures which were used in the context of this research will be briefly explained. Samples of the application of each procedure will also be provided for further clarification. In the second stage of the calibration framework post-validation phase (Section 4.4.6.2), the k-means clustering method (Gnanadesikan, 1977) was used to detect the clusters of solutions on the effective portion of the Pareto front, each representing a region of attraction in the parametric space. In addition, a backward elimination procedure (Mardia *et al*., 1979; Johnson and Wichern, 1988) based on the PCA of the free overfall data was conducted to find the principal variables that mainly govern the end-depth ratio (*EDR*).

V.2 K-MEANS CLUSTER ANALYSIS

Cluster analysis is a statistical technique used to classify or group objects of similar kind into meaningful sets or clusters by means of maximizing the degree of similarity (homogeneity) of the characteristics possessed within each cluster, and heterogeneity between clusters (Blashfield and Aldenderfer, 1978). Cluster analysis was first discussed in the social sciences during the 1930s and its popularity grew in the 1960s when biological taxonomists began using clustering methods for classificatory research. Clustering techniques have been applied in many fields including anthropology, archaeology, biology, medicine, market segmentation, statistics, psychology, psychiatry, pattern recognition, and other social sciences (Blashfield and Aldenderfer, 1978; Steinley, 2006).

The different methods of cluster analysis fall mainly into two families: hierarchical methods and iterative partitioning methods (nonhierarchical methods) (Gnanadesikan, 1977).

Hierarchical clustering can be "agglomerative" where clustering builds up toward a single cluster, or "divisive" where clustering breaks up into smaller subsets and is often represented by a tree or a "dendogram" (Gnanadesikan, 1977). The agglomerative method begins at the top of the tree with each data point as its own cluster, and similar entities are linked together sequentially based on the defined linkage rules. Clusters are built gradually as separate data points (entities) merge into larger clusters. Clustering continues until one cluster contains the entire dataset. In contrast, the divisive method begins at the roots of the tree with the whole set in one cluster and continuously divides it into smaller clusters (Gnanadesikan, 1977).

Unlike hierarchical methods, iterative partitioning begins with a predetermined number of clusters. Centroids are assumed, estimated, or computed for each cluster and data points are assigned to the cluster with the closest centroid. After allocation, new centroids are recalculated followed by updated cluster membership. Based on the new centroids, members may be reassigned if they are closer to a different cluster's centroid. This process continues until no reassignments occur (Gnanadesikan, 1977; Blashfield and Aldenderfer, 1984).

Best known for its simplicity and computational efficiency, k-means method is one of the most popular methods of nonhierarchical clustering (Gnanadesikan, 1977). In this technique, first, the numbers of clusters are determined and accordingly, data points are assigned to the clusters in a way that the means across clusters are as different from each other as possible. The final clusters are found by an iterative process of minimizing the variability within each cluster and maximizing the variability between clusters (without any overlap between clusters). This process contains the following steps:

1- The items are randomly separated into K initial clusters and the centroid (mean) of each cluster is calculated

2- The distance (normally the Euclidian distance) of each item to the centroid of all clusters is measured and items are reassigned to the nearest cluster.

3- Step 2 is repeated for all individuals until no more reassignments take place.

Example

Table (V-1) shows the measured variables (X_1 and X_2) for four items where the objective is to divide them into k = 2 clusters.

Item	X_1	X_2
A	7	2
B	-1	4
C	2	-3
D	-4	-1

Table (V-1): Raw data.

Following the first step, the items are arbitrarily partitioned into two clusters, such as (AB) and (CD), and the coordinates (mean) of the clusters' centroid are calculated (Table (V-2)).

Cluster	$\overline{X_1}$	$\overline{X_2}$
(AB)	$\frac{7+(-1)}{2}=3$	$\frac{2+4}{2}=3$
(CD)	$\frac{2+(-4)}{2}=-1$	$\frac{-3+(-1)}{2}=-2$

Table (V-2): Coordinates of cluster centroids.

At step 2, the Euclidian distance of each item to the centroid of the clusters is measured:

$$d^2(\mathrm{A},(\mathrm{AB}))=(7-3)^2+(2-3)^2=17 \quad \text{(V-1)}$$

$$d^2(\mathrm{A},(\mathrm{CD}))=(7+1)^2+(2+2)^2=80 \quad \text{(V-2)}$$

Since A is closer to cluster (AB) than cluster (CD), it is not reassigned. Continuing,

$$d^2(\mathrm{B},(\mathrm{AB}))=(-1-3)^2+(4-3)^2=17 \quad \text{(V-3)}$$

$$d^2(\mathrm{B},(\mathrm{CD}))=(-1+1)^2+(4+2)^2=36 \quad \text{(V-4)}$$

B is reassigned to cluster (CD) giving cluster (BCD) and the following updated centroid coordinates (Table (V-3)):

Cluster	$\overline{X_1}$	$\overline{X_2}$
(A)	7	2
(BCD)	-1	0

Table (V-3): Coordinates of updated cluster centroids.

Again Step 2 is repeated and each item is checked for reassignment (Table (V-4)):

Cluster	A	B	C	D
(A)	0	80	50	130
(BCD)	125	16	18	10

Table (V-4): Squared distances to group centroids.

It can be observed that each item is assigned to the cluster with the nearest centroid and hence the process stops. The final clusters are (A) and (BCD)

V.3 PRINCIPAL COMPONENT ANALYSIS (PCA)

PCA is a statistical method for reducing the dimensionality of a large dataset while retaining as much information as possible by computing a compact and optimal description of the data (Flury, 1988; Jolliffe, 1986). This technique uses the correlation coefficient between different variables to create a subset of independent components (also known as principal components or eigenvectors). This subset is a linear combination of the original variables, and represents a large proportion of the variation in the system. The unique feature of PCA is that the first principal component produced in the analysis, tends to account for a large degree of variability in the data as possible. The next component accounts for the maximum variance that has not been explained by the first component and so on (Johnson and Wichern, 1988). In general, the number of principal components is equal to the number of original variables; however, for most of the datasets, the first few principal components account for most of the

variance (as long as there is at least one dominant structure within the data). As a result, the rest of the principal components can be ignored with the minimal loss of information. To apply the PCA on a dataset, the following steps should be taken (Smith, 2002):

1- Normalizing the dataset.
2- Calculating the covariance matrix.
3- Calculating the unit eigenvectors and eigenvalues of the covariance matrix.
4- Ordering the eigenvectors (components) by their eigenvalue, from highest to lowest. This gives the components in order of significance.
5- Selecting the components and forming a coefficient matrix from the eigenvectors.
6- Mapping the data on the selected eigenvectors.

Based on PCA, Mardia *et al*. (1979) introduced a procedure for discarding redundant variables and selecting principal variables. In this approach, the important characteristics (variables) of the dataset that contribute most to its variance are retained by ignoring the dominant variables of less important components. This variable elimination process can be summarized as follows:

1- First, the matrix of the normalized independent variables is formed.
2- The PCA is then applied to the normalized data and the variance explained by each of the corresponding principal components is calculated. Based on the results, the number of sufficient components for describing most of the variations (e.g. 90%) in the dataset is found.
3- The eigenvalue vector and the principal component coefficient matrix (eigenvector matrix) for the principal components are derived from PCA.
4- The coefficient matrix is searched and the variable that has the largest absolute coefficient value (most dominant variable) for the component with the smallest eigenvalue (least important component) is found and eliminated from the entire variable set.
5- PCA is again performed on the remaining variables and steps 3 to 5 are repeated.
6- This elimination process continues until the number of sufficient components (defined in step 2) is obtained. The remaining variables are the principal variables.

Example- rectangular free overfall

The detailed application of the introduced backward elimination procedure as applied to a rectangular free overfall is outlined here as an example. The goal is to find the principal variables from the set of $\{b, h_e, (h_e / b), S_0, S_c, \sqrt{S_0}, \sqrt{S_c}, (S_0 / S_c), \sqrt{(S_0 / S_c)}\}$ that are important in estimating the critical depth.

The first step is to prepare the normalized matrix of the variables. This is done by subtracting the mean from each of the data dimensions and dividing the result by the difference of maximum and minimum of that variable. Next PCA is applied to the normalized matrix. The covariance matrix (Table (V-5)) is formed and the eigenvalues (Table (V-6)) and unit eigenvectors (Table (V-7)) of the covariance matrix are calculated. Table (V-6) and Figure (V-1) indicate that the first 4 components account for nearly 95% of the variability within the data (see Figure (6-10)). Following the elimination procedure, the most dominant variable of the least important component is detected and eliminated. Table (V-7) shows that $\sqrt{(S_0 / S_c)}$ has the largest absolute coefficient value and hence should be removed.

In the next step, the normalized dataset matrix with eight variables (original dataset without $\sqrt{(S_0 / S_c)}$) is formed and the previous step is repeated. The covariance matrix is formed and the eigenvalue and eigenvectors (Table (V-8)) are calculated. Here, the critical depth, S_c, is found as the dominant variable of the least important component (component number VII). S_c is removed from the dataset and the elimination procedure is continued until 4 variables are left (Table (VIII). These variables are the principal variables that mainly govern the end-depth ratio (*EDR*) in rectangular free overfall.

	B	h_e	h_e/b	S_0	S_c	$\sqrt{S_0}$	$\sqrt{S_c}$	S_0 / S_c	$\sqrt{S_0 / S_c}$
B	0.142	-0.027	-0.033	0.040	0.011	0.060	0.011	0.014	0.030
h_e	-0.027	0.028	0.011	-0.018	0.004	-0.023	0.005	-0.007	-0.014
h_e/B	-0.033	0.011	0.017	-0.013	-0.001	-0.019	0.001	-0.004	-0.010
S_0	0.040	-0.018	-0.013	0.084	-0.007	0.087	-0.010	0.030	0.049
S_c	0.011	0.004	-0.001	-0.007	0.020	-0.006	0.023	-0.005	-0.008
$\sqrt{S_0}$	0.060	-0.023	-0.019	0.087	-0.006	0.100	-0.009	0.029	0.053
$\sqrt{S_c}$	0.011	0.005	0.001	-0.010	0.023	-0.009	0.029	-0.008	-0.015
S_0 / S_c	0.014	-0.007	-0.004	0.030	-0.005	0.029	-0.008	0.020	0.026
$\sqrt{S_0 / S_c}$	0.030	-0.014	-0.010	0.049	-0.008	0.053	-0.015	0.026	0.040

Table (V-5): Covariance matrix.

	I	***II***	***III***	***IV***	***V***	***VI***	***VII***	***VIII***	***IX***
Eigenvalue	0.2839	0.1095	0.0417	0.0192	0.0139	0.0074	0.0035	0.0008	0.0001
Percentage of variability	59.17	22.81	8.68	4.01	2.90	1.54	0.72	0.17	0.03

Table (V-6): Eigenvalues of the covariance matrix.

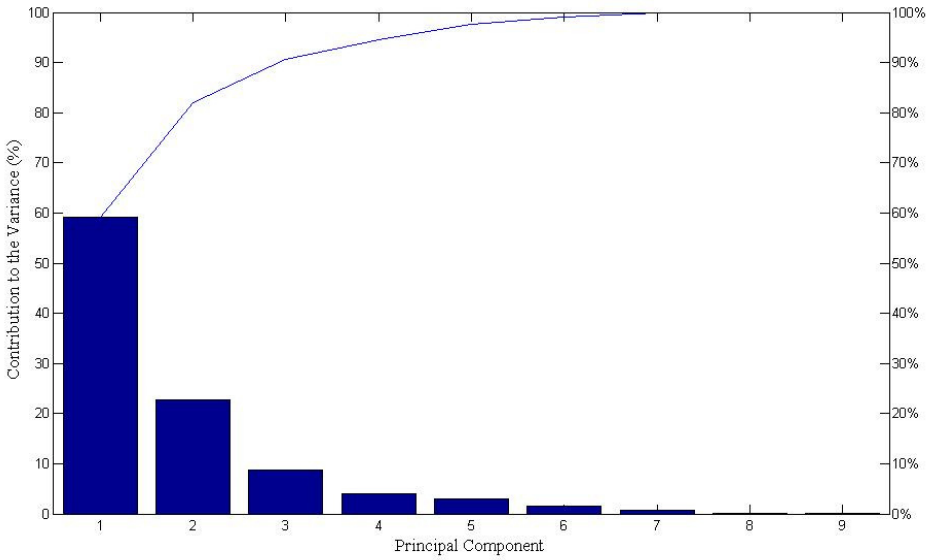

Figure (V-I): The percentage of total variability described by each principal component.

variable	*Principal component*								
	I	***II***	***III***	***IV***	***V***	***VI***	***VII***	***VIII***	***IX***
B	-0.52	-0.75	-0.22	-0.26	-0.05	0.19	-0.07	0.02	-0.01
h_e	0.17	0.04	0.29	-0.86	-0.24	-0.29	0.00	-0.02	0.02
h_e/B	0.15	0.15	0.15	-0.24	0.08	0.91	0.20	0.05	-0.06
S_0	-0.48	0.35	0.29	0.02	-0.17	0.14	-0.67	0.22	0.13
S_c	0.02	-0.25	0.52	0.10	0.32	-0.13	0.09	0.61	-0.40
$\sqrt{S_0}$	-0.56	0.23	0.24	0.10	-0.33	-0.06	0.57	-0.22	-0.28
$\sqrt{S_c}$	0.05	-0.30	0.65	0.18	0.15	0.03	-0.01	-0.49	0.44
S_0 / S_c	-0.18	0.17	-0.05	-0.20	0.65	-0.05	-0.22	-0.47	-0.45
$\sqrt{S_0 / S_c}$	-0.32	0.23	-0.12	-0.19	0.50	-0.12	0.34	0.28	**0.58**

Table (V-7): Eigenvectors of the covariance matrix.

variable	*Principal component*							
	I	***II***	***III***	***IV***	***V***	***VI***	***VII***	***VIII***
B	-0.58	-0.71	-0.21	-0.27	-0.07	0.17	0.07	-0.01
h_e	0.18	0.02	0.31	-0.88	0.17	-0.26	-0.01	0.02
h_e/B	0.16	0.13	0.15	-0.22	-0.30	0.87	-0.15	-0.08
S_0	-0.49	0.43	0.25	-0.04	-0.04	0.07	0.71	-0.09
S_c	0.01	-0.25	0.54	0.18	-0.18	-0.16	-0.11	**-0.73**
$\sqrt{S_0}$	-0.58	0.32	0.19	0.02	0.33	0.04	-0.64	0.03
$\sqrt{S_c}$	0.03	-0.30	0.66	0.23	-0.02	0.04	0.06	0.64
S_0 / S_c	-0.18	0.18	-0.04	-0.11	-0.85	-0.33	-0.22	0.20

Table (V-8): Eigenvectors of the covariance matrix.

variable	*Principal component*			
	I	***II***	***III***	***IV***
B	-0.80	-0.55	0.15	-0.22
h_e	0.21	-0.12	-0.52	-0.82
$\sqrt{S_0}$	-0.57	0.73	-0.38	-0.02
$\sqrt{S_c}$	-0.02	-0.39	-0.76	0.53

Table (V-9): Eigenvectors of the covariance matrix.